FINAL REPORT

THREE-DIMENSIONAL ANALYSIS

OF

INDUCER FLUID FLOW

By

PAUL COOPER and HEINRICH B. BOSCH

Prepared for

NATIONAL AERONAUTICS AND SPACE ADMINISTRATION

FEBRUARY 11, 1966

Contract NAS 3-2573

Technical Management
NASA Lewis Research Center
Cleveland, Ohio
Liquid Rocket Technology Branch
Werner R. Britsch

TRW *ACCESSORIES DIVISION*

TRW INC. • 23555 EUCLID AVENUE
CLEVELAND, OHIO 44117

ABSTRACT

Analytical studies were conducted to provide means for improving
the design of inducers for high-speed, high-flow rocket engine pumps.
Exact and approximate methods are presented for obtaining three-
dimensional solutions to turbomachine flows with losses and vapori-
zation, and results are presented for two sample inducers. The exact
method solves four non-linear differential equations of motion simul-
taneously by finite-difference and relaxation techniques that employ
a "total residual" concept. Conclusions on inducer performance and
design are made on the basis of several approximate solutions of both
incompressible and two-phase flows, together with analysis of fluid
thermal and scale effects. Fortran IV listings of the analysis com-
puter programs are presented.

ACKNOWLEDGMENTS

TABLE OF CONTENTS

TABLE OF CONTENTS (Con't.)

LIST OF FIGURES

LIST OF FIGURES (Continued)

LIST OF TABLES

THREE-DIMENSIONAL ANALYSIS OF INDUCER FLUID FLOW

By Paul Cooper and Heinrich B. Bosch
TRW Accessories Division

SUMMARY

This report presents the results of three-dimensional analytical studies of inducer fluid flow performance. A system of equations and boundary conditions is presented for any general continuum flow. Specifically, two-phase flow and losses are contemplated, and we employed a thermodynamic equilibrium model to describe these. The bubbles in two-phase flow are assumed to be infinitesimal in size and infinitely many in number, thus allowing continuum treatment.

An exact method was employed for solving the resulting four simultaneous nonlinear differential equations, boundary conditions and other relations by finite difference methods. A relaxation process makes those corrections to an initial field such that the "total residual" of the field is reduced sufficiently. Several solutions were obtained; first, of simple problems having known answers, and finally for two sample, variable-lead helical inducers (6.2° and 12° inlet tip blade angles respectively) on coarse grids. The validity of the method for both two-phase and liquid flows was established empirically. Studies of these results indicate that more accurate solutions can be obtained with finer grids.

An approximate method of solution was also developed to obtain rapid solutions for analyzing the resulting inducer performance and fluid and scale effects. Curves of average pressure-rise versus net positive suction head (NPSH) for the two sample inducers were obtained for different values of the thermodynamic vaporization parameter implied by the model. These results appear to have some correlation with existing theory on fluid effects or scaling, and they lead to conclusions on the character of the flow at various values of NPSH. Studies of these theories and data have indicated the areas of design optimization that can be undertaken with the analysis methods presented. Empirical modifications to the equilibrium model of the programs would give a more accurate description of the two-phase flow and losses. They would also account for thermodynamic non-equilibrium effects to the extent that they are not distinguishable in the test data employed for such modifications. Fortran IV listings for both analysis methods are included.

INTRODUCTION

Because of their ability to pump fluids under cavitating conditions, inducers are employed for pressurizing the inlets of high speed, high pressure rocket engine pumps. To predict inducer performance and inlet pressurization requirements for various fluids and speeds and to improve design methods, a precise knowledge of the internal flow is required. Incompressible, lossless, approximate analysis methods derived from the work of Stanitz (reference 1) and Hamrick et al (reference 2) are available, (references 3, 4, 5). However the typically two-phase flows with loss that occur in inducers lead to loading distributions and overall performance that cannot be described by an entirely single-phase isentropic flow analysis. Thus the design approaches for inducers generally ignore the blade-to-blade flow field effects and utilize blade element methods with empirically distributed losses (reference 6); the overall sizes, speeds and average velocities being determined as one-dimensional consequences of basic suction parameter requirements (reference 7).

The present program was instituted to obtain three-dimensional methods of analyzing the inducer flow field and to apply the results to the improvement of design criteria, performance prediction and scaling laws in continuation of similar work performed under a previous contract (reference 8).

Our main effort was directed to obtaining an exact three-dimensional method of solution that would allow the inclusion and easy modification of two-phase and loss effects. Of several approaches that we investigated, the successful one was the simplest, obtaining solutions directly in terms of the pressure and three velocity components. At first we attempted what appeared to be a simpler dual-stream-function analysis of the relative flow field (using techniques similar to those of references 9, 10, 11), but complexities in the iteration and the boundary conditions arose (see Appendix B). Starting with the vector momentum and continuity equations of Section I and allowing for whatever state, energy and loss relations would be necessary to describe the real fluid effects, we reduced the basic problem to one of solving four scalar non-linear partial differential equations (Section II. A. 1) throughout the relative flow field, which includes the region within an inducer channel as well as the extensions of this region upstream and downstream. We solve the four scalar equations together with an equation of state by applying each of them in finite-difference form to all points of a general, non-orthogonal grid which we construct in the relative flow field. (Appendix A develops the transformations required to convert finite differences in this grid to derivatives in the usual right-circular-cylindrical coordinate system used for the equations.) The solution emerges by the application of corrections to assumed values of the unknowns at each point in cyclic fashion. These corrections are those which reduce the "total residual", i. e., the sum of the squares of the residuals of each of the four finite difference equations at all points in the field.

Before obtaining inducer solutions by this method, we checked it on two simpler problems for lossless axial flow through a paddle wheel channel. The first problem was wheel type flow, for which we obtained satisfactory solutions to both incompressible and two-

2

phase flow, using a barotropic vaporization relation for the latter. In the second problem we verified our solution to incompressible, irrotational flow with the results in Stanitz's three-dimensional potential-flow solution (reference 12). Both of these simple problems revealed effects of grid point density and the total number of unknowns on the resultant accuracy and calculation times. Finally we obtained incompressible, lossless solutions to the flows in two sample, variable-lead, radial-element-bladed inducers having inlet tip blade angles of 6.2° and 12° respectively. While accuracy was reasonable for the number of grid points used, our present understanding of the problem indicates that finer grid meshes will improve this accuracy.

Further iteration would normally be required to obtain completed solutions by altering the positions of the initially assumed upstream and downstream extensions of the blades until they are unloaded. Another solution of this type for the 12° inducer with two-phase, lossless flow demonstrated that no additional complications or calculation times are required for the inclusion of these real fluid effects.

In addition to the exact method of three-dimensional solution, we introduced (Section III) a more rapid, approximate method to assist in the investigations of design, performance, and scaling parameters. This method assumes the flow to be restricted to annuli bounded by stream surfaces of revolution whose upstream locations (in our case, at the blade leading edge) are fixed. Two-phase effects in an approximate blade-to-blade solution are taken into account using the barotropic state relation. The solution is obtained by adjusting the positions of the stream surfaces to achieve simple meridional equilibrium along quasi-normals at several stations from inlet to outlet. We obtained solutions by this method to the 6.2° and 12° sample inducers, and correlations with the results of the exact method are presented. We obtained further solutions with loss and two-phase flow, demonstrating the shifts of loading and velocity distributions that occur due to these effects, together with the deterioration in overall performance that occurs when the net positive suction head is reduced (Section IV). These theoretical runs also show the changes in performance that occur with corresponding variations of the scaling or fluid vaporization parameters, giving substance to certain theories of thermodynamic effects on performance first advanced by Stepanoff (references 13 and 14).

We have included Fortran IV digital computer programs (Appendixes C and D) for both methods of analysis, which are applicable to any shapes of inducer hub, shroud and blades. The approximate method is best suited to rapid analysis of performance, or for determining whether the geometry in question should be analyzed by the longer, exact program. Thus the results of this work are methods for obtaining reasonable approximations of actual inducer flows, giving overall pressure rise and efficiency and radial distributions of average pressure and velocity at exit, as well as complete distributions of fluid density, pressure and velocity throughout the flow channel.

A	cross sectional area or passage area normal to associated velocity component
a, b, c	direction cosines of wall boundary, (equation II. 9)
a, b, c	variable-lead constants of blade pressure surface, (equation D. 1 See figures II. 12 and II. 18).
B	fluid thermodynamic constant, $(= \rho_f \, T^*)$
B*	blade force coefficient, (equation III. 6)
b	blade height
D	diameter
D	number of independent discrete variables, (equation II. 14)
D	diffusion factor, (Section IV. A. 2 only)
D_h	hydraulic diameter $(= \dfrac{4A}{p})$
E	number of governing finite difference equations, (equation II. 13)
F	friction force per unit mass, (equation I. 2)
f	friction loss factor, (equation I. 14)
g_0	constant relating mass and force in Newton's second law
H	total head $(= \dfrac{p}{\rho} + \dfrac{V^2}{2\,g_0}$
H_i	total energy per unit mass or ideal total head, (equation IV. 24)
$H_{L, d}$	diffusion head loss, (equation IV. 9)
$\Delta \overline{H}$	mass-averaged total head rise of inducer, (equations II. 30 and III. 25)
h	enthalpy
i	average angle of incidence between the blade and relative streamline direction at inlet $(= \beta_{b, 1} - \beta_{flow, \, 1})$
J	mechanical equivalent of heat
k	cavitation number, (equation III. 38)
L	loss of available energy per unit mass, (equation I. 9)
M	integer in relaxation process, (see Section II. A. 3)
m	distance along streamline or meridional plane, (figure III. 1)

* This list does not apply to Fortran symbols, which are defined in Appendixes B and C.

1 See Note on Units of Numerical Quantities at end of this list.

N	inducer rotative speed in revolutions per unit time $\left(= \dfrac{\Omega}{2\pi}\right)$
n	distance in direction normal to streamline or surface
n'	distance from hub in quasi-normal direction (figure III.1)
n_b	number of blades
NPSH	net positive suction head $\left(\equiv \dfrac{\bar{P}_1 - p_{sat}}{\rho_f}\right)$
P	total pressure; viz., the pressure resulting from isentropic stagnation (only in incompresssible flow does $P = p + \dfrac{\rho V^2}{2g_o}$)
P_s	shaft power delivered to fluid, (equations II.31 and III.29)
$\hat{P}_s$	power coefficient $\left(\equiv g_o\, P_s / \rho_f\, \Omega^3\, r_t,1^5\right)$
p	static pressure (called "pressure")
p	perimeter of flow channel
P_{sat}	vapor pressure
$\Delta \hat{p}_v$	dimensionless local depression of pressure below vapor pressure, (equation IV.8)
Q	total volume flow rate
q	volume flow rate per channel
R	residual, (equation II.5)
R_m	machine Reynolds number, (equation III.31)
R_T	total residual, (equation II.15)
R*	star residual, (equation II.16)
r	radial coordinate: radius from axis of rotation
r_c	radius of curvature of streamline in meridional plane
RMS	root-mean-square residual, (equation II.18)
S	suction specific speed, (equation III.37), IV.15 and IV.16). Note that these equations define a unitless or truly dimensionless S. To convert to the usual, large numerical values of S based on gpm, rpm and $\dfrac{\text{ft-lbf}}{\text{lbm}}$, multiply the unitless S by 17,180
s	entropy
T	temperature
T*	thermodynamic vaporization constant $\left(= \dfrac{B}{\rho_f}\right)$
t	time
t	blade thickness (equation A.2)

T_q	torque
TSH	difference in values of $NPSH_{min}$, (see figure IV. 6 and equations IV. 19 and IV. 20). Called "thermodynamic suppression head".
U	blade velocity ($= \Omega r$)
U	streamline unbalance, (equation III. 10)
u	radial component of relative velocity ($= V_r$)
V	absolute velocity of fluid
v	circumferential component of relative velocity ($= V_\theta - \Omega r$)
$\left(\dfrac{V}{L}\right)_p$	"performance $\dfrac{V}{L}$ ", (equations IV. 19 and IV. 20)
W	velocity of fluid relative to inducer
w	axial component of relative velocity ($= V_z$)
w	mass flow rate (equation III. 4)
w_T	total mass flow rate, (equations II. 27 and III. 24)
x	two-phase fluid quality (equation IV. 6)
z	axial coordinate: distance from selected point on blade leading edge
α	successive variation ratio (see Section II. A. 3)
α , β, γ	general coordinate surfaces, (see Appendix A)
β	angle between circumferential direction and blade or relative flow direction
Γ	circulation, (equation II. 36)
γ	angle between axial and meridional streamline directions, (figure III. 1)
γ'	angle between quasi-normal and radial direction, (figure III. 1)
Δ, δ	prefixes meaning "change of" or "increment of"
δ	angle of deviation of relative flow (W) from blade ($= \beta_b - \beta_{flow}$)
δ^*	boundary layer displacement thickness
ϵ	convergence constant (equation II. 19 and III. 11)
ζ	diffusion loss factor, (equation I. 15)
ζ_c, ζ'	diffusion coefficients, (equation IV. 10)
η	efficiency, (equation III. 23)
$\overline{\eta}$	overall efficiency, (equations II. 32 and III. 30)
Θ	vaporization parameter, (equation III. 36)
θ	circumferential coordinate

λ	distance in direction of relative streamline
λ	stream function constant, (Appendix B only)
μ	three-dimensional stream function (Appendix B only)
ν	kinematic viscosity
ξ	hub-to-tip radius ratio
ρ	density
$\bar{\rho}$	blade-to-blade average density, (equation III. 19)
σ	blade solidity (= blade tip arc length/exit tip circumference)
σ	three-dimensional stream function (Appendix B only)
$\mathcal{T}$	circumferential direction vector, (figure II.1)
$\varnothing$	flow coefficient, (equation III. 34)
ϕ	velocity potential
Ψ	inducer total head rise coefficient, (equation III. 33)
Ψ_p	inducer static pressure head rise coefficient, (equation II. 21)
Ψ_s	dimensionless NPSH, (equation IV. 11)
Ψ_{sp}	cavitation coefficient, (equation III. 35. Based on static pressure, as with k).
Ω	inducer angular velocity in radians per unit time
$\bar{\omega}$	loss coefficient, (equation III. 22)

SUBSCRIPTS

b	blade
ex	blade trailing edge (exit)
f	liquid (applies to properties ρ and s only)
f	if all mass flowing existed as liquid
fg	change from liquid to vapor at constant temperature and pressure
g	vapor
h	hub
i	streamline index used in approximate analysis, where i = 1 at hub and i = q_i at shroud (see figure III. 1)

i, j, k	grid point indexes used in exact analysis
i'	annulus index used in approximate analysis; where i' = 1 in annulus adjacent to hub, and i' = q_i -1 in annulus adjacent to shroud. Fluid quantities so modified are assumed to exist midway between the two adjacent streamlines, (see figure III. 1)
j	station index used in approximate analysis (see figure III. 1) j = 1 at inlet; j = q_j at outlet
j'	station halfway between j and j - 1 used in approximate analysis, (see figure III. 4).
M	mean
m	meridional component
NC	value at non-cavitating conditions, (entirely liquid flow field)
p	pressure side of blade or channel
q_i, q_j	(see definitions of subscripts i and j respectively)
r	radial component
s	suction side of blade or channel
sat	at saturated liquid conditions
T	total
t	blade tip (at shroud. Also at inlet unless otherwise specified)
z	axial component
θ	circumferential component
o	far upstream
1	blade leading edge (inlet) except in Appendix B*
2	blade trailing edge (exit) except in Appendix B*

SUPERSCRIPTS

⟶	vector quantity
o	unit vector
—	average
⋀	dimensionless

*NOTE: the words "inlet" and "exit" (or "outlet") apply to blade leading and trailing edges respectively—not to the mathematical upstream and downstream throughflow boundaries which can be at different locations.

Note on Units of Numerical Quantities

Unless otherwise specified, values of all dimensional quantities are presented in units of the primary dimensions which are characteristic for inducers:

Primary dimension	Characteristic value or unit
Length	$r_{t,1}$
Time	$\dfrac{1}{\Omega}$
Mass	$\rho_f \, r_{t,1}^{3}$
Force	$\dfrac{\rho_f}{g_o} \, \Omega^2 \, r_{t,1}^{4}$

Thus the data is effectively dimensionless, each numerical quantity being expressed as some multiple of a characteristic value. Typical results for specific quantities are as follows:

Quantity	Characteristic Value
Density	ρ_f
Velocity	$\Omega \, r_{t,1}$
Pressure	$\dfrac{\rho_f}{g_o} \, \Omega^2 \, r_{t,1}^{2}$
Mass flow rate	$\rho_f \, \Omega \, r_{t,1}^{3}$

In this system, ρ_f, $r_{t,1}$, Ω, and g_o will have numerical values of 1, since they are each equal to their respective characteristic values.

Values of coefficients and dimensionless parameters are unitless by definition.

9

SECTION I

FLUID FLOW RELATIONS

The physical assumptions, basic equations and boundary conditions required for obtaining three-dimensional solutions of the flow field for an inducer or other turbomachine (see figure I.1) are presented in this section. Methods of representing fluid state and losses and of determining required boundary conditions are discussed.

A. The Flow Model

In order to have a complete and tractable turbomachine performance analysis, the continuum flow concept is desirable so that the flow field does not need to be broken into parts requiring different mathematical procedures for single- and two-phase regions. Therefore, depending on the local state requirements, the fluid is either a liquid or a variable-density homogeneous, two-phase medium (with infinitely many small bubbles dispersed in a fog-like manner). The flow is assumed to be adiabatic, steady and cyclic, (i.e., similar in all channels of the machine or uniformly periodic).

1. Equations of Motion

In an absolute frame of reference, the general vector equations of continuity and momentum for such a flow are respectively as follows:

$$\nabla \cdot (\rho \vec{V}) = 0 \tag{I.1}$$

$$\frac{g_0}{\rho} \nabla p + (\vec{V} \cdot \nabla) \vec{V} + \vec{F} = 0 \tag{I.2}$$

where all symbols are defined in a table preceding this section. The friction force vector F appears in reference 15, page 45, and is not a body force term. It is a general, and convenient way of including any suitable loss mechanism. The classical transformation of these two equations into one equation in terms of velocity potential (reference 12) is not possible if we wish to retain the generality required for the typical solutions with two-phase flow and various forms of loss description. Thus a simultaneous solution of the equations of motion is necessary, and this is accomplished conveniently if we describe motion in the field relative to the rotating blade channel (figure I.1). The resulting relative velocities are easily converted to absolute velocities.

The continuity and momentum equations (I.1, I.2) are expressed as follows in terms of the relative velocity vector $\vec{W} = \vec{V} - \vec{\Omega} \times \vec{r}$:

Continuity $\qquad \nabla \cdot (\rho \vec{W}) = 0 \tag{I.3}$

Direction of
Rotation

a) View Into Inlet

Shroud

Hub

Axis of
Rotation

b) Meridional View

Downstream
Throughflow
Boundary

Direction
of
Rotation

Blade Trailing
Edge

Blade Leading
Edge

Pressure Side
of Channel

Stagnation Stream
Surface
(Extension of
Blade)

Suction Side of
Channel

Upstream Throughflow
Boundary

c) Developed View on
Cylinder of Radius r

$\vec{W}$

$\vec{\Omega r}$

$\vec{V}$
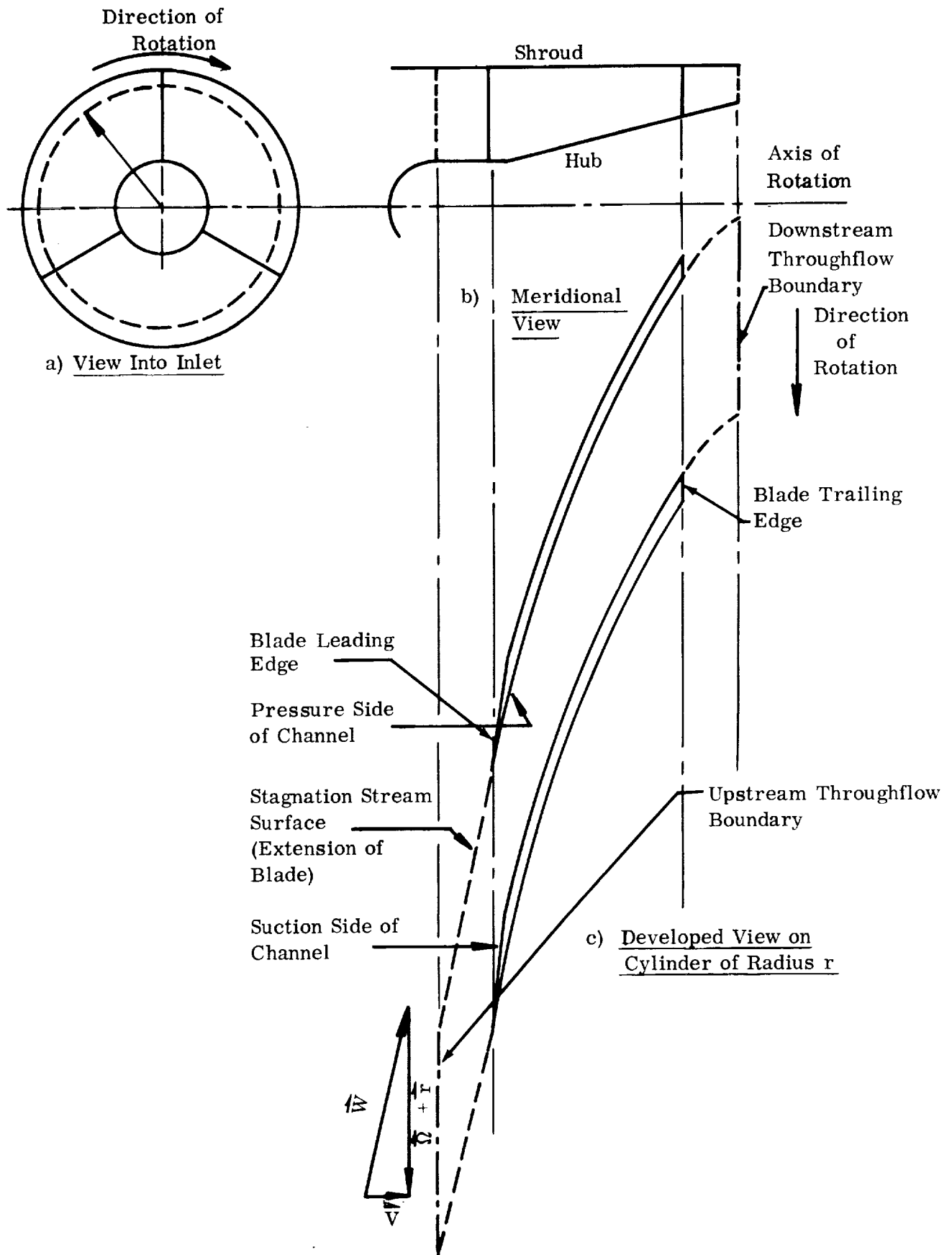
FIGURE I. 1. TYPICAL FLOW BOUNDARIES, INCLUDING UPSTREAM AND DOWNSTREAM
FLOW REGIONS

11

$$\underline{\text{Momentum}} \quad \frac{g_o}{\rho} \nabla p - \Omega^2 \vec{r} + (\vec{W} \cdot \nabla) \vec{W} + 2 \vec{\Omega} \times \vec{W} + \vec{F} = 0 \tag{1.4}$$

where Ω is the angular velocity of the channel. The density ρ is given by any convenient equation of state at all points, generally as follows:

$$\underline{\text{State}} \quad \rho = \rho \, (p, \; h, \; \vec{W}, \; \nabla p) \tag{1.5}$$

where the enthalpy h is found from the adiabatic energy equation <u>along</u> streamlines:

$$\underline{\text{Energy}} \quad dh = d \left(\frac{\Omega^2 r^2}{2 g_o J} \right) - d \left(\frac{W^2}{2 g_o J} \right) \tag{1.6}$$

Thus, with an expression for F, we have a complete system of equations; viz., (I.3) through (I.6). (Note that equations I.1 and I.2 remain interchangeable with I.3 and I.4 respectively). Observe that no requirements of thermodynamic equilibrium are imposed by this system.

2. Relations for Two-Phase Flow and Loss Effects

The forms of the state and $\vec{F}$ relations can be changed to suit the particular real fluid effects of the problem. Specific expressions for them appear and are clearly noted in the Fortran IV listings of Appendixes C and D, but they may be changed easily and without effect on the rest of the program. These expressions, which we employed to account for two-phase effects and losses, are based on the following assumptions (as in reference 8):

a) Thermodynamic equilibrium exists; i.e., the $\vec{W}$ and ∇p terms are absent from the state equation (I.5).

b) The fluid is liquid for pressure p above the saturation pressure p_{sat}. It is a homogeneous, two-phase, compressible continuum for $p < p_{sat}$; i.e., bubbles are considered infinitesimal in size and infinitely many in number.

c) The fluid is barotropic; i.e., $\rho = \rho \, (p)$. Also, the liquid density is constant. This eliminates also the h term from the state equation (1.5), and makes p_{sat} a constant.

d) Losses are caused by friction and diffusion and are point functions of velocity and position.

Assumption (a) ignores recent research on venturi flow (reference 16) but is considered to be a reasonable approximation for the turbulent, more disturbed flows in an inducer. Existing performance correlations of fluid thermal effects

are based on thermodynamic equilibrium or a uniform departure from it in all cases. The continuum requirement of assumption (b) is an essential characteristic of the problem as already formulated.

The constant liquid density in assumption (c) is acceptable for the relatively low pressure ranges encountered in inducers. However, for two-phase flow, any losses result in a pressure defect (as compared to the no-loss case) and an entropy increase, (see equations I. 4 and I. 12), both of which would generally affect the density. Barotropicity exists if density is a function of the pressure only --- a first order assumption for the adiabatic vaporization-condensation process being considered. For example, with typical values of pressure rise, liquid hydrogen (reference 19) has much greater changes of p_{sat} due to losses than most other fluids; yet in an 80% efficient inducer, the value of p_{sat} increases by less than 1% of the static pressure rise of the machine--- much of this increase occurring at higher (liquid) pressures.

Our barotropic state expression was developed in reference (8) and is as follows:

$$\rho = \begin{cases} \rho_f & , \ p \geq p_{sat} \\[2em] \dfrac{\rho_f}{1 + T^* (p_{sat} - p)} & , \ p < p_{sat} \end{cases} \tag{1.7}$$

where

$$T^* = \left[\frac{ds_f}{dp} \ \frac{\frac{\rho_f}{\rho_g} - 1}{s_{fg}} \right]_{sat} = \frac{B}{\rho_f}$$

We assume that T^* is essentially unchanged for a small value of quality, which yields a large volume of vapor. This approach is justified by an examination of charts of thermodynamic properties. Observe that the assumption (c) of barotropicity eliminates the need for the energy equation I. 6). However, equation (I. 6) would be required if two-phase barotropicity is unacceptable; and a new state expression in terms of p and h would have to be included. These relations can easily be added to the FORTRAN listings at the same places occupied by equation (I. 7). Also required with the energy equation would be the methods for following streamlines should a non-uniform distribution of absolute stagnation enthalpy and whirl be imposed at inlet.

With the exception of blade tip leakage allowances, assumption (d) is probably true, especially because of the rather long flow passages and the turbulent motion and the sudden diffusions due to bubble collapse. In effect, it assumes

13

that the momentum losses due to friction and diffusion are immediately distributed from blade-to-blade across the flow passage, (reference 8). Secondary flow effects on these losses are included, as discussed in Section IV. A. 2. Using assumption (a), we can say that the work $Fd\lambda$ done against friction as a particle moves through a distance $d\lambda$ along a streamline is a <u>loss</u>, dL, of available energy, (for adiabatic flow; i.e., no heat transfer across streamlines), (reference 20):

$$dL = \vec{F} \cdot \vec{d\lambda} = g_0 \, J \, T \, ds \tag{I. 9}$$

This connects the losses with the momentum equation and the vector $\vec{F}$, which may now be expressed as

$$\vec{F} = \frac{dL}{d\lambda} \frac{\vec{W}}{|W|} \tag{I. 10}$$

since the friction force vector is always parallel to the streamline direction λ. The magnitude $\frac{dL}{d\lambda}$ is found from equation (I. 13).

Also for thermodynamic equilibrium it is interesting to note that

$$dh = \frac{dp}{\rho J} + T \, ds \tag{I. 11}$$

which, when substituted with equation (I. 9) into the energy equation (I. 6), gives the familiar streamline component equation of the vector momentum equation (I. 4):

$$\frac{g_0 \, dp}{\rho} = d \left(\frac{\Omega^2 r^2}{2} \right) - d \left(\frac{W^2}{2} \right) - dL \tag{I. 12}$$

Our form for the loss dL utilizes a combination of friction and diffusion relations dependent upon the velocity and the local hydraulic diameter of the channel:

$$dL = \underbrace{f \frac{d\lambda}{D_h} \frac{W^2}{2}}_{\text{FRICTION}} - \underbrace{\zeta d \left(\frac{W^2}{2} \right)}_{\text{DIFFUSION}} \tag{I. 13}$$

where the diffusion term applies only when $\frac{dW}{d\lambda} < 0$, and $D_h = 4A/p$. Specific values of the friction and diffusion factors are presently those determined by the smooth-pipe (reference 21) and sudden-enlargement relations (Section IV), respectively:

$$f = 0.00714 + \frac{0.6104}{\left(\frac{W \, D_h}{\nu} \right)^{0.35}} \tag{I. 14}$$

14

$$\zeta = \frac{1 - \dfrac{W + \Delta W}{W}}{1 + \dfrac{W + \Delta W}{W}} \qquad (I.15)$$

where ΔW is the discontinuous diffusion occurring from incidence and bubble collapse, which are assumed to result in Borda-Carnot (sudden expansion type) losses, (see Figure IV. 2). That these relations give a fair indication of the losses is demonstrated in Section III. Further discussion about the merits of the factors f and ζ as here defined appears in Section IV. Note that the idea of losses as a function of position together with the pressure could be used to describe the leakage losses at the blade tip locations. Because of this method of describing losses, the only aspect of the boundary layers that we need to include in the analysis is an allowance for their displacement thicknesses when setting up the boundary conditions.

B. Boundary Conditions

Figure I.1 shows the boundaries of a typical inducer channel. We class them as follows:

    1) Wall boundaries

        a) Hub and shroud (not necessarily cylindrical or conical), and the pressure and suction sides of the channel (blades); all including estimated boundary layer displacement thicknesses.

        b) Extensions of the blades and hub and shroud; i.e., the upstream and downstream stagnation stream surfaces and other boundary surfaces.

    2) Throughflow boundaries: Upstream and downstream.

1. Wall Boundaries

The conditions that must be applied at the wall boundaries are as follows: First, since no fluid may pass across them,

$$\vec{W} \cdot \vec{n} = 0 \qquad (I.16)$$

where n is a vector normal to the surface. This is the only condition required at boundaries (1a). On the stagnation-stream-surface extensions of the blades (1b), however, we require the additional condition that they exert no load on the fluid. This condition is satisfied if the pressures are equal at any given r and z on each of two corresponding surfaces. Thus we also satisfy the requirement that the flow be uniformly periodic, since these surfaces are spaced uniformly about the axis; i.e., only their θ locations

15

differ and these by exactly $\frac{2\pi}{n_b}$, where n_b is the number of blades in the machine.

Boundaries (1b) must be coincident only with the stagnation stream surfaces that extend from the blades. For other locations, the three-dimensional velocity field would include and can be discontinuous at the stagnation stream surfaces. It is simpler for the boundaries to be located at such discontinuities. We understand this readily by calling to mind the three-dimensional corkscrew motion that superimposes itself on the relative throughflow field, as illustrated in figure I.2. For two-dimensional flow in the field I.1, view (c), there is no discontinuity in velocity as one passes from one channel to the next, except in the loss case, for which a discontinuity exists downstream (and upstream in the recirculating-flow case). So, even in two-dimensional problems, there are only special cases in which "quasi-boundaries" (reference 22) can be extended upstream and downstream in any direction (not necessarily that of the stagnation stream surface)-- on which one could apply simply the condition of uniform periodic behavior in all variables.

To solve the three-dimensional problem with the required unloaded stagnation stream surfaces, one must first assume their locations with care, keep them fixed and proceed with the calculations. Only a few cycles of computation by the exact method (Section II) will reveal the correctness of these locations; and they may then be changed as required to unload the surfaces (reference 8, page 4-34) and the calculations resumed.

The required extent of these upstream and downstream regions depends on the type of problem being solved. For example, in two-phase cases at design flow rates, where nearly complete unloading of the leading edge region occurs, there is generally very little influence of inducer flow on the upstream field. In that case, the upstream region with its stagnation stream surfaces could very probably be reduced in extent; (they were omitted altogehter -- both upstream and downstream in the approximate solution of Section III). Similar elimination of the downstream region may be possible quite often, since inducer blades are very lightly loaded (due to the high solidity), and the resulting relative exit deviation angles are small. In the general case, however, reference to the fields used in other work seems to indicate that an extension of each of these regions of approximately one channel width away from the blading would be sufficient for imposing uniform conditions on the throughflow boundaries (references 23 and 24) without introducing unrealistic results such as would be produced by external flow singularities.

Rotation
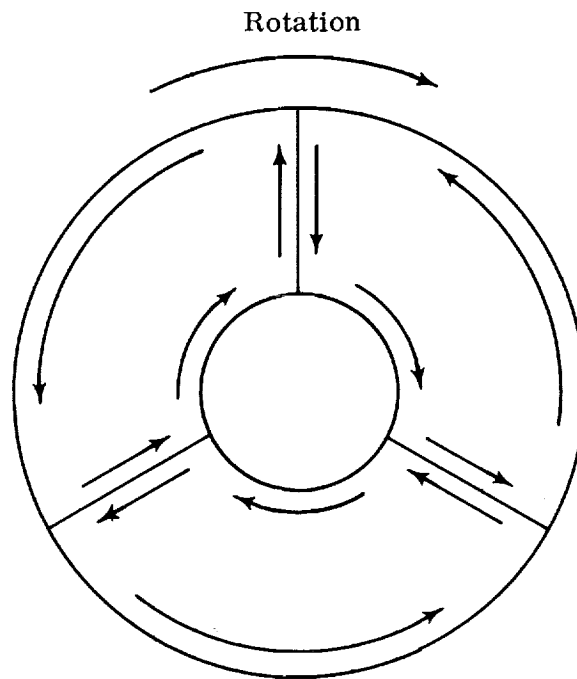
FIGURE I.2. RELATIVE EDDY-FLOW AT TYPICAL INDUCER CROSS SECTION.
Particularly characteristic of downstream through flow boundary.

2. Throughflow Boundaries

The mathematical conditions required at the throughflow boundaries are not so readily deduced from the kind of physical certainty that we had concerning the wall boundaries. Therefore, we conducted studies of other types of problems to determine the physical conditions that are implied by the known mathematical procedures of simpler examples. We could then translate these physical conditions into analytical statements in terms of the variables in our problem, just as we did for the wall boundaries. For example in a three-dimensional problem in terms of the velocity potential ϕ such that $\nabla^2 \phi = 0$, we must specify either ϕ or its normal derivative $d\phi/dn$ everywhere on all boundaries. Since $\vec{V} = \nabla \phi$, we interpret this as requiring a statement about the component of velocity normal to every point on the boundary. Furthermore, in order for the velocity potential ϕ to exist, a statement about the fluid rotation had to be made; viz, $\nabla \times \vec{V} = 0$. Also, if the rotation is specified at one point on a streamline, it will be automatically determined at all other points on that streamline. This is a consequence of the vorticity relations that are another form of the governing equation. Finally, if the pressure is known at one point in such a field, it can be determined everywhere else from the resulting velocity field; for example, by equation (I.4)

These observations lead us to the following conclusions about minimum required conditions on the throughflow boundaries in the general, three-dimensional problem:

a) Specify the relative rotation $\nabla \times \vec{W}$ over a complete cross section of the flow -- preferably at the upstream throughflow boundary, since that is where it is most likely to be known.

b) Specify the distribution of relative velocity component $\vec{W} \cdot \vec{n}$ normal to the upstream and downstream throughflow boundaries so as to satisfy continuity. (Note that this is also being done at the wall boundaries by equation (I.16)).

c) Specify the pressure p at one point -- again preferably on the upstream boundary.

The application of conditions (a) and (b) to the exact method of solution consists of specifying the distributions of the throughflow velocity and of the derivatives of the other two components on the upstream throughflow boundary (equation II.10, 11, 12). In the actual finite-difference procedure (Section II.A.2) this is accomplished by specifying the distributions of all three components of velocity on the upstream boundary, and of two of these components at the next throughflow station adjacent to that boundary. Condition (c) defines the pressure field -- and that of the

18

density ρ when a barotropic relation, e. g. equation (I. 7), is used. If a more general form of the state equation (I. 5) is required, the distribution of ρ or of the enthalpy h (which, with p, defines ρ) would also be needed at the upstream boundary.

We found that if any more complete information about the variables is available at the throughflow boundaries, it can greatly reduce the amount of calculation required to reach a solution. Such distributions must be compatible with the required ones; viz., conditions (a), (b), and (c). Thus we always specify a complete distribution of pressure at the upstream boundary, since the one that is compatible with the required velocity distributions can usually be determined easily.

Conditions (a), (b) and (c) are not necessarily the only set of minimum required boundary conditions upstream and downstream. An alternate set can be found; for example, it is possible to specify at the downstream boundary a distribution of velocity direction instead of the normal velocity component magnitude (condition (b)). We successfully solved two-dimensional examples of potential flow by both methods, and in Section II some of our earlier solutions by the exact methods were obtained by specifying (both components of) the directions at the downstream boundary.

Additional evidence that we have an adequate set of throughflow boundary conditions as discussed in the foregoing paragraphs can be obtained from the well-known procedures of approximate methods (reference 2). Our approximate solution (Section III) specifies the upstream distributions of all three velocity components and the compatible pressure distribution in addition to the necessary single value at a point. The downstream deviation angle distribution (one component of the direction) is specified. The restriction of the flow to annuli between stream surfaces of revolution about the axis of rotation probably accounts for the other component of downstream direction as well as the remaining parts of the upstream rotation distribution.

So it appears that conditions (a), (b) and (c) with or without substitution of downstream directions in (b) together with additional compatible distribution(s) are the proper throughflow boundary conditions. With the wall conditions discussed earlier (Section II. B. 1), we have a complete set of boundary conditions on our three-dimensional problems. Although there is considerable empirical evidence of their validity, further study would be required to obtain a rigorous mathematical proof of these conclusions (see, for example, references 25 and 26).

SECTION II

THREE-DIMENSIONAL SOLUTION (EXACT METHOD)

A. METHOD OF SOLUTION

In this section, the basic flow equations are expressed in scalar form and their finite-difference approximations are presented. Next, the numerical treatment of boundary conditions is examined and an algorithm is developed for a numerical solution of the system of finite-difference equations, and certain effects of grid size are discussed. Finally, the form of the results and their relationship to inducer performance is discussed.

1. Scalar and Finite-Difference Form of Basic Flow Equations

We construct a cylindrical coordinate system (figure II. 1) which rotates in the same direction at the same angular speed, Ω, as the flow channel (figure I. 1). This relative coordinate system is described by three mutually perpendicular unit vectors where $\overset{o}{r}$ points in the direction of increasing r, $\overset{o}{\tau}$ points in the direction of rotation, and $\overset{o}{z}$ points along the axis of rotation.

The components of the vector equation of momentum (I. 4) in the directions of r, θ and z are, respectively (reference 9),

$$\frac{g_o}{\rho} \frac{\partial p}{\partial r} + u \frac{\partial u}{\partial r} + \frac{v}{r} \frac{\partial u}{\partial \theta} + w \frac{\partial u}{\partial z} - \frac{1}{r} (v + r\Omega)^2 + F_r = 0 \tag{II. 1}$$

$$\frac{g_o}{r\rho} \frac{\partial p}{\partial \theta} + u \frac{\partial v}{\partial r} + \frac{v}{r} \frac{\partial v}{\partial \theta} + w \frac{\partial v}{\partial z} + \frac{uv}{r} + 2u\Omega + F_\theta = 0 \tag{II. 2}$$

$$\frac{g_o}{\rho} \frac{\partial p}{\partial z} + u \frac{\partial w}{\partial r} + \frac{v}{r} \frac{\partial w}{\partial \theta} + w \frac{\partial w}{\partial z} + F_z = 0 \tag{II. 3}$$

where u, v, and w are the radial, circumferential and axial components, respectively, of W, and F_r, F_θ and F_z are the corresponding components of the vector F.

The equation of continuity, in scalar form is

$$\frac{u}{r} + \frac{\partial u}{\partial r} + \frac{1}{r} \frac{\partial v}{\partial \theta} + \frac{\partial w}{\partial z} + \frac{1}{\rho} (u \frac{\partial \rho}{\partial r} + \frac{v}{r} \frac{\partial \rho}{\partial \theta} + w \frac{\partial \rho}{\partial z}) = 0 \tag{II. 4}$$

This system of four partial differential equations, together with the applicable relations for density and the scalar F's (equations I. 7 and I. 10) and the attendant boundary conditions (see Section I. B), constitutes the complete

20
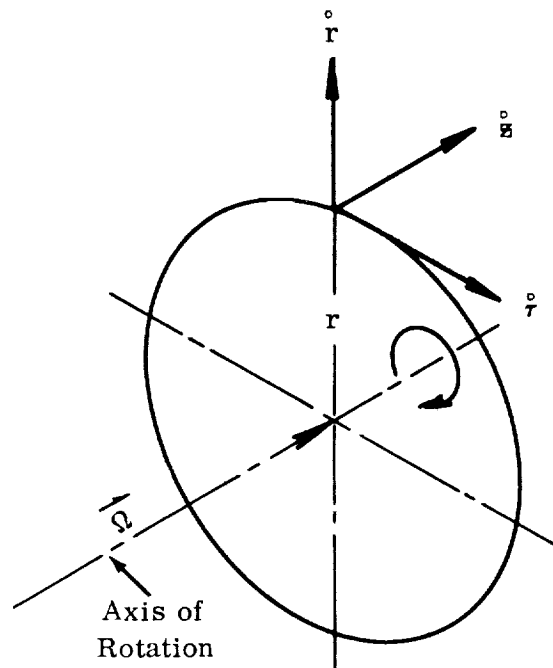
FIGURE II.1.   ROTATING COORDINATE SYSTEM AND RELATIVE BASE VECTORS

set of relations required. To obtain a numerical solution, we represent the flow field by a grid of points of intersection of three families of surfaces. Each such grid point is identified by three indexes as shown in figure II. 2.

Next, corresponding to each of the equations (II. 1) through (II. 4), four residuals are computed at each grid point as follows:

$$(R1)_{i,j,k} = \left\{ \frac{g_o}{\rho} \left[\frac{\partial p}{\partial r}\right] + u \left[\frac{\partial u}{\partial r}\right] + \frac{v}{r} \left[\frac{\partial u}{\partial \theta}\right] + w \left[\frac{\partial u}{\partial z}\right] \right.$$
$$\left. - \frac{1}{r} (v + r\Omega)^2 + F_r \right\}_{i,j,k} \tag{II. 5}$$

$$(R2)_{i,j,k} = \left\{ \frac{g_o}{r\rho} \left[\frac{\partial p}{\partial \theta}\right] + u \left[\frac{\partial v}{\partial r}\right] + \frac{v}{r} \left[\frac{\partial v}{\partial \theta}\right] + w \left[\frac{\partial v}{\partial z}\right] \right.$$
$$\left. + \frac{uv}{r} + 2u\Omega + F_\theta \right\}_{i,j,k} \tag{II. 6}$$

$$(R3)_{i,j,k} = \left\{ \frac{g_o}{\rho} \left[\frac{\partial p}{\partial z}\right] + u \left[\frac{\partial w}{\partial r}\right] + \frac{v}{r} \left[\frac{\partial w}{\partial \theta}\right] + w \left[\frac{\partial w}{\partial z}\right] + F_z \right\}_{i,j,k} \tag{II. 7}$$

$$(R4)_{i,j,k} = \left\{ \frac{u}{r} + \left[\frac{\partial u}{\partial r}\right] + \frac{1}{r} \left[\frac{\partial v}{\partial \theta}\right] + \left[\frac{\partial w}{\partial z}\right] \right.$$
$$\left. + \frac{1}{\rho} \left(u\left[\frac{\partial p}{r}\right] + \frac{v}{r} \left[\frac{\partial p}{\partial \theta}\right] + w \left[\frac{\partial p}{\partial z}\right] \right) \right\}_{i,j,k} \tag{II. 8}$$

The values of the first three residuals are measures of the local non-equilibrium in the radial, circumferential and axial directions, respectively, and $(R4)_{i,j,k}$ gives a measure of the extent to which local mass conservation is violated.

The local density $\rho_{i,j,k}$, is computed from a state equation (see Section I. A. 3) and the terms $(F_r)_{i,j,k}$, $(F_\theta)_{i,j,k}$ and $(F_z)_{i,j,k}$ from given loss formulae, if any. These four differential equations will yield residuals for assumed distributions of the variables, u, v, w and p. It would be possible to assume a ρ distribution also — which would then cause the state equation (I. 7) to yield residuals. However, this is not necessary, since we have an explicit algebraic relation for ρ in terms of the (assumed) p values (equation I. 7). A similar statement can be made about the F terms.

22
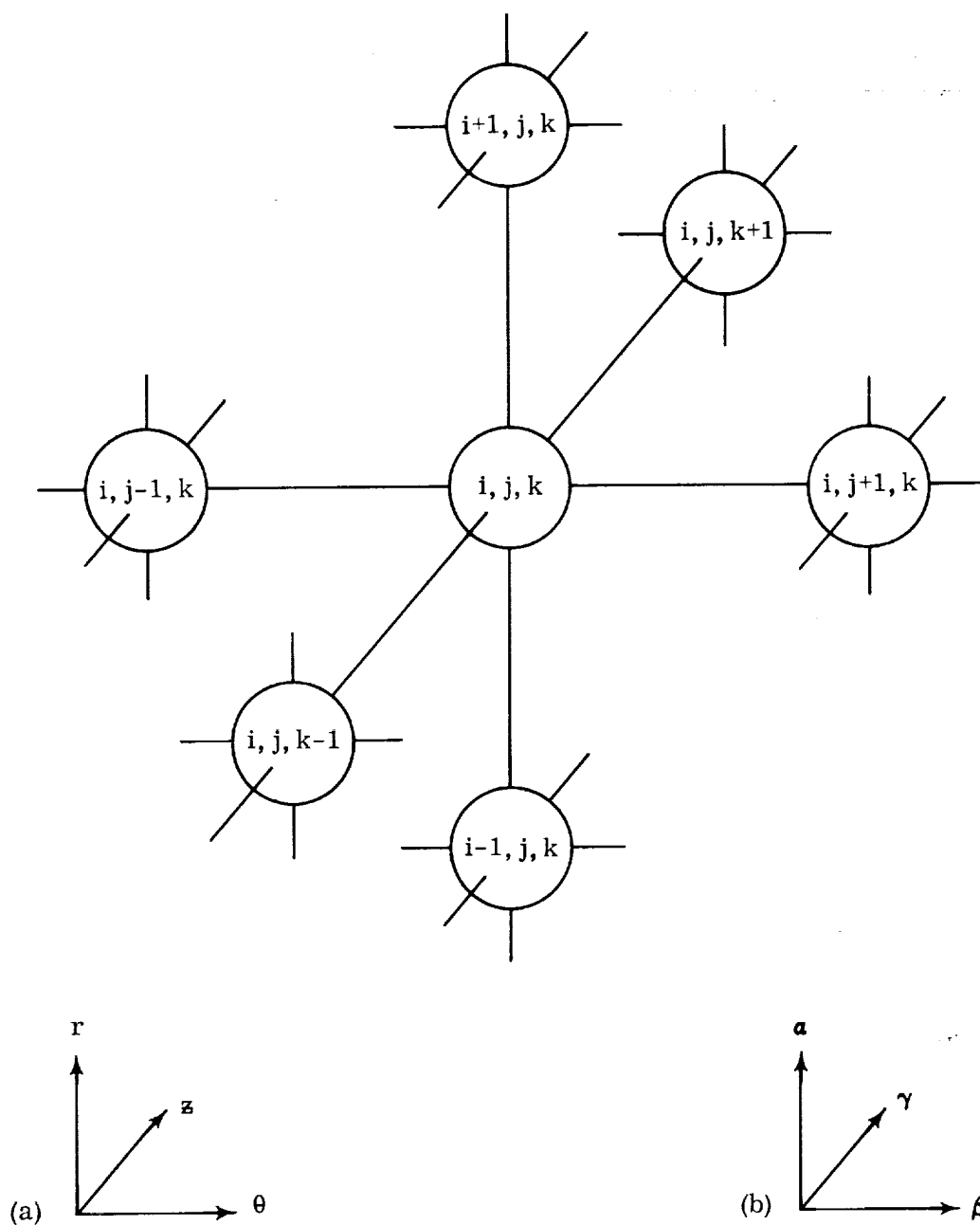
FIGURE II.2. TYPICAL "STAR" OF GRID POINTS FOR FINITE-DIFFERENCE
EQUATIONS IN (a) CYLINDRICAL OR (b) GENERAL COORDINATE SYSTEMS.

All indicated partial derivatives are computed from their usual, second-order, finite-difference approximations (reference 27, pp. 245-6). For example, at an internal point for a cylindrical coordinate grid,

$$\left[\frac{\partial p}{\partial r}\right]_{i,j,k} = \frac{p_{i+1,j,k} - p_{i-1,j,k}}{2\Delta r}$$

$$\left[\frac{\partial u}{\partial \theta}\right]_{i,j,k} = \frac{u_{i,j+1,k} - u_{i,j-1,k}}{2\Delta \theta}$$

$$\left[\frac{\partial w}{\partial z}\right]_{i,j,k} = \frac{w_{i,j,k+1} - w_{i,j,k-1}}{2\Delta z}$$

where Δr, $\Delta \theta$ and Δz are the finite increments between grid points in the radial, circumferential and axial directions, respectively.

At a boundary point, an appropriate one-sided difference expression is used. For example, if the point (i,j,k) lies on the hub, we use

$$\left[\frac{\partial p}{\partial r}\right]_{i,j,k} = \frac{p_{i+1,j,k} - p_{i,j,k}}{\Delta r}$$

and similarly for other variables and at other boundary points. This is exactly the formula which would result if a linear extrapolation were made to a fictitious point outside the boundary and then the above, second-order formulae used.

These formulae are valid if the boundaries are coordinate surfaces, as in figures II.5 and II.8. For boundaries of arbitrary shape, a special coordinate transformation is applied to the equations before the finite-difference equations are determined. This transformation, which does not alter the following discussion, is described in Appendix A.

An ideal solution to the system of finite-difference equations is a distribution of values, $p_{i,j,k}$, $u_{i,j,k}$, $v_{i,j,k}$, and $w_{i,j,k}$, which satisfies all boundary conditions and makes the four residuals, $(R1)_{i,j,k}$ through $(R4)_{i,j,k}$, vanish at all grid points.

Observe, however, that at an internal point the central value of the pressure, $p_{i,j,k}$, is absent from all four residuals (equations II.5 through II.8). Therefore, these four local residuals alone are ineffective in determining a proper value for $p_{i,j,k}$. There are other reasons why more than the four

24

point resuduals must be considered at a time. These reasons, due to the finite-difference treatment of boundary conditions, are discussed next.

2. Special Considerations at Boundary Points

At every wall boundary point, the three velocity components must satisfy the condition of equation (I. 16), which is

$$\vec{W} \cdot \vec{n} = 0$$

In terms of the grid points, this becomes

$$u_{i,j,k} \, a_{i,j,k} + v_{i,j,k} \, b_{i,j,k} + w_{i,j,k} \, c_{i,j,k} = 0 \qquad \text{(II. 9)}$$

where $a_{i,j,k}$, $b_{i,j,k}$ and $c_{i,j,k}$ represent the components of the vector n, normal to the wall boundary at grid point (i,j,k). This immediately imposes a dependence of one of the velocity components upon the other two (see Appendix A), in addition to the relationships already required by the four governing equations (II. 5) through (II. 8).

One important feature of the present problem is the fact that at each grid point, there is a <u>system</u> of equations to be satisfied. This poses some difficulties at boundary points. Note that in a problem involving a single equation and a single variable, it is sufficient to have the boundary value of the variable determined solely by the imposed boundary condition without requiring that the governing finite-difference equation be satisfied there also (reference 27, pp. 260-265). In our problem, however, <u>four</u> values (p, u, v, and w) have to be determined at a boundary point. The single condition (II. 9) is obviously insufficient, especially in view of the fact that this condition is independent of $p_{i,j,k}$. We therefore require that the four governing finite-difference equations be satisfied at a boundary point as well as the imposed boundary condition. This is a redundancy of the entire system of finite-difference equations in terms of the total number of discrete values. No mathematical inconsistency is implied here, since the governing equations must be satisfied everywhere in the field, including the boundaries. However the numerical procedure that we are using introduces errors because it employs linear extrapolations at the boundaries. The correct extrapolations are obscure, and we have found the linear ones to be most practical in this work. Further discussion (see Section II. A. 5) will demonstrate that the effect of this numerical inconsistency in the boundary regions vanishes as the finite spacing between adjacent grid points is diminished.

Over the entire inlet region, the three components of the vorticity vector, $\nabla \times \vec{W}$, are specified (see Section I. B). These components are given by

25

$$(\nabla \times \vec{W})_r = \frac{1}{r}\left[\frac{\partial w}{\partial \theta} - \frac{\partial}{\partial z}(rv)\right] \tag{II.10}$$

$$(\nabla \times \vec{W})_\theta = \frac{\partial u}{\partial z} - \frac{\partial w}{\partial r} \tag{II.11}$$

$$(\nabla \times \vec{W})_z = \frac{1}{r}\left[\frac{\partial}{\partial r}(rv) - \frac{\partial u}{\partial \theta}\right] \tag{III.12}$$

It is therefore sufficient to specify the distributions of $w_{i,j,k}$ only on the first station $(k=1)$, and $u_{i,j,k}$ and $v_{i,j,k}$ on the first two stations $(k=1,2)$ since, with these specified values, all partial derivatives appearing in the above three expressions can be computed.

The remaining boundary conditions discussed in Section I.B are imposed on the finite-difference problem by fixing distributions of $p_{i,j,k}$ on the first station and $w_{i,j,k}$ on the last one.

Let I, J and K denote the total number of radial, circumferential and axial grid-stations, respectively. Then the total number, E, of governing finite-difference equations (corresponding to equations (II.5) through (II.8)) is

$$E = 4IJK \tag{II.13}$$

remembering that ρ and the F terms are specified by explicit formulae in terms of pressure and velocity. Since there are then three velocity components and one pressure to be determined at each grid point, the total number of discrete variables* is also 4IJK. However, the values of some of these discrete variables are fixed (as by throughflow boundary conditions) and some are determined by the values of other variables (as by wall boundary conditions, equation (II.9)). Thus the total number, D, of independent discrete variables can be computed to be

	2 velocity components		Specified:
	determined by		Upstream: u, v, w, p
	equation (II.9)		Station adjacent to
	Hub &		upstream: u, v,
	Shroud	Blades	Downstream: w
D = 4IJK −	(2 JK +	21K +	7IJ)

$$= 4IJK - \left[2K(I+J) + 7IJ\right] \tag{II.4}$$

Thus, as a consequence of the boundary conditions, the number of governing finite-difference equations is clearly greater than the number of independent

*By "discrete variable", we mean the value of a variable at a specific grid point; e.g.,
$p_{i,j,k}$.   26

discrete variables, $(E > D)$. Such is the nature of the general boundary value problem, which suggests a "least-sum-of-squared-residuals" approach, (reference 28, pp. 209-210).

3. <u>Computational Algorithm Using Star Residuals</u>

The above observations lead us to define a "total residual"

$$(\text{II. 15})$$

$$R_T = \sum_{i=1}^{I} \sum_{j=1}^{J} \sum_{k=1}^{K} \left[(R1)^2_{i,j,k} + (R2)^2_{i,j,k} + (R3)^2_{i,j,k} + (R4)^2_{i,j,k} \right] \geq 0$$

Since the vanishing of all residuals at all grid points is completely equivalent to the condition $R_T = 0$, the purpose of the computational algorithm will be to obtain discrete distributions of the three velocity components and the pressures which will tend to minimize the value of R_T.

A change in the value of a variable at point (i, j, k) can affect the residuals computed at no more than the seven points of a "star" centered at point (i, j, k), as shown in figure II. 2. This portion of R_T which is affected by a change at point (i, j, k) will be called the "star residual at point (i, j, k)" and is defined by

$$R^*_{i,j,k} = \sum_{i,j,k}^{*} \left[(R1)^2_{i,j,k} + (R2)^2_{i,j,k} + (R3)^2_{i,j,k} + (R4)^2_{i,j,k} \right] \qquad (\text{II. 16})$$

where the symbol $\displaystyle\sum_{i,j,k}^{*}$ denotes summation over the seven points of the star centered at point (i, j, k). (If this central point is a boundary point, this star may have only 6, 5 or 4 points.) Thus, the method will consist of determining values of the independent discrete variables at each point (i, j, k) which will tend to minimize the value of $R^*_{i,j,k}$.

Considering general applicability and ease of programming, the computational algorithm which was constructed consists of trying a predetermined sequence of corrections to each independent discrete variable at each grid point and accepting only those variations which reduce the value of the local star residual (and thus reduce the value of the total residual). This procedure is applied, repeatedly cycling through the entire three-dimensional grid of points until an accuracy criterion (discussed in Section II. A. 4) is satisfied.

27

Specifically, four initial variations are selected: δu, δv, δw, δp. Also, an integer, M, and a number, $0 < \alpha < 1$, are fixed. At each grid point, the value of $R^*_{i,j,k}$ is first computed, using the current values of u, v, w, and p at the surrounding grid points. To determine an "improved" value of $u_{i,j,k}$, for example, $R^*_{i,j,k}$ is recomputed, successively using

$$u_{i,j,k} \pm \delta u, \quad u_{i,j,k} \pm \alpha \delta u, \quad u_{i,j,k} \pm \alpha^2 \delta u, \quad \ldots, \quad u_{i,j,k} \pm \alpha^n \delta u$$

until either a reduced value of $R^*_{i,j,k}$ is obtained or until $n = M$, where $0 \le n \le M$. If one of the variations $u_{i,j,k} \pm \alpha^n \delta u$ yields a lower value for $R^*_{i,j,k}$ then that variation is recorded as the new value of $u_{i,j,k}$. Otherwise, no change is made. Exactly the same procedure is applied to the other variables and only those variations are accepted which effect further reductions of $R^*_{i,j,k}$. The successive treatment of all the grid points in the field in this manner constitutes one relaxation "cycle." Therefore, by construction, the algorithm guarantees a monotonic reduction of R_T. (We found empirically that $M = 3$, $\alpha = 0.1$ and $\delta u = \delta v = \delta w = \delta p = 0.1$ gave good results where the initial distributions were obtained from one-dimensional calculations, as in Section II. B. 3.)

With each trial variation, the values of $\rho_{i,j,k}$, $(F_r)_{i,j,k}$, $(F_\theta)_{i,j,k}$ and $(F_z)_{i,j,k}$ are recalculated from the appropriate formulae, before the corresponding $R^*_{i,j,k}$ is recomputed. At a wall boundary point, one of the three velocity components is selected as dependent upon the other two (see Appendix A) and its value is computed from equation (II.9). All values which are fixed by throughflow boundary conditions are, of course, not varied.

At the beginning of each succeeding cycle, the magnitudes of δu, δv, δw and δp are set equal to the respective maximum values of the variations which were accepted during the entire previous cycle.

Thus, the magnitudes of the individual trial variations are automatically decreased as a solution is approached. The values of α and M remain fixed.

It is possible that the theoretical rate of convergence can be improved by a compound method such as suggested by Marquardt (reference 29) or Golffeld, Quandt and Trotter (reference 30). We note, however, that both of these methods ultimately rely on the choice of an "accelerating parameter" which is successfively varied until the actual numerical value of R_T (i. e. the quadratic functional to be minimized) is decreased. Much additional empirical work is required to adapt such methods successfully to a given problem, as evidenced by the following example: We selected a problem for which we had obtained a solution by the above-described method of successive variations. We modified the computer program so that the star residual reduction was accomplished by a gradient technique, based on a second order

Taylor-approximation to R^* in terms of x, (where x denotes one of the discrete variables, u, v, w, or p, to be determined. The resulting iterative formula was

$$(x + \delta x) = x - \left[\left(\frac{\partial R^*}{\partial x}\right)\right] \Big/ \left[\left(\frac{\partial^2 R^*}{\partial x^2}\right)\right] \qquad \text{(II. 17)}$$

provided $\dfrac{\partial^2 R^*}{\partial x^2} > 0$. The indicated first and second order derivatives were computed from values of R^* corresponding to three trial values of the variable x. A comparison of the chronology of the root-mean-square residual

$$\text{RMS} = \sqrt{\frac{R_T}{4IJK}} \qquad \text{(II. 18)}$$

for both methods is shown in Figure II. 3. After some time, the gradient method became less effective whereas the method of successive variations continued convergence at an almost constant rate. Thus our algorithm with possible modifications such as in α and M remains as the currently most practical approach. This is due partly to its programming simplicity as applied to the specific finite-difference problem treated here and to the fact that other methods which at first seemed attractive from a computing time standpoint were less effective.

4. <u>Accuracy Criterion</u>

In order to relate the value of RMS (see equations (II. 15) and (II. 18)) to actual inducer performance note first that the three "momentum residuals" given by equations (II. 5), (II. 6) and (II. 7) have the units of a head gradient, or velocity-squared divided by a length. If the "continuity residual", equation (II. 8), is multiplied by a characteristic constant velocity, e. g. $\Omega r_{t, 1}$(*), then the root-mean-square residual, RMS, can be interpreted as a typical error in local head gradients. Also the continuity residual then has a magnitude that is comparable to that of the other residuals, which gives it the correct perspective for adjustment purposes, (see equation II. 15). We now require that the value of RMS be small compared to a characteristic head gradient for the inducer, such as $(\Omega r_t)^2/r_t$ That is, we require that

$$\text{RMS} < \epsilon \, (\Omega^2 r_{t, 1}) \qquad \text{(II. 19)}$$

where ϵ is some small number, say $\epsilon = .01$.

---

* Note that this velocity is equal to unity if the problem is being solved nondimensionally.
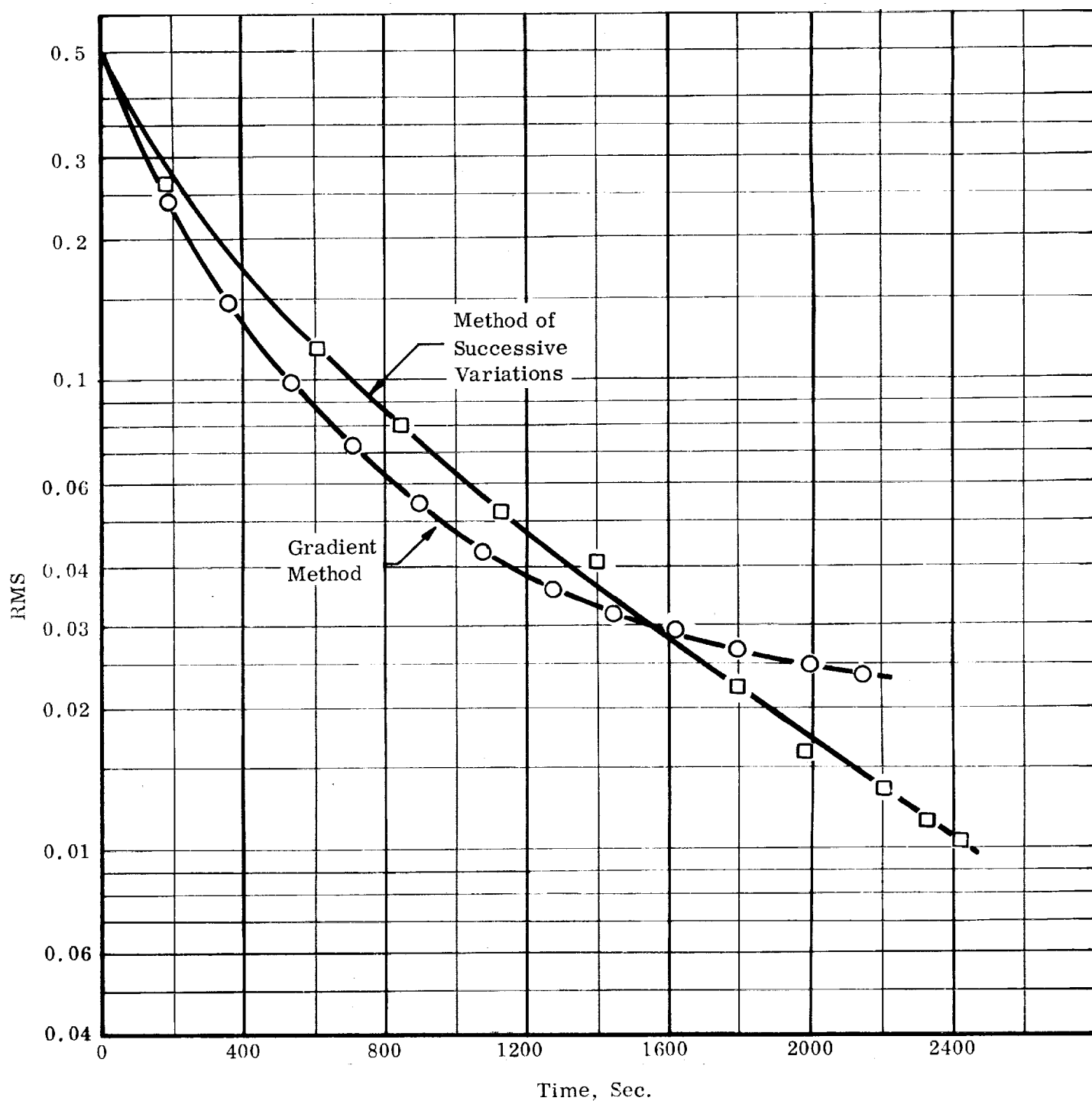
FIGURE II. 3. COMPARISON OF METHOD OF SUCCESSIVE VARIATIONS AND GRADIENT
METHOD. Root-mean-square, residual (RMS) vs. running time on IBM 7070. (The Univac
1107 that we used in subsequent runs takes about 1/50 of the time.)

If the values of $p_{i,j,k}$, $u_{i,j,k}$, $v_{i,j,k}$ and $w_{i,j,k}$ are randomly distributed about the "correct" values, then about half of the residuals can be expected to be positive and the other half negative. The cumulative effect of all residuals from inlet to outlet for this distribution of variables would result in a head rise error at outlet which is still much less than $\epsilon(\Omega^2 r_{t,1})\,\Delta m$. Δm represents meridional inlet-to-outlet distance along a typical streamline. However, should a biased distribution of values exist, such as an initial distribution of $p = o$ everywhere, then we can expect the residuals to be dominantly of one sign, (although they might all still be of approximately the same magnitude as in the above case) and the cumulative effect would be an error in head rise of order

$$\epsilon(\Omega^2 r_{t,1})\,\Delta m \tag{II. 20}$$

From the definition of the static pressure head coefficient for an inducer

$$\Psi_p = \frac{\Delta \bar{p}/\rho_f}{(\Omega r_{t,1})^2/g_o} \tag{II. 21}$$

we see that, in this case, the error in $g_o\,\Delta \bar{p}\;\rho_f$ at the outlet would be comparable to $\left(\epsilon\,\dfrac{1}{\Psi_p}\,\dfrac{\Delta m}{r_{t,1}}\right)$ times the correct head rise of the machine.

Hence a more realistic convengence requirement would be RMS $< \left(\dfrac{\epsilon}{\Psi_p}\,\dfrac{\Delta m}{r_{t,1}}\right)(\Omega^2 r_t)$ but since ϵ can be chosen to suit specific cases of $\dfrac{\Delta m}{r_{t,1}}$ and Ψ_p, we have retained generality by stating simply that RMS $< \epsilon(\Omega^2 r_{t,1})$. It is therefore advantageous to estimate the initial values of the pressure and velocities by a preliminary, one-dimensional calculation of the flow. This is demonstrated in the discussion in Section II. B. 3.

Finally, if the grid effects or limitations on computing time make it impossible to achieve negligibly small values of all the residuals, the acceptability of a particular numerical solution must then be determined by more than just the value of RMS. In the case of the investigations of our (Section II. B), series of examples we were limited by computer size and cost to coarse grids. Thus in most of these examples the numerical procedure (see Section II. A. 2) made it impossible for us to reduce RMS to the satisfactorily low value ϵ that would make it the only necessary criterion for an accurate solution. Furthermore this required us to impose a limit on the time or number of computation cycles, which usually was reached before ϵ could be achieved. Therefore, in our presentation of examples in Section II. B we compare the actual distributions of p, u, v and w with known solutions, whenever possible; and we examine the circulation and other representative quantities in addition to the behavior of the residuals.

5. Effects of Grid Point Density

There is an effect which the density of grid points has on the minimum attainable total residual (equivalently, the root-mean-square residual, RMS, as defined by equation (II.18)) for a given finite-difference problem when the method of star residuals is applied. This is due to the linear extrapolation of the discrete variables which is made at boundary points. If it is required that the discrete variables satisfy all governing finite-difference equations at boundary points in addition to the appropriate boundary conditions, as discussed in Section II.A.2, the correct extrapolation formulae would be required at boundaries in order for the system of equations to yield zero residual. For example, incorrect extrapolations which satisfy one differential equation normal to a boundary will produce boundary values of the variables that will not completely satisfy the other equations—particularly those that govern motion parallel to the boundary. Since a linear extrapolation is used, a linear behavior is forced on the variables in a region extending one grid space from the boundaries to the interior of the field. For a relatively coarse grid, this discrepancy will be dominant and, consequently, the total residual, R_T, can only be minimized to some non-zero value. As the grid is refined, however, the linear approximation to the variables extends over a much smaller region and the effect of the discrepancy diminishes. Thus the minimum attainable total residual can be expected to approach zero as the mesh size (distance between adjacent grid points) approaches zero.

To illustrate this effect, we consider the problem of solving, by use of star residuals, the equations of incompressible flow which is irrotational in the absolute frame of reference:

$$\nabla \cdot \vec{W} = 0 \tag{II.22}$$

$$\nabla \times \vec{W} + 2\vec{\Omega} = 0 \tag{II.23}$$

We will discuss a two-dimensional solution of these equations over a region which is a cross section perpendicular to the axis of a paddle-wheel channel (see figure II.8). The scalar equations are

$$\frac{u}{r} + \frac{\partial u}{\partial r} + \frac{1}{r} \frac{\partial v}{\partial \theta} = 0 \tag{II.24}$$

$$\frac{v}{r} + \frac{\partial v}{\partial r} - \frac{1}{r} \frac{\partial u}{\partial \theta} + 2\Omega = 0 \tag{II.25}$$

where $u = 0$ on the hub ($r = r_h$) and shroud ($r = r_t$) and $v = 0$ on the blade surfaces.* We obtained solutions to this problem, by the method of star residuals, on grids of 5 x 5, 9 x 7, 9 x 9 and 15 x 15 points,

---

*This special, two-dimensional problem will be referred to again in Section II.B.2.

requiring the discrete values of u and v to satisfy the finite-difference equations resulting from equations (II. 24) and (II. 25) in addition to the boundary conditions on the hub, shroud and blade surfaces. Each problem was run to "convergence", i. e. until the root-mean-square residual (RMS) could not be reduced much further. This yielded essentially the minimum obtainable RMS. The results (see figure II. 4) indicate that the minimum attainable total residual approaches zero with diminishing mesh size. Therefore, any numerical discrepancy (due to requiring that the discrete variables satisfy all governing finite-difference equations in addition to the boundary conditions) vanishes as the density of grid points is increased.

Another numerical phenomenon, the "take-up effect", is a second order grid effect that is noticeable especially when coarse grids are employed. It is the property that yields lower minimum RMS residual results for a given grid cross-section as the number of independent discrete variables D (see definition near the end of Section II. A. 2) is increased. The preceding two dimensional problem is an example. Its minimum RMS residual is given in Figure II. 4. Extending it axially into the third dimension increases D, adding residuals of the axial component equations which will be adjusted to non-zero values. (As shown in reference 12, the same two-dimensional solution is expected on all subsequent $r - \theta$ planes.) This changes slightly the adjacent downstream two-dimensional distributions, making it possible to reduce their residuals further than was possible in the purely two-dimensional problem.

Also, changes to the system of equations or boundary conditions is a way to change D in a given field. In any case, the residuals thereby added have the ability to "take-up" some of the error caused by boundary effects, which process yields a lower minimum RMS, for the given grid cross-section. Figure II. 9 gives the results for this same problem (using for initial values the answers that produced the 9 x 7 point in Figure II. 4) as D was increased over that of the purely two-dimensional 9 x 7 field. (See Section II. B. 2 for more detail on the problem.) Figure II. 11 shows that this "take-up effect" is subordinate to the grid-point density one, because the effect (on minimum RMS) of increasing D is limited — as might be expected if the two-dimensional 9 x 7 grid cross-section example we have been using were to be extended infinitely in the axial direction. Finally, in the normal case of a fixed three-dimensional field with a fixed system of equations and boundary conditions, D cannot be varied, and there is no take-up effect — only the (primary) grid point density effect. However, as will be demonstrated in Section II. B, we did vary D in some of our investigations; and these distinctions of grid phenomena must be remembered as one examines the results.
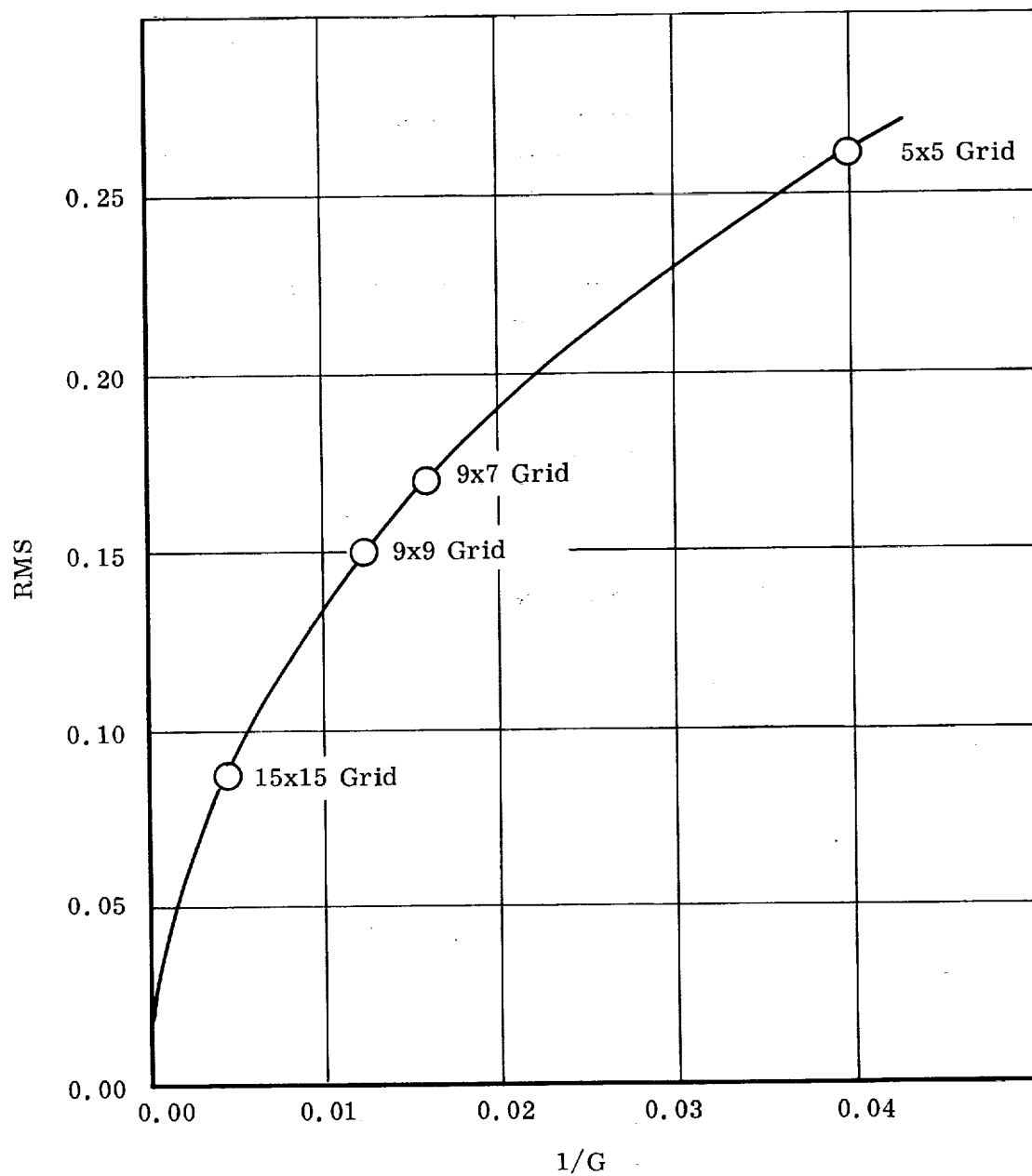
FIGURE II. 4 EFFECT OF GRID POINT DENSITY. Minimum attainable root-mean-square residual (RMS) as a function of the number of grid points (G) for two-dimensional solutions of $\left\{ \nabla \cdot \widetilde{W} = 0, \ \nabla \times \widetilde{W} + 2\, \widetilde{\Omega} = 0 \right\}$ by star residuals.

6. Form of the Results

The results of a computer run consist of three-dimensional distributions of relative velocity components, pressures, and the accompanying densities. These distributions directly indicate blade-to-blade pressure loadings and inlet-to-outlet velocity distributions on the blade surfaces and their extensions. But to obtain the customary overall performance parameters, certain averaged quantities must be extracted from these distributions. For this purpose a data reduction program was written. Details of this program are presented in Appendix C.

The <u>mass-averaged</u> parameters are calculated from finite-difference approximations of the following formulae:

Static Pressure Head

$$\left(\frac{\bar{p}}{\rho}\right) = \frac{\int_{r_h}^{r_t} \int_{\theta_p}^{\theta_s} \left(\frac{p}{\rho}\right) (\rho w)\, r\, dr\, d\theta}{w_T} \tag{II. 26}$$

where the total mass flow rate across the inlet plane of one channel is calculated from

$$\frac{w_T}{n_b} = \int_{r_h}^{r_t} \int_{\theta_p}^{\theta_s} (\rho w)\, r\, dr\, d\theta \tag{II. 27}$$

Absolute Velocity Head

$$\left(\overline{\frac{v^2}{2\,g_0}}\right) = \frac{\int_{r_h}^{r_t} \int_{\theta_p}^{\theta_s} \frac{1}{2g_0}\left[u^2 + (v + r\,\Omega)^2 + w^2\right] (\rho w)\, r\, dr\, d\theta}{w_T} \tag{II.28}$$

Input Energy

$$\overline{(UV\theta)} = \frac{\int_{r_h}^{r_t} \int_{\theta_p}^{\theta_s} \left[r\Omega\,(v + r\,\Omega)\right] (\rho w)\, r\, dr\, d\theta}{w_T} \tag{II. 29}$$

The above three quantities are calculated at the channel inlet and at the outlet. From these we obtain

Total Head Rise

$$\Delta \bar{H} = \left(\frac{\bar{p}}{\rho}\right)_2 - \left(\frac{\bar{p}}{\rho}\right)_1 + \left(\frac{\overline{V^2}}{2g_0}\right)_2 - \left(\frac{\overline{V^2}}{2g_0}\right)_1 \qquad \text{(II. 30)}$$

Shaft Power Delivered to Fluid

$$\frac{P_s}{n_b} = \left[\overline{(UV_\theta)}_2 - \overline{(UV_\theta)}_1\right] \frac{w_T}{n_b} \bigg/ g_0 \qquad \text{(II. 31)}$$

Overall Efficiency

$$\bar{\eta} = \frac{\Delta \bar{H} \, w_T}{P_s} \qquad \text{(II 32)}$$

Further details of the calculations are given in Appendix C.

B. APPLICATION AND RESULTS

The results of applying the method of solution to a sequence of problems are presented in this section. The problems were solved in order of gradually increasing complexity, and Table II. 1 shows the purpose and general result of each one. We employed three types of geometry to determine a) the ability of the program to proceed to a correct solution, b) the grid effects and attainable accuracy and c) the applicability to inducer flow analysis.

The specific geometries were

    (1)   Paddle-wheel channel with wheel-type axial flow (liquid and two-phase).

    (2)   Paddle-wheel channel with irrotational, incompressible, axially constant flow (reference 12).

    (3)   Two typical, variable-lead inducer channels, including upstream and downstream flow regions (liquid and two-phase).

The geometry of each channel is presented, followed by selected numerical results and a discussion of some of the phenomena which they illustrate. All problems are solved nondimensionally, according to the system presented at the end of the List of Symbols prior to Section I.

TABLE II.1

LIST OF COMPUTER RUNS FOR THREE-DIMENSIONAL (EXACT METHOD) SOLUTION

RUN	CHANNEL GEOMETRY	GRID AND TYPE OF FLOW (ALL LOSSLESS)	PURPOSE OF RUN	GENERAL RESULT
E-1	Paddle-Wheel (figure II. 5)	3x3x3, Incompressible, wheel-type	To establish that program proceeds correctly to solution.	Converged to minimum RMS residual small enough to eliminate need for other criteria. Demonstrated grid-point density effect on accuracy of numerical results.
E-2	Paddle-Wheel (figure II. 5)	3x3x3, Two-phase, wheel-type	To determine workability of and additional time required for two-phase solution.	Converged to negligible RMS. Showed negligible additional calculating time for two-phase flow.
E-3	Paddle-Wheel (figure II. 8)	9x7x3, Incompressible, Irrotational (downstream flow directions fixed)	To solve more typical three-dimensional problem for which answers are known.	Converged to larger RMS than above. Demonstrated grid point-density effect and ability to get correct answers.
E-4	Paddle-Wheel (figure II. 8)	9x7x3, Incompressible, Irrotational (downstream flow directions free)	To check influence of downstream boundary conditions.	Converged to lower RMS than Run E-3. Demonstrated "take-up effect".
E-5	Paddle-Wheel (figure II. 8)	9x7x5, Incompressible, Irrotational (downstream flow directions free)	To check ability of program to solve larger field.	Converged to lower RMS than Run E-4. Demonstrated take-up effect and general three dimensional problem capability.
E-6	6.2° variable-lead inducer, including upstream flow region (figure II. 12)	5x5x10, Incompressible	To demonstrate three-dimensional analysis capability for inducers with low inlet blade angle $\beta_{b, t, 1}$.	Converged to RMS that still allowed some error due to coarse grid. Grid with highly oblique intersections worked. (Could have contributed to errors).
E-7	12° variable-lead inducer, including upstream and downstream flow region (figure II. 18)	5x5x22, Incompressible	To test higher $\beta_{b, t, 1}$ inducer and thereby obtain higher accuracy due to less oblique grid intersections.	Converged toward higher RMS than for 6.2° inducer, but answers were more realistic; although grid and other possible effects introduced errors.
E-8	12° variable-lead inducer, including upstream and downstream flow region (figure II. 18)	5x5x22, Incompressible (forced pressures)	To eliminate need for adjusting pressures in lossless, incompressible flow, thereby decreasing errors due to grid effects.	Converged toward higher RMS than Run E-7, but adverse effects on average accuracy were absent, giving realistic results.
E-9	12° variable-lead inducer, including upstream and downstream flow region (figure II. 18)	5x5x22, Two-phase	To check ability of method to handle two-phase flow calculations in inducers.	Two phase calculations proceeded properly without consumption of additional time. As in above runs, stagnation stream-surfaces were not adjusted; and this prevented good two-phase answers.

1. Paddle-Wheel Channel With Wheel-Type Flow

The geometry of this six-bladed channel is shown in figure II.5. The primary purpose of solving the first two problems on a 3 x 3 x 3 grid was to have a simple checkout of the computer program. Due to the special shape of the channel, the wall boundary conditions (equation (II.9)) are simply

$$\left.\begin{array}{l} u_h = u_t = 0.0 \\[2mm] v_s = v_p = 0.0 \end{array}\right\} \qquad\qquad\text{(II.33)}$$

Boundary conditions, known correct answers, and obtained results are shown in tables II.2 and II.3. Initial assumptions for both runs were made to differ from their correct values randomly by about 0.2.

Run E-1: All Liquid Flow

The correct solution has

$$\left.\begin{array}{l} u = 0.0 \\[2mm] v = 0.0 \\[2mm] w = 1.0 \end{array}\right\} \text{everywhere}$$

The only pressure gradient is in the radial direction. Integration of this radial gradient gives

$$p = p_h + \frac{1}{2}\ \rho_f\ \frac{\Omega^2}{g_o}\ (r^2 - r_h^2) \qquad\qquad \text{II.34)}$$

Setting $p_h = 0$, this gives correct answers of the continuous problem as

$$p_h = 0.0$$

$$p_M = 0.16406$$

$$p_t = 0.46875$$

where the subscript M denotes the grid point half-way between hub and tip. Solving the finite-difference analogs of equation (II.5) simultaneously at the three grid points, however, gives

$$
\begin{array}{ll}
\Omega & = 1.0 \\
r_{t,1} & = 1.0 \\
r_h & = 0.25 \\
\Delta r & = 0.375 \\
\Delta \theta & = \pi/6 \\
\Delta z & = 0.375
\end{array}
$$
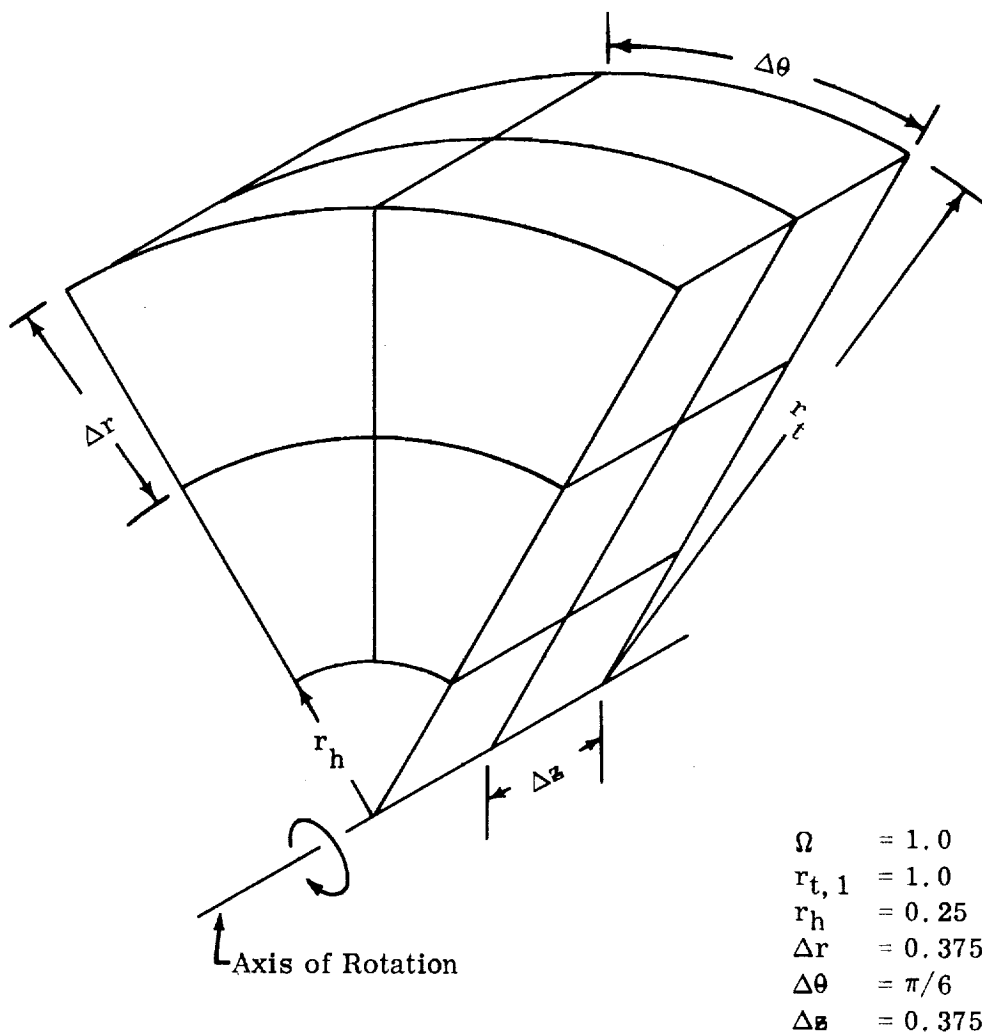
FIGURE II.5. PADDLE-WHEEL CHANNEL FOR WHEEL-TYPE, AXIAL
   FLOW CALCULATIONS.   Runs E-1, 2.

TABLE II. 2

RUN E-1: PADDLE WHEEL CHANNEL WITH WHEEL-TYPE,
AXIAL, LIQUID FLOW

	LOCATION (c)	p	u	v	w	RESIDUAL (a)
Typical Randon	Hub	0.0	0.0	-0.19	1.18	----
Initial	Mean	0.08	0.19	-0.19	1.19	----
Assumptions	Tip	0.04	0.0	-0.18	1.21	----
	Hub	0.0	0.0	0.0	1.00	0.0
Correct	Mean	0.09375	0.0	0.0	1.00	0.0
Answers	Tip	0.46875	0.0	0.0	1.00	0.0
Results	Hub	-0.00781	0.0	0.00156	1.00475	0.00968 (b)
Showing	Mean	0.08625	0.00156	-0.00038	1.00394	0.00500
Max. Error	Tip	0.46156	0.0	-0.00156	1.00269	0.00399

<u>Imposed Boundary Conditions</u>

Upstream: p = 0.0   (at one point on hub)
              u = 0.0
              v = 0.0
              w = 1.0

Downstream: Directions fixed by requiring that

$$\frac{u}{w} = 0.0$$

$$\frac{v}{w} = 0.0$$

---

a   This residual is the root-mean-square of the four local residuals

b   Accuracy criterion is $\Omega^2 r_{t,1} = 1.0$. See equation (II. 19)

c   Applicable to any grid point on the surface of revolution—hub, mean or tip.
    See Figure II. 5.

TABLE II. 3

RUN E-2: PADDLE-WHEEL CHANNEL WITH WHEEL-TYPE,
AXIAL, LIQUID AND TWO-PHASE FLOW

	LOCATION (c)	p	ρ	u	v	w	RESIDUAL (a)
Typical Random	Hub	0.0	0.5	0.0	-0.19	1.18	----
Initial	Mean	0.0	0.5	0.19	-0.19	1.19	----
Assumptions	Tip	0.0	0.5	0.0	-0.18	1.21	----
	Hub	0.897	0.905	0.0	0.0	1.00	0.0
Correct	Mean	0.983	0.985	0.0	0.0	1.00	0.0
Answers	Tip	1.358	1.000	0.0	0.0	1.00	0.0
Results	Hub	0.895	.907	0.0	-0.00004	1.00386	0.00216 (b)
Showing	Mean	0.979	.980	-0.00133	-0.00006	1.00298	0.00098
Max. Error	Tip	1.354	1.000	0.0	-0.00002	1.00188	0.00090

Imposed Boundary Conditions

Upstream: p = 0.897
u = 0.0
v = 0.0
w = 1.0

Downstream: None

---

a   This residual is the root-mean-square of the four local residuals

b   Accuracy criterion is $\Omega^2 r_{t,1} = 1.0$. See equation (II.19)

c   Applicable to any grid point on the surface of revolution — hub, mean or tip.
See Figure II.5.

$$p_0 \quad = 0.0$$

$$p_M \quad = 0.09375$$

$$p_t \quad = 0.46875$$

The discrepancy at point M is due to the linear approximations made at the hub and tip points.

In Section II. A. 5 we explained that incorrect extrapolations would not satisfy all the differential equations simultaneously. However in this example we have simply a one-dimensional problem because the answers yield no variation in the axial and tangential directions with only one equation (II. 34). Thus it is possible to attain all zero residuals, although the results for the discrete problem disagree at one point with the solution of the continuous problem. (See the discussion of "discretization error" in reference 27). Results of this problem are shown in figure II. 6 and table II. 2.

Run E-2: Liquid and Two-Phase Flow

For this problem, we were able to determine values of p_h, p_M, and p_t so that, for $\rho_f = 1.0$, $p_{sat} = 1.0$ and $T^* = 1.0$ (see equations (I. 7) and (I. 8), it was again possible to have all residuals equal to zero in the finite-difference solution. Using the same initial assumptions for velocities as in Run E-1 and zero for pressures, figure II. 7 shows that after 110 relaxation cycles the RMS value continues to approach zero, as expected for this case. Table II. 3 shows how close the results are to the known, correct values. We observed that inclusion of the state equation in the computations did not cause any perceivable increase in running time per relaxation cycle.

2. Paddle-Wheel Channel with Irrotational Flow

The geometry for this channel is shown in figure II. 8. The hub-to-tip radius ratio as well as the blade-to-blade angles were obtained directly from figure 2 of reference 12. The channel which we consider here is a portion of the channel used by Ellis and Stanitz (for which complete, detailed results are presented in reference 12) upstream of where the effects of radial flow are felt. This is a hypothetical problem since the paddle-wheel portion of the channel would have to extend infinitely far upstream in order to yield an irrotational, axially constant flow pattern.

However, it is another problem whose numerical solution can be determined by simpler methods. This problem also demonstrates the finite-difference
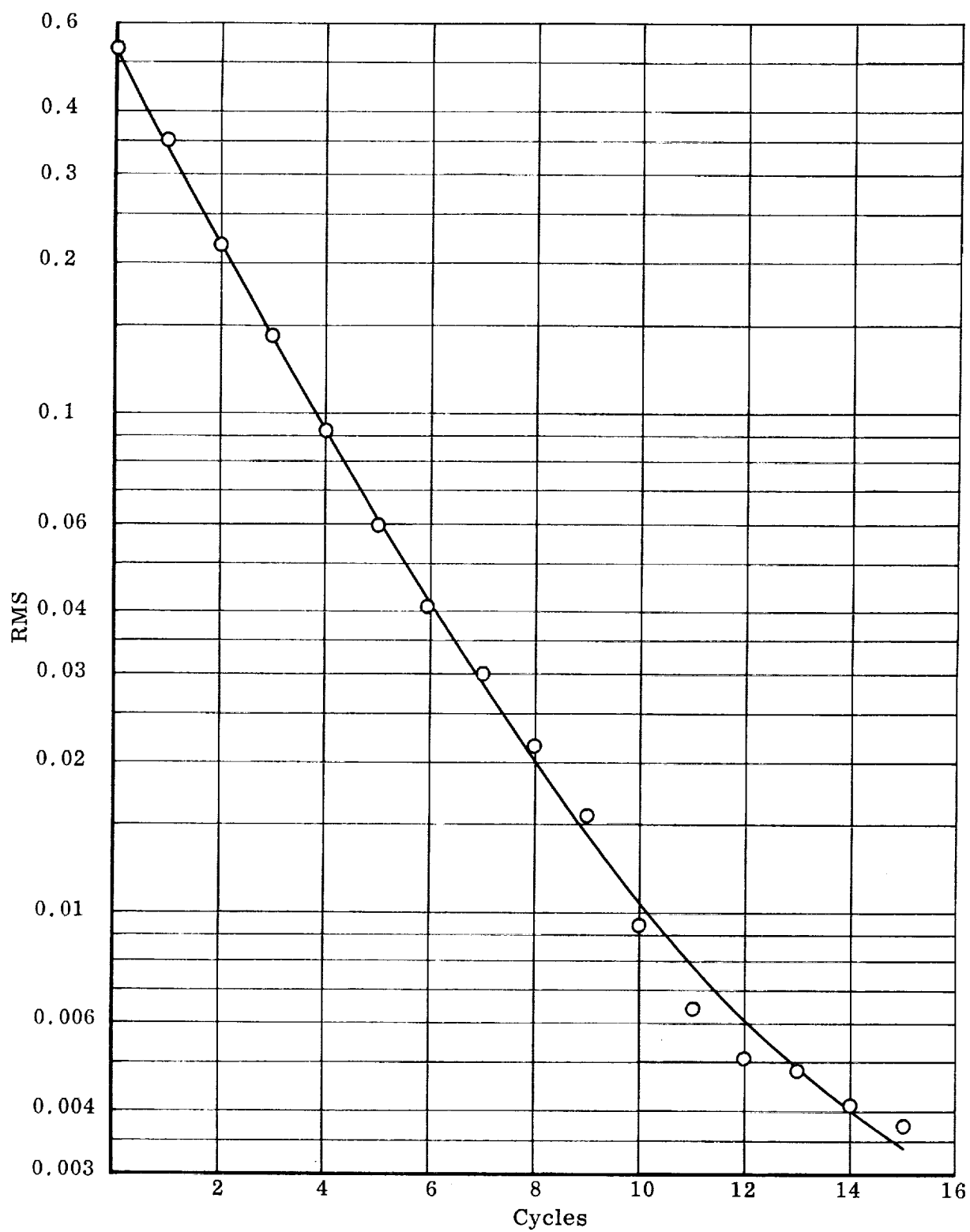
FIGURE II. 6.   INCOMPRESSIBLE, LOSSLESS, WHEEL-TYPE FLOW.   Run E-1.
Root-mean-square residual (RMS) vs. number of relaxation cycles.
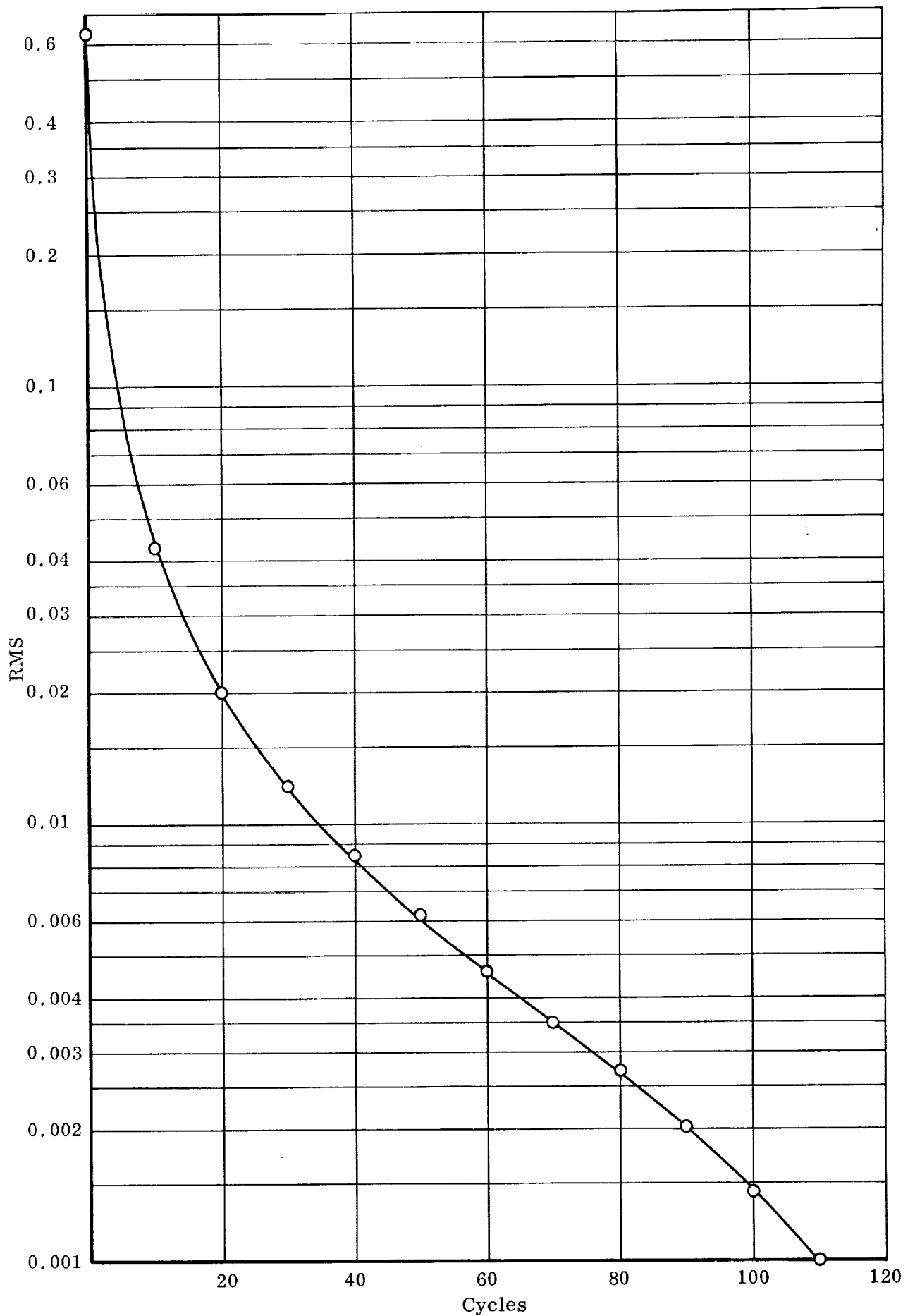
FIGURE II. 7.   TWO-PHASE, LOSSLESS, WHEEL-TYPE FLOW. Run E-2. Root-mean-square residual vs. number of relaxation cycles.

44

$$\Omega = 1.0$$
$$r_{t,1} = 1.0$$
$$r_h = 0.369$$
$$\Delta r = 0.0789$$
$$\Delta \theta = 0.0954$$
$$\Delta \mathfrak{z} = 0.0789$$
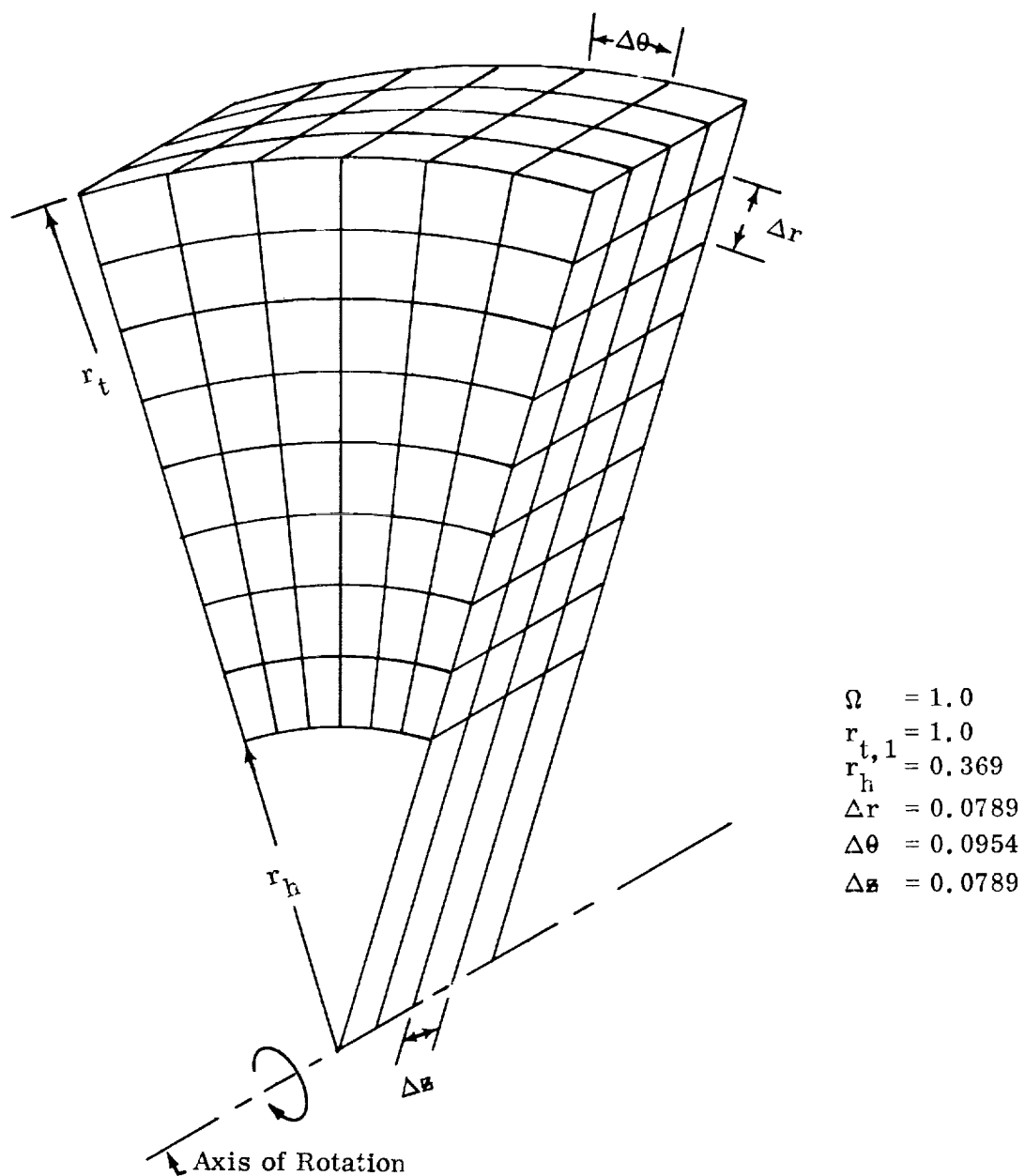
FIGURE II. 8. PADDLE-WHEEL CHANNEL FOR IRROTATIONAL, AXIAL
FLOW CALCULATIONS. Runs E-3, 4, 5.

phenomenon of our method which is called the "take-up effect".

The solution of this special three-dimensional problem is merely an axial propagation of a two-dimensional flow pattern with relative rotation of $2\,\Omega$. It is, therefore, a propagation in the z -direction of the solution of the equations

$$\frac{u}{r} + \frac{\partial u}{\partial r} + \frac{1}{r}\frac{\partial v}{\partial \theta} = 0 \tag{II. 24}$$

$$\frac{v}{r} + \frac{\partial v}{\partial r} - \frac{1}{r}\frac{\partial u}{\partial \theta} + 2\,\Omega = 0 \tag{II. 25}$$

This problem was presented in Section II. A. 5. As starting values for velocities in the three-dimensional problem, we used the numerical results of the two-dimensional problem on a 9 x 7 grid and applied them at all axial stations, along with a constant through-flow velocity of $w = 1.0$. Initial distributions for pressure were obtained from

$$p = p_0 + \frac{\rho_f}{2g_0}\left[\Omega^2\,(r - r_0{}^2) - (u^2 - u_0{}^2) - (v^2 - v_0{}^2)\right] \tag{II. 35}$$

which is a consequence of applying the streamline component of the momentum equation (I. 4) with an assumption of constant "inlet" pressure infinitely far upstream. The subscript o denotes a reference point, arbitrarily selected at the intersection of the "pressure blade" surface with the hub. The corresponding initial RMS value is 0.169. This RMS value is not zero because of the effect of the relatively coarse grid, explained in Section II. A. 5, (see the 9 x 7 point in Figure II. 4).

On the upstream throughflow boundary of this channel, we fixed the distributions of u and v in accordance with the results of the two-dimensional irrotational flow problem solved in Section II. A. 5. The w distribution on that boundary was set at unity and we fixed the value of p_0 at the reference point of equation (II. 35). On the downstream throughflow boundary, we imposed flow directions by fixing the values of the ratios u/w and v/w, using the upstream data. Although this set of boundary conditions is valid since they are known results, the impossibility of determining downstream flow directions for the general inducer problem is apparent. For a discussion of alternate throughflow boundary conditions, please see Section I. B. 2.

For this problem, the following three runs were made:

Run E-3: 9 x 7 x 3 Grid With Exit Flow Directions Fixed

Since this is solved three-dimensionally, we will not require the axial derivatives to be zero. Therefore, all values on the second and third axial planes are free to readjust so as to improve the radial and circumferential residual nonequilibrium at the sacrifice of small axial gradients in accordance with the "take-up effect," and the resulting RMS value after ten relaxation cycles is 0.090 (see figure II.9). The amount of readjustment which occurs due to the take-up effect is small as can be seen in figure II.10.

Run E-4: 9 x 7 x 3 Grid With Exit Flow Directions Free

With the same grid of points as for the previous run, we lifted the downstream requirement that the ratios u/w and v/w have specified values. (See discussion below.) This introduced more independent discrete variables D for the same number of governing finite-difference equations (see Sections II.A.1 and 2). As in the previous run, this permitted more readjustment of the variables to further reduce the residual amount of nonequilibrium and the results of 20 cycles for this run are shown in figures II.9 and II.10.

Run E-5: 9 x 7 x 5 Grid With Exit Flow Directions Free

Again using the same grid spacing as in the previous two runs, but extending the channel by adding two axial stations, we made another 2-cycle run. The additional axial stations enabled further "take-up" of axial gradients and a further reduction of the minimum RMS value was attained (figure II.9).

The lifting of the downstream throughflow direction requirement did not result in a radically different flow pattern (see figure II.10) probably because the initial distributions were very close to the correct values. A complete set of boundary conditions is still required for the general problem (see Section II.B.3).

In all three of these runs the coarse grid-point density caused the minimum RMS residual to be too high to serve as the only criterion for judging the accuracy of the solutions. In fact (as will be seen) it is quite possible for the answers to be correct on the average but for the minimum RMS to be high, as was discussed in Section II.A.4. Further, in the absence of any "take-up" by axial gradients— as is the case in our two dimensional solution of equations (II.24) and (II.25) (see Figure II.4) — the effects of the relatively large resulting RMS residual appear to be felt mainly in a fairly uniform way near boundaries, tending to yield better average answers. The take-up effect, while reducing the minimum obtainable

47
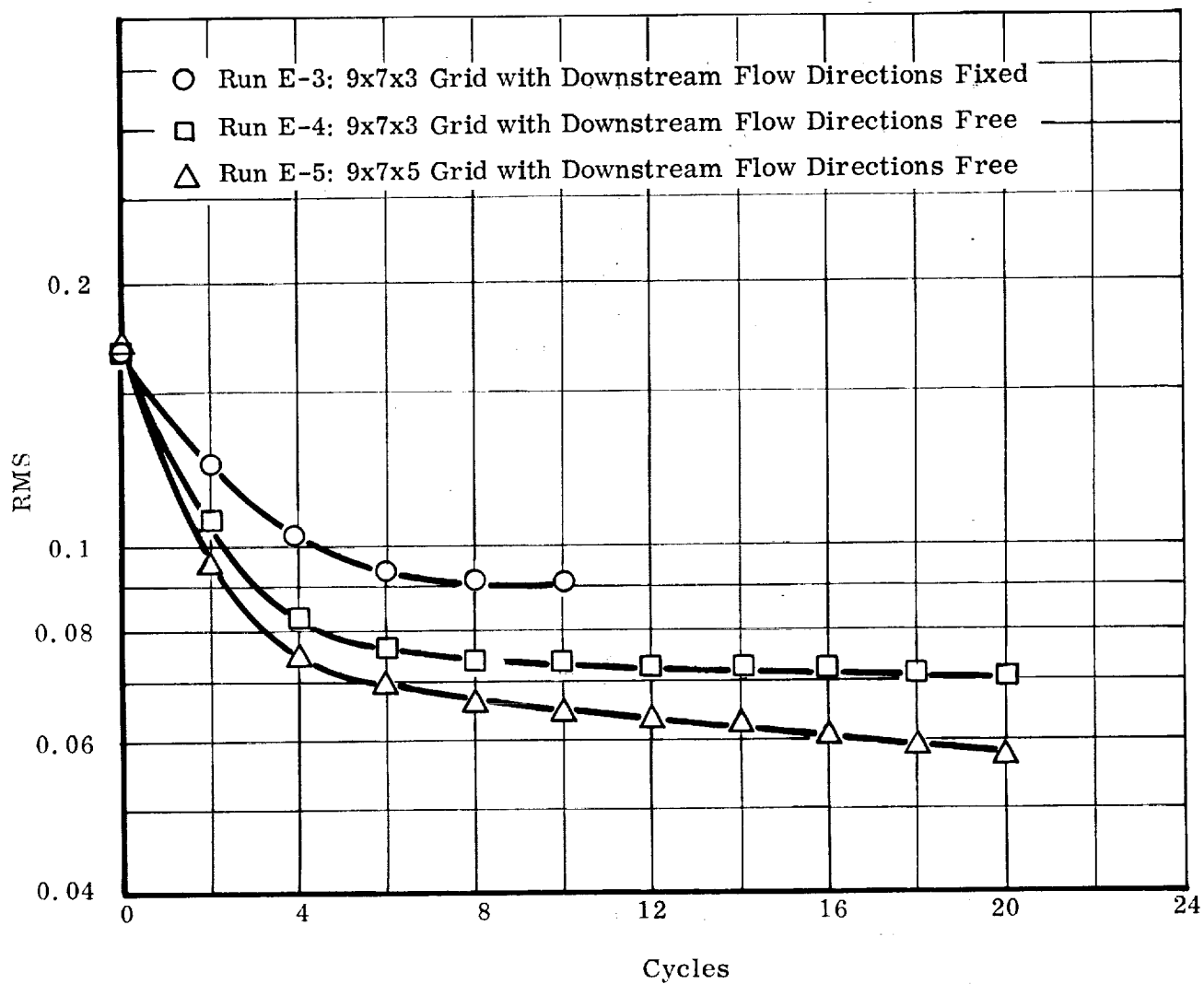
FIGURE II. 9.   DEMONSTRATION OF THE "TAKE-UP EFFECT" WITH INCOMPRESSIBLE, IRROTATIONAL FLOW.   Root-mean-square residual (RMS) vs. number of relaxation cycles.
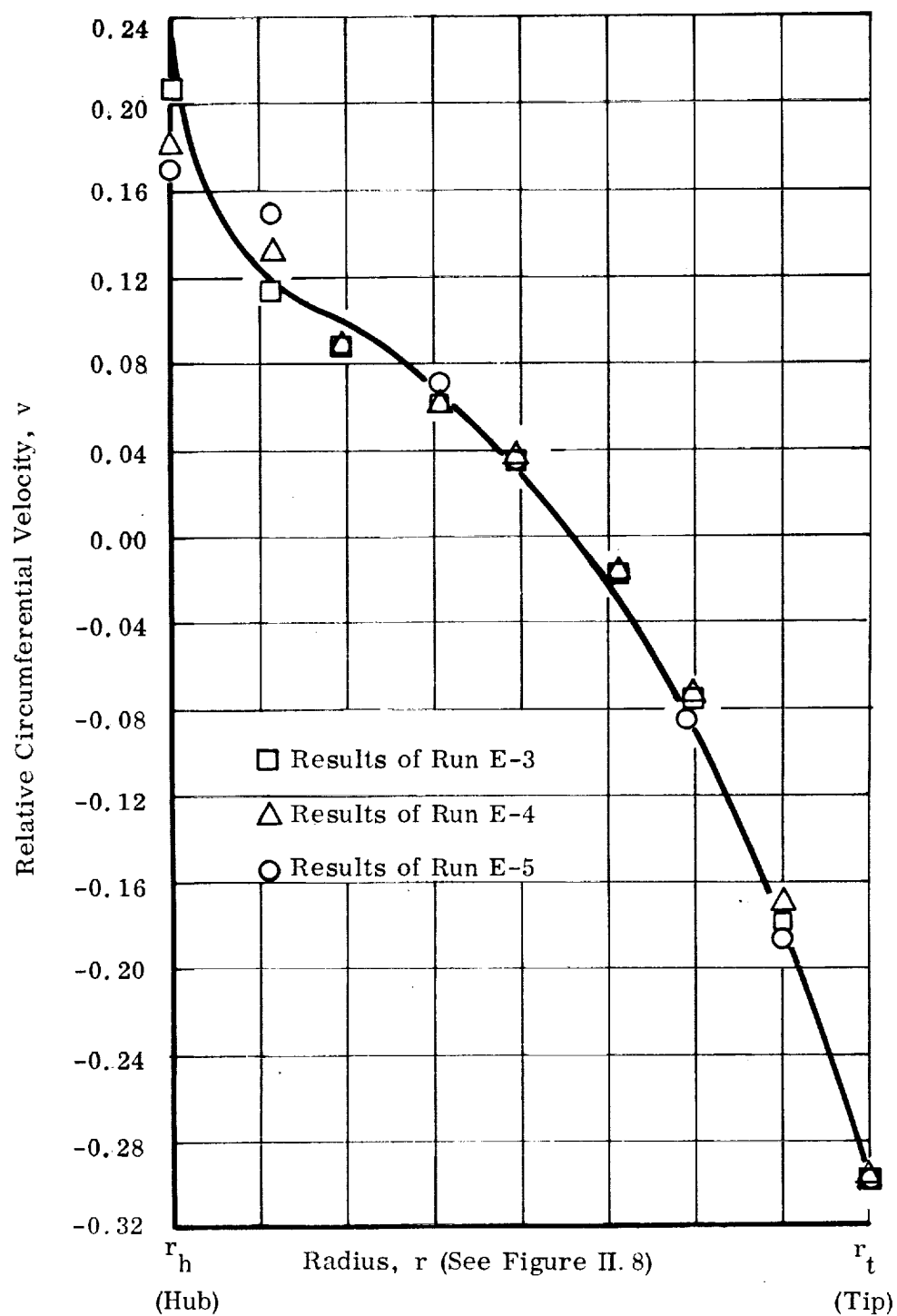
FIGURE II. 10.   VELOCITIES IN INCOMPRESSIBLE, IRROTATIONAL FLOW.
    Distributions along channel center line on exit plane.

RMS residual, never reduces it far enough to guarantee accurate answers—and it propagates errors (especially axially). The net result of the take-up effect — as long as coarse grids are used — is then a decrease in the accuracy of the average answers. Examination of the relative circulation around the perimeter of the passage at exit — a useful criterion of average accuracy — will demonstrate this point.

Figure II.10 shows that the largest deviations in the velocity field occur close to the hub. With this we expect to see a corresponding change in the calculated circulation, Γ.

By definition

$$\Gamma = \oint \vec{W} \cdot \vec{dp} \tag{II.36}$$

where the integral is taken around the boundary of a channel cross section.

By Stokes' Theorem

$$\Gamma = \int_A \nabla \times \vec{W} \cdot \vec{dA} \tag{II.37}$$

where the integral is taken over the entire area of the cross section.

Since

$$\nabla \times \vec{W} = -2\vec{\Omega} \tag{II.38}$$

for irrotationality (see reference 9, p.11), we have

$$\Gamma = -\int_A 2\vec{\Omega} \cdot \vec{dA} = -\Omega(r_t^2 - r_h^2)(\theta_s - \theta_p) \tag{II.39}$$

Calculating the absolute value of this with the dimensions shown in Figure II.8, we obtain the theoretical circulation for this problem as $\Gamma_{true} = 0.49444$. Substituting boundary velocities into an approximation to equation (II.36) and comparing these calculated values of circulation at exit to the theoretical value we have the following table of results:

TABLE II.4

COMPARISON OF CALCULATED RELATIVE CIRCULATION AT CHANNEL
EXIT WITH THEORETICAL CIRCULATION FOR RUNS E-3, 4, 5

For Results of	Γ_{calc} / Γ_{true}
Ellis & Stanitz (reference 12)	0.999
Initial values from equations (II.24, 25).	0.958
Run E-3 - Cycle 10	0.919
Run E-4 - Cycle 20	0.907
Run E-5 - Cycle 20	0.891

This illustrates the error propagating capabilities of the take-up effect
where coarse grids are used. The residual amounts of nonequilibrium,
due to finite-difference approximations made at boundary points (see
Sections II. A. 2 and 5), are reduced in exchange for some circulation
around the boundary, thus distorting the purely two dimensional field
of the cross-sections.

The phenomenon of the "take-up effect" is summarized in figure II.11
where the minimum attainable RMS values for each run are estimated
from figure II.9, as explained in Section II. A. 5.

3.   Three-Bladed, Variable-Lead Inducer Channels

To demonstrate the applicability of the computer program to general
problems, two typical inducer channels were selected, each with
variable-lead, radial-element blades. Figure II.12 shows the general
geometry for these inducers.

For each channel a "natural" coordinate system is selected so that the
channel boundaries become coordinate surfaces. A development of the
necessary transformation formulae and a discussion of special
conditions and restrictions are given in Appendix A. The first inducer
flow problem is described by

Run E-6: 6.2° Inducer - 5 x 5 x 10 Grid

The lead equation for the blades of this inducer is

$$r \tan \beta_b = \frac{dz}{d\theta} = \underbrace{.10857}_{a} + \underbrace{.03444}_{c} z^2 \qquad \text{(II.40)}$$
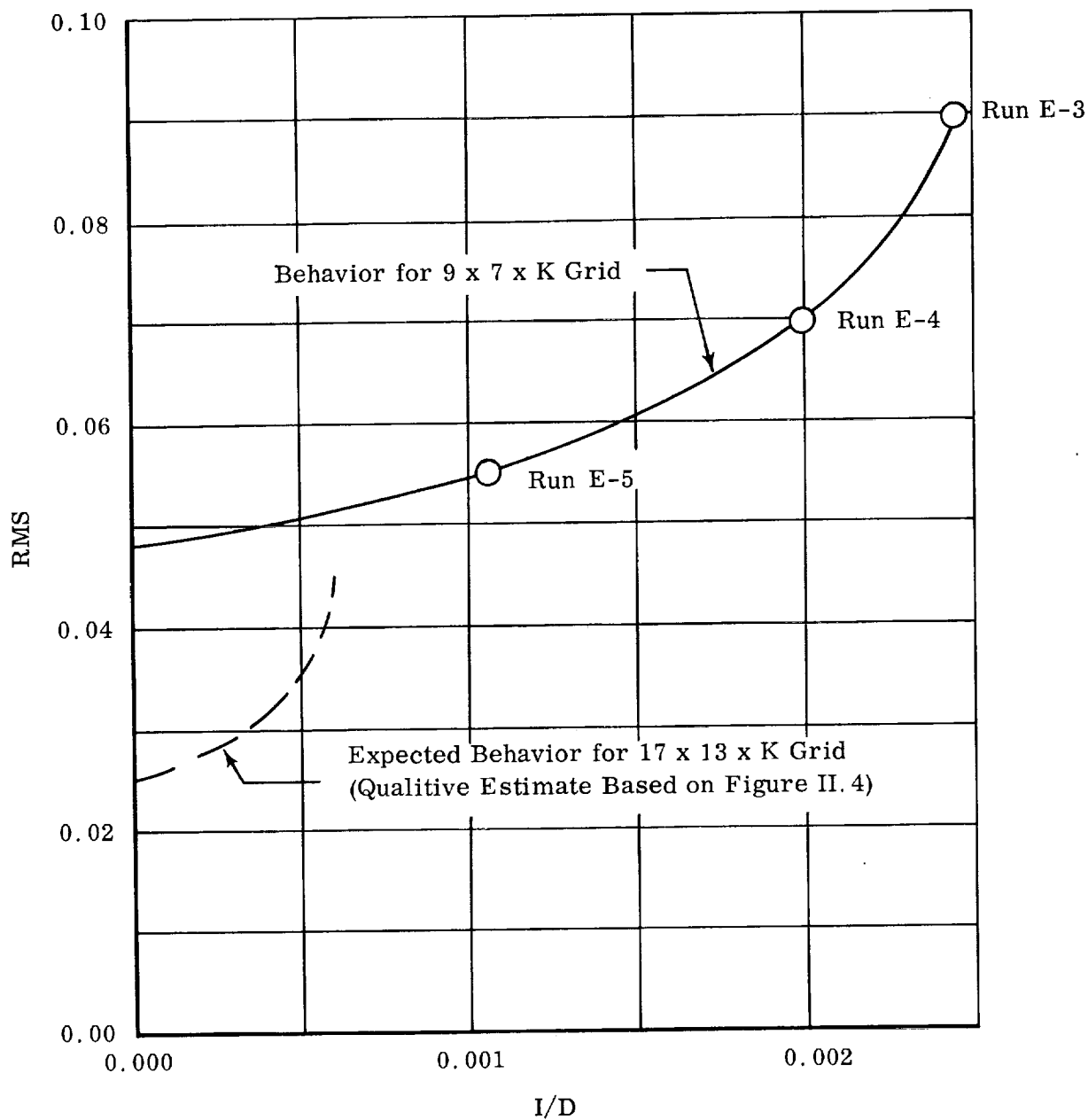
FIGURE II.11. INFLUENCE OF THE TAKE-UP EFFECT AND GRID POINT DENSITY
ON ATTAINABLE ACCURACY. Three-dimensional incompressible irrotational
flow. Minimum attainable root-mean-square residual (RMS) as a function of
number of independently adjustable discrete variables (D).

a) View Into Inlet

Notes on Geometry:

Three radial-element blades.

Lead equation for pressure side of blade:

$$\frac{d\theta}{dz} = 0.10857 + 0.03444\,z^2$$

Solidity: $\sigma = 5.9$

Suction sides of blades faired from zero at $z = 0.0$ to full thickness at $z = 0.1086$. Full thickness maintained thereafter.

Linear dimensions given in units of tip radius.

b) Meridional View

c) Developed View of Blade Tip
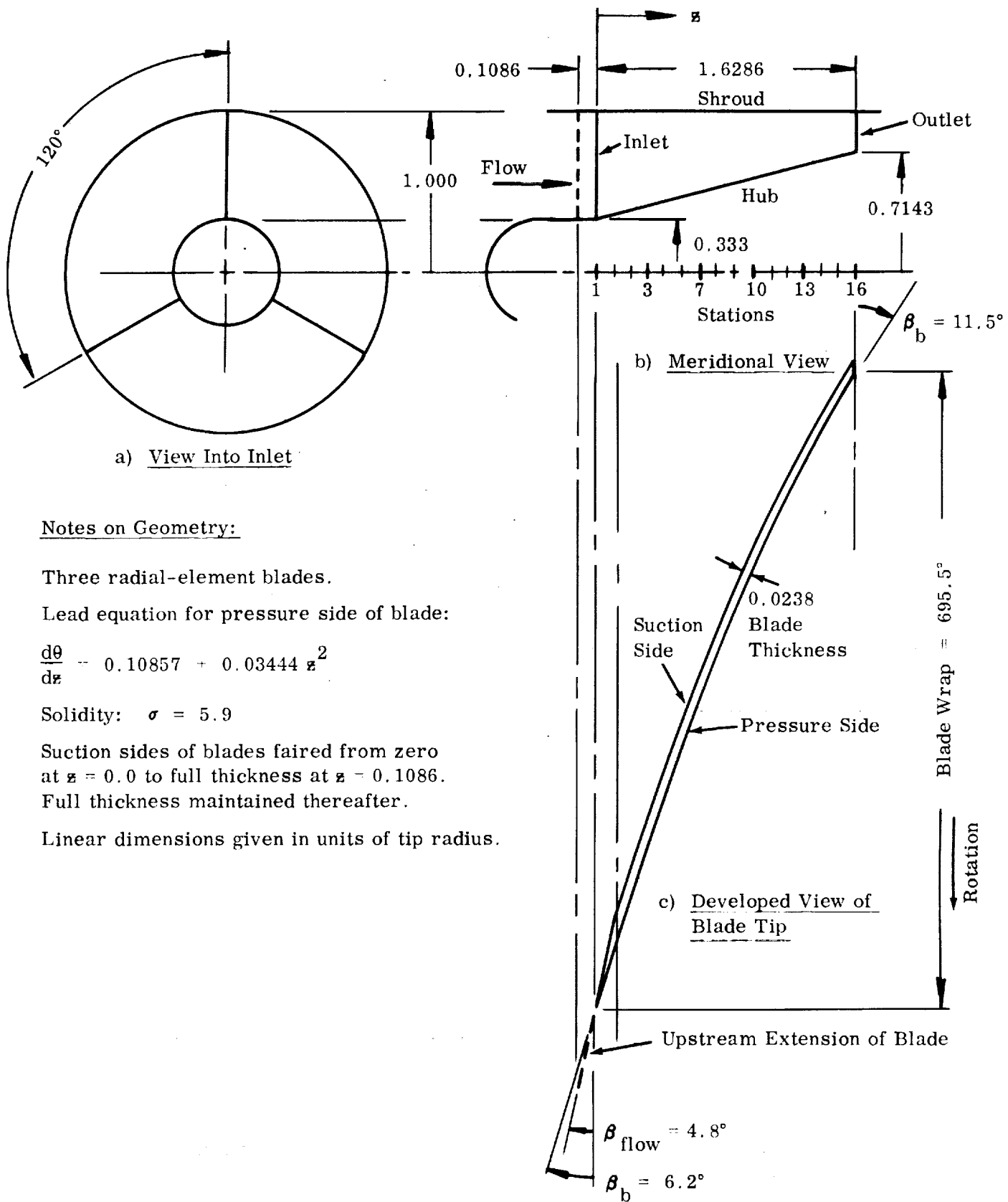
FIGURE II.12. VARIABLE-LEAD INDUCER GEOMETRY FOR 6.2° BLADE TIP INLET ANGLE.

53

where z = 0 at the blade leading edge. This gives blade tip angles of 6.2° and 11.5°, respectively, at the leading and trailing edges.

The finite-difference grid includes one station at a distance of approximately one-half of a channel width upstream of the blade leading edge. The angle of these upstream stagnation surfaces is chosen so that

$$\frac{d\theta}{dz} = \frac{\Omega}{w} \tag{II.41}$$

For a nondimensional rotative speed of Ω = 1.0 and inlet axial velocity of w_1 = 0.08302, this results in an inlet incidence angle of i = 1.45°.

The initial throughflow velocities, w, are made to vary linearly from inlet to outlet where the trailing edge distribution is the one which resulted from an earlier version of Run A-1 (see Section III.B.1). These velocities turned out to be approximately 7% low at exit due to failure to allow for blade blockage (see figure III.5). Therefore, this is equivalent to a physical incompatibility in that "less comes out than goes in". The method of star residuals, however, still finds a solution with minimum total residual for the imposed boundary conditions. The remaining runs in this section demonstrate that this inconsistency in the specified exit velocity does not affect the basic nature of the resulting velocity distributions.

The radial velocities, u, are distributed linearly from hub to shroud at each axial station, so that they are estimated by

$$u = w \frac{dr}{dz}$$

where the slope $\frac{dr}{dz}$ varies linearly from hub to shroud. The relative circumferential velocities are estimated by

$$v = wr \frac{d\theta}{dz}$$

where $\frac{d\theta}{dz}$ is an average, measured halfway between the blade surfaces at each axial station. This is done in order to get a fair approximation of the unknowns at the beginning of the problem. For the same reason, initial pressures are calculated at each grid point from

$$p = \frac{\rho_f}{2g_o} (r^2 \Omega^2 + w_1^2 - u^2 - v^2 - w^2) \tag{II.42}$$

which is a consequence of integrating the momentum equation (I.12) along streamlines with the above velocity components and p = 0 on the upstream axial plane.

54

The RMS reduction for a 25-cycle run of this problem is shown in figure II. 13. Initial and final hub-to-tip distributions of area-averaged pressures and absolute velocity components at the blade trailing edge are presented in figure II. 14. The behavior of the mass-averaged performance parameters shown in Figure II. 15 indicates that these stabilized after about 16 relaxation cycles. The remaining cycles served to effect local alterations of the internal distributions to further reduce the value of RMS.

Note that the pressures in figure II. 16 indicate some loading at the leading edge. This loading increases somewhat inside the channel and there is a tendency to unload at the blade trailing edge. Had we extended the grid several stations downstream of the trailing edge, this unloading would have been stronger, as will be shown in the remaining runs.

Another effect which we learned about is a result of the relatively coarse grid and high degree of obliqueness of the (α, β, γ) - coordinate system used (see Appendix A). The combination of low blade angle and large axial grid distance Δs causes the "streamline distance" $\Delta \gamma$ between the points to be about four times the circumferential distance $\Delta \beta$ between them and about seven times the channel width. Therefore the distances between points in a "star" are highly nonuniform and the finite-difference formulae are not representative of the local partial derivatives (see equation A. 3). A "reasonable" grid, therefore, would have required twice as many points each in the radial and circumferential directions, and about ten times as many axial stations; i.e. a 10 x 10 x 100 grid. This would have extended computer running times beyond practical limits. In spite of these remarks, however, we point to the relatively good quality of the results which are attainable even with such a coarse grid as we used.

In all of the preceding runs, the variables at each grid point were adjusted in the sequence (u, v, w, p). We found by experimenting that considerable savings in overall running time can be achieved by altering this sequence. Thus, for the sequence (p, u, v, w) we noticed the running time per cycle reduced by about 3% and the reduction of RMS values improved by about 14% per cycle. The result is an improvement of about 16% in the overall RMS-reduction per time. Further improvement in performance of the computer program was indicated when the sequence (p, w, v, u) was used. Although we recommend this latter adjustment sequence - and this sequence is used in all remaining runs of the three-dimensional method - we believe that the optimum order of adjusting the variables depends largely on the initial distributions. For each type of problem, therefore, an adjustment sequence which shows an improved convergence rate may be determined experimentally although ultimate convergence to the minimum obtainable total residual (as discussed in Section II. A. 5) is always assured.
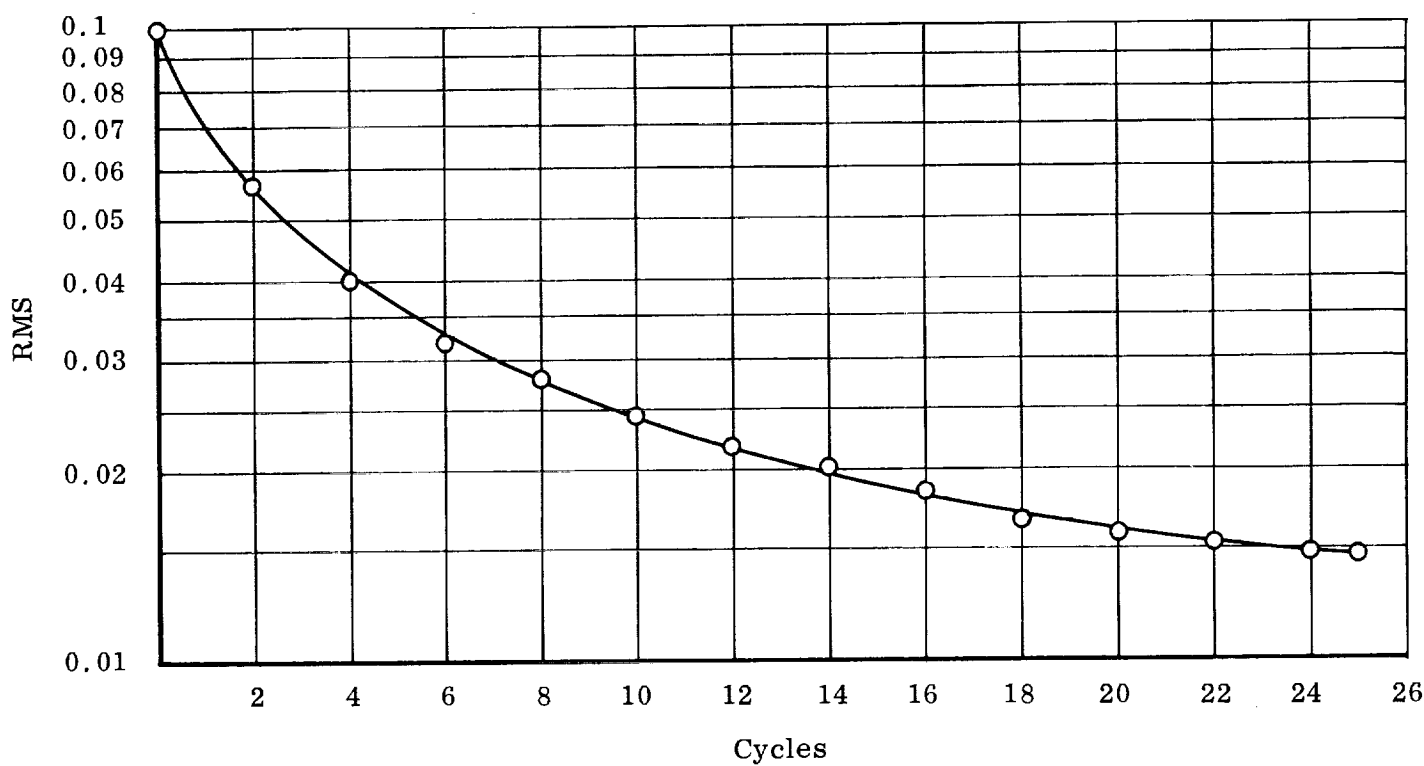
FIGURE II.13.   RESIDUAL RELAXATION DATA FOR INCOMPRESSIBLE, LOSSLESS FLOW IN 6.2° INDUCER. Run E-6. Root-mean-square residual vs. number of relaxation cycles.
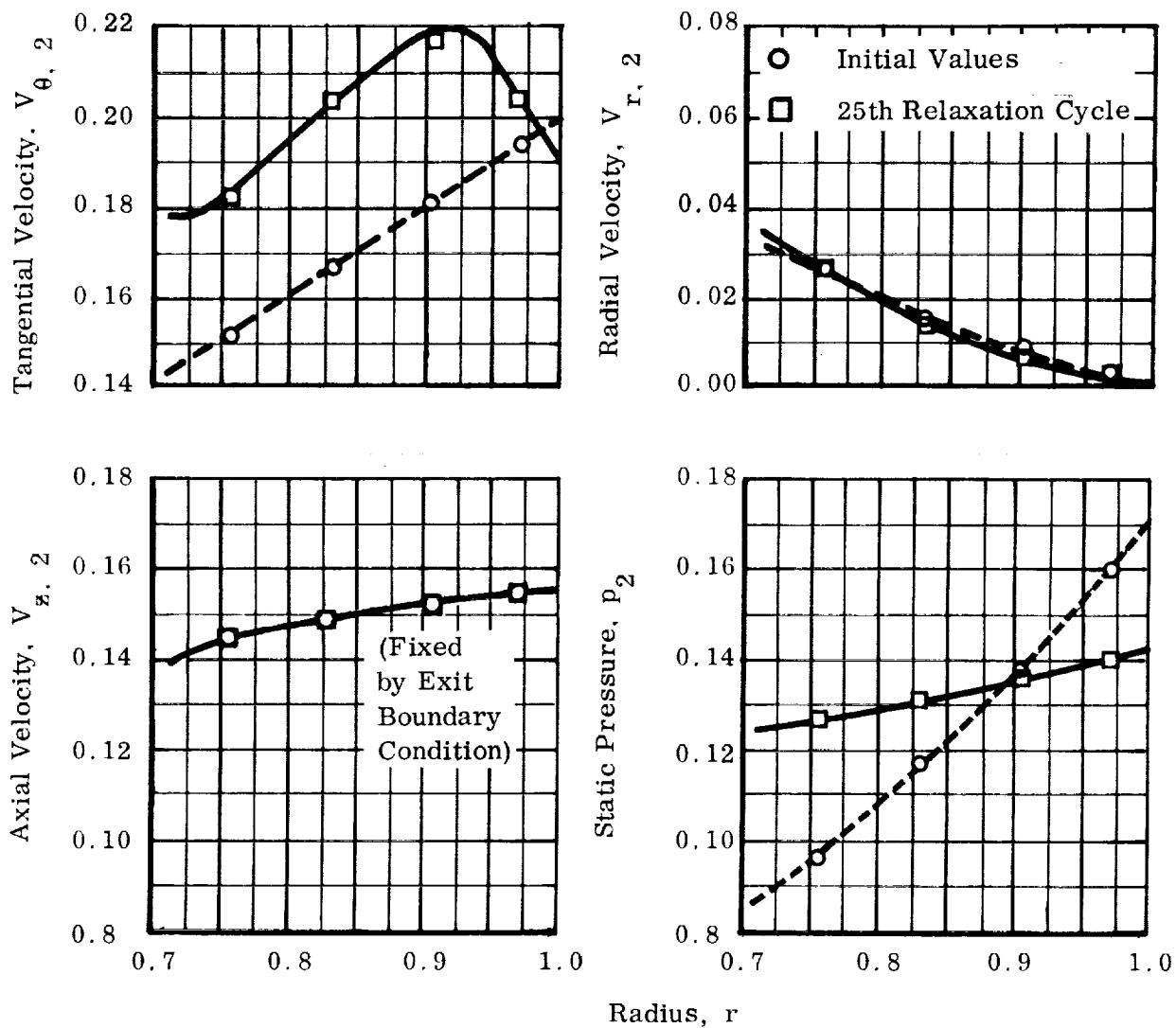
FIGURE II.14. RADIAL DISTRIBUTIONS OF OUTLET VELOCITY AND PRESSURE
FOR INCOMPRESSIBLE, LOSSLESS FLOW IN 6.2° INDUCER. Run E-6. Area
averages of blade-to-blade results.
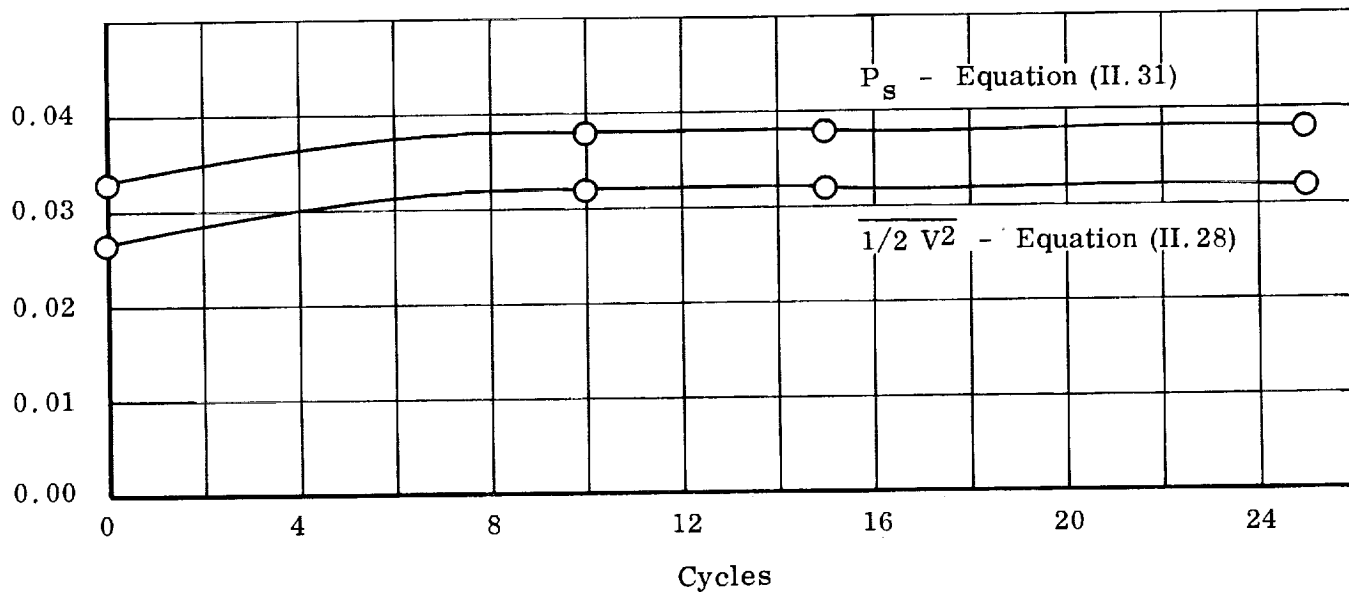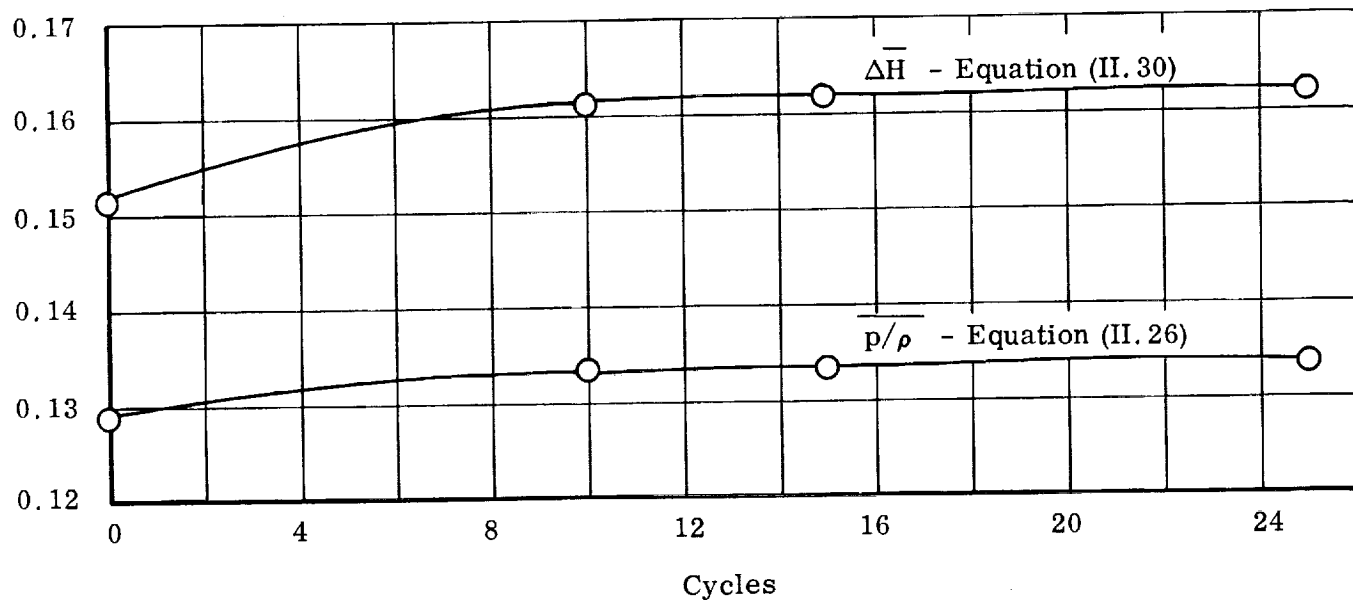
FIGURE II.15. OVERALL PERFORMANCE RELAXATION DATA FOR
INCOMPRESSIBLE, LOSSLESS FLOW IN 6-2° INDUCER. Run E-6.
Mass-averaged outlet parameters vs. number of relaxation cycles.
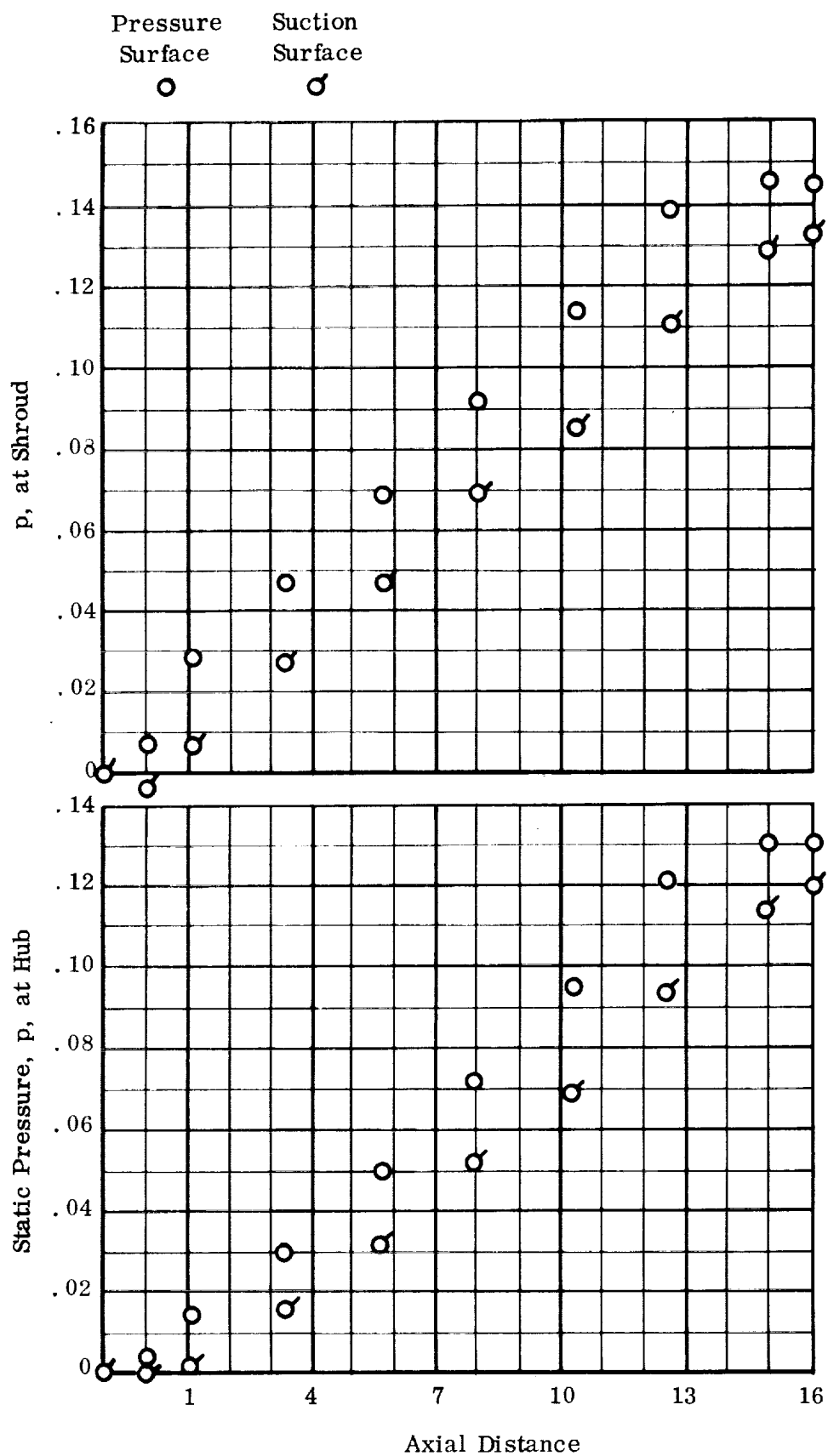
FIGURE II. 16.   AXIAL DISTRIBUTIONS OF BLADE SURFACE PRESSURE
FOR INCOMPRESSIBLE, LOSSLESS FLOW IN 6.2° INDUCER: Run E-6.

FIGURE II.17. AXIAL DISTRIBUTION OF BLADE SURFACE VELOCITY
FOR INCOMPRESSIBLE LOSSLESS FLOW IN 6.2° INDUCER: Run E-6.

In view of the above observations, we next analyzed an inducer channel of the same overall dimensions as the above one but with higher blade angles. The grid we selected has 2.2 times as many points, and we extended the flow field upstream and downstream of the blades by an axial distance equivalent to approximately one channel width. This is consistent with other numerical calculations of fluid flow fields (see, for example, references 23 and 24). The geometry used for the remaining computer runs is shown in figure II.18.

The lead equation for the pressure surfaces of the blades of this inducer is

$$r \tan \beta_b = \frac{dz}{d\theta} = \underbrace{.21256}_{a} + \underbrace{.09830}_{c} z^2 \tag{II.43}$$

where $z = 0$ at the blade leading edge. This gives blade tip angles of $12°$ and $24.5°$, respectively, at the leading edge ($z = 0.0$) and the trailing edge ($z = 1.62857$).

The finite-difference grid includes three axial stations each upstream and downstream of the blade system. The angle for the upstream stagnation surfaces is again calculated from equation (II.41). With an inlet axial velocity of $w = 0.17633$, this results in an incidence angle of $2°$ at the leading edge, which was chosen as a representative value for these inducer calculations.

The initial throughflow velocities, w, are chosen so that mass conservation is satisfied one-dimensionally from inlet to outlet. As was done in the case of the $6.2°$ inducer, the radial velocities, u, are distributed linearly from hub to shroud at each axial station so that

$$u_h = w \left(\frac{dr}{dz} \right)_h$$

where $\left(\frac{dr}{dz} \right)_h$ is the slope of the hub. The relative circumferential velocities are given by

$$v = wr \frac{d\theta}{dz}$$

where $\frac{d\theta}{dz}$ is an average, measured halfway between the blade surfaces at each axial station.

a) View Into Inlet

120°

Notes on Geometry:

Three radial-element blades.

Lead equation for pressure side of blade:

$$\frac{d\theta}{dz} = 0.21256 + 0.09830 \, z^2$$

Solidity: $\sigma = 2.9$

Suction sides of blades faired from zero at $z = 0.0$ to full thickness at $z = 0.1086$. Full thickness maintained thereafter.

Linear dimensions given in units of tip radius.

0.3258   1.6286   0.3258
Shroud
Outlet
1.000   Flow   Inlet
Hub
0.7905
0.333   0.7143
1 3 7 10 13 16
Station

b) Meridional View

$\beta_{flow} = 29.7°$

$\beta_b = 24.5°$

Downstream Extension of Blade

Suction Side

0.0238 Blade Thickness

Blade Wrap = 331.5°

Rotation

Pressure Side

Upstream Extension of Blade

$\beta_b = 12°$

$\beta_{flow} = 10°$

c) Developed View of Blade Tip

FIGURE II. 18.   VARIABLE-LEAD INDUCER GEOMETRY FOR 12° BLADE TIP INLET ANGLE.

Initial values of pressures are again calculated from

$$p = \frac{\rho_f}{2g_o} (r^2 \Omega^2 + w_1^2 - u^2 - v^2 - w^2) \tag{II.42}$$

The downstream stagnation stream surfaces are initially selected so that no energy is added to the flow downstream of the blade trailing edge. We simulate this condition by requiring that V_θ remain axially constant for constant r. Since

$$V = V_\theta - r\Omega$$

this is equivalent to requiring that $\frac{v}{r}$ remain constant. But

$$r \frac{d\theta}{dz} = \frac{1}{\tan \beta_b} = \frac{v}{w} = \frac{vA}{q} \tag{II.44}$$

where A is the channel cross section area and q is the constant volume flow rate. Therefore the stagnation stream surface angles are calculated from

$$\frac{d\theta}{dz} = \left(\frac{v}{rq}\right) A \tag{II.45}$$

i. e. the rate of change of angle with axial distance is proportional to cross section area. Note that finally the only way to obtain no energy addition by the stagnation stream surfaces is to adjust them and re-compute until no pressure difference exists across them.

Run E-7: 12° Inducer - 5 x 5 x 22 Grid

The first run with the above described inducer channel was made for an incompressible, lossless fluid. Figure II.19 shows that the value of RMS is still being reduced after fifteen relaxation cycles. As was the case for Run E-6, however, we see that the values of relative circulation (figure II.20) have reached their final levels by the eighth relaxation cycle. In figure II.22 we present a chronology of the hub-to-tip distributions of the pressures and velocity components at the inducer exit plane. The final pattern for these area-averaged quantities has emerged by the 15th relaxation cycle.

The resulting hub-to-tip distribution of absolute circumferential velocity V_θ is not one which would be expected from simple radial equilibrium
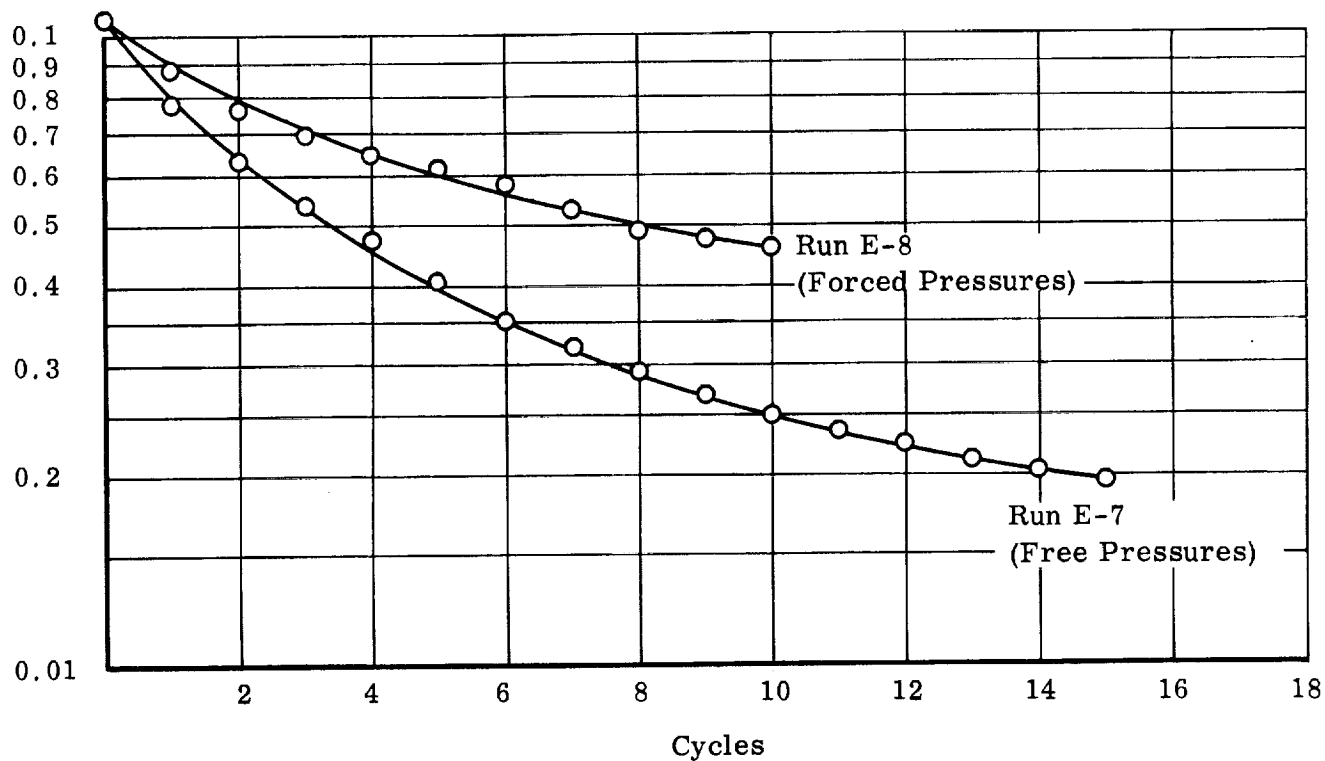
FIGURE II.19. RELAXATION DATA FOR INCOMPRESSIBLE, LOSSLESS
   FLOW IN 12° INDUCER. Runs E-7, 8. Root-mean square residual (RMS) vs.
   number of relaxation cycles.
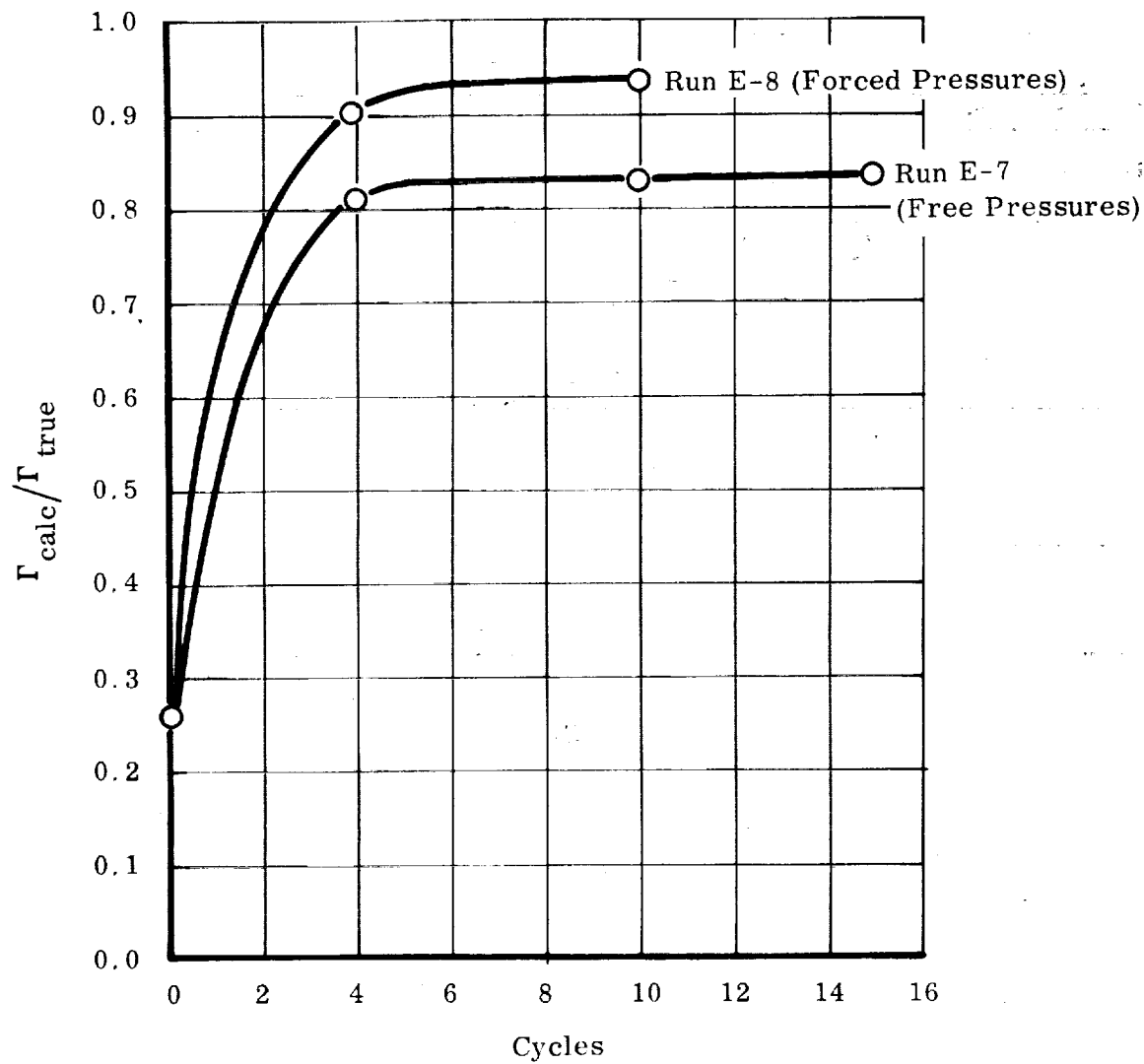
FIGURE II.20. CIRCULATION RELAXATION DATA AT EXIT FOR
INCOMPRESSIBLE, LOSSLESS FLOW IN 12″ INDUCER.
Runs E-7, 8. Relative circulation ratio ($\Gamma_{calc} / \Gamma_{true}$) vs.
number of relaxation cycles.
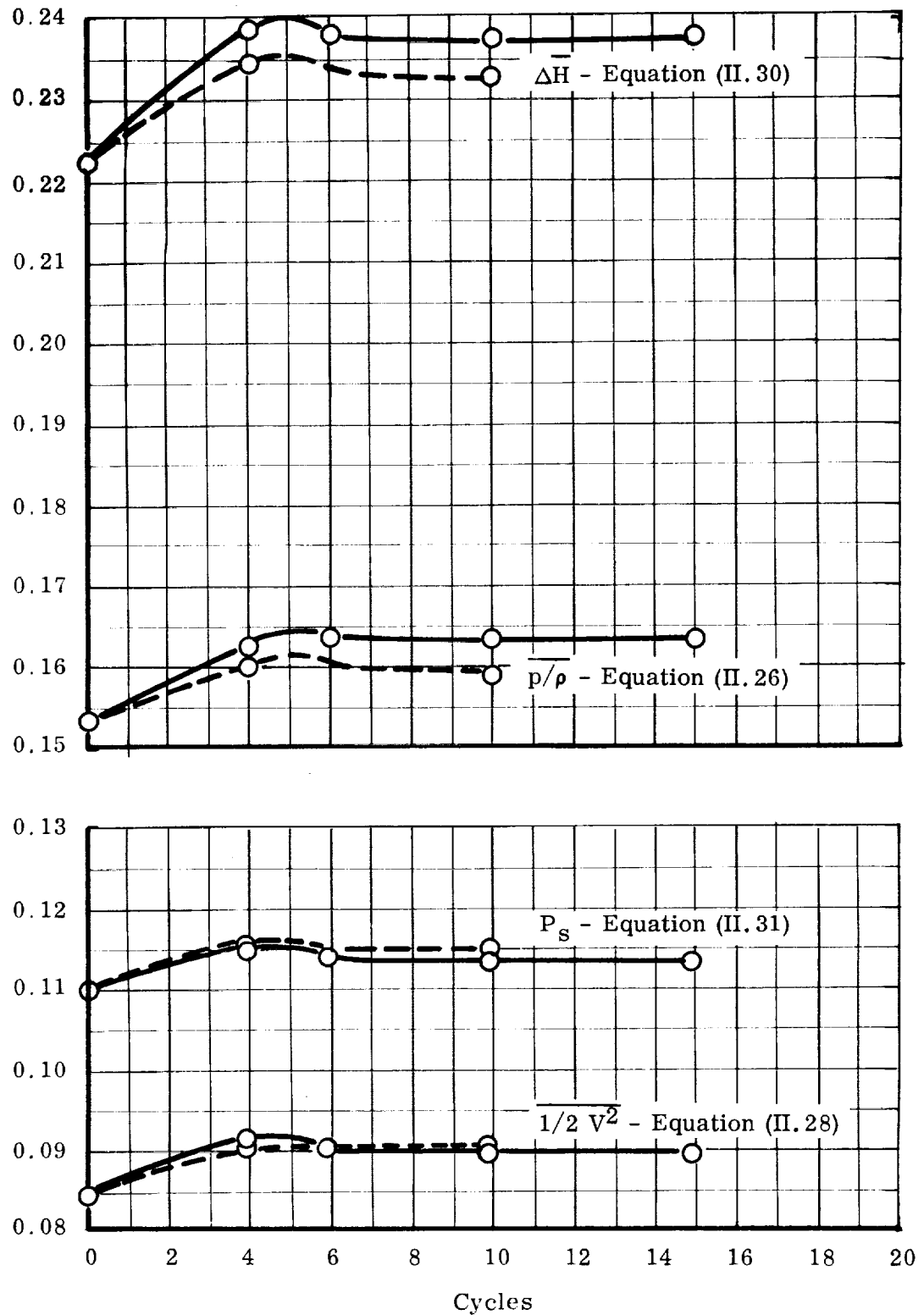
FIGURE II.21. OVERALL PERFORMANCE RELAXATION DATA FOR INCOMPRESSIBLE, LOSSLESS FLOW IN 12° INDUCER. Runs E-7, 8. Mass-averaged outlet parameters vs. number of relaxation cycles.
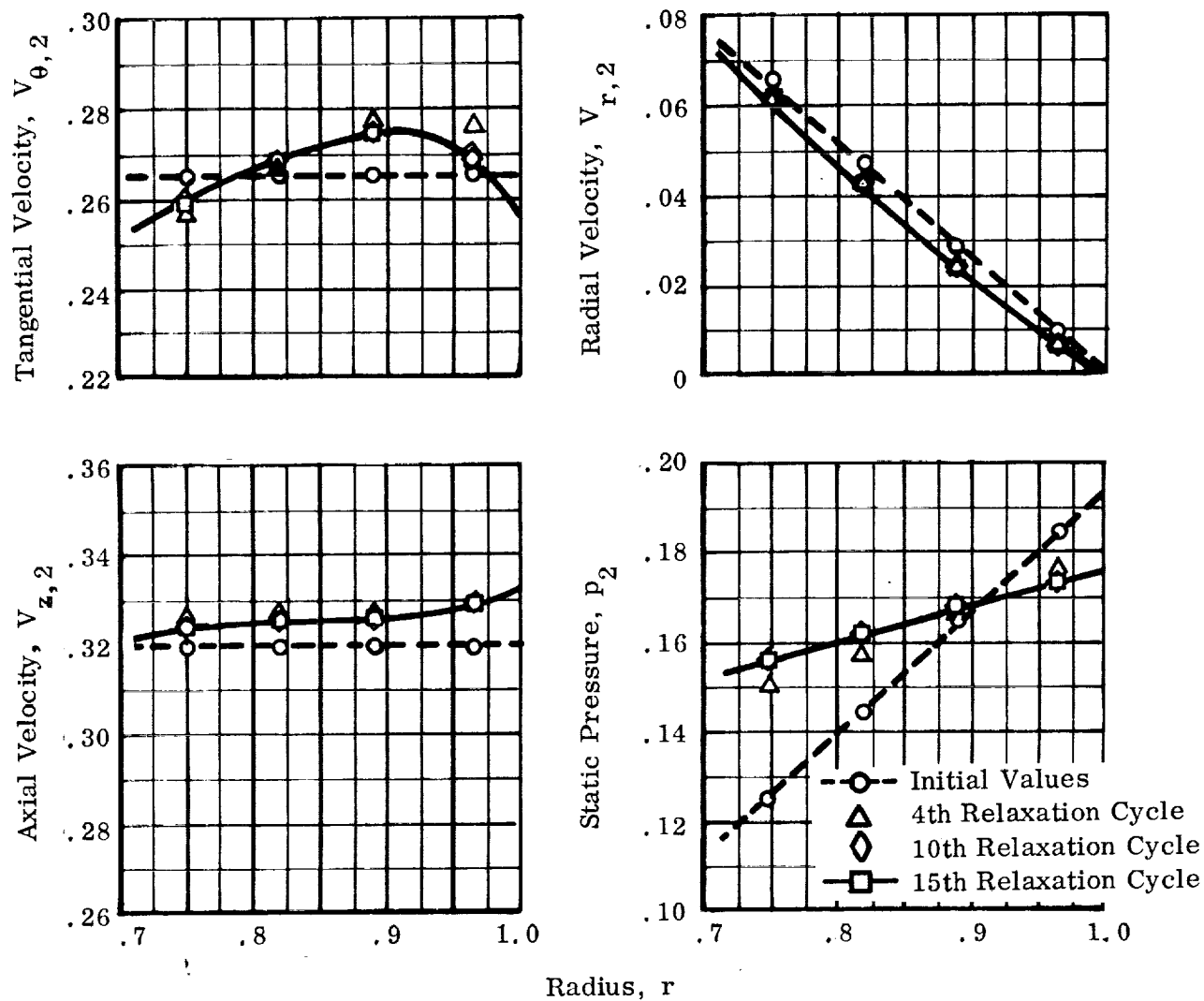
FIGURE II. 22.   RADIAL DISTRIBUTIONS OF OUTLET VELOCITY AND PRESSURE
FOR INCOMPRESSIBLE, LOSSLESS FLOW IN 12° INDUCER: FREE PRESSURES.
Run E-7.   Area averages of blade-to-blade results.

solutions of inducers. For example, those of reference 6 can be shown to tend toward free vortex flow: V_θ high at the hub and low at the tip. (In subsequent runs we did achieve this. See Figures II.23 and III.6.) The flow pattern of relative circulation counter to the direction of rotation of the machine, however, was present in the distributions of the relative velocity components. Part of this may be due to the fact that the circumferential distance between grid points at the trailing edge is approximately 3/5 of the channel width. Another reason may be the fact that the absolute value of pressure is inconsequential in satisfying the equations of motion (for an incompressible fluid) and that only the local pressure gradients need be approximately correct (see equations (II.5) through (II.8). To test this hypothesis we made the following run for comparison.

Run E-8: 12° Inducer - 5 x 5 x 22 Grid - Forced Pressures

The geometry and initial assumptions for this run are exactly the same ones as were used for the previous run. During the relaxation procedure, however, the pressures are forced to satisfy

$$p = \frac{\rho_f}{2g_o} (r^2 \Omega^2 + w_1^2 - u^2 - v^2 - w^2) \qquad (II.42)$$

This requirement introduces no mathematical inconsistency, because, for zero inlet pressure, no inlet whirl, no losses and an incompressible fluid, equation (II.42) applies exactly everywhere in the flow field. Each time one of the relative velocity components is varied at a grid point (see Section II.A.3), the corresponding local value of the pressure is immediately calculated from equation (II.42). Therefore, $p_{i,j,k}$ is no longer an independent discrete variable.

Recalling the discussion of the take-up effect from Section II.B.2, we would expect the value of RMS to be higher for this run with forced pressures than they were for the previous run, since D is lower due to this elimination of $p_{i,j,k}$. This comparison is shown in figure II.19. However, figure II.20 shows that the relative circulation at exit is closer to the true value when the pressures are forced to satisfy equation II.42 than when they are free to be adjusted independently. From figure II.21 we see that the values of shaft power, P_s, and exit velocity head, $\frac{V^2}{2g_o}$, are essentially the same for these two comparative runs. The value of the mass-averaged exit pressure head, $(\overline{p/\rho})$, settles at 0.1635 for free pressures and at 0.1590 for forced pressures. A one-dimensional calculation with zero deviation predicts a value of 0.1406 at the root-mean-square radius, $r = 0.869$, at the blade trailing edge. The most prominent effect of forcing the pressures to satisfy equation (II.42) is seen in the hub-to-tip distribution of V_θ (see figure II.23). As was mentioned above, this is the type of distribution we would expect for this problem.
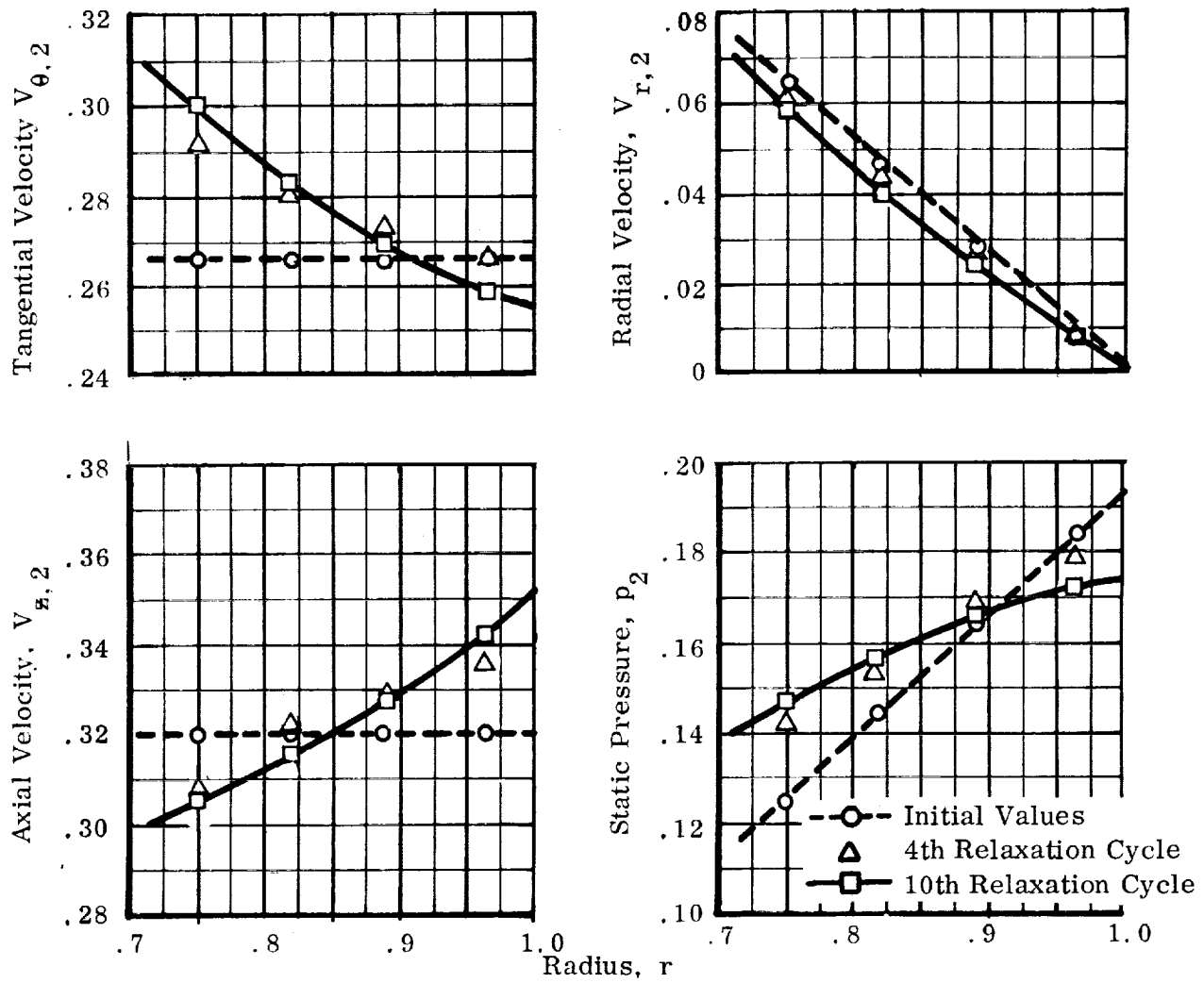
FIGURE II. 23. RADIAL DISTRIBUTIONS OF OUTLET VELOCITY AND PRESSURE
FOR INCOMPRESSIBLE, LOSSLESS FLOW IN 12° INDUCER: FORCED
PRESSURES. Run E-8. Area averages of blade-to-blade results.

Figures II. 24 and II. 25 show a comparison of the resulting relative velocity distributions on the blade surfaces for the two runs. Notice that the numerical oscillations, present in the run where the pressures are free, are almost absent in the comparable run with forced pressures. This could be simply a grid-point density effect coupled with boundary extrapolation influence. Comparison of the distributions of static pressure on the blade surfaces is shown in figures II. 26 and II. 27. The latter shows that unloading of the blades downstream of the trailing edges is shown very definitely in the run with forced pressures.

Run E-9:   12° Inducer - 5 x 5 x 22 Grid - Two-Phase Flow

The purpose of this final run with the exact three-dimensional solution method is to demonstrate that it will work for two-phase inducer flow calculations.   Our equation of state

$$\rho = \begin{cases} \rho_f & , \ p \geq p_{sat} \\ \dfrac{\rho_f}{1 + T^* (p_{sat} - p)} & , \ p < p_{sat} \end{cases} \tag{I. 7}$$

was easily incorporated into the computer program.   Because of the two-phase flow effects, equation III. 42) is no longer applicable, of course.

Again, exactly the same geometry and initial assumptions were used as in the preceding two runs.   The following parameters were used for the state equation:

$$p_{sat} = 0.0$$

$$\rho_f = 1.0$$

$$T^* = 40.0$$

which simulates a flow of 36°R hydrogen or 450°F water in an inducer running at a blade inlet tip speed of 447 feet per second.   Since the upstream pressure is also zero, the hydrogen or water would be at the boiling point upstream of the inducer inlet.

The RMS values for this five-cycle run differed from the corresponding RMS values of Run E-7 by less than 0.002.   At the end of the fifth cycle the blade surface distributions of relative velocity (figure II. 28) are essentially the same as those at the end of the 15th cycle of the comparable incompressible run (figure II. 24), although the oscillations of some of the distributions are somewhat reduced.   This seems to indicate that these oscillations are part of the numerical behavior for this size grid.
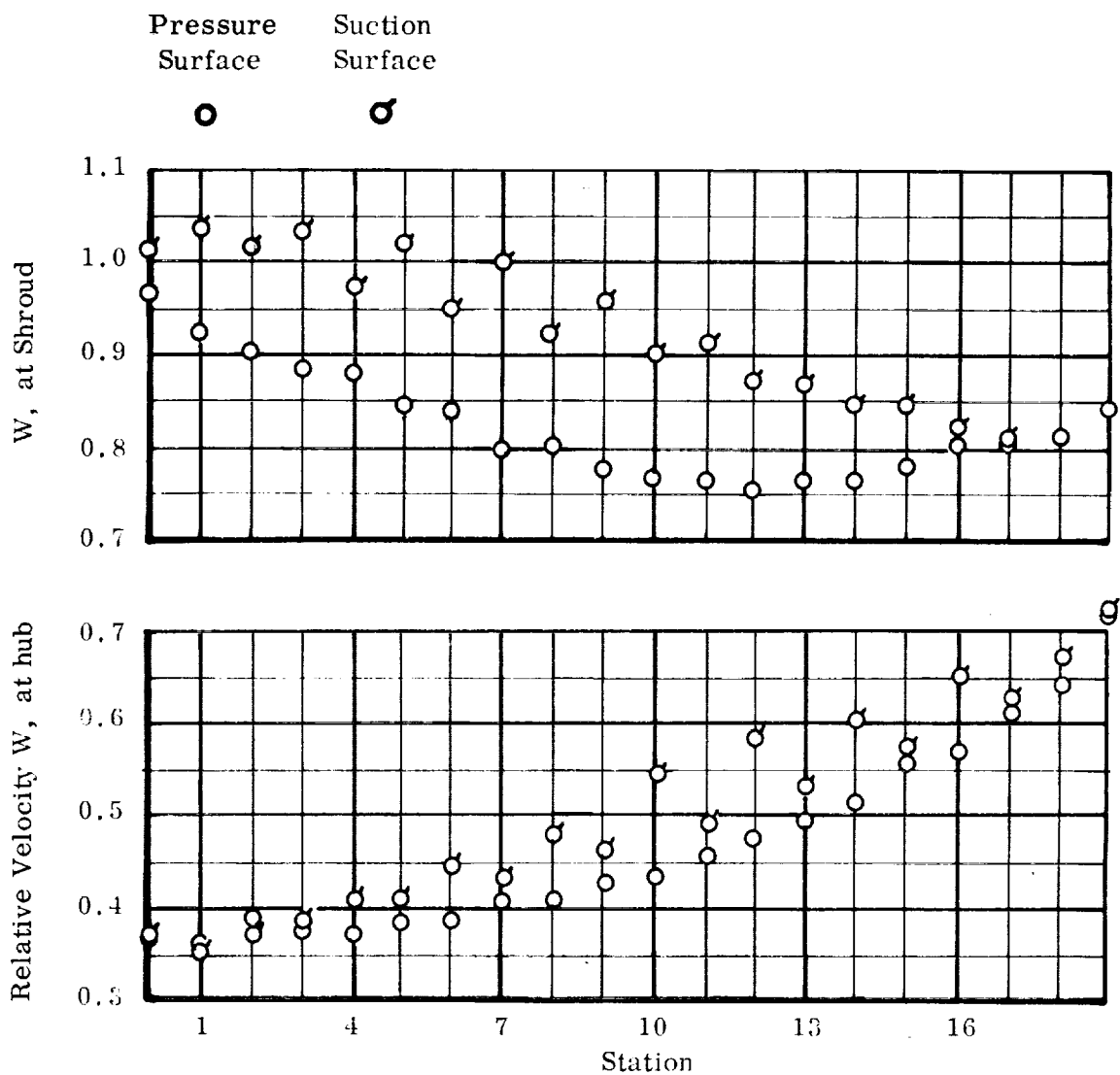
FIGURE II.24. AXIAL DISTRIBUTION OF BLADE SURFACE VELOCITY FOR INCOMPRESSIBLE, LOSSLESS FLOW IN 12° INDUCER FREE PRESSURES. Run E-7.
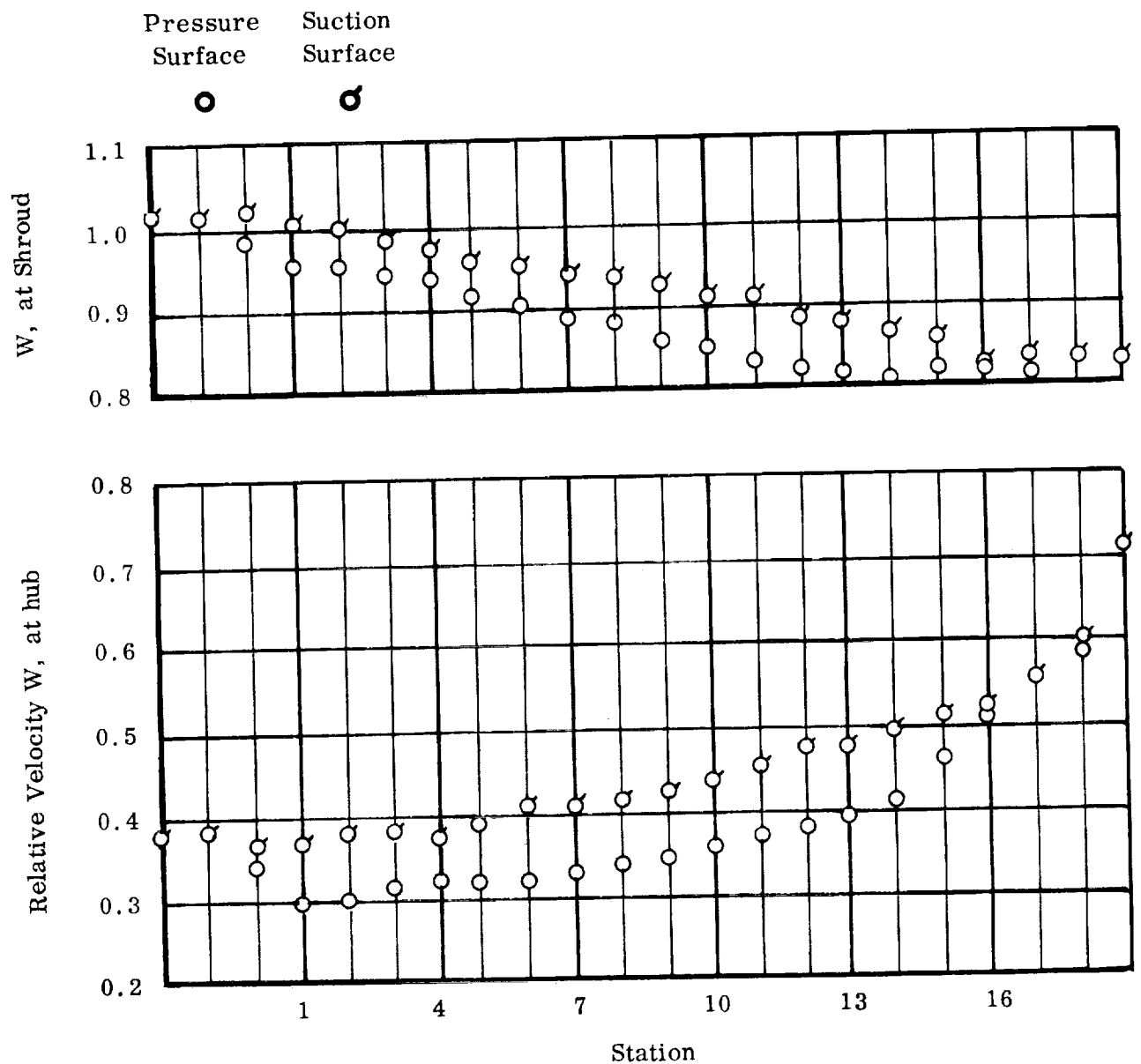
FIGURE II. 25. AXIAL DISTRIBUTIONS OF BLADE SURFACE VELOCITY FOR
INCOMPRESSIBLE, LOSSLESS FLOW IN 12° INDUCER: FORCED PRESSURES.
Run E-8
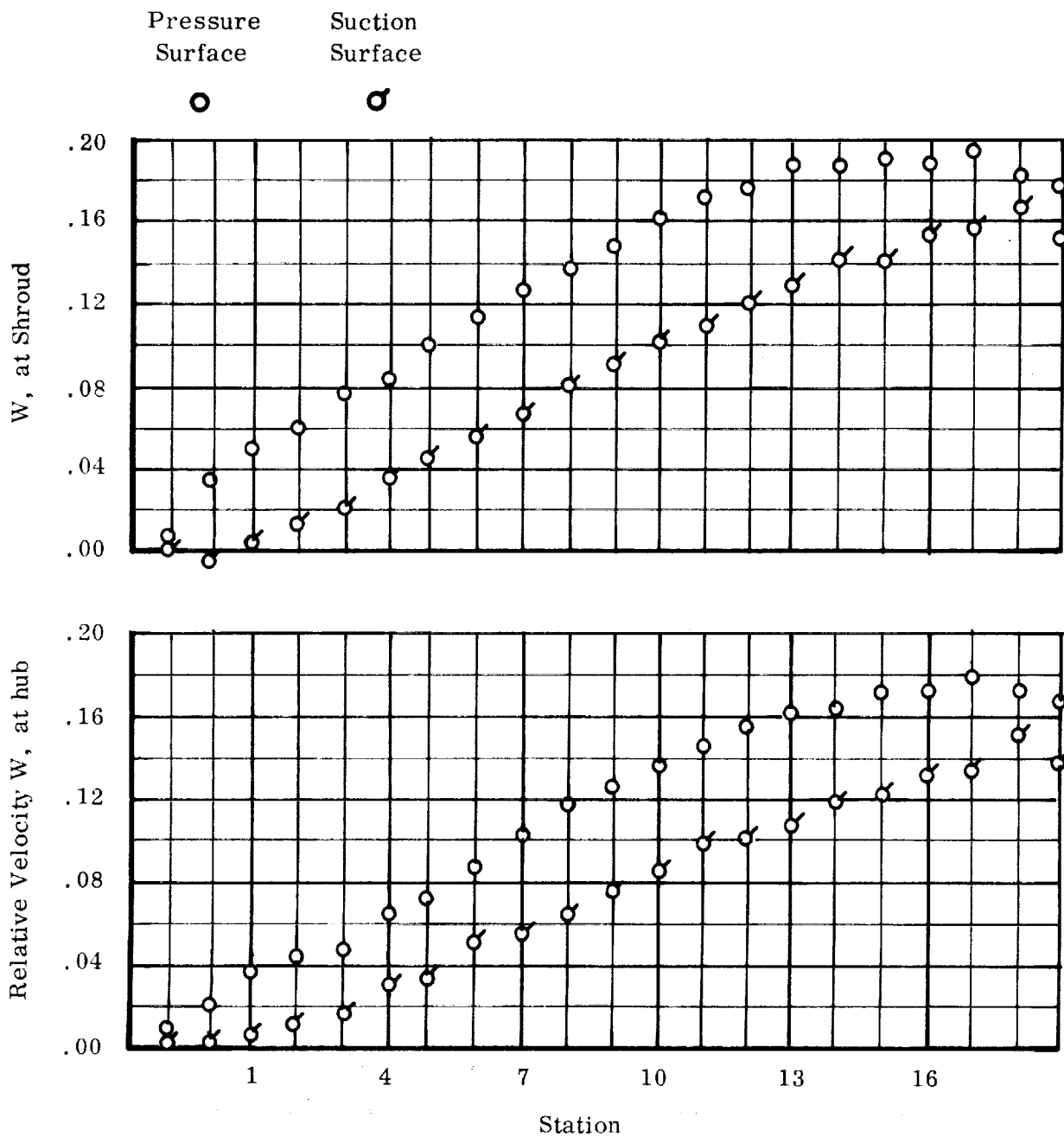
FIGURE II.26.   AXIAL DISTRIBUTION OF BLADE SURFACE PRESSURE FOR
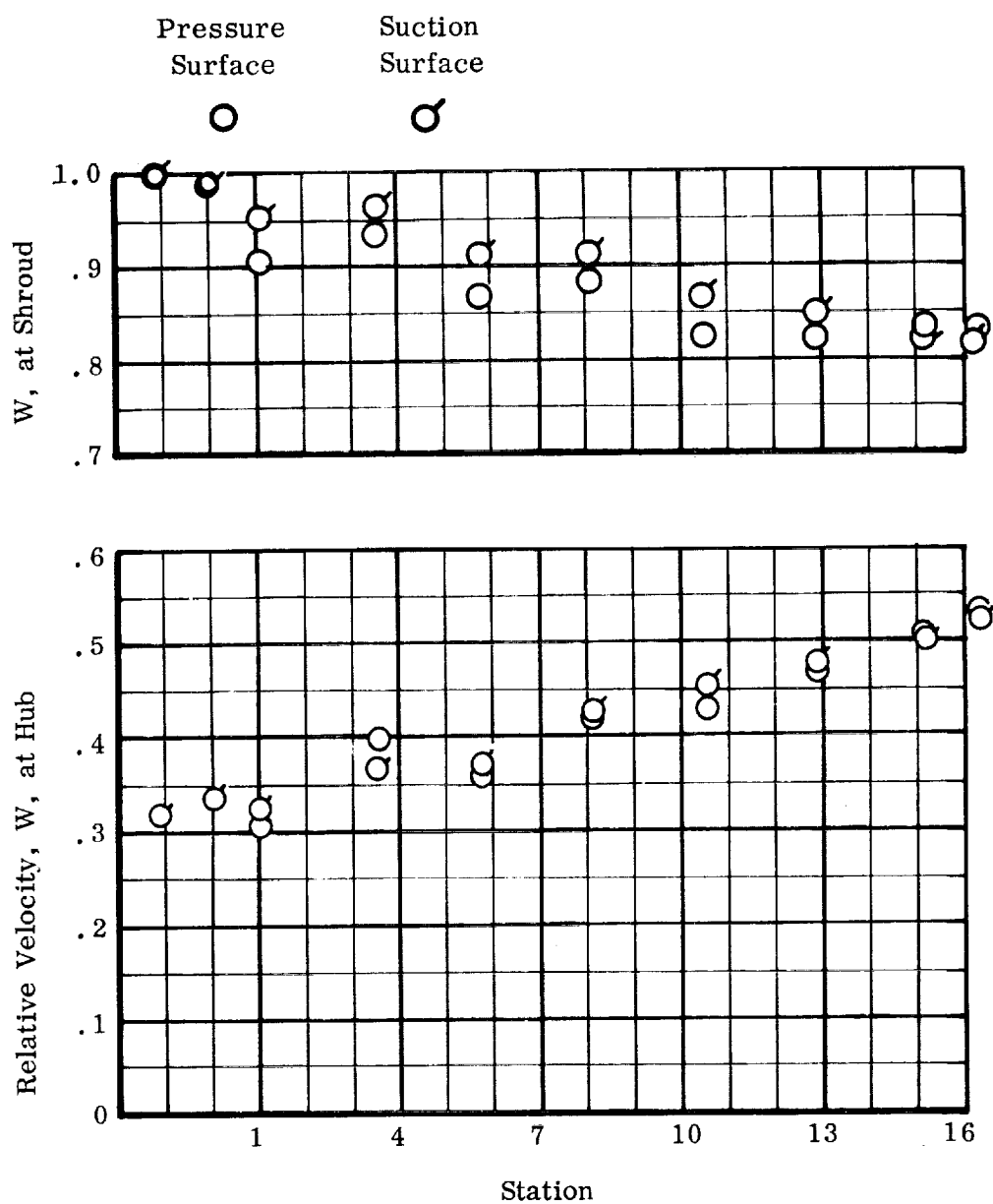   INCOMPRESSIBLE, LOSSLESS FLOW IN 12° INDUCER: FREE PRESSURE.
    Run E-7.

73
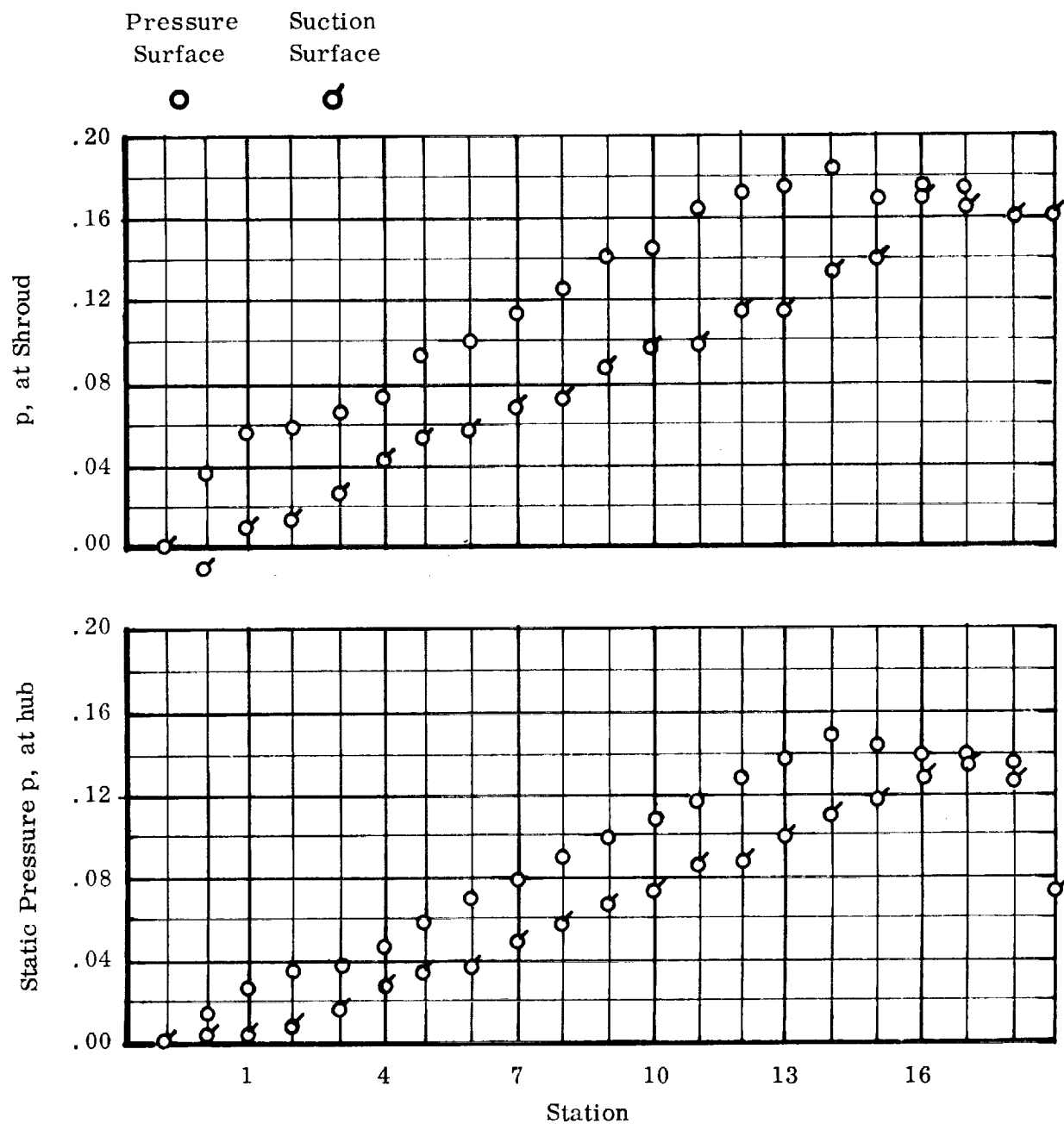
FIGURE II.27. AXIAL DISTRIBUTIONS OF BLADE SURFACE PRESSURES FOR INCOMPRESSIBLE, LOSSLESS FLOW IN 12° INDUCER: FORCED PRESSURES. Run E-8
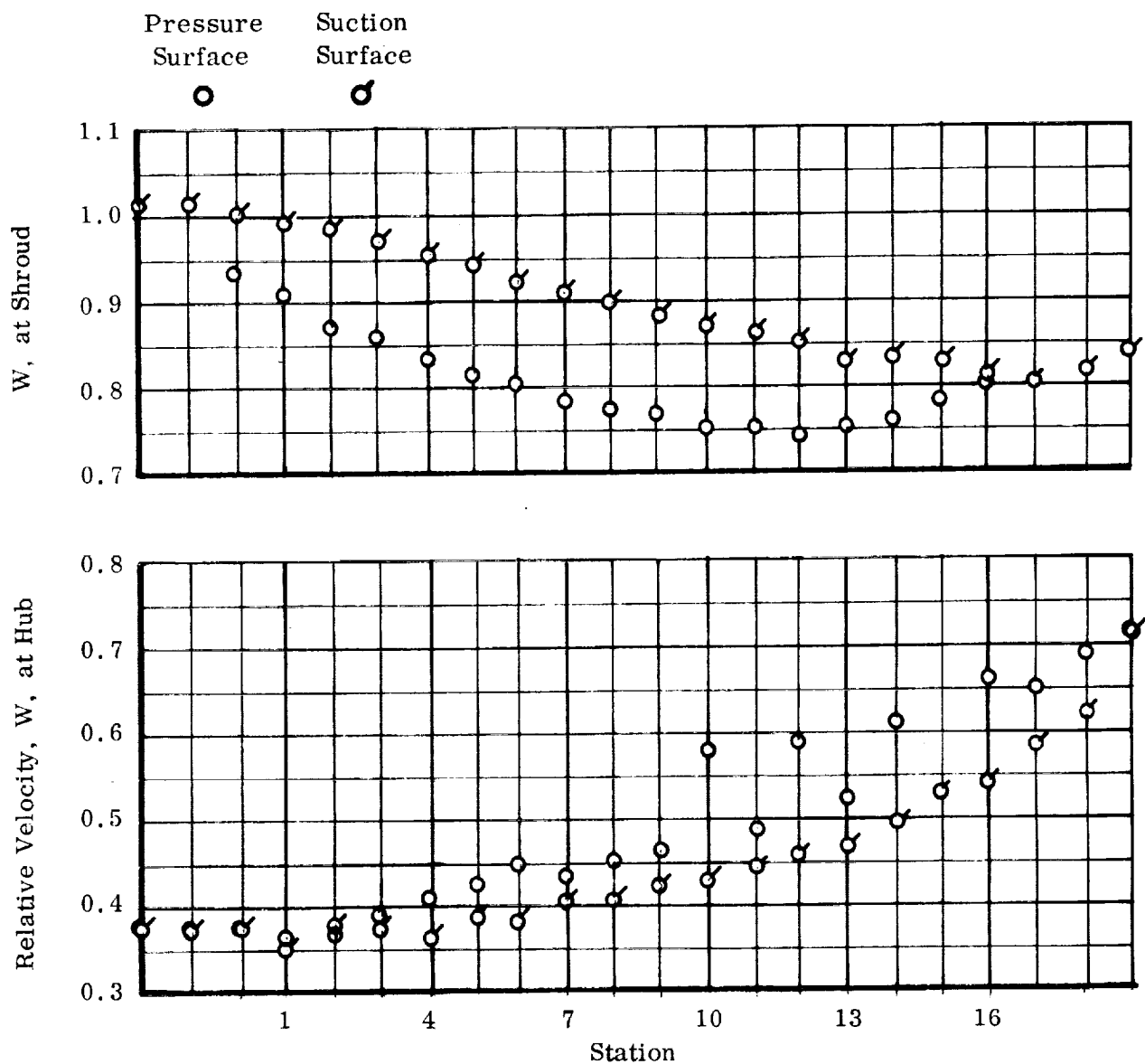
FIGURE II.28.   RELATIVE VELOCITIES (W) ALONG BLADES OF 12°
INDUCER CHANNEL FOR HOMOGENEOUS TWO-PHASE, LOSSLESS
FLOW: Run E-9.

Because the upstream stagnation surfaces, as we have selected and fixed them, actually do work on the fluid, by the time the fluid reaches the blade leading edge its pressure is already above saturation pressure. This is where the selection of proper stagnation surfaces is crucial. The internal density distributions indicate vapor in the flow region upstream of the blade leading edge. This vaporous region is small compared to the entire flow passage. For a value of $T^* = 40.0$ and an inlet pressure equal to vapor pressure, we would expect a large portion of the passage to fill with vapor (see table III.1 and figure III.24). The apparent unloading of the blades, especially at the tip, is due to the fact that figure II.26 shows the results of 15 relaxation cycles whereas in figure II.29 are shown the results of only five cycles - i.e. the solution has not been carried far enough to give the correct answers. The rotational flow pattern for both the two-phase and the incompressible run are essentially the same. All hub-to-tip distributions at the blade trailing edge, for example, differ from each other by less than 0.001.
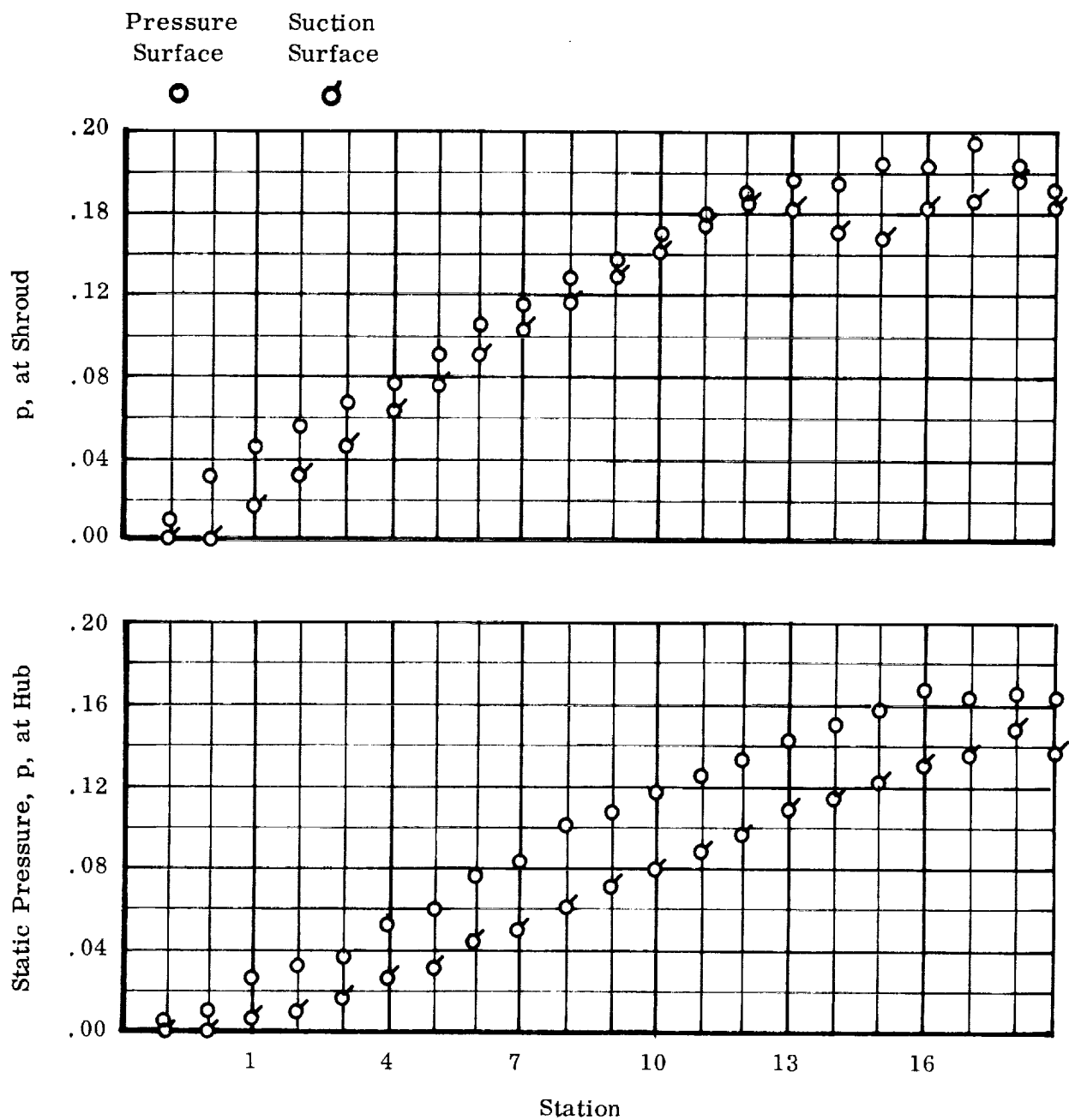
FIGURE II.29. AXIAL DISTRIBUTIONS OF BLADE SURFACE PRESSURE FOR TWO-PHASE, LOSSLESS FLOW IN 12° INDUCER: Run E-9.

C. CONCLUDING REMARKS ON EXACT METHOD OF SOLUTION

The foregoing sequence of examples demonstrates the capabilities of our numerical approach to an exact method for obtaining three-dimensional solutions of general, continuum fluid flows in turbomachinery. That the method gives valid answers is empirically evident as we now review the results of these examples.

1. Review of Problems Solved

The paddle-wheel channel examples with lossless, wheel-type flow indicate that a convergent solution is always possible — the resulting root-mean-square (RMS) residual for the incompressible case (run E-1) being much less than one percent. While this capability for minimizing the RMS residual is borne out by all the other examples, run E-2 (similar to E-1) illustrates it best by producing an answer of 1/10 of one percent, with no sign that this is remotely close the attainable minimum (Figure II.7). Furthermore, run E-2 shows that two-phase flow effects can be included successfully — and with no perceptible increase in computing time. Finally, these two simple examples illustrate the deviations from the true answers that are caused by discretization, i.e. by a finite number of grid points (3 x 3 x 3). Even though the system of finite difference equations and other conditions can essentially be satisfied in this special case, the solution to the comparable continuous problem (infinite number of grid points) yields a different radial distribution of the pressure.

The three examples (runs E-3, 4, 5) of incompressible, irrotational flow in a paddle-wheel channel illustrate the grid effects of typical problems. Here we observe the numerical inconsistency of the (essentially arbitrary) linear extrapolations at boundary points with the more complicated pressure and velocity variations there; i.e., the RMS residual achieves a minimum (or nearly so) that is non-zero in each case. Even though this residual is far enough from zero (Figure II.9) for completely wrong answers to be allowable by it, the results are fairly accurate (Figure II.10). In fact, the experiments that we conducted in runs E-4 and E-5 wherein we changed the problem of run E-3 by extending the number of points and unknowns (without altering grid point density) shows that a lower residual does not guarantee more accurate answers, (unless it is sufficiently low): The additional adjustment of variables that was possible in runs E-4 and E-5 illustrates this "take-up effect".

The foregoing discretization error is probably not dominant in runs E-3, 4 and 5, because the cross-sectional density of grid points is about seven times greater than was the case in runs E-1 and 2, (9 x 7 versus 3 x 3). The answers were acceptable — even with the relatively high RMS residual results. We used approximately correct values as initial assumptions, and starting with this lack of bias is probably the way to obtain reasonable results when the minimum obtainable RMS residual is not low enough to guarantee them. The numerical inconsistencies responsible for this inability to obtain such a minimum would be less dominant for a greater density of grid points.

The sample inducer examples that we studied in runs E-6 through 9 had no parallel sets of previously known answers by which the results could be judged directly — as was possible with all the other cases. However, results for similar geometries using accepted simple radial equilibrium methods, (as was done in reference 6, and by us in Section III,) give an indication of what to expect. The 5 x 5 grid point cross-section with the many additional points obtained by reason of the greater channel length (up to 22 cross-sections) typical of inducers, yield the kind of answers that would be expected from our knowledge of the irrotational flow results for the paddle-wheel channel, (runs E-3,4,5). These inducer problems yield minimum RMS residuals of order similar to that of runs E-3,4,5. (cf. Figures II-9, 13, 19). Although the grid-point cross-section is 5 x 5, (vs. 9 x 7 for runs E-3,4,5) the channel inclination angle is quite shallow and yields the higher grid-point density that probably accounts for the differences between the inducers and the paddle-wheel channel.

However, a greater grid point density is needed to avoid the further numerical errors that were probably introduced by using the convenient arrangement with highly oblique intersections of the coordinate surfaces, (Figure A-2). This results from the fact that inducer channels are inclined at such a low angle β to the tangential direction.

The foregoing conclusions about the take-up effect apply to the differences between the 12° inducer results for free vs. forced pressures, (runs E-7 vs. E-8). The latter problem had fewer unknowns and thereby accounts for the higher RMS residual, (Figure II-19). Here again, these residuals were high enough in both cases to allow wrong answers, but the forced-pressure case seems to have insured reasonably accurate answers. In effect, biasing the pressures toward results that are consistent with the velocities reduces the grid-point density that is required; however, it restricts the problem to the lossless case — which is what we solved in all our examples with the method.

Finally, we could have obtained more accurate answers in the inducer examples if we had adjusted the initially estimated upstream and downstream extensions of the blades to unloaded positions as the solutions proceeded. The errors that we introduced by not doing this are probably small compared to those that are caused by the coarse-grid effects. However, the two-phase flow results of run E-9 are influenced by the fact that the slight loading that did occur on the upstream stagnation stream surfaces prevented vapor from forming in the locations where its effects are known to be most pronounced. Here again we have demonstrated that two-phase flow calculations introduce no significant changes in computing time and complexity.

2. Recommendations for Future Work

Since the numerical accuracy of this exact method appears to have a direct relationship with the density of grid points, one must provide the attendant necessary computer storage space and running time to reduce the residuals sufficiently, (see Appendix C). This is characteristic of any valid finite difference technique.

A review of the data that we obtained in checking the method indicates that in its present form the program (Appendix C) would probably give satisfactory results if one would apply it to any typical inducer channel as follows:

a) Use a grid of 10 x 10 x 50 points, which compares to 5 x 5 x 22 that we used.

b) Extend the stagnation stream surface boundaries about one channel width upstream and downstream as we did it runs E-7, 8, 9.

c) Adjust the locations of these surfaces after each set of ten relaxation cycles to maintain them in an unloaded condition; i. e. , there should be no pressure differences across them at the same radial and axial locations.

d) Change the subroutine ADJ (Appendix C) to force the pressures to satisfy equation II. 42 as we did in run E-8. This eliminates the treatment of losses in detail; however, other expressions similar to equation II. 42 can be devised to distribute losses arbitrarily and to handle two-phase flow in combination with the barotropic relation (equation I. 7) — subject to the inlet conditions of uniform pressure and zero whirl.

As here proposed, the problem may yield a satisfactory solution in less than twenty-five relaxation cycles at a cost of about one half hour of computing time per cycle, (see Univac 1107 data in Appendix C). Proposal (d) on "forcing" the pressures may not be necessary if more computing time is allowed. It is simply a way of keeping the problem within present limits of computer storage and calculation times, as the general case would require even more grid points than 10 x 10 x 50 for an accurate solution.

Further work on the method itself could yield the reductions in calculation time that would allow the use of finer grids with the general problem (pressures not forced) on existing computers. A method for automatically adjusting the stagnation stream surfaces would save the time required to do it by hand in (c) above. As concerns the computational algorithm itself, lower RMS residual values could be attained by treating the wall boundary conditions (equation II. 9) as additional residuals and by independently adjusting all velocity components at boundary points, (see Appendix A).

More advanced residual reduction techniques could be introduced to accelerate the convergence rate, which might be partly accomplished with the existing program by a judicious selection of weights to be assigned to the various residuals at each grid point. As in the case of all developments and modifications in this method, such improvements would require the closest cooperation between the fields of numerical mathematics and fluid dynamics.

SECTION III

APPROXIMATE THREE-DIMENSIONAL SOLUTION

A. METHOD OF SOLUTION

This section gives the assumptions and method for obtaining a rapid, approximate
solution to the system of equations and boundary conditions presented in Section I.
The resulting program (Appendix D) can obtain answers in about a minute on existing
computers and may therefore be used for purposes of assisting in design evaluations.
However, such answers cannot describe the detailed three- dimensional flow patterns
that include, e. g., blade loading at the leading and trailing edges and relative cork-
screw motion within the passages. Any basic study of the inducer flow field must
be made by the exact method of the preceeding section.

The philosophy for this approximate approach is primarily that of reference 1 in that
several assumed two-dimensional solutions of the blade-to-blade field are coupled
with a complementary two-dimensional meridional solution. As reasonable approxi-
mations for inducers, we have neglected the effects of streamline curvature in the
meridional plane and of blade forces normal to the streamlines in that plane. Also
presented is the form of the results which can be correlated with other theoretical or
experimental data.

1. Restrictions of the Analysis

We imposed the following restrictions on the fluid motion to obtain an approximate
solution:

a) The fluid flows through the inducer (figure III. 1) in annuli; i. e., in the
   spaces between stream surfaces of revolution formed by rotating about
   the axis of rotation the meridional projections of the streamlines of such
   a flow. (Unless otherwise noted, the term streamlines will hereafter refer
   to these projections.)

b) The stream surfaces have initially fixed locations at the leading edge of
   the inducer blade (figure III. 1, view b). The upstream set of boundary
   conditions is applied at that leading edge, thus precluding backflow.

c) Average relative velocity and pressure conditions exist at mid-passage
   from blade to blade, (see figure II. 2). These averages are results of the
   meridional solution, and they are the quantities employed (with additional
   assumptions) to determine the blade-to-blade solutions. Where two-phase
   flow exists, we allow the meridional and blade-to-blade solutions to be
   dependent on one another.

d) The direction of the average relative velocity in a given annulus differs
   from that of the blade meanline in the blade-to-blade plane (figure III. 2)

b) View of Meridional Plane
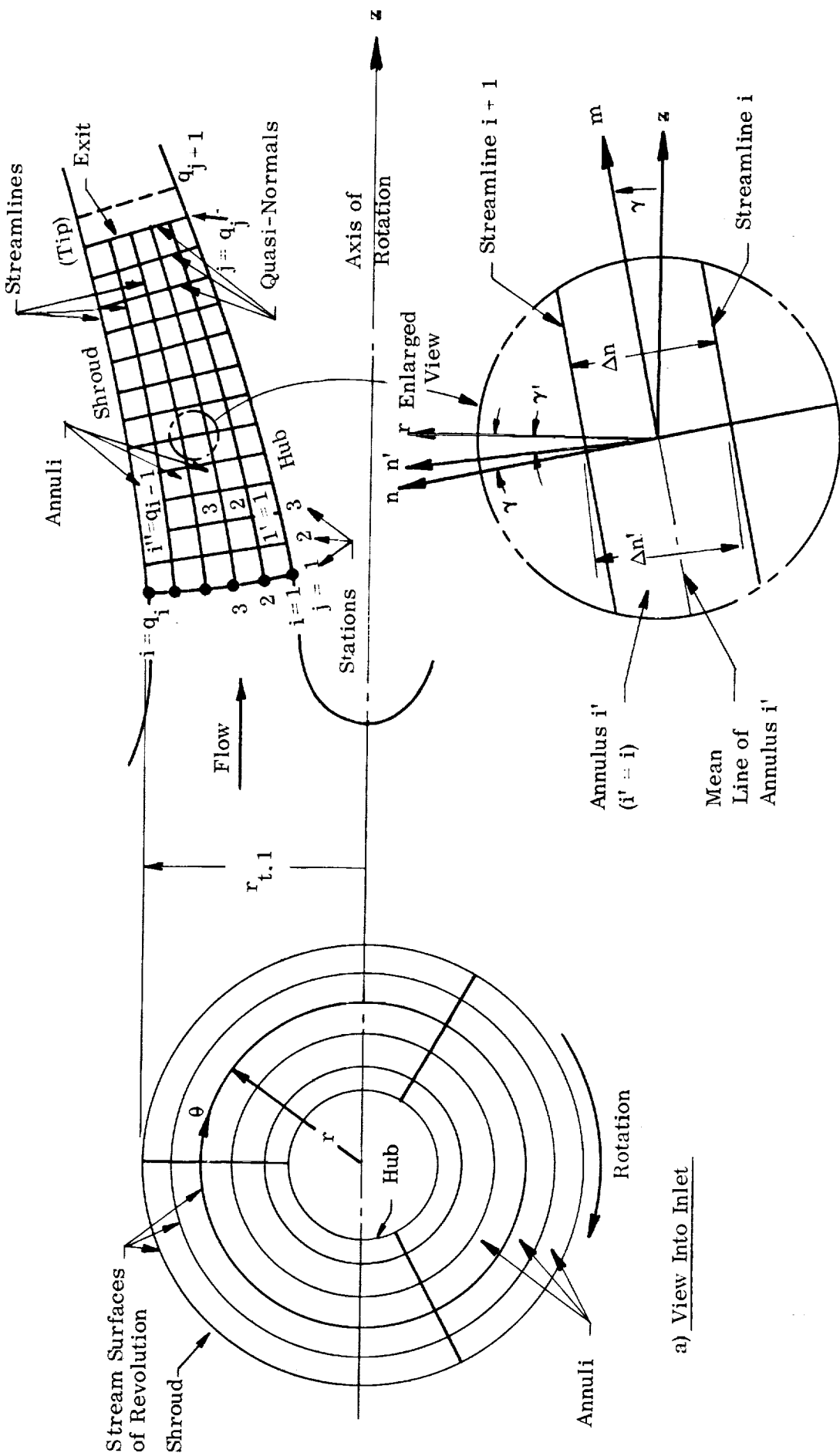
FIGURE III.1. TYPICAL FLOW FIELD FOR APPROXIMATE METHOD OF SOLUTION

a) View Into Inlet

a) Developed View of Surface of Revolution Generated by Mean Line of Annulus (See Fig. III.1)

Rotation

$\theta_{p,j'}$

$W_{j'}$

β_{qj}

W_{qj}

δ_{ex}

δ^*_{ex}

$\beta_{b,qj}$

$\overline{W}_{j'}$

$\overline{\theta}_{j'}$

m

Pressure Side of Channel: "Blade Pressure Surface"

* Boundary Layer Displacement Thickness

δ^*_{ex}

δ* Boundary Layer Displacement Thickness

$\theta_{s,j}$

θ

Suction Side of Channel: "Blade Suction Surface"

Streamline-Balancing (Main) Stations j, j-1

Blade-to-Blade Analysis Station j'

1   2   3   j-1   j q_j (Exit)

j'
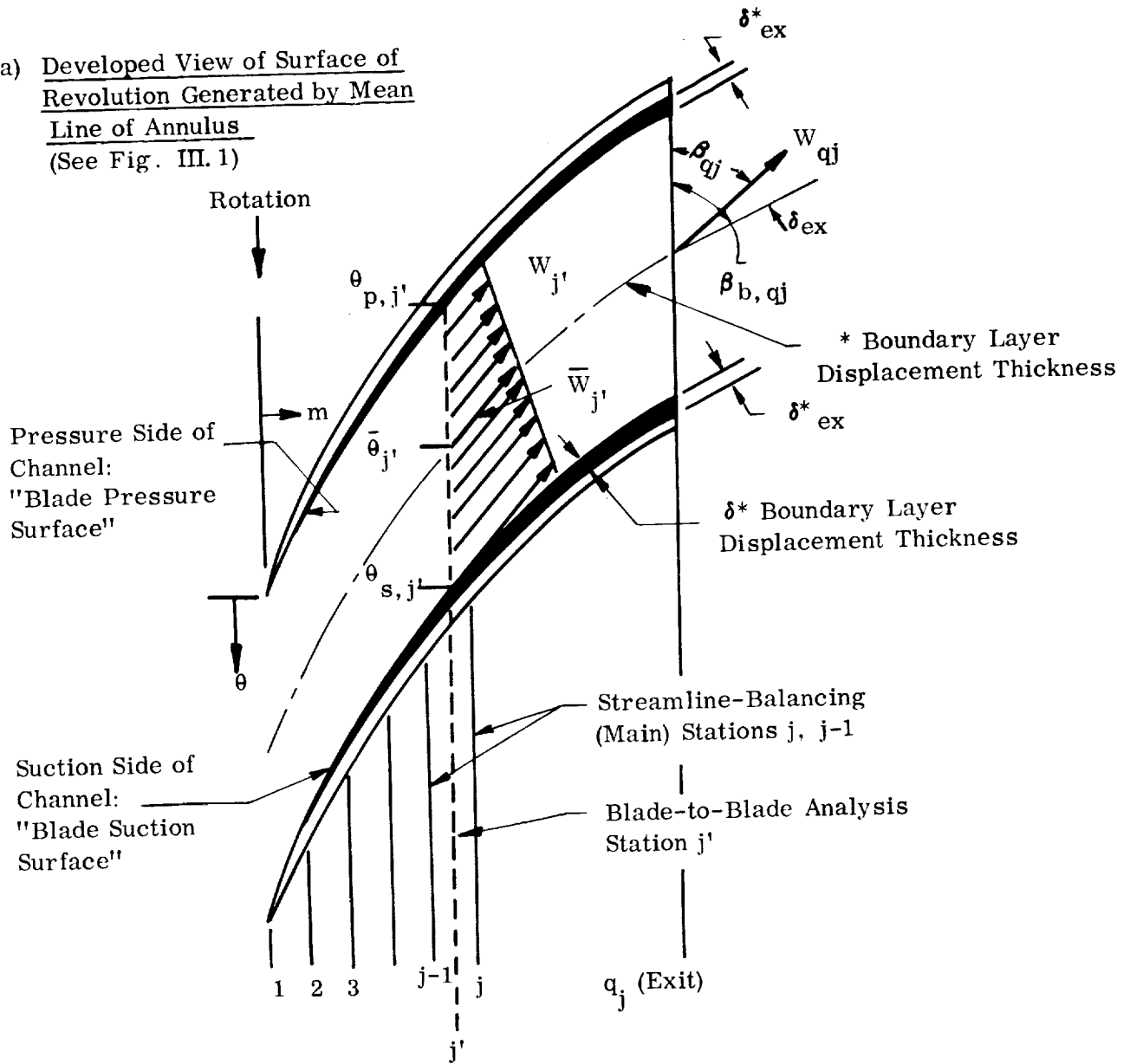
b) Velocity Diagram at Station j'

$V_{j'}$

$V'_{\theta,j'}$

$V_{m,j'}$

$\Omega r_{j'}$

$\beta_{j'}$

$\overline{W}_{j'}$
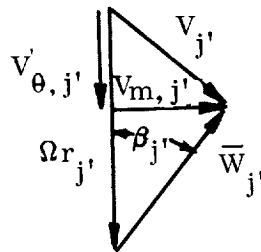
FIGURE III.2. BLADE-TO-BLADE FLOW ANALYSIS, SHOWING RELATIVE VELOCITY FIELD IN AN ANNULUS. Note that this analysis is carried out at an intermediate station; j', in order to find the loads caused by the changes of average flow quantities from one main station to the next.

by a predetermined deviation angle. In order to close the relative velocity diagrams at exit, this angle is assumed to vary approximately with the sixth power of length from the zero inlet value to the imposed exit value on that annulus. The component of direction in the meridional plane is that of the mean line between the two bounding streamlines (figure III.1).

The task is to find the equilibrium locations of the streamlines along each of several fixed straight-line meridional quasi-normals in turn at successive stations from inlet to outlet. At station 1, the blade leading edge, no such balance is required, as the locations there are fixed by restriction (b).

Although the relative corkscrew motion that can occur in a real flow is precluded by restriction (a), Stanitz showed (reference 12) that this superimposed motion has little effect on the velocities and pressures of an essentially single-phase lossless flow in the interior of the machine. Furthermore, we found that the total amount of this relative rotation experienced by the internal fluid seldom exceeds one-half turn because of the low work level of inducers. Finally, at low NPSH, the inlet region of an inducer commonly unloads due to two-phase effects, which would then make restriction (a) more acceptable there.

For the low blade-to-blade loadings of inducers, restrictions (c) and (d) should be reasonable. The deviation angle distribution of (d) amounts to negligible deviation except in the latter third of the blading, if imposed. In this way, the blade exit unloading phenomenon can be approximately simulated.

This reasoning simply means that our approximate solution ought to give a fair indication of inducer performance. However the three-dimensional (exact) method employs none of these restrictions; and, when applied with sufficient accuracy, it is the ultimate standard for a final design. Furthermore, basic observations of loss distributions and their effects can be understood best in the light of an exact solution — even one of a lossless flow.

2. Scalar Equations and Boundary Conditions

The foregoing restrictions lead to a natural set of varying directions in which to apply the equations of motion, using the (r, θ, z) right circular cylindrical coordinate system (figures III.1, 2):

    a) The relative flow direction λ, which is that of the foregoing restriction (d).

    b) The direction of the straight-line meridional quasi-normal n'.

    c) The tangential or blade-to-blade direction θ.

It is in these directions that we now express the three component equations of the vector momentum equation (I.2 or I.4). Since λ is the relative streamline direction, we use the streamline momentum equation (I.12) of Section I.A.2:

$$\frac{g_o \, dp}{\rho} = d\left(\frac{\Omega^2 r^2}{2}\right) - d\left(\frac{W^2}{2}\right) - dL \qquad \text{(III. 1)}$$

In the n' direction, we have the following simple normal equilibrium equation:

$$\frac{g_o}{\rho} \frac{dp}{dn'} = \frac{V_\theta^2 \cos \gamma'}{r} \qquad \text{(III. 2)}$$

and in the θ direction, we use the moment of momentum equation in terms of the average velocities and blade surface pressures, (reference 3, Appendix; and reference 15, p. 287):

$$\frac{g_o}{\rho} \frac{p_p - p_s}{\theta_s - \theta_p} = V_m \frac{d(r V_\theta)}{dm} \qquad \text{(III. 3)}$$

Note that equation III. 3 is an integrated form of the scalar momentum equation in the θ direction (equation II. 2), which is

$$\frac{\partial p}{\partial \theta} = \frac{\rho}{g_o} V_m \frac{d}{dm} (r V_\theta) \qquad \text{(III. 3a)}$$

We require continuity throughout each annulus as follows:

$$dw = d\left[\rho r \, \Delta n \, (\theta_s - \theta_p) \, \eta_b \, V_m\right] = 0 \qquad \text{(III. 4)}$$

Together with boundary conditions and equations (I. 7) and (I. 13) for two-phase flow and loss effects when required, equations (III. 1, 2, 3, 4) constitute the complete set of relations used in this method.

We note that equation (III. 2) is obtained from the complete normal equilibrium equation for this annulus-type flow problem (reference 4, p. 29):

$$\frac{g_o}{\rho} \frac{\partial p}{\partial n} = \underbrace{\frac{V_\theta^2 \cos \gamma}{r}}_{\substack{\text{Pressure} \\ \text{Gradient}}} \underbrace{\frac{V_\theta^2 \cos \gamma}{r}}_{\substack{\text{Centrifugal} \\ \text{Action}}} - \underbrace{\frac{V_m^2}{r_c}}_{\substack{\text{Streamline} \\ \text{Curvature}}} + \underbrace{\frac{B^*}{r} V_m \frac{d (r V_\theta)}{dm}}_{\substack{\text{Blade Force}}} \qquad \text{(III. 5)}$$

where

$$B^* = r \frac{\partial \theta}{\partial z} \sin \gamma - r \frac{\partial \theta}{\partial r} \cos \gamma \qquad \text{(III. 6)}$$

Furthermore, (see figure III.1)

$$\frac{dp}{dn'} = \frac{\partial p}{\partial n}\frac{dn}{dn'} + \frac{\partial p}{\partial m}\frac{dm}{dn'} \qquad\qquad\qquad (III.7)$$

If the quasi-normals are approximately perpendicular to the streamlines, we see that the last term of equation (III.7) may be neglected and that $\frac{dp}{dn'} \approx \frac{dp}{dn}$. Omitting the effects of meridional streamline curvature and of the blade forces only in the quasi-normal direction; i.e., the last two terms of equation (III.5), we then obtain the simple normal equilibrium equation (III.2). Provided we take the care to specify the (fixed) locations of the quasi-normals properly, the fairly axial, long, straight meridional fields and nearly radial-element-blades of inducers should make this omission of terms less serious.

In accordance with the restriction in Section II.A.1, we summarize the boundary conditions on this problem as follows:

a) The wall boundaries (Section I.B.1) extend only from the blade leading to trailing edge. Beside the blades, hub and shroud, these also include the stream surfaces of revolution (streamlines), whose locations are fixed at the upstream boundary.

b) The upstream throughflow boundary (Section I.B.2) is at the blade leading edge. There we specify for each annulus the respective inlet values of p, V_m and V_θ. The direction of V_m is determined by the given slope of the blade leading edge (not necessarily a straight line in the meridional plane); therefore, V_r and V_z are implicitly specified. No tangential variation of these quantities is assumed.

c) At the downstream throughflow boundary (the blade trailing edge), we specify the respective predetermined values of the tangential average exit deviation angle δ_{ex} for each annulus. The exact locations of these annuli result from the solution; however their positions can be estimated closely enough to find the necessary values of δ_{ex} if its distribution from hub to shroud is not uniform. The program as presently constructed requires that a quasi-normal coincide with the blade trailing edge, and therefore, that this edge be a straight line in the meridional plane.

3. Meridional Streamline Balancing Procedure

Determining the equilibrium positions of the meridional stream surfaces of revolution chosen at inlet is the object of this approximate method. We identify the coordinates of each streamline by the index (subscript) i where

86

$$\underbrace{1}_{\text{Hub}} \leq i \leq \underbrace{q_i}_{\text{Shroud}}$$

Similarly, each quasi-normal is identified by the index (subscript) j (the <u>Station</u> number) where

$$\underbrace{1}_{\substack{\text{Blade} \\ \text{Leading} \\ \text{Edge}}} \leq j \leq \underbrace{q_j}_{\substack{\text{Blade} \\ \text{Trailing} \\ \text{Edge}}}$$

All fluid variables (p, ρ, W, V) are associated with annuli, not the streamlines; i.e., they are assumed to exist on the mean line of annulus i' which lies midway between streamlines i and i + 1. Thus the total number of annuli is $q_i - 1$. The same identification applies to the average coordinate quantities $n'_{i',j}$, (with corresponding $r_{i',j}$, and $z_{i',j}$,) which locate the mean line of annulus i'. The computational procedure begins from the specified data by calculating the mass flow rates w_i, and relative velocities $W_{i',j}$, for each annulus i' at the blade leading edge station (j = 1). We then proceed as follows at station 2 (j = 2):

a) We estimate the streamline positions $n'_{i,j}$, , $r_{i,j}$ and $z_{i,j}$ on the quasi-normal j by assuming the same spacing proportions as at j - 1. Next we find the corresponding channel angle data $\theta_{s,i',j}$ and $\theta_{p,i',j}$ from a blade subroutine for the given blade shape and thickness, which includes boundary layer displacement thickness. From this and similar data at stations j - 1 and j + 1, we obtain the relative flow angle $\beta_{i',j}$ in the plane tangent to the mean stream surface of each annulus i', allowing for deviation, if any, (see figure III.2).

b) Applying the continuity equation (III. 4) in finite-difference form we obtain the average velocities $V_{m,i',j}$ as follows:

$$V_{m,i',j} = \frac{w_{i'}}{\left[\rho r \Delta n (\theta_s - \theta_p)\right]_{i',j}} \tag{III. 8}$$

With the angles β we now obtain also the velocities V_θ and W. If we are not restricted to an incompressible analysis, this and the following step are coupled to the blade-to-blade solution in the portions of the machine where vaporization occurs. In such a case, the value of $\rho_{i',j}$ is unknown and must be found from an iteration of equations III. 8 and III. 9 with steps (a) through (f) of the blade-to-blade solution for two-phase flow, (see Section III. A. 4).

c) Next we obtain the average pressures $p_{i',j}$ from the <u>streamline momentum</u> (equation (III.1)) expressed in finite-difference form:

$$p_{i',j} = \left\{ p_{j-1} + \frac{\rho_j + \rho_{j-1}}{2g_o} \left[\frac{\Omega^2}{2} \left(r_j^2 - r_{j-1}^2 \right) - \frac{1}{2} \left(W_j^2 - W_{j-1}^2 \right) - dL \right] \right\}_{i'} \qquad \text{(III. 9)}$$

where dL is similarly expressed by finite-difference forms of equations (I.13, 14, 15).

d) Now we form the streamline unbalances $U_{i,j}$ for all i from the <u>simple normal equilibrium equation</u> (III.2), (i = i):

$$U_{i,j} = \left| \frac{p_{i'} - p_{i'-1}}{n'_{i'} - n'_{i'-1}} - \frac{(\rho_{i'} + \rho_{i'-1})}{4g_o} \frac{\left(V_{\theta,i'}^2 + V_{\theta,i'-1}^2 \right)}{r_i / \cos \gamma'} \right|_j \qquad \text{(III. 10)}$$

where no U's are needed for the hub and shroud streamlines (i = 1 and q_i respectively). These indicate the extent of error in the original estimates of the streamline positions in step (a).

In the following steps, we adjust the streamline locations $n'_{i,j}$ at station j to satisfy the same accuracy criterion developed in Section II. A. 4. Here, we require (similar to relation (II.19) that the unbalance U be limited as follows:

$$U \leq \epsilon \, (\Omega^2 \, r_t) \frac{\rho_f}{g_o} \qquad \text{(III. 11)}$$

where ϵ is some small number.

The relation of this error to the overall results is less serious than the discussion of Section II. A. 4 would indicate. It affects the hub-to-shroud distributions, but not the accuracy of the inlet-to-outlet annulus results in themselves. Continuity is satisfied in each annulus, and the correct pressure rise from inlet to outlet of it will result if on the average each annulus is balanced with relation to the others. Any cumulative effect due to bias in the unbalances is small, and in the lossless case it is non-existent — the overall pressure rise error then depending on bias in the unbalances (due to $\epsilon \neq 0$) at the exit station only. Note that "unbalance" U is an error in the normal pressure gradient $\frac{dp}{dn'}$, (i. e., $\frac{dp}{dr}$ in typical inducers).

The <u>adjustment sequence</u> at station j follows:

e) If all the $U_{i,j}$ satisfy condition (III.11), we consider the problem solved from the inlet to this station j. In such a case, we proceed to the next

station (j + 1) and repeat the steps just outlined, beginning with step (a).
If, however, this required accuracy does not exist, we execute the following
steps starting with streamline i = 2 at station j:

f) We determine a new streamline position $(n' + \Delta n')_{i,j}$ by the second order
Taylor approximation, (see equation (II. 17)):

$$n' + \Delta n' = n' - \left(\frac{\partial U}{\partial n'} \Big/ \frac{\partial^2 U}{\partial n'^2} \right) \qquad \text{(III. 12)}$$

where the U derivatives are evaluated by moving the streamline by
amounts $\pm\, \delta n'$ and executing steps (b) through (d) for each such movement.
In the event that the U versus n' relation is not sufficiently second order
for the adjustment given by equation (III. 12) to cause a reduction in $U_{i,j}$,
we accept whichever result of the $\pm\, \delta n'$ calculations did cause a reduction,
if indeed one occurred. (This alternate method was necessary in the two-
phase flow cases. It does not force a wrong answer but merely insures
that the unbalance U will be reduced in cases where the usual method cannot
accomplish this.) If required to obtain U reduction, $\delta n'$ is reduced as in
the method of successive variations (Section II. A. 3) at the end of each
cycle.

g) We repeat step (f) for the next streamline, i = 3, and so on through $i = q_i - 1$,
which completes one (hub-to-shroud) iteration cycle. Then we return to
step (e).

In certain cases where a very small value of ϵ in equation III. 11 would
require may iteration cycles, the number of cycles can be limited and the
results accepted at the accuracy then achieved, (see Appendix D).

4. Blade-To-Blade Solution

Except for cases where pressures in the blade-to-blade solution are lower than the
vapor pressure p_{sat}, there is no influence of this solution on the meridional one of
the foregoing section. For two-phase solutions, we make a blade-to-blade check for
vaporization each time an average density $\rho_{i',j}$ is required by steps (b) and (c) of
that section. The blade-to-blade solution associated with a given station j is actually
carried out at j' which is halfway between j and j - 1, (see figure III. 2). The results
are the fluid relative velocities $W_{p,i',j'}$ and $W_{s,i',j'}$, pressures $p_{p,i',j'}$ and $p_{s,i',j'}$,
and densities $\rho_{p,i',j'}$, and $\rho_{s,i',j'}$ on the pressure and suction sides of the channel,
respectively.

The meridional field does of course determine the blade-to-blade solution, and the
key to this is the moment of momentum equation (III. 3). To use simply this equation
two assumptions are required; viz., a θ distribution of one of the variables and a
statement about the accumulated losses versus θ. For the first, a linear distribution
$p(\theta)$ (reference 2) or $W(\theta)$ (reference 1) is generally assumed. Both of these give

nearly the same results for the light loads in the incompressible case. However, in the two-phase case the linear pressure approach causes unrealistically high W's on the non-liquid suction side of the channel besides specifying an appreciable pressure variation over a region that is essentially vaporous (reference 8, p. 4-16). So we chose the linear velocity model, which best fits all cases. For the second assumption, the only convenient approach is to state that $\int_i dL$ along all relative streamlines in annulus i from inlet to station j' is uniform. Then the streamline momentum equation (I.12) holds on all streamlines from blade to blade (r = constant), and it may be employed together with the state equation (I.7) to relate the θ distributions of the variables p, W and ρ.

Having chosen the linear velocity model, we next obtain the relationship between $W(\theta)$ and the velocities of the meridional solution which are averages. As in reference 1, we assume

$$\left(\frac{W_s + W_p}{2} \right)_{i',j'} = \overline{W}_{i',j'} \tag{III. 13}$$

The average velocity

$$\overline{W}_{i',j'} = \left(\frac{W_j + W_{j-1}}{2} \right)_{i'} \tag{III. 14}$$

as does the pressure, $\overline{p}_{i',j'}$, lies at mid-passage, where $\overline{p}$ is defined similarly. In accordance with the foregoing assumption about the losses, we now combine the moment of momentum equation (III. 3) with the following form of equation (I. 2) for use in the θ direction (r = constant):

$$\frac{g_0\, dp}{\rho} = - W\, d\, W \tag{III. 15}$$

Assuming

$$- \frac{p_p - p_s}{\theta_s - \theta_p} = \frac{dp}{d\theta} \tag{III. 17}$$

we obtain

$$\left(\frac{dW}{d\theta} \right)_{i',j'} = \left[\left(\frac{\overline{V}_m}{\overline{W}} \right)_{j'} \frac{(r_j V_{\theta,j} - r_{j-1} V_{\theta,j-1})}{m_j - m_{j-1}} \right]_{i'} \tag{III.18}$$

90

where, by assumption, $\left(\dfrac{dW}{d\theta}\right)_{i',j'}$ = constant with θ, and with equation (III. 13) we now have the blade-to-blade velocity distribution. Applying equation (III. 15) and remembering that the mid-passage value is $\bar{p}_{i',j'}$, we immediately obtain the pressure distribution if ρ is constant. This completes the blade-to-blade solution for the incompressible case.

For two-phase flow, we proceed as in the incompressible case for all portions of the blade-to-blade region in which $p \geq p_{sat}$, (see figure (III. 3). In the portion where $p < p_{sat}$, we determine the density distribution from a combination of the two-phase state relation (I. 7) and equation (III. 15); and the pressure on the blade surfaces is similarly calculated. There are various forms of these combinations, depending upon how much of the passage is occupied by liquid or two-phase fluid, (see figure III. 3). This completes the blade-to-blade solution for the two-phase case.

In the course of the meridional solution (Section III. A. 3) steps (b) and (c) required an average $\rho_{i',j}$ that can be obtained only from an iterative portion of the blade-to-blade solution at station j' when two-phase flow exists at j'. Once the final, correct $\rho_{i',j}$ is supplied by this iteration for the balanced streamline positions at station j, the final blade-to-blade solution is made as outlined in the preceeding paragraphs for both the incompressible and two-phase flow cases and for all annuli at station j'. The iterative steps for obtaining $\rho_{i',j}$ are as follows:

a) Assume $\rho_{i',j} = \rho_f$

b) Execute steps (b) and (c) of the meridional solution.

c) Obtain the blade-to-blade density distribution from the applicable combination of equations (I. 7) and (III. 15).

d) Calculate the blade-to-blade average density:

$$\bar{\rho}_{i',j'} = \left(\dfrac{\displaystyle\int_{\theta_p}^{\theta_s} \rho\, d\theta}{\theta_s - \theta_p}\right)_{i',j'} \tag{III. 19}$$

e) Check continuity at station j' as follows: *

$$\bar{\rho}_{i',j'} \overset{?}{=} \dfrac{\rho_{i',j} + \rho_{i',j-1}}{2} \tag{III. 20}$$

---

* A better form of continuity check than that of equations (III. 19 and 20) is simply that

$$\left(\int_{\theta_p}^{\theta_s} \rho\, W\, d\theta\right)_{i',j'} \overset{?}{=} \dfrac{\rho_{i',j} + \rho_{i',j-1}}{2}\; \bar{W}_{i',j'}\, (\theta_s - \theta_p) \tag{III 21}$$

This would avoid the slight continuity errors introduced by the concept of an average density $\bar{\rho}$ at station j' in equation (III. 19).
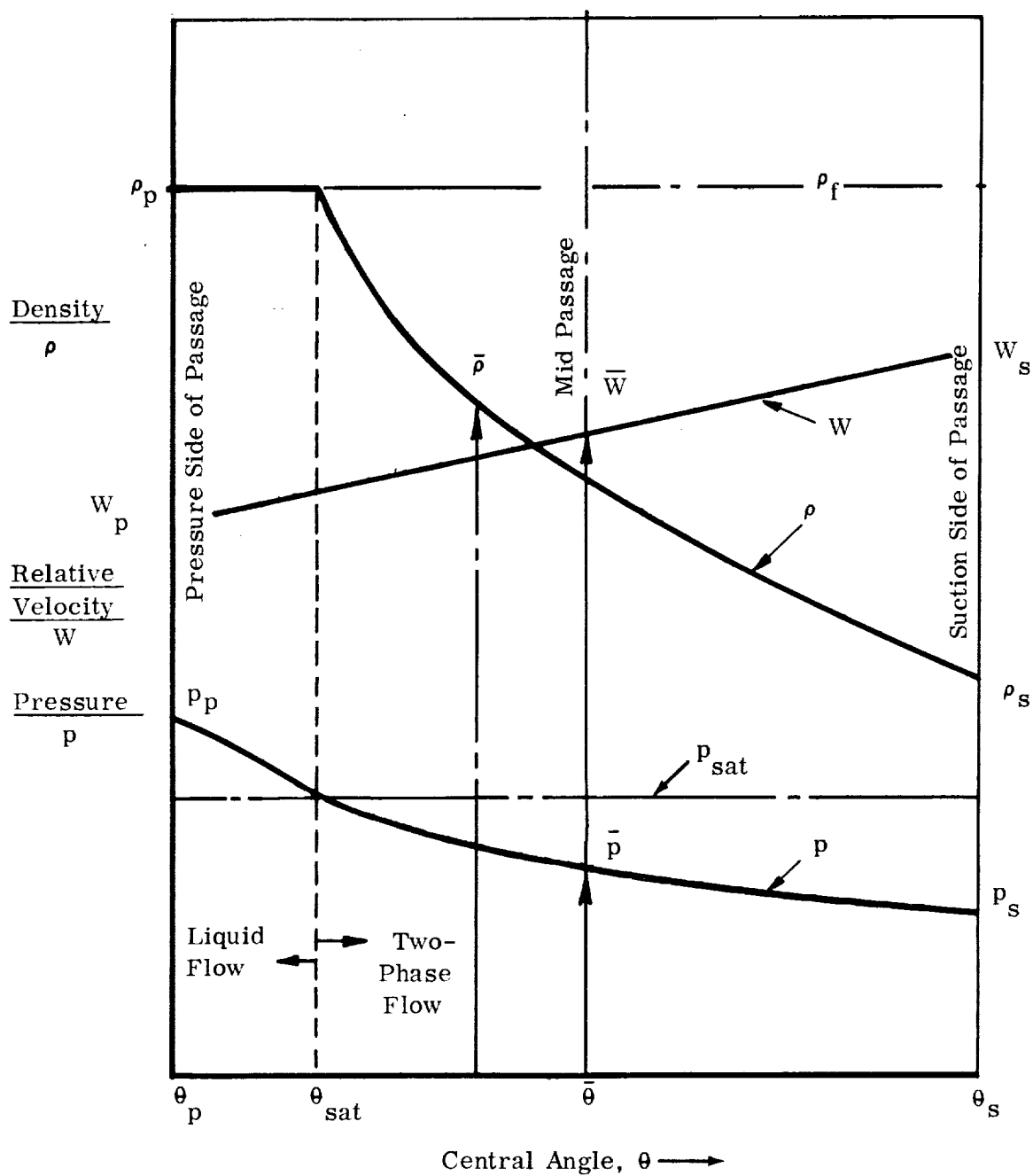
FIGURE III. 3. BLADE-TO-BLADE DISTRIBUTIONS OF FLUID FLOW
VARIABLES. At station j' (between stations j and j-1 see Fig. III. 2).

f)   If the difference between these averages is greater than .001 of the right hand side, we reduce $\rho_{i',j}$ by a small amount and repeat steps (b) through (f). If the difference is less than .001, we accept the current value of $\rho_{i',j}$ for use with the meridional solution, (steps (b) and (c)).

Figure III. 4 shows the kind of variation that results for each side of equation (III. 20) as the assumed average density $\rho_{i',j}$ is changed from ρ_f to successively lower values. The iteration procedure contains safeguards to avoid the solution bb (figure III. 4) for negative blade loading and to handle properly the choked annulus case for which no solution exists. First, if solution aa exists, it will be reached first as the blades unload with decreasing values of the assumed $\rho_{i',j}$. We found that if no solution aa exists, there will be no bb solution either, since a negative blade loading causes a reduction of average pressure from station j - 1 to j with corresponding increased vaporization. So, if no solution exists; i.e., if the annulus is choked for current positions of the two bounding streamlines, this fact is noted by the computer, and we use the value of $\rho_{i',j}$ for essentially zero blade loading (specifically, the value obtained at the point in the iteration for which $V_\theta = 0$) in steps (b) and (c) of Section III. A. 3. If the streamline adjustment sequence ultimately yields no balanced positions of the streamlines at station j (steps (e), (f) and (g) of Section III. A. 3) for which all the annuli are unchoked at j'; an appropriate message is printed at the end of a maximum allowable number of balancing cycles, and the calculations are discontinued.

5.   Form of the Results

The procedures for obtaining the meridional and blade-to-blade solutions yield sets of hub-to-shroud results at each station j and at j'; i.e., respectively along and between the quasi-normals of the meridional solution from inlet to outlet. At j we give the resulting set of streamline coordinate locations r and z and the final unbalances U. The set of average annulus values W, V_m, V_r, V_θ, V_z, p and ρ are each also given for j. At j', we give the blade-to-blade results for each annulus at the blade surfaces and at mid-passage; viz., W_p, W_s, $\overline{W}$, p_p, p_s, $\bar{p}$, ρ_p, ρ_s; and $\bar{\rho}$, which does not lie at mid-passage, (see figure III. 3) and equation (III. 19)).

At the blade trailing edge (j = q_i) we also calculate blade element performance data and finally the overall performance of the machine. The blade element data applies to fluid in each annulus and is calculated as follows:

a)   Total head loss coefficient:

$$\overline{\omega}_i = \left[\frac{\dfrac{U_2 V_{\theta,2}}{g_0} - \dfrac{U_1 V_{\theta,1}}{g_0} - \left(\dfrac{p_2}{\rho_2} - \dfrac{p_1}{\rho_1} + \dfrac{V_2^{\,2}}{2 g_0} - \dfrac{V_1^{\,2}}{2 g_0} \right)}{W_{t,1}^{\,2} / (2 g_0)} \right] \tag{III. 22}$$

93

FIGURE III.4. ITERATIVE METHOD OF OBTAINING BLADE-TO-BLADE
SOLUTION FOR TWO-PHASE FLOW. The velocity, pressure, and
density distributions from blade to blade resulting from an initial
assumption of $\rho_{i',j}$ lead to the average $\rho_{i',j'}$. Subsequent values for
$\rho_{i',j}$ are attempted until the process converges.

94
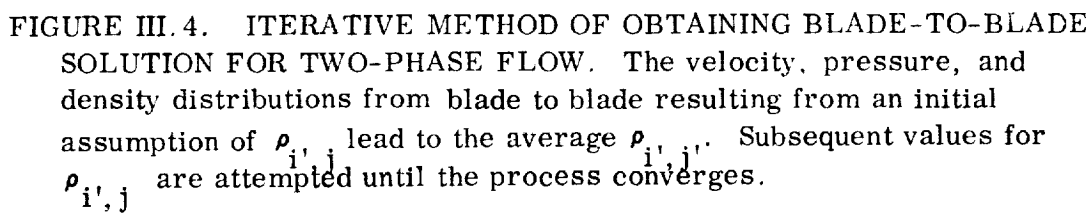
b) Annulus efficiency:

$$\eta_{i'} = \left(\frac{\dfrac{p_2}{\rho_2} - \dfrac{p_1}{\rho_1} + \dfrac{V_2{}^2}{2g_0} - \dfrac{V_1{}^2}{2g_0}}{\dfrac{U_2 V_{\theta,2}}{g_0} - \dfrac{U_1 V_{\theta,1}}{g_0}} \right)_{i'}$$

(III. 23)

The overall performance is calculated from the proper averages of the annulus (i') data at inlet and outlet:

a) Mass flow rate:

$$w_T = \sum_{i'=1}^{q_i - 1} w_i$$

(III. 24)

where the w_i are given by equation III. 4 for use in the program calculations.

b) Mass-averaged total head rise

$$\Delta \overline{H} = \frac{\displaystyle\sum_{i'=1}^{q_i - 1} \left(\frac{p_2}{\rho_2} - \frac{p_1}{\rho_1} + \frac{V^2}{2g_0} - \frac{V_1{}^2}{2g_0} \right)_{i'} w_{i'}}{w_T}$$

(III. 25)

c) Mass-averaged pressure (calculated at inlet and at outlet):

$$\overline{p} = \frac{\displaystyle\sum_{i'=1}^{q_i - 1} p_{i'} w_{i'}}{w_T}$$

(III. 26)

d) Mass-averaged absolute velocity head calculated (at inlet and at outlet):

$$\frac{\overline{V^2}}{2g_0} = \frac{\displaystyle\sum_{i=1}^{q_i - 1} \left(\frac{V_m{}^2 + V_\theta{}^2}{2g_0} \right)_{i'}}{w_T}$$

(III. 27)

e) Torque:

$$T_q = \frac{1}{g_o} \sum_{i=1}^{q_i - 1} (r_2 V_{\theta,2} - r_1 V_{\theta,1})_{i'} \ w_{i'} \qquad \text{(III. 28)}$$

f) Shaft power input:

$$P_s = \Omega \, T_q \qquad \text{(III. 29)}$$

g) Overall efficiency:

$$\overline{\eta} = \frac{\displaystyle\sum_{i'=1}^{q_i - 1} \left(\frac{p_2}{\rho_2} - \frac{p_1}{\rho_1} + \frac{V_2^2}{2g_o} - \frac{V_1^2}{2g_o} \right)_{i'} \ w_{i'}}{P_s} \qquad \text{(III. 30)}$$

Observe that the overall efficiency $\overline{\eta}$ is equivalent to an energy average of the elemental efficiencies $\eta_{i'}$.

B. EXAMPLES AND RESULTS

The approximate method was used to solve a series of problems on the same variable-lead inducers to which we applied the exact method in Section III. B. 3. This section presents the results for the 6.2° and 12° inducers - which are described in figures II.12 and II.18, respectively - for (1) incompressible, lossless flow, and (2) other runs with loss and two-phase flow. In table III. 1 we list the representative runs reported in this section; although we made some additional runs to obtain more data for the conclusions of Section IV. As in Section II. B we performed all calculations nondimensionally, according to the system presented at the end of the list of symbols.

1. Incompressible Results and Correlations for Lossless Flow

We now compare the results of the approximate method of solution with those of the exact method, (Runs numbered A and E, respectively), using the following data from table III.1:

a) 6.2° Inducer:

   Runs A-1 and E-6
   Figures III, 5, 7, 8

TABLE III.1

REPRESENTATIVE APPROXIMATE THREE-DIMENSIONAL SOLUTIONS OF FLOW IN TWO SAMPLE INDUCERS

Flow Type	Run No.	Field Streamlines x Stations	Error[1] U_{max}	Vaporization Parameter[2] $\Theta = \frac{B}{g_o} U_{t,1}^2$	Reynolds No. $R_m = \frac{\Omega r_{t,1}}{\nu}$	Suction Specific Speed S (III.37)	Cav. Coeff. Ψ_{sp} (III.35)	Cav. No. k (III.38)	Press.-Rise Coefficient Ψ_p (II.21)	Total Head Coeff. Ψ (III.33)	Power Coeff. P_s (See List of Symbols)	Efficiency $\bar{\eta}$ (III.30)
1. SAMPLE INDUCER HAVING 6.2° INLET TIP BLADE ANGLE: $\varnothing_1 = .0830$; i = 1.45°												
Incompressible with No Losses	E-6	(Exact Method)[2]			∞				.1338	.1622	.0382	1
	A-1	8x16	.010		∞				.1235	.1480	.0343	1.0000
	A-2	4x6	.010		∞				.1237	.1483	.0344	1.0000
Incompressible with Losses	A-3	8x16	.010		5.0x10⁷				.0815	.1067	.0355	.6962
	A-4	4x16	.010		5.0x10⁷				.0823	.1074	.0355	.7019
	A-5	4x16	.001		2.5x10⁷				.0801	.1053	.0355	.6873
Two-Phase with Losses	A-6	4x16	.001	10	2.5x10⁷	∞	-.0034	-.0068	.0962	.1246	.0387	.7223
	A-7	4x16	.01	10	2.5x10⁷	92,900	0	0	.0971	.1043	.0355	.6808
	A-8	4x16	.040/.005	40	5.0x10⁷	58,300	.0030	.0060	.0809	.1061	.0355	.6925
	A-9	4x16	.034/.001	1000	2.5x10⁷	40,500	.0070	.0140	.0783	.1035	.0356	.6744
2. SAMPLE INDUCER HAVING 12° INLET TIP BLADE ANGLE: $\varnothing_1 = .1763$; i = 2.00°												
Incompressible with No Losses	E-7	(Free p) (Exact Method)[3]			∞				.1646	.2375	.1140	1
	E-8	(Forced p) (Exact Method)			∞				.1590	.2330	.1144	1
	A-10	8x16	.010		∞				.1522	.2266	.1116	1.0000
	A-11	4x16	.010		∞				.1523	.2267	.1116	1.0000
Incompressible with Losses	A-12	8x16	.010		5.0x10⁷				.1423	.2168	.1123	.9505
	A-13	4x16	.010		5.0x10⁷				.1425	.2170	.1123	.9515
	A-14	4x16	.001		2.5x10⁷				.1422	.2167	.1123	.9497
Two-Phase with Losses	A-15	4x16	.020/.001	10	2.5x10⁷	∞	-.0145	-.0283	.1898	.2738	.1261	.9343
	A-16	4x16	.019/.010	10	2.5x10⁷	43,300	0	0	.1404	.2148	.1124	.9413
	A-17	4x16	.001	40	5.0x10⁷	37,700	.0035	.0068	.1401	.2145	.1124	.9398
	A-18	4x16	.002/.001	1000	2.5x10⁷	30,200	.0100	.0194	.1400	.2145	.1125	.9390

1 See Equation (III.10). Where two numbers for the maximum streamline unbalance error U_{max} are listed, the smaller one was achieved everywhere except in the two-phase flow regions. See figures III.23 and III.24.

2 RMS residual = .015 (See Figure II.13).

3 RMS residual = .020 and .046 for runs E-7 and E-8 respectively (See Figure II.19).

4 Zero - NPSH runs. Two-phase flow in inlet lines. Therefore $\varnothing_{1,f} \neq \varnothing_1$:

6.2° inducer: $\varnothing_{1,f} = .0812$; $i_f = 1.55°$; $\varnothing_{1,f}/\varnothing_1 = .9671$

12° inducer: $\varnothing_{1,f} = .1540$; $i_f = 3.25°$; $\varnothing_{1,f}/\varnothing_1 = .8734$

b) 12° Inducer:

Runs A-10, E-7 and E-8
Figures III. 6, 9, 10, 11, 12, 13

On each inducer, we used an 8 x 16 field; i. e. , one with eight stream-
lines including hub and shroud, and sixteen stations including the blade
leading and trailing edges. Because of the special geometry we used
equally-spaced radial lines for the quasi-normals at each station. The
eight streamlines were equally spaced at station 1.   Refer to figures II. 12
and II. 18 for geometrical details, including the axial locations of the
stations.

The overall performance data also appears in table III. 1 in terms of the static pressure
rise coefficient Ψ_p, total head rise coefficient Ψ, power coefficient $\hat{P}_s$ and overall
efficiency $\bar{\eta}$. These are the non-dimensional values of the corresponding quantities
presented in Section III. A. 5. The corresponding data for the exact methods of solution
of these two inducers is also given (from figures II. 15 and II. 21). We obtained a fairly
close correlation of these results and the approximate ones (Run A-10) for the 12°
inducer. Lack of such a correlation for the 6. 2° inducer is probably the result of a
7% error in the fixed outlet throughflow velocity distribution that we made in applying
the exact method, (see description of Run E-6 in Section II. B. 3).

This difference is more clearly shown in the radial distributions of velocity and
pressure at the blade trailing edge in figure III. 5, especially for the V_z component,
which distribution was fixed in Run E-6.   The unusual V_θ distribution of run E-6
is probably due to the grid effect. Figure III. 6 for the 12° inducers shows close cor-
relations between Runs A-10 and E-8, the latter being the forced-pressure case of the
exact method, (see the Run E-8 discussion in Section II. B. 3). Because the quasi-
normal direction n' is radial, equation III. 2 becomes that for simple radial equilibrium;
so, we expect this governing equation of Run A-10 to give the type of V_θ and V_z distri-
butions shown for this radial-element-bladed inducer. Figure 2 and equation 13 of
reference 6 show that the V_θ distribution for lossless flow is essentially free vortex.

As we compare these results, we must keep in mind the high numerical accuracy that
we were able to achieve with the approximate method as compared to that of the exact
method of analysis, (U_{max} vs. RMS residual). The overall numerical error for a
given RMS residual (an average) can be higher than the product of it times the length
of the inducer, (see Section II. A. 4 and equation II. 20); but this error for a given
U_{max} is of order less than U_{max} times the radial length of passage at inducer exit.
(Refer to the discussion in step (d) of Section III. A. 3, and note the negligible differences
between the results of the runs in Table III. 1 for U_{max} = . 01 and . 001.) Note
however that high numerical accuracy of an approximate method does not guarantee
exact results. On the other hand, evidence of tests is that the simple normal (or
radial) equilibrium assumption used in the approximate methods is a reasonable basis
for judging results. Finally we must remember that the numerical inaccuracies of the
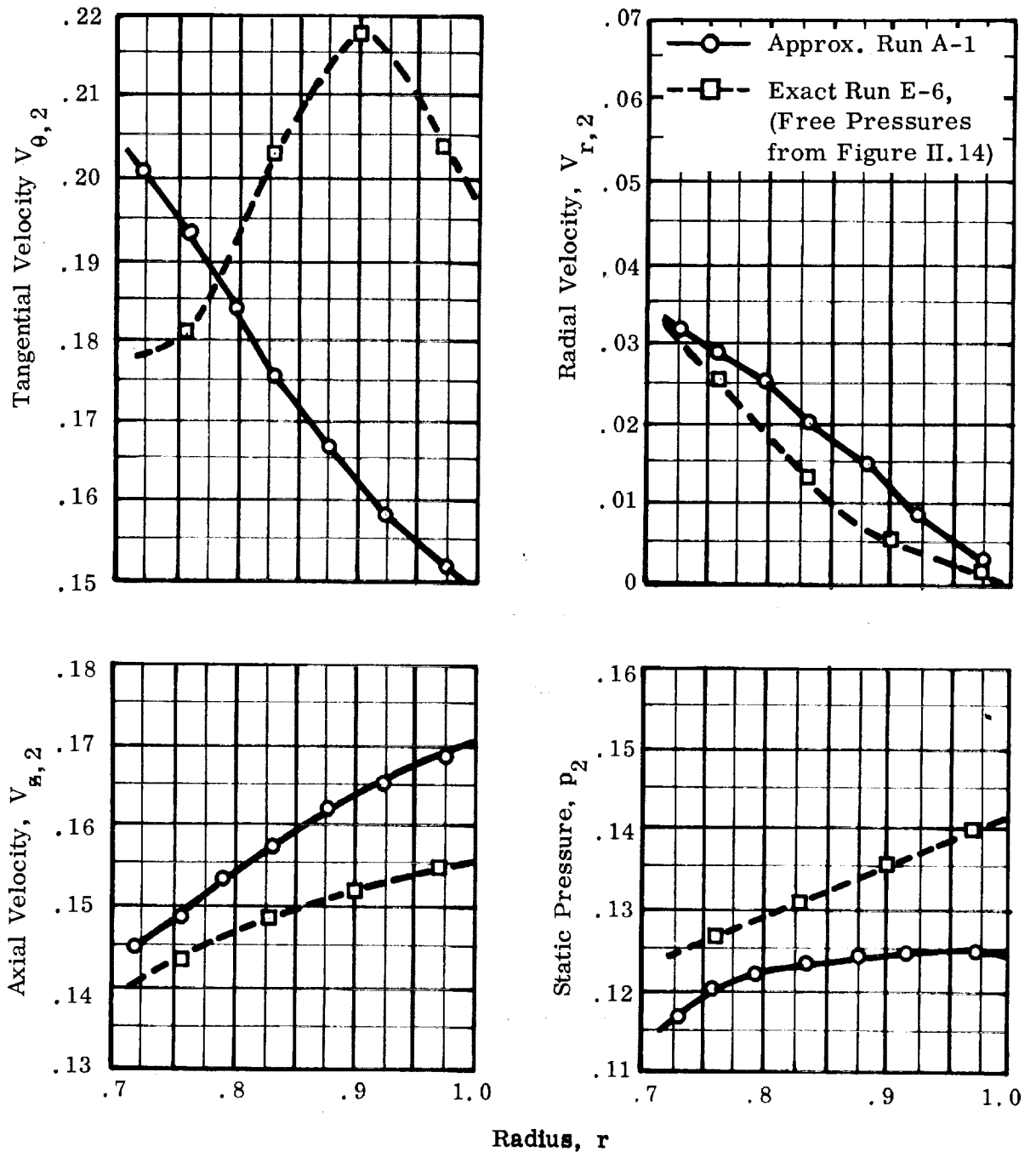
FIGURE III.5. DISTRIBUTIONS OF VELOCITY AND PRESSURE AT BLADE
TRAILING EDGE FOR INCOMPRESSIBLE, LOSSLESS FLOW IN 6.2°.
By the exact method are also given for fixed V_z distribution shown.

99
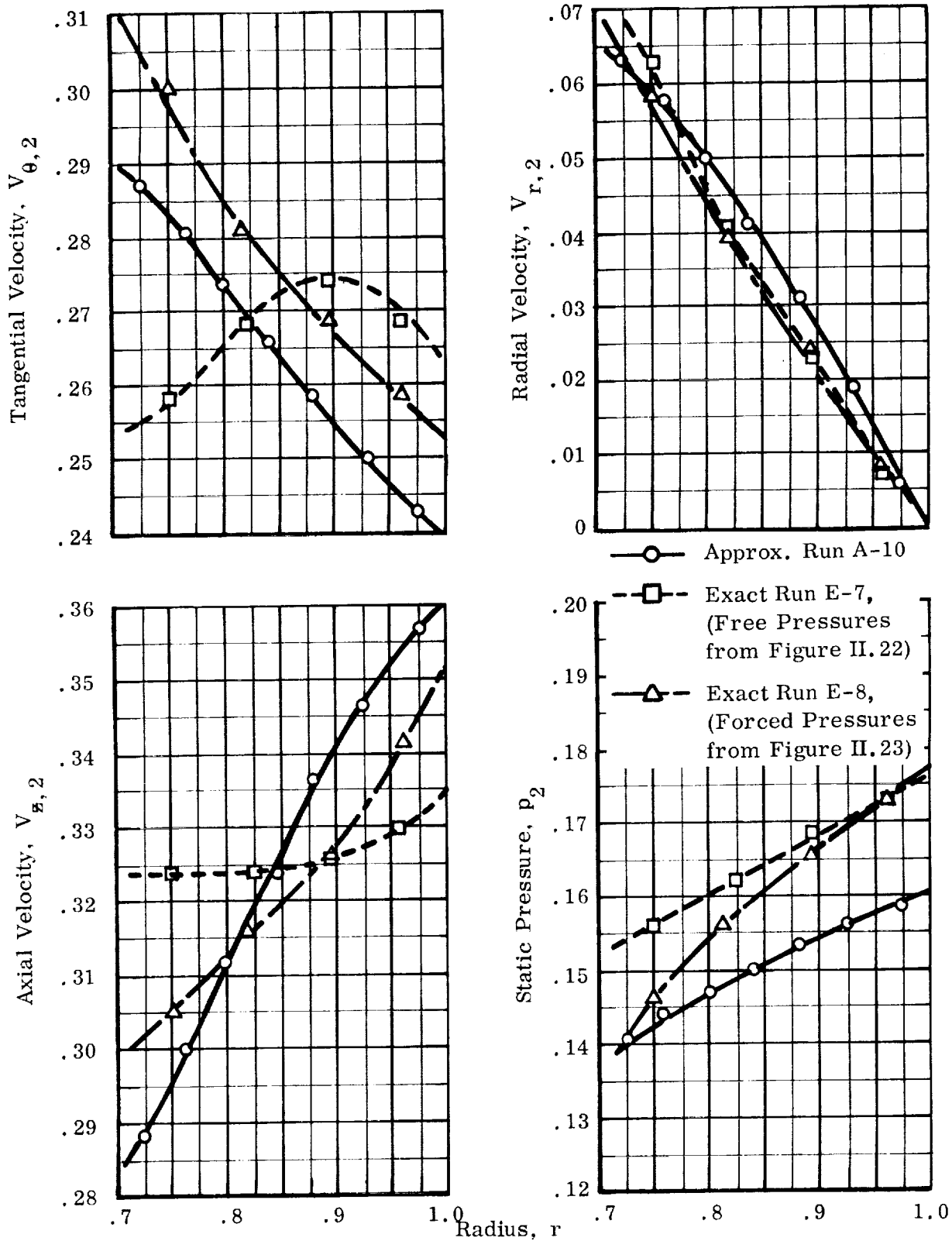
FIGURE III. 6. RADIAL DISTRIBUTIONS OF OUTLET VELOCITY AND PRESSURE AT BLADE TRAILING EDGE FOR INCOMPRESSIBLE LOSSLESS FLOW IN 12° INDUCER, SHOWING CORRELATION WITH EXACT METHOD

coarse grids that we used for the exact method do cause errors, but that this does not invalidate the method; (see the discussion at the end of Section II).

The blade surface relative velocity and pressure distributions at hub and tip from inlet to outlet are shown in figures III. 7 and III. 8 respectively for the 6. 2° inducer. Blade-to-blade differences are generally comparable for A-1 and E-6. (See figures II. 12 and II. 18 for station locations). For the 12° inducer similar correlations of Run A-10 appear in figures III. 9 and III. 11, with the free-pressure run E-7, and in figures III. 10 and III. 12 with the forced-pressure run E-8. The absence of deviation allowance in the approximate run A-10 could account for the high loads obtained by it at exit. The extension of the flow analysis into the downstream region in the runs E-7 and E-8 might be responsible for some of the unloading observed at exit, especially in figures III. 10 and III. 12.

Finally, for the latter three runs, figure III. 13 gives the correlation for the distributions of pressure and relative velocity from blade to blade at constant radius and axial position. This data is shown for a point halfway from hub to shroud in the interior of the 12° inducer. Here, as in the radial distributions at exit, the forced pressure and approximate runs (E-8 and A-10) correlate better; although, there appears to be a persistent kink in the velocity distributions obtained by the exact method. This needs to be distinguished from the approximate approach which assumes a linear velocity distribution from blade to blade.

This completes the presentation of results by the approximate method which are directly comparable with those of the exact method. The two-phase run E-9 by the exact method requires changed positions of its upstream stagnation stream surfaces (so that they are unloaded) in order to obtain a solution with which we could correlate comparable approximate results.

2. Effects of Two-Phase Flow and Losses

We made two sets of runs on the 6. 2° and 12° inducers to investigate the effects of the loss relation (I. 13) and the barotropic vaporization equation II. 7). These runs are summarized in table III. 1.

First we compare the foregoing incompressible, lossless runs with those for incompressible flow with loss

6. 2° Inducer: Runs A-3, 4, 5 in figures III. 14, 16, 17 are compared with Runs A-1 and 2 which are corresponding results for no loss.

12° Inducer: Runs A-12, 13, 14 in figures III. 15, 16, 18 are similarly compared with Runs A-10 and 11.

We found that a 4 x 16 field gives the same results as does an 8 x 16 field — within a very small error. The exit radial distributions of figures III. 14 and III. 15 show this for the 8 x 16 runs A-1, 3, 10, 12, which compare with the 4 x 16 runs A-2, 4, 11, 13

101
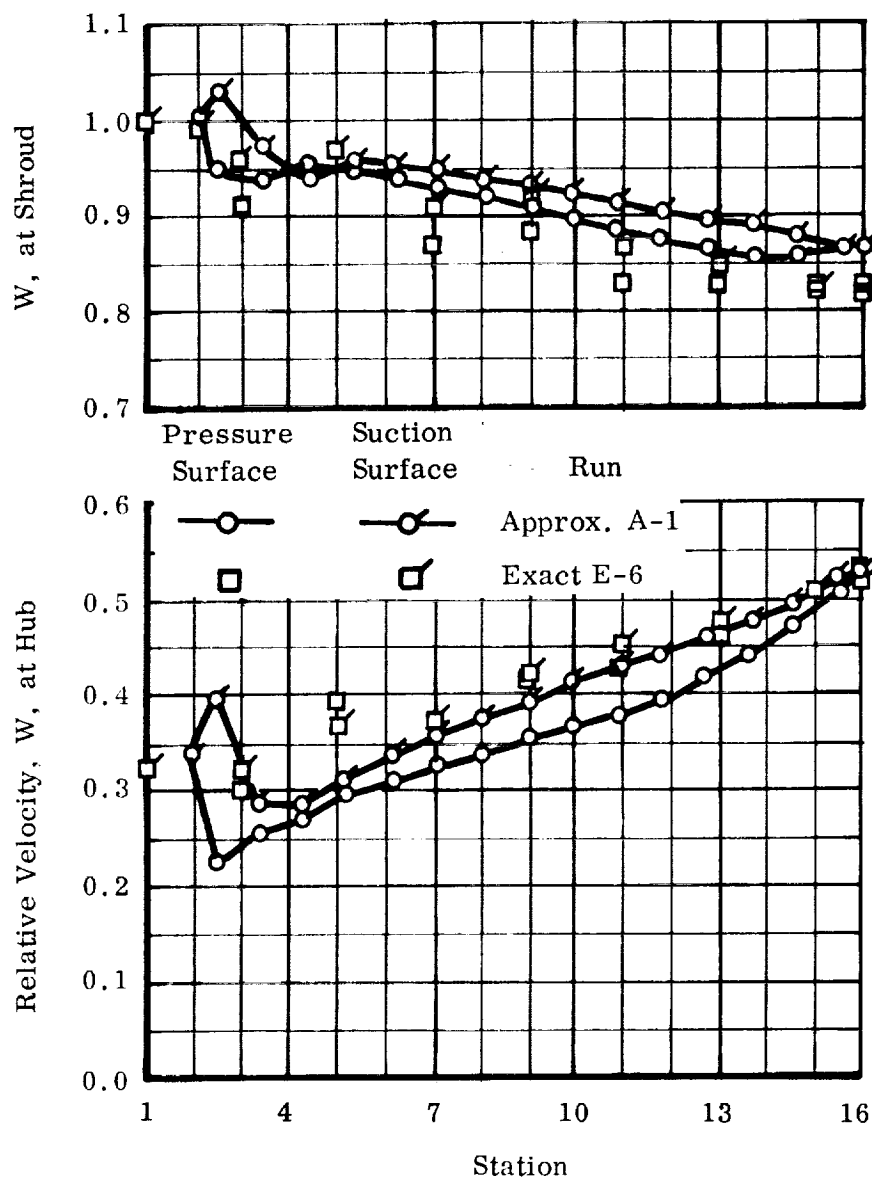
FIGURE III.7. AXIAL DISTRIBUTION OF BLADE SURFACE VELOCITY FOR
INCOMPRESSIBLE, LOSSLESS FLOW IN 6.2° INDUCER. Results by exact
method are also shown for the fixed $V_{z, 2}$ distribution of Figure II.14.
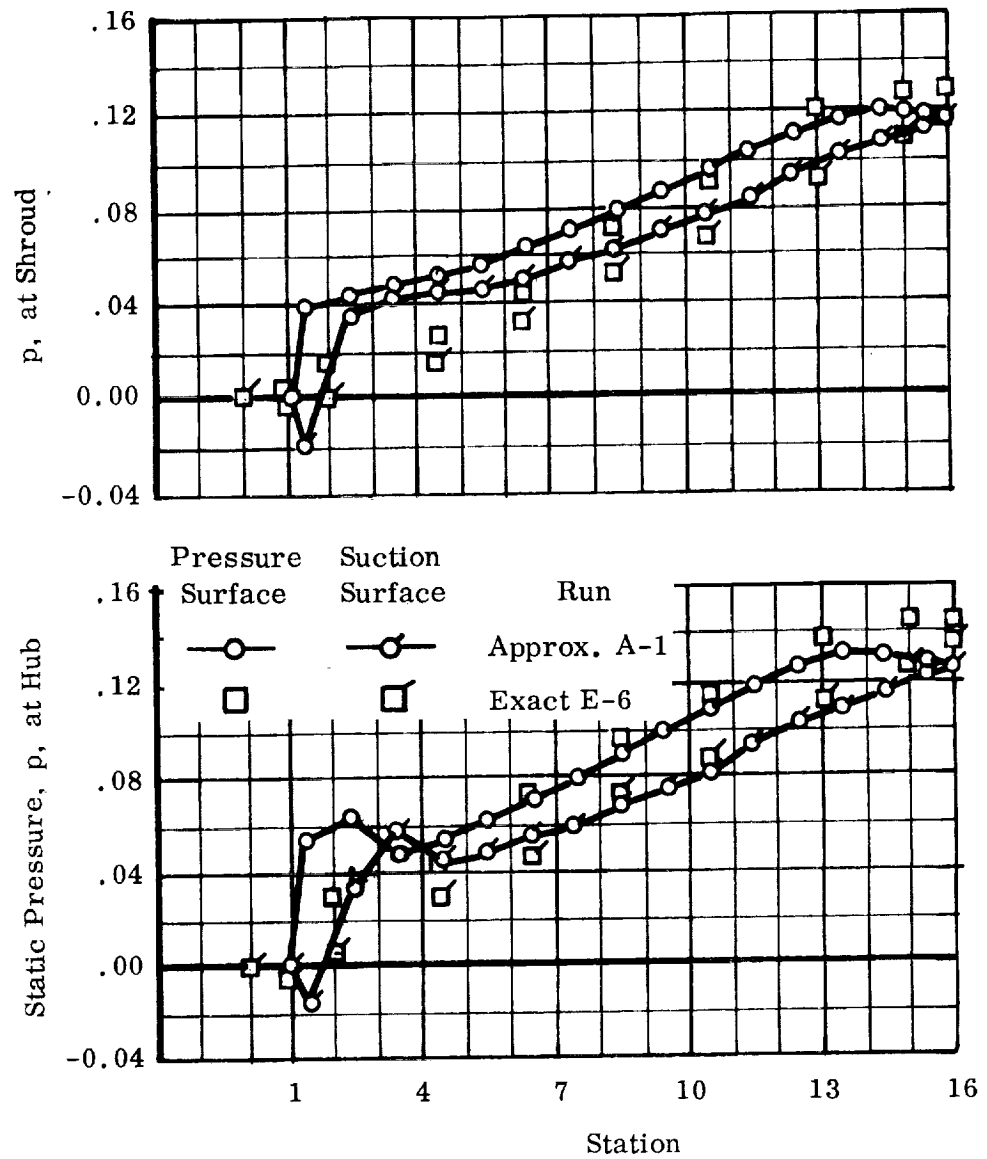
FIGURE III. 8.   AXIAL DISTRIBUTIONS OF BLADE SURFACE PRESSURE
FOR INCOMPRESSIBLE, LOSSLESS FLOW IN 6.2° INDUCER. Results
by the exact method are also shown for the fixed $V_{z, 2}$ distribution of
Figure II. 14.

103
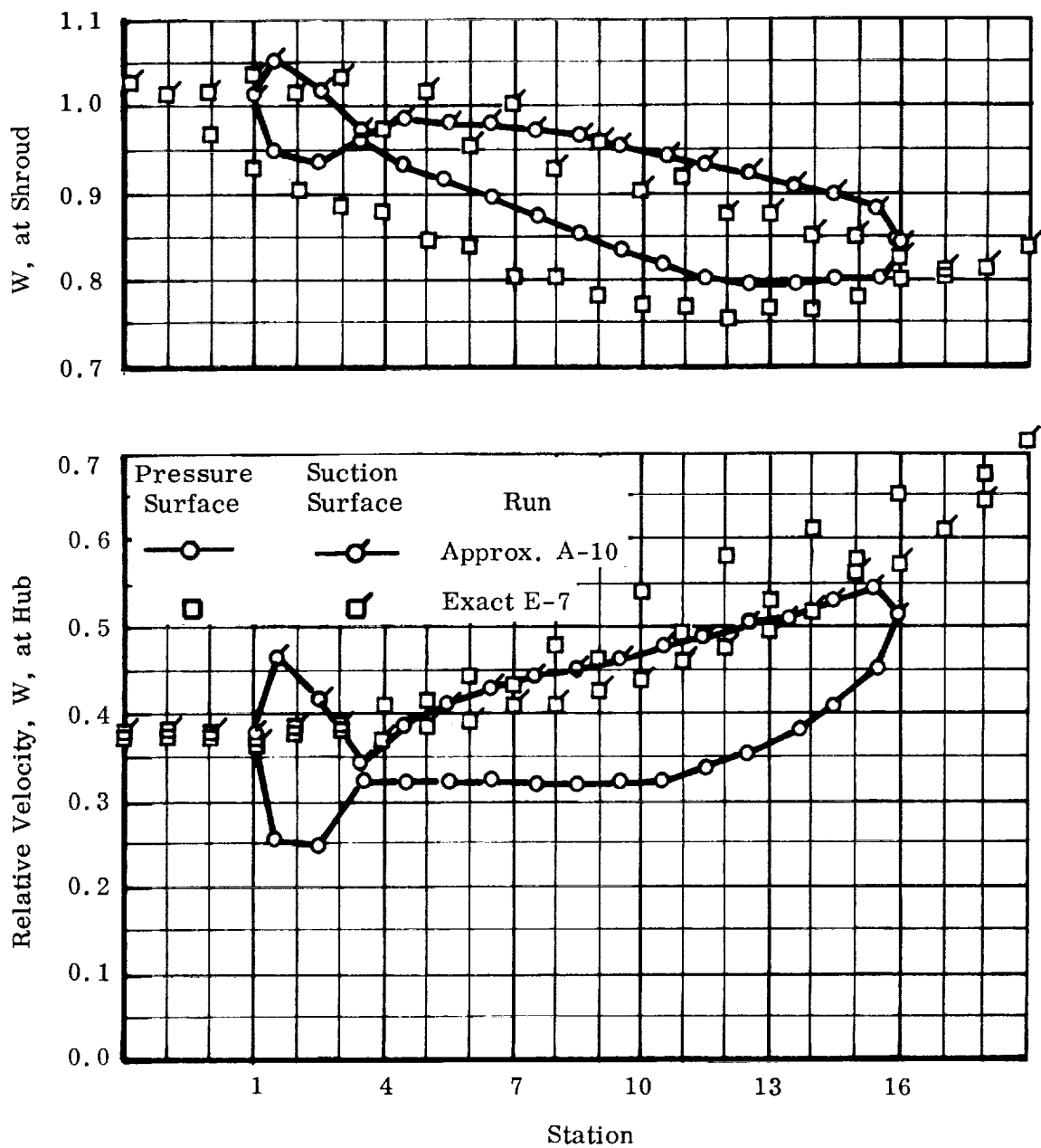
FIGURE III.9. AXIAL DISTRIBUTIONS OF BLADE SURFACE VELOCITY
FOR INCOMPRESSIBLE, LOSSLESS FLOW IN 12° INDUCER, SHOWING
CORRELATION WITH EXACT METHOD FREE PRESSURE RESULTS.
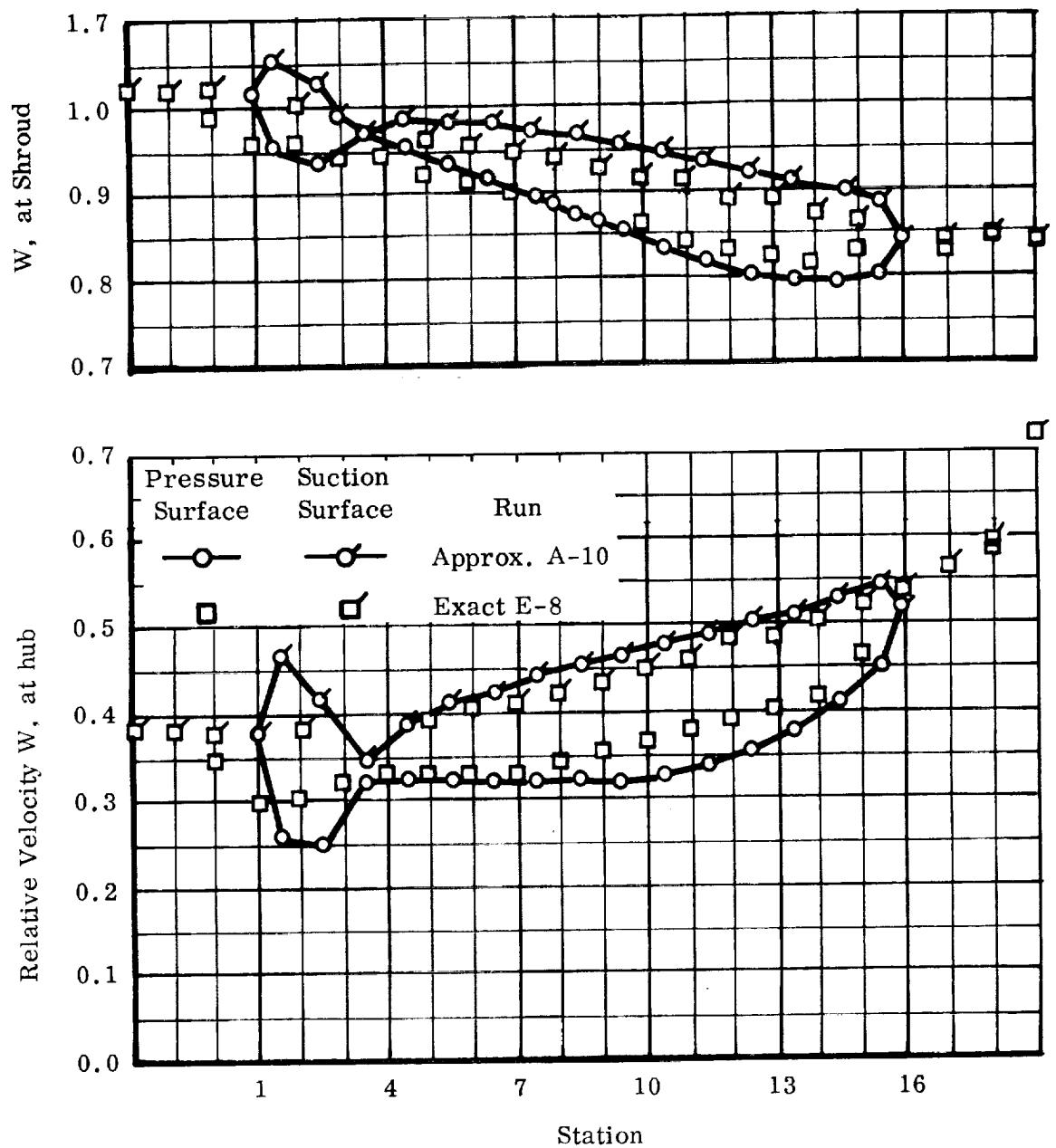
FIGURE III.10. AXIAL DISTRIBUTIONS OF BLADE SURFACE VELOCITY
FOR INCOMPRESSIBLE, LOSSLESS FLOW IN 12° INDUCER, SHOWING
CORRELATION WITH EXACT METHOD FORCED PRESSURE RESULTS.
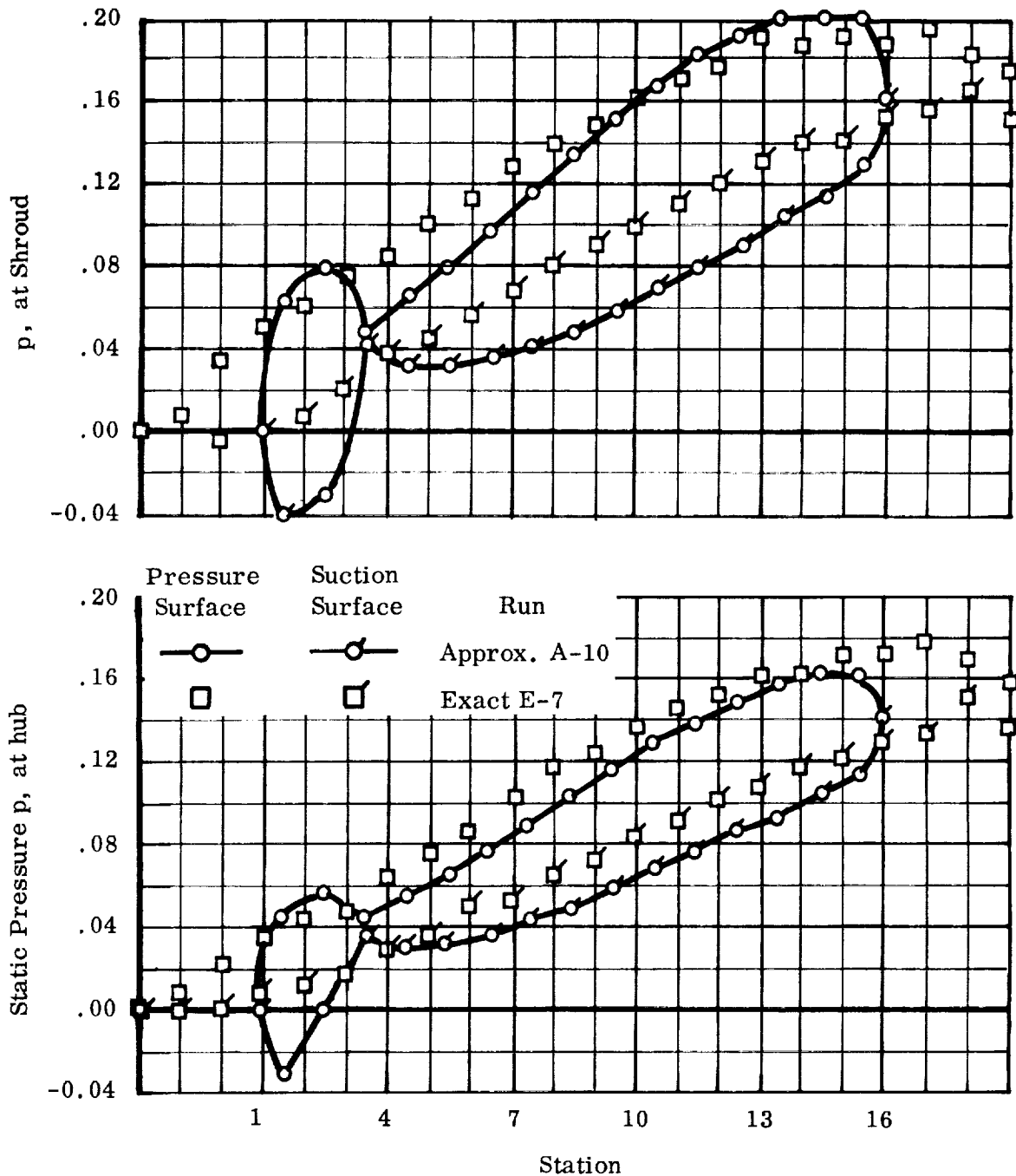
FIGURE III.11. AXIAL DISTRIBUTIONS OF BLADE SURFACE PRESSURE
FOR INCOMPRESSIBLE, LOSSLESS FLOW IN 12° INDUCER, SHOWING
CORRELATION WITH EXACT METHOD FREE PRESSURE RESULTS.
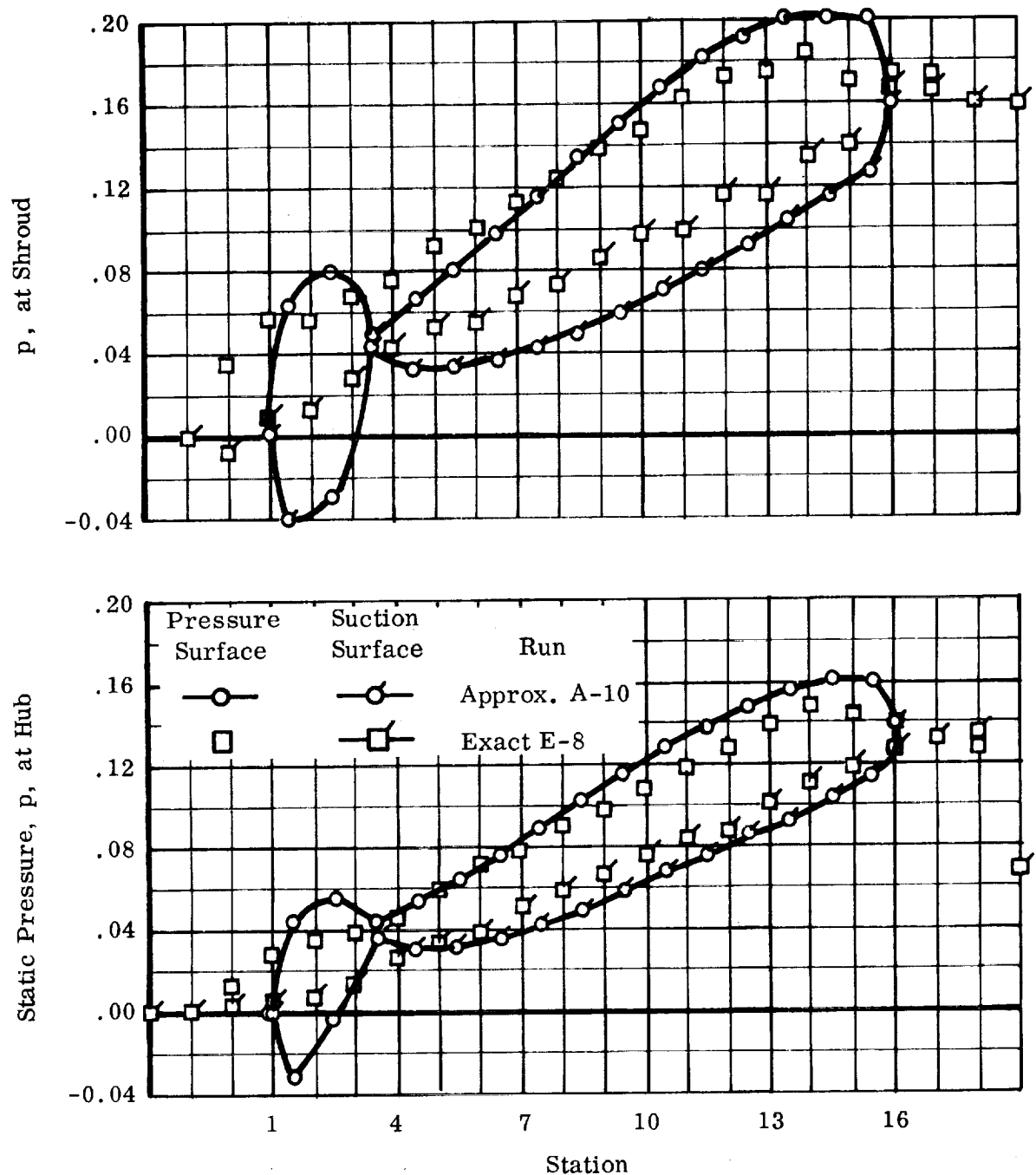
FIGURE III.12. AXIAL DISTRIBUTIONS OF BLADE SURFACE PRESSURE FOR INCOMPRESSIBLE LOSSLESS FLOW IN 12° INDUCER, SHOWING CORRELATION WITH EXACT METHOD FORCED PRESSURE RESULTS.

	Run No.	Method
O	A-10	Approximate
□	E-8	Exact: Forced Pressure
△	E-7	Exact: Free Pressure

Relative Velocity W

Static Pressure p

Circumferential Position, θ
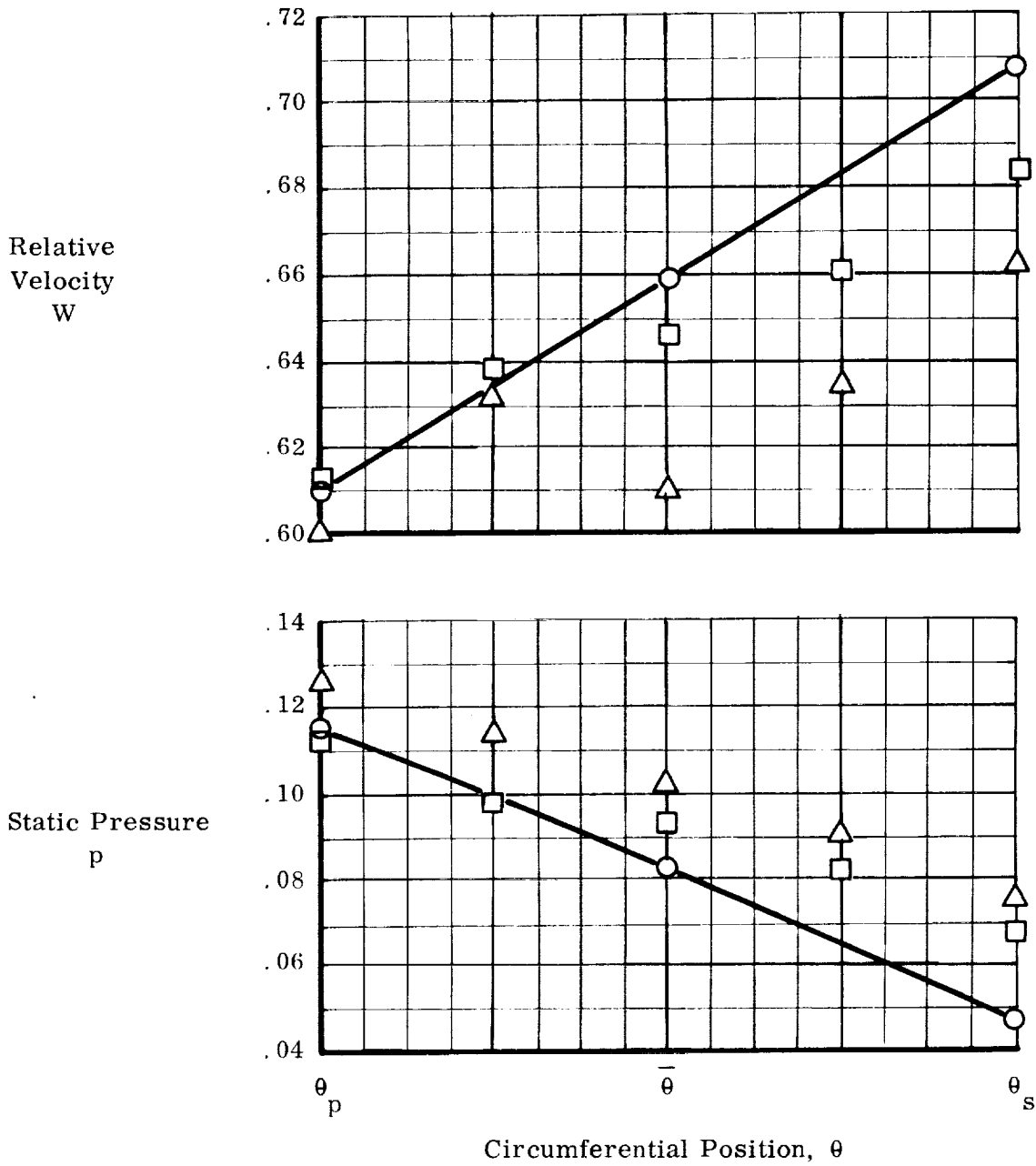
FIGURE III. 13.   BLADE-TO-BLADE DISTRIBUTIONS OF PRESSURE AND RELATIVE VELOCITY, SHOWING COMPARISON OF EXACT AND APPROXIMATE METHODS. Incompressible lossless flow in 12^c inducer at the central interior point, $z = .7600$ and $r = .7556$.

respectively. Because of this accuracy and a greatly reduced computing time, all approximate runs reported employed a 4 x 16 field, except for A-1, 3, 10, 12. The approximate positions of the resulting three annuli are shown in figures III. 23 and III. 24.

We define the parameter that determines the variation in loss as the machine Reynolds number:

$$R_m \equiv \frac{\Omega\, r_{t,1}^2}{\nu} \qquad\qquad \text{(III. 31)}$$

Table III. 1 shows the two values of R_m that we used. $R_m = 2.5 \times 10^7$ results if either inducer has a 5.37 inch inlet tip diameter and pumps liquid 36°R hydrogen at 9,550 rpm. At 19,100 rpm, this gives $R_m = 5 \times 10^7$. Similarly we get 2.5×10^7 pumping 267°F water at 9,550 rpm with a 6-inch diameter inlet. The resulting Reynolds number effect, (cf. runs A-4 and A-5 in figure III. 14), is noticeable for the 6.2° inducer, which has a large solidity and therefore much skin friction loss (equation I. 14). For the 12° inducer, which had much less solidity, the difference between runs A-13 and A-14 is barely discernable in figure III. 15 and the overall performance data of table III. 1. This frictional difference between the two machines also accounts for the much greater effect of any loss on the results for the 6.2° inducer which had about 70% efficiency as compared to 95% for the 12° inducer. Especially noticeable is the change in exit velocity distributions caused by losses, (figure III. 14).

The differences between the 6.2° and 12° inducers for these incompressible loss cases is seen in another way in figure III. 16 which gives the corresponding blade element data. NASA test results (reference 31) and a 12° constant-lead inducer are given for qualitative comparison purposes. Our resulting theoretical distributions of loss coefficient $\bar{\omega}$ appear to be qualitatively correct. The NASA inducer has a high $\bar{\omega}$ at the tip, probably because of tip leakage and secondary flow losses and maybe because of the low blade angle at outlet as compared to the 12° variable-lead inducer (figure II. 18). Our loss coefficients (equations I. 14 and I. 15) may need to be increased and distributed differently to give accurate results. (See the discussion in Section IV.)

Figures III. 17 and III. 18 show the loss effects on blade surface velocity and pressure distributions. Here the data is given simply for the mean annulus, the location of which changes very little with the different solutions, (figures III. 23 and III. 24). The same differences between the 6.2° and 12° inducers are evident here also.

Next we present the comparisons of these incompressible, loss runs with those for two-phase flow with loss as summarized in table III. 1.

6.2° Inducer: Two-phase runs A-7 and A-9 are compared with incompressible run A-5 in figures III. 19, 20, 21, 23.
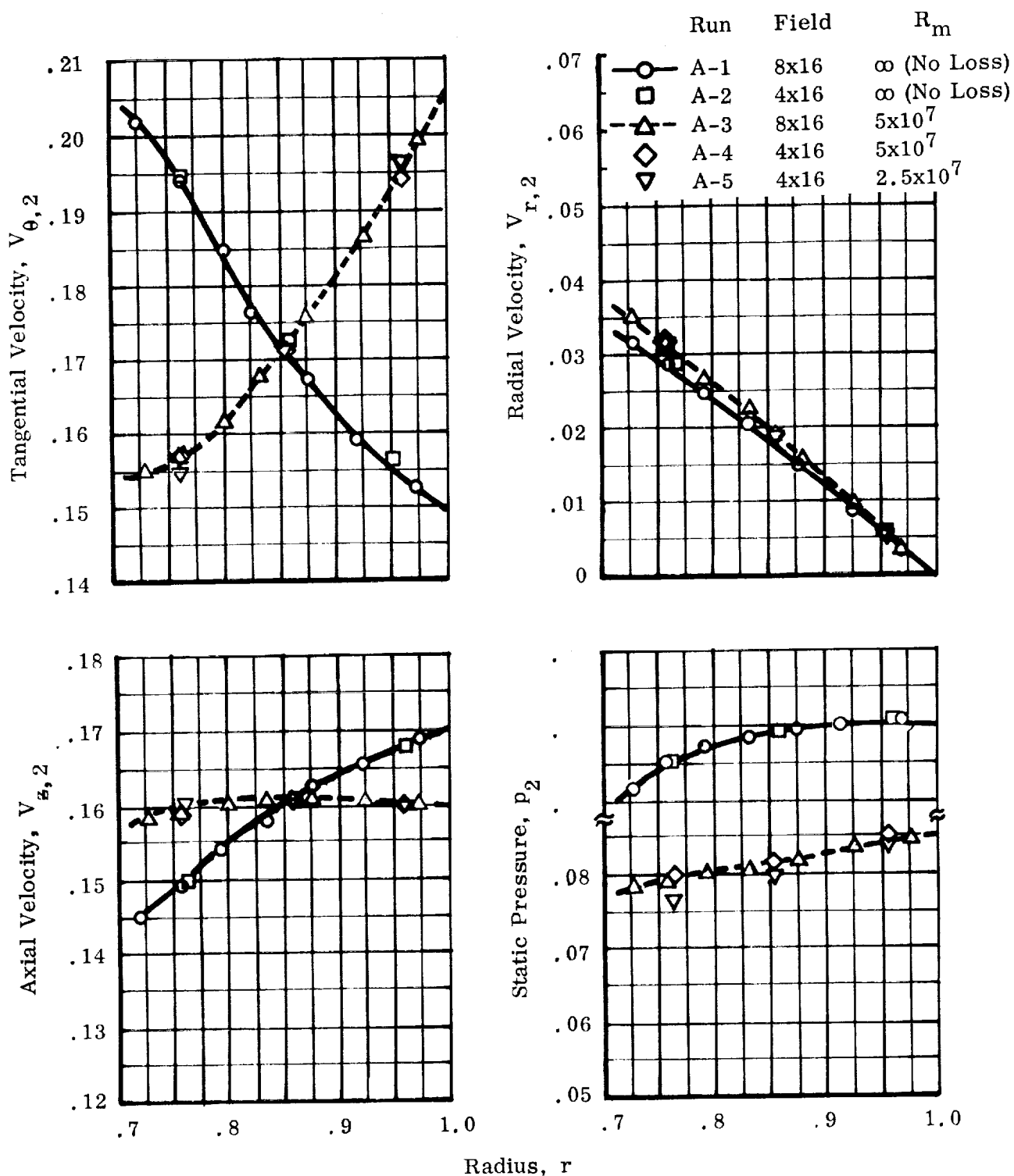
FIGURE III.14. EFFECT OF LOSSES ON RADIAL DISTRIBUTIONS OF OUTLET VELOCITY AND PRESSURE FOR INCOMPRESSIBLE FLOW IN 6.2° INDUCER. Note accuracy of results of runs with three annuli (4x16) as compared to those for seven annuli (8x16). Also note Reynolds Number effect in runs with loss.

110
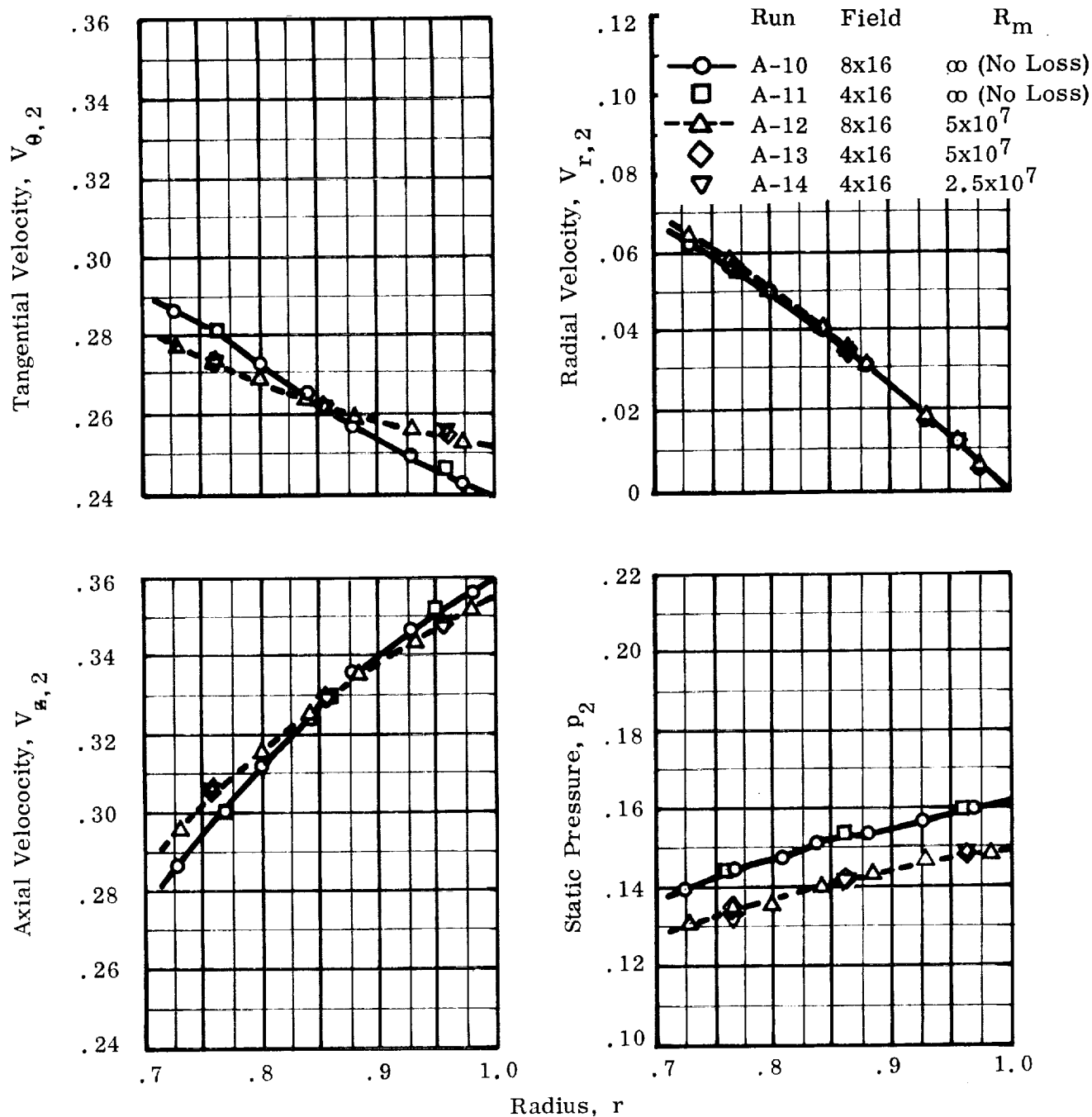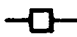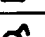
FIGURE III-15.   EFFECT OF LOSSES ON RADIAL DISTRIBUTIONS OF OUTLET
VELOCITY AND PRESSURE FOR INCOMPRESSIBLE FLOW IN 12° INDUCER.
Note close correlation of three-annulus (4x16) and seven-annulus (8x16) results.
Also note Reynolds Number effect.

	Run	R_m	Field	Inducer	Notes
—□—	A-3	5×10^7	8 x 16	6.2°	See Table III.1 for further information on these analytical results.
◘	A-4	5×10^7	4 x 16	6.2°	
◘	A-5	2.5×10^7	4 x 16	6.2°	
—□—	A-12	5×10^7	8 x 16	12°	
◘	A-13	5×10^7	4 x 16	12°	
◘	A-14	2.5×10^7	4 x 16	12°	
--○--	NASA Ref. 31 p.44	4×10^6	Test Data	NASA 12° Const. Lead	$\overline{\phi} = .1570 \qquad \sigma = 1.9$ Cold Water: $\nu \approx 1$ cs
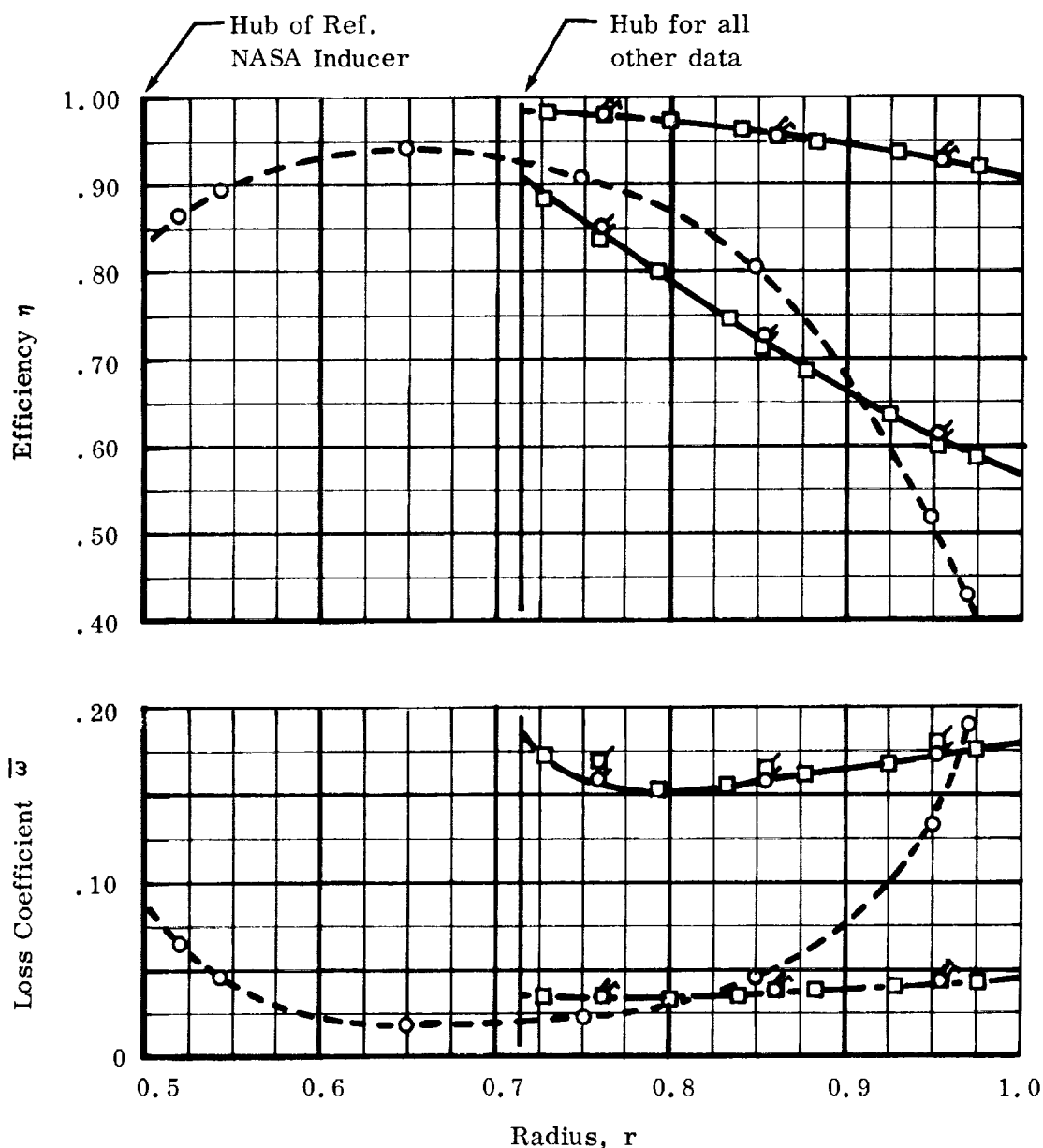
FIGURE III.16.   COMPARISON OF INCOMPRESSIBLE FLOWS WITH LOSS FOR 6.2 AND 12° INDUCERS.   RADIAL DISTRIBUTIONS OF OUTLET ANNULUS EFFICIENCY AND LOSS COEFFICIENT.   Also shown are experimental results for a flat plate 12° NASA inducer with a constant hub-to-tip radius ratio.

112

	Run No.	Blade Surface	Description
O	A-2	Pressure	No Loss
♂		Suction	
□	A-5	Pressure	Loss $R_m = 2.5 \times 10^7$
◻		Suction	
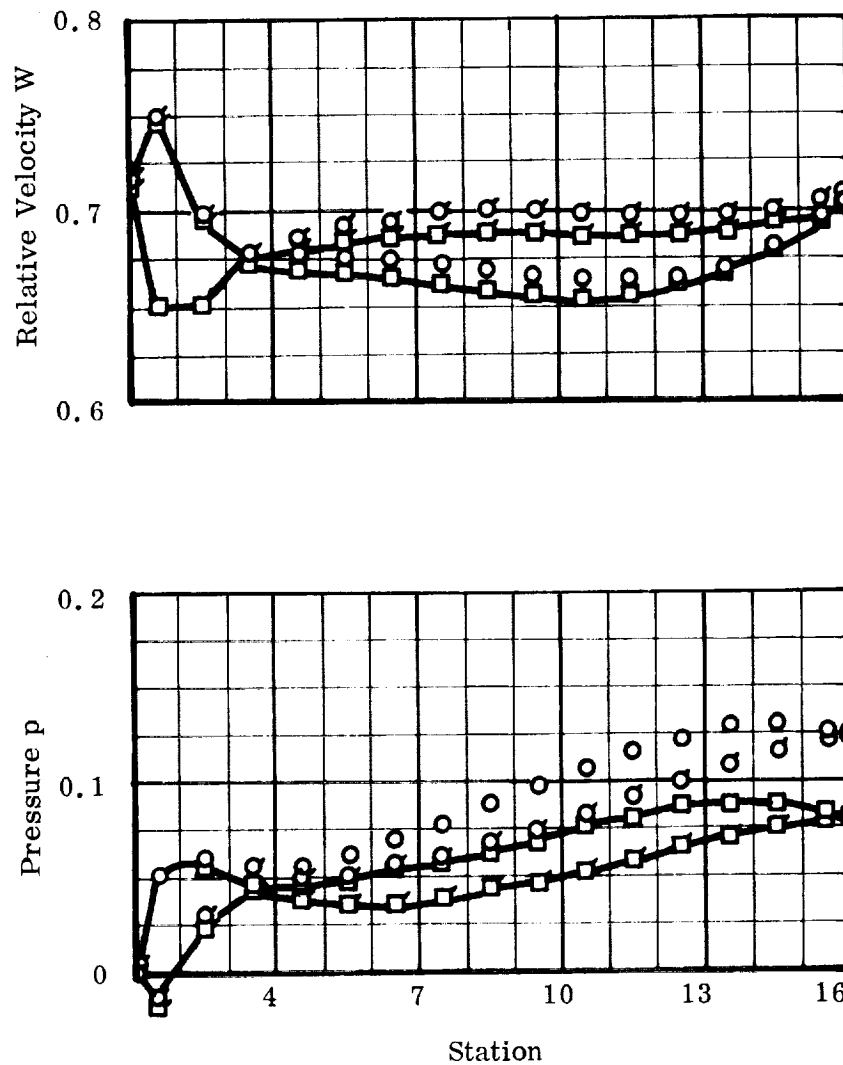
FIGURE III.17. COMPARISON OF BLADE SURFACE DATA FOR INCOMPRESSIBLE FLOWS WITH AND WITHOUT LOSS FOR 6.2° INDUCER. Axial distributions of velocity and presure in mean annulus.

113

	Run No.	Blade Surface	Description
O	A-11	Pressure	No Loss
⊘		Suction	
□	A-14	Pressure	Loss $R_m = 2.5 \times 10^7$
⬚		Suction	
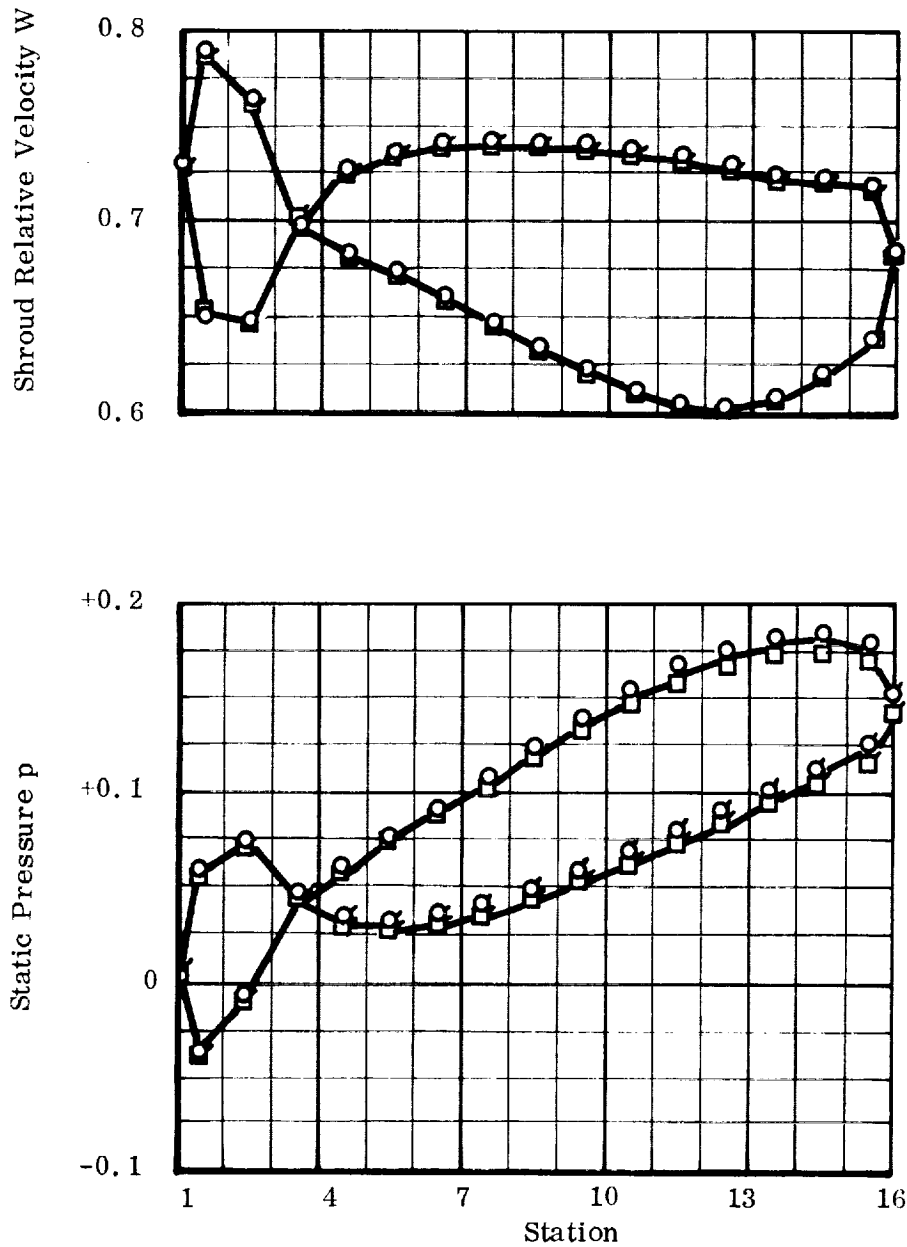
FIGURE III. 18.   COMPARISON OF BLADE SURFACE DATA FOR
INCOMPRESSIBLE FLOWS WITH AND WITHOUT LOSS FOR 12°
INDUCER.   Distributions of velocity and pressure in mean annulus.

114

12° Inducer: Two phase runs A-16 and A-18 are compared with incompressible run A-14 in figures III.19, 20, 22, 24.

These six runs were all made at the same machine Reynolds number, $R_m = 2.5 \times 10^7$. Single-phase liquid flow existed just upstream of the blading and the inlet flow co-efficients $\emptyset_{1,f}$ for the 6.2° and 12° inducers were 0.083 and 0.1763 respectively.

In order to understand the two-phase phenomena as shown in these results, we should first review the performance parameters involved. For a given inducer, reference 8 showed that our flow model analyzes the influence of four dimensionless parameters on a fifth one. We express this as follows:

$$\Psi = \Psi(\emptyset_{1,f}, R_m, \Psi_{sp}, \Theta) \tag{III. 32}$$

where the following definitions apply:

Total head rise coefficient

$$\Psi \equiv \frac{g_o \, \Delta \overline{H}}{U_{t,1}{}^2} \tag{III. 33}$$

Inlet liquid flow coefficient

$$\emptyset_{1,f} \equiv \frac{w_T}{\rho_f \, A_1 \, U_{t,1}} \tag{III. 34}$$

Machine Reynolds number

$$R_m \equiv \frac{\Omega \, r_{t,1}{}^2}{\nu} \tag{III. 31}$$

Cavitation coefficient

$$\Psi_{sp} \equiv \frac{\overline{p}_1 - p_{sat}}{\dfrac{\rho_f}{g_o} U_{t,1}{}^2} \tag{III 35}$$

Vaporization parameter

$$\Theta \equiv \frac{B}{g_o} U_{t,1}{}^2 \equiv \frac{\rho_f \, T^*}{g_o} U_{t,1}{}^2 \tag{III. 36}$$

115

where T* is defined in equation (I. 8). Table III. 1 lists these for each run. Because of the many existing cavitation parameters, we have listed other useful forms in table III. 1 besides Ψ_{sp}. These all express dimensionlessly the excess of inlet pressure over vapor pressure:

Suction specific speed:

$$S \equiv \frac{N \sqrt{Q_f}}{\left[g_0 \left(\frac{\overline{P}_1 - p_{sat}}{\rho_f} \right) \right]^{3/4}} \tag{III. 37}$$

Cavitation number:

$$k \equiv \frac{\overline{p}_1 - p_{sat}}{\frac{\rho_f U_{t,1}^2}{2g_0} (1 + \emptyset_{1,f}^2)} \tag{III. 38}$$

The effect of different combinations of inducer speeds and fluids at constant values of these cavitation parameters is expressed by the vaporization parameter Θ, (equation III. 36). Accordingly, we made two-phase runs for various combinations of Ψ_p and Θ, holding R_m and $\emptyset_{1,f}$ constant. Figures III. 19 through III. 24 give data for $\Theta = 10$ and 1000.* Even though we used a lower Ψ_{sp} for the $\Theta = 10$ case, the volume of vaporizing fluid, and its effect on performance was considerbly less than for the $\Theta = 1000$ cases. Therefore, the incompressible case and the $\Theta = 1000$ case for each inducer are presented in figures III. 19 and III. 20. The exit radial distributions, given in the first of these figures, show the effects of internal two-phase motion primarily on the pressure. This is shown also in the overall performance data of table III. 1. The loss coefficient data in figure III. 20 shows that most of the effects are felt at the tip, as would be expected. The fact that we did not get more two-phase performance deterioration (as compared to non-cavitating values) is probably due to our omission of tip leakage vortex vaporization effects and our apparently low loss factors, which apparently did not allow for the actual distribution of secondary flow losses; (see foregoing discussion of incompressible flow with loss). Also, if we had concentrated an additional annulus near the shroud, our results might have shown more performance deterioration. The average relative velocity of this annulus would be higher and would therefore lead to larger local pressure drops and the consequent vapor formation. In early check-out work that we did on this method using a 2 x 16 field (one annulus only) we were able to obtain two-phase solutions at slightly lower NPSH than was possible with the 4 x 16 field.

---

* For dimensional examples to which these solutions apply. See Table IV. 1.

	Run No.	Θ	Flow	Inducer
O	A-5		Incompressible	6.2°
□	A-9	1000	Two-Phase	6.2°
△	A-14		Incompressible	12°
◇	A-18	1000	Two-Phase	12°
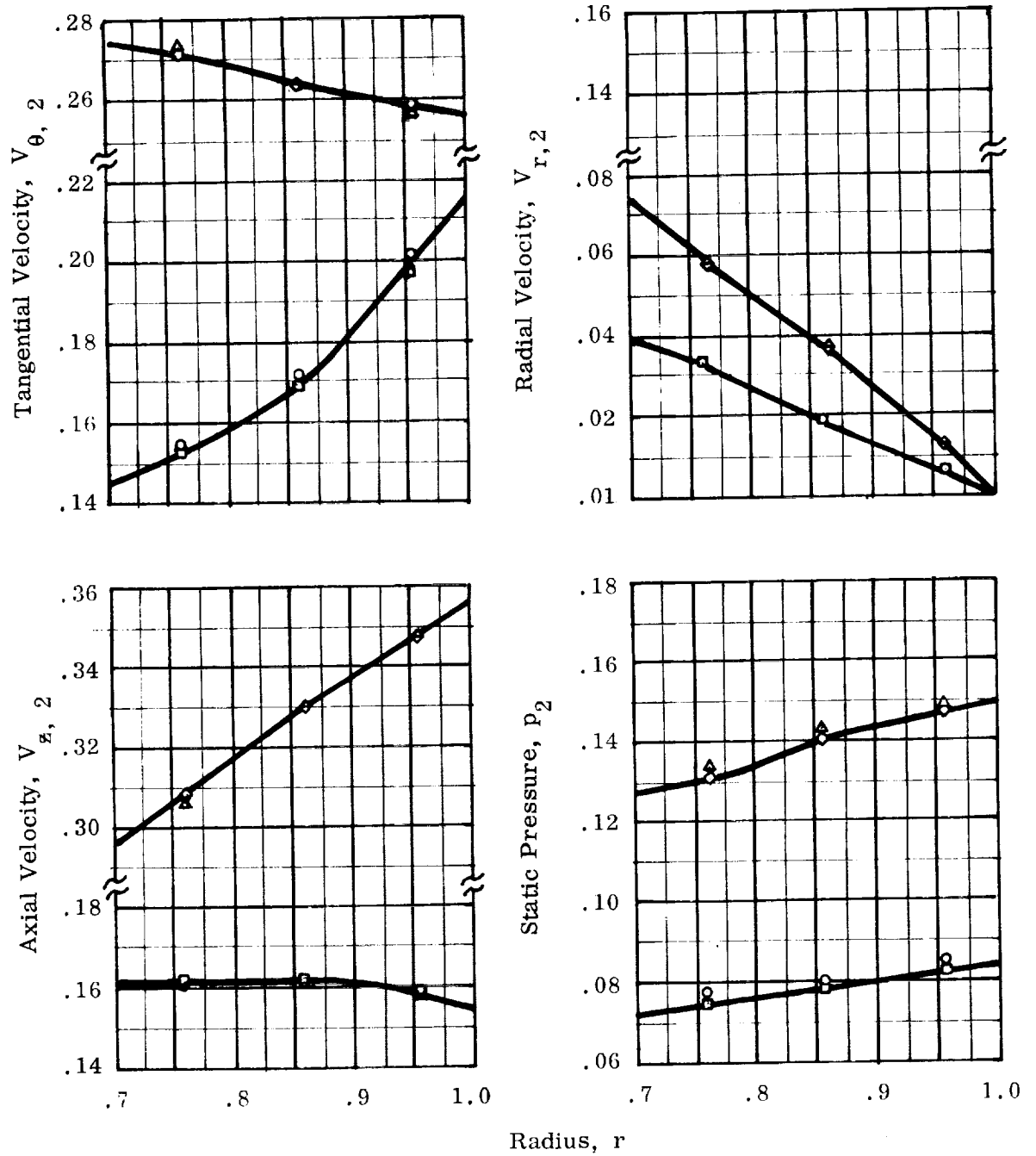
FIGURE III.19.   EFFECT OF TWO-PHASE FLOW WITHIN BLADES ON RADIAL
DISTRIBUTIONS OF OUTLET VELOCITY AND PRESSURE FOR 6.2 AND 12°
INDUCERS (R_m = 2.5 x 10^7).

	Run No.	Description	Inducer
—○—	A-5	Incompressible	6.2°
--□--	A-9	Two Phase	6.2°
—△—	A-14	Incompressible	12°
--◇--	A-18	Two Phase	12°
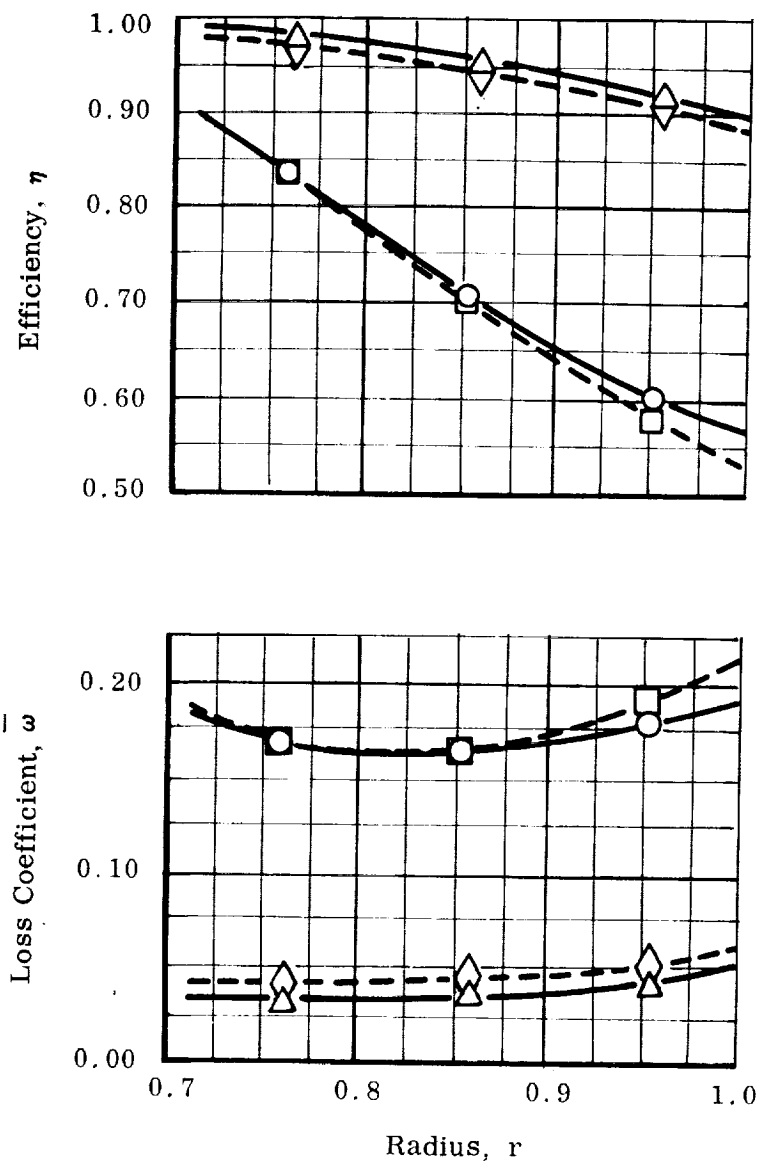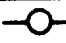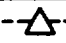
FIGURE III.20. COMPARISON OF OUTLET PARAMETERS FOR TWO PHASE AND INCOMPRESSIBLE FLOWS WITH LOSS IN 6.2° AND 12° INDUCERS. Reynolds number, R_m = 2.5 x 10^7. Radial distributions of outlet annulus efficiency and loss coefficient at blade trailing edge.

	Run No.	Θ	Blade Surface	Description
—○—	A-5		Pressure	Incompressible
—□—			Suction	
--△--	A-7	10	Pressure	Two-Phase
--◇--			Suction	
—⬡—	A-9	1000	Pressure	Two-Phase
—⬡—			Suction	
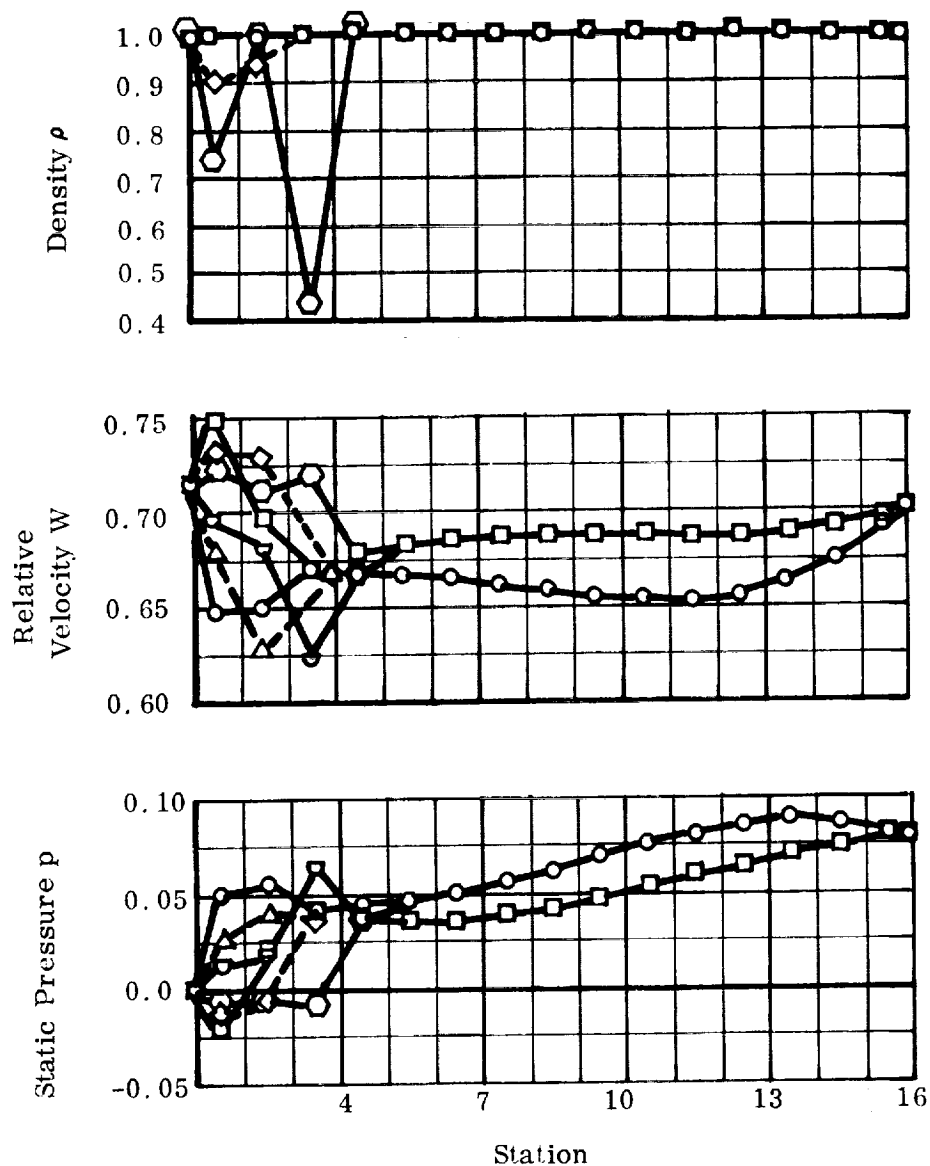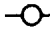
FIGURE III. 21. EFFECT OF TWO-PHASE FLOW ON AXIAL
DISTRIBUTIONS OF BLADE SURFACE PRESSURE, RELATIVE
VELOCITY, AND DENSITY IN MEAN ANNULUS OF 6. 2° INDUCER.
NOTE: Answers are approximately the same as in Run No. A-5
unless otherwise shown.

	Run No.	Θ	Blade Surface	Description
—O—	A-14		Pressure	Incompressible
—□—			Suction	
-△-	A-16	10	Pressure	Two-Phase
-◇-			Suction	
—▽—	A-18	1000	Pressure	Two-Phase
—O—			Suction	
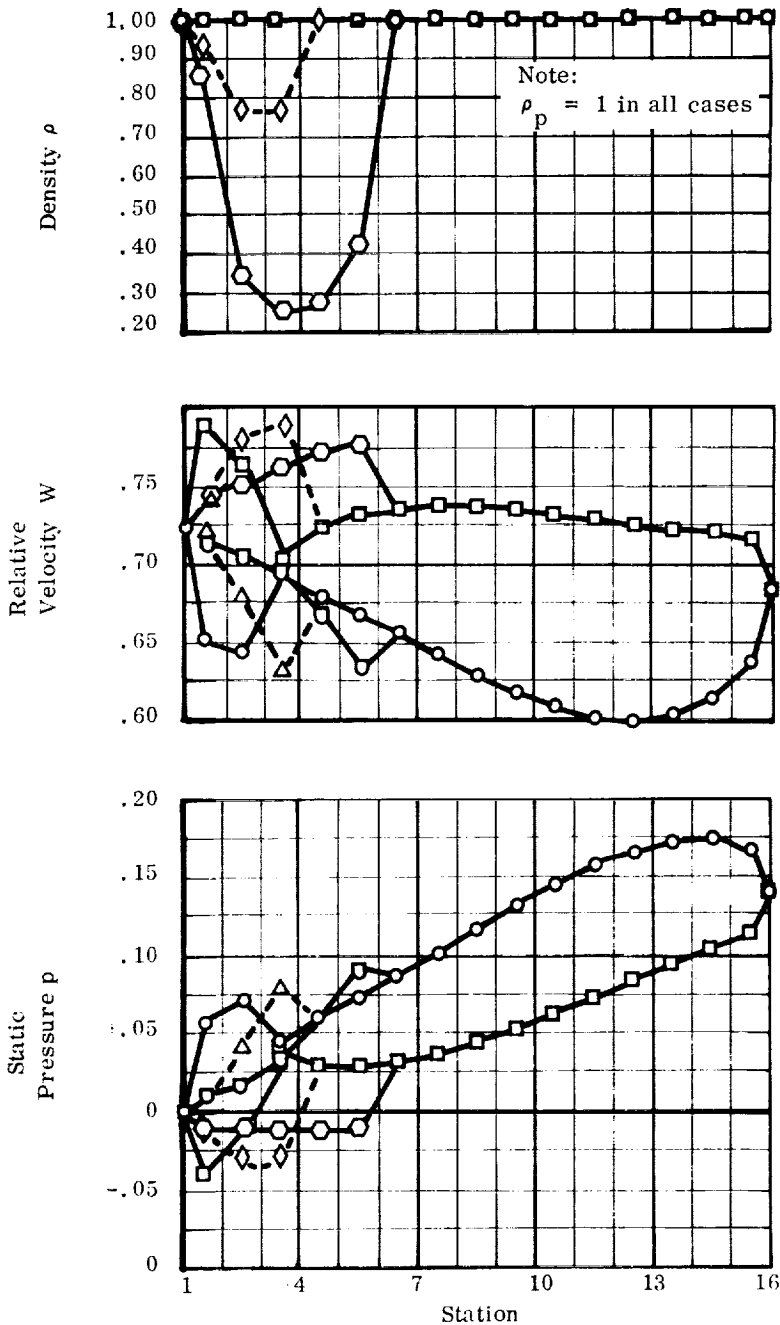
Note:
$\rho_p = 1$ in all cases

FIGURE III. 22. EFFECT OF TWO-PHASE FLOW ON AXIAL DISTRIBUTIONS
OF SURFACE PRESSURE, VELOCITY, AND DENSITY IN MEAN ANNULUS
OF 12° INDUCER. Note: Answers Are Approximately The Same As In Run
No. A-14 Unless Otherwise Shown.
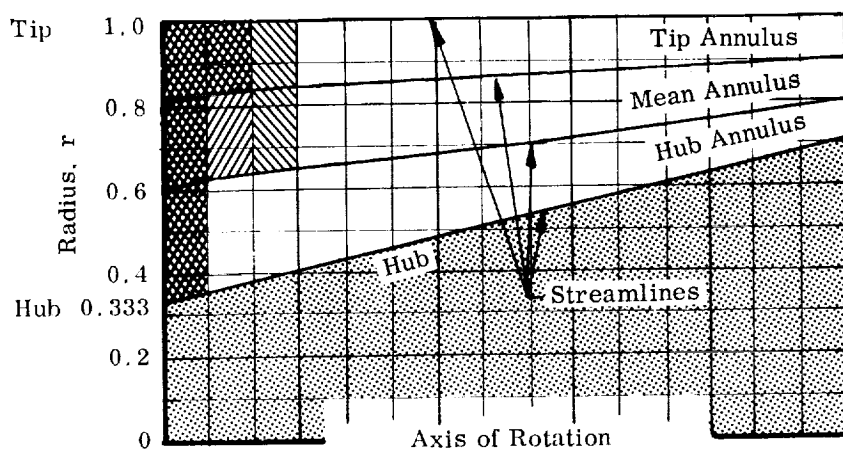
Tip 1.0

Radius, r

0.8

0.6

0.4

Hub 0.333

0.2

0

Tip Annulus

Mean Annulus

Hub Annulus

Hub

Streamlines

Axis of Rotation

(a) Extent of Two Phase Flow

Region of Two Phase Flow*	Run No.	Key	Type of Flow
None	A-14	—O—	Incompressible
▨	A-16	--□--	Mild Cavitation
▧	A-18	--△—	Severe Cavitation

*All portions of inducer contain liquid flow unless otherwise indicated.

(b) Average Pressure in Mean Annulus

0.2

Average Static Pressure, p

0.1

0

A-5

A-9

4   7   10   13   16

Station
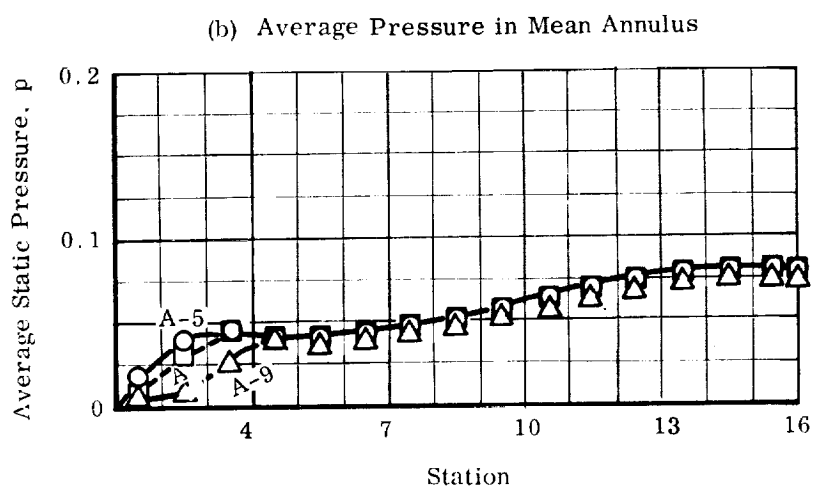
FIGURE III.23.   DOMAINS OF TWO-PHASE & INCOMPRESSIBLE FLOWS
FOR 6.2 INDUCER. Losses included: $R_m = 2.5 \times 10^7$. Postions
of streamlines are approximately as shown for all 3-annulus runs
with this inducer. Note that extent of two-phase region increases
with severity of cavitation (part a), and that pressure buildup is
correspondingly delayed (part b).
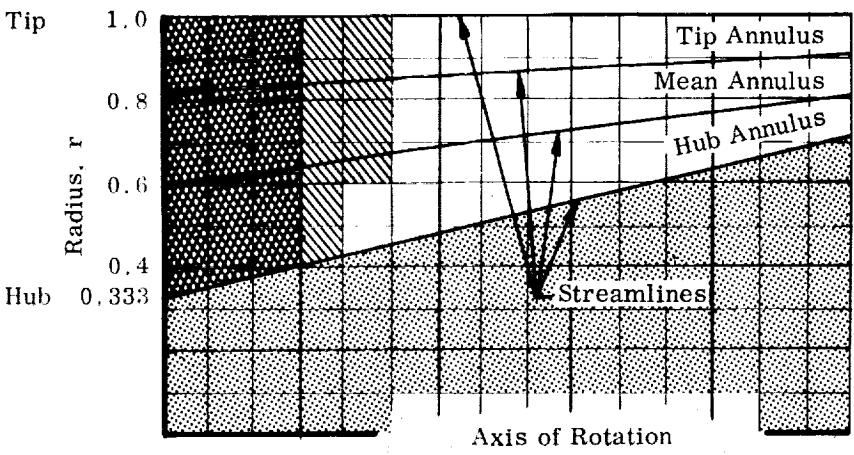
(a) Extent of Two Phase Flow

Region of Two Phase Flow*	Run No.	Key	Type of Flow
None	A-14	──O──	Incompressible
▨	A-16	──□──	Mild Cavitation
▩	A-18	──△──	Severe Cavitation

*All portions of inducer contain liquid unless otherwise indicated.
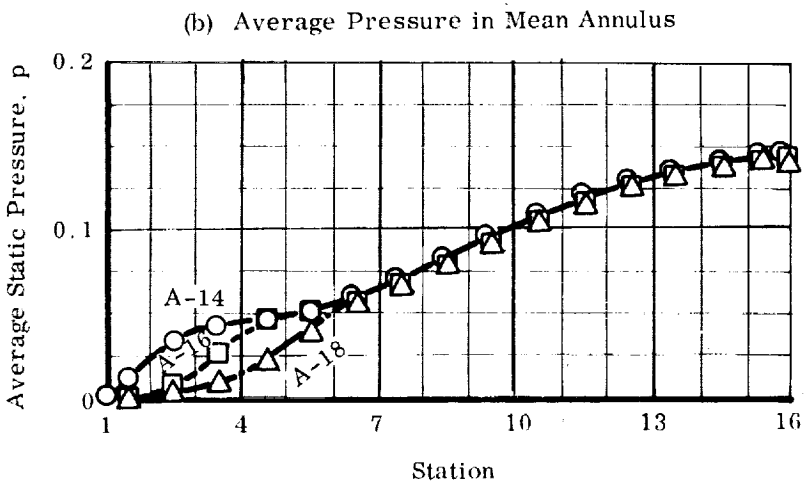
(b) Average Pressure in Mean Annulus

FIGURE III.24. DOMAINS OF TWO-PHASE & INCOMPRESSIBLE FLOWS FOR 12° INDUCER. Losses included: R_m ~ 2.5 x 10^7. Positions of streamlines are approximately as shown for all 3-annulus runs with this inducer. Note that extent of two-phase region increases with severity of cavitation (part a) and that pressure buildup is correspondingly delayed (part b).

122

The fact that the upstream regions within inducer blading unload at low Ψ_{sp} and high Θ is shown in figures III. 21 and III. 22, where the distributions of blade surface density, velocity and pressure in the mean annulus are given in three cases for each inducer. First, the incompressible case gives the "front loading" characteristic of inducers. Second, the $\Theta = 10$ case produces some front unloading and a density reduction on the suction side of the blade. Finally the $\Theta = 1000$ case produces more unloading and a greater suction side density reduction. Thus it appears that even though $\Psi_{sp} = 0$ in the cases of $\Theta = 10$, there was only mild cavitation due to the low vapor volume. $\Theta = 1000$ at higher Ψ_{sp} was the more severe case as evidenced by the overall performance deterioration that occurred, (see figures IV.4 and IV. 3) In all cases the essentially unchanged outlet velocities require that the blades must carry the same load. It merely shifts back farther into the inducer under cavitating conditions.

A more graphic illustration of these same two-phase effects appears in figures III. 23 and III. 24, where the portions of the machine occupied by two-phase fluid are shown in part (a). Table III. 1 shows that we probably did not compute runs A-7 and A-9 for the 6.2° inducer with sufficient streamline balancing accuracy as compared with run A-18 for the 12° inducer on this basis. This accounts for the lack of vapor in at least the mean annulus between stations 2 and 3 ($j' = 3$) in figure III. 23. The unloading phenomenon is illustrated in parts (b) of these figures in the effect that it had on the distribution of average static pressure rise in each case.

C.   CONCLUDING REMARKS ABOUT THE APPROXIMATE METHOD OF SOLUTION

The streamline balancing method of obtaining a rapid, approximate solution to single and two-phase inducer flows gives accurate numerical results even when only three annuli (four streamlines) are used for the calculations. It is a way of quickly judging or grading an inducer to determine whether the more detailed and lengthy analysis by the exact method is merited. (An exact description of the flow can be obtained only by this latter method, and by using a sufficiently fine grid.)

In this approach we employed assumptions that appear to be justified for typical inducers, but which may cause some inaccuracies. These are the omission of the meridional streamline curvature and blade force effects and of the upstream and downstream flow regions; the restriction of flow to concentric annuli; and the blade-to-blade analysis assumptions (Section III. A. 4). Results for incompressible flow are in accordance with known data where the same assumptions are used, (e. g. , reference 6).

Results for two-phase flow are qualitatively correct; and they demonstrate the ability of the method to describe the blade loading shifts that occur at low NPSH. The loss factors appear to be weak, because these two-phase effects did not cause sufficient pressure rise deterioration as compared to that of tests. For example, the comparison of our 12° variable-lead inducer with the NASA 12° constant lead one in Figure III. 16 shows greater loss at the blade tips of the latter, which yielded lower efficiency than we obtained on our somewhat similar configuration. However, empirical adjustment of these factors could be used to offset any inadequacies, since the loss mechanisms

appear to give qualitatively good results. (It might also be necessary to concentrate one of the annuli near the shroud to produce two-phase performance deterioration.) In the following section, we discuss this possibility of loss factor adjustment as we use these results in the analysis of performance and design requirements.

The Fortran IV listings for this method currently include a blade coordinate subroutine for radial-element, variable-lead blades. These listings together with other computational details including running time estimates appear in Appendix D.

SECTION IV

INFLUENCE OF FLUID PHENOMENA ON THE
PERFORMANCE AND DESIGN OF INDUCERS

In the foregoing sections we presented solutions of inducer flows using analytical methods. These included a model for real fluid effects that can be changed in accordance with experimental evidence without too much difficulty. In this section we review the results of those and other solutions that include these effects to determine the capabilities of our model for predicting performance and optimizing designs. Since an inducer generally experiences some two-phase flow and losses, we will first examine specific properties of our relations (I. 7) and (I. 13) for describing these phenomena, (Section IV. A). Then in Section IV. B, we will summarize our predictions of overall performance and their correlations with recent theories for scale or fluid thermal effects. This is followed by resulting observations about design optimization, (Section IV. C).

A.   CHARACTERISTICS OF EQUILIBRIUM TWO-PHASE FLOW AND LOSS MODEL

1.   Two Phase Flow at Inducer Inlet

A homogeneous two-phase or single-phase flow in thermodynamic equilibrium is implied by equations (I. 7) and (I. 13). Combined with various forms of the momentum and continuity laws, these relations enable us to analyze situations from three-dimensional inducer motion to one-dimensional duct flow (reference 8, p. 4-54).

Of particular interest is the fluid state for vaporizing flow at the inducer inlet. This information is required for the boundary conditions of the analytical methods of solution, (Section II and III). Also, if such an upstream two-phase condition does exist, we need this to determine the proper design blade angles at inlet. In fact, Adams (reference 32) uses equilibrium vaporization theory to explain his test results of lifting boiling fluid in a pump inlet line.

Accordingly, equation (I. 7) and (I. 13) are used with continuity and the streamline momentum equation for a one-dimensional analysis of the upstream duct flow. The latter equation in the absolute frame is (cf. equation I. 12)

$$- \frac{g_o \, dp}{\rho} = VdV + F \tag{IV. 1}$$

A special case is the essentially lossless acceleration that occurs in a machine having a converging inlet duct. Here, the density is

125

expressed in terms of the velocity as follows:

$$\rho = \rho_f \sqrt{\dfrac{1}{\dfrac{B}{g_o}\,(V^2 - V_{sat}^2) + 1}} \qquad\text{(IV. 2)}$$

or in terms of the corresponding dimensionless parameters for inducers,

$$\dfrac{\rho}{\rho_f} \equiv \hat\rho = \sqrt{\dfrac{1}{\Theta\,(\emptyset_1^2 - \hat V_{sat}^2) + 1}} \qquad\text{(IV. 3)}$$

where V_{sat} is the velocity at the saturated liquid condition. Note that V_{sat} is zero if the inducer is sucking boiling liquid from a tank. We used this equation to calculate the two-phase inlet densities and pressure for our zero-NPSH runs A-6 and A-15 (table III. 1).

Corresponding to $\left(\dfrac{\rho}{\rho_f}\right)$ are the volume ratio of vapor-to-liquid for the mixture $\left(\dfrac{V}{L}\right)$ and the ratio of the two-phase inlet flow coefficient to that which would exist for liquid at the same mass flow rate $\emptyset_1/\emptyset_{1,f}$, (equation I. 7):

$$\left(\dfrac{V}{L}\right) = \dfrac{1}{\rho/\rho_f} - 1 = T^*\,(p_{sat} - p) \qquad\text{(IV. 4)}$$

and

$$\dfrac{V_1}{V_{1,f}} = \dfrac{\emptyset_1}{\emptyset_{1,f}} = \dfrac{1}{(\rho/\rho_f)_1} \qquad\text{(IV. 5)}$$

Aside from considerations of whether a given inducer can pump fluid with a high inlet (V/L); we see from equation IV. 5 that when it pumps liquid at inlet, i. e., $(V/L)_1 = 0$, an excessive incidence angle between liquid and blade would result with a machine designed to handle the same mass flow rate at such high $(V/L)_1$. To illustrate this fact, figure IV. 1 shows plots of the preceding three equations for various values of the vaporization parameter Θ defined by equation (III. 36).

In all this work we must remember that the barotropic state relation (I. 7) for two-phase motion is good only for low mixture quality x, where
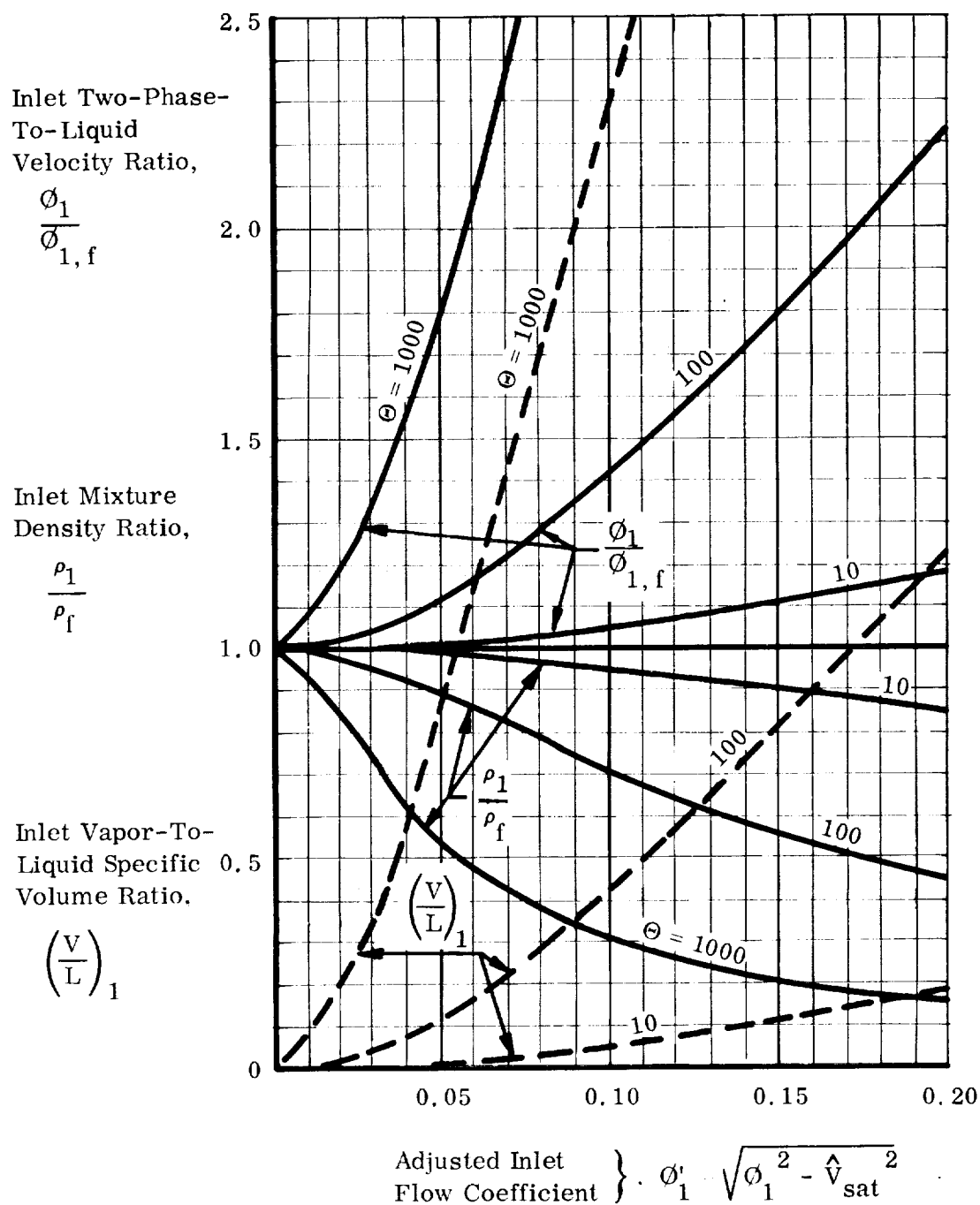
FIGURE IV.1. HOMOGENEOUS, TWO-PHASE FLUID STATE AT INDUCER INLET. Effect of the vaporization parameter Θ is shown for lossless acceleration from boiling liquid (sat) condition.

127

$$x = \left(\frac{ds_f}{dp} \cdot \frac{1}{s_{fg}}\right)(p_{sat} - p) = \left(\frac{T^*}{\frac{\rho_f}{\rho_g} - 1}\right)_{sat} (p_{sat} - p) = \frac{\Theta}{\left(\frac{\rho_f}{\rho_g} - 1\right)_{sat}} \Delta \hat{p}_V \qquad \text{(IV. 6)}$$

and the dimensionless suppression pressure is

$$\Delta \hat{p}_V \equiv \frac{g_o}{\rho_f}\ (p_{sat} - p) \qquad \text{(IV. 7)}$$

We note further that the dimensionless form of the state equation (I. 7) is

$$\hat{\rho} \equiv \frac{\rho}{\rho_f} = \frac{1}{1 + \Theta \Delta \hat{p}_V} \qquad \text{(IV. 8)}$$

For most cases involving this kind of flow, x is small for the minimum values of $\hat{\rho}$ encountered, and this relation is an adequate representation of the equilibrium model. For example, in liquid hydrogen at 36°F, (reference 19)

$$\frac{B}{g_o} = \left(\frac{\rho_f T^*}{g_o}\right) = .0002 \ \frac{\sec^2}{ft^2}$$

$$\rho_f/\rho_g = 52.8$$

By selecting the values in equation IV. 8 that give minimum $\hat{\rho}$, (and therefore maximum x), we have

$$\Theta \ \left(= \frac{B}{g_o}\ U_{t,1}^2\right) = 40$$

$$\Delta \hat{p}_V = .1$$

We obtain from equations (IV. 4,6, 8), using ρ_f / ρ_g from reference 19

$$x = .077$$
$$\rho/\rho_f = .2$$
$$V/L \ (= \Theta \Delta \hat{p}_V) = 4$$

For most fluids, T^* is roughly proportional to ρ_f/ρ_g; so, we conclude from equation IV. 6 that this value of x is typical of that obtained for the largest

concentrations of vapor in inducers. Since $\Delta \hat{p}_v$ is quite large, (compared with the inducer head-rise coefficient Ψ — similarly defined in equation III. 33), and since this example is for a high inducer inlet tip speed, viz., $U_{t,1}$ = 447 ft/sec., our barotropic relation (I. 7) or (IV. 8) should be applicable in most cases. (Refer to the barotropicity dicussion in Section I. A. 1).

2. Discussion of Losses

A good prediction of equilibrium two-phase and liquid flow within an inducer depends on the accuracy of the factors and methods for evaluating losses, as well as the equation of state. Besides blade tip leakage, two types of loss can be distinguished, (equation I. 13); viz., skin friction or Reynolds-number-dependent losses, and diffusion or inertial losses. For friction losses we are using an empirical relation (equation I. 14) for smooth pipes to express the friction factor f. This loss also depends on the local hydraulic diameter of the channel which is assumed constant for all annuli at a given station. A correction to this is probably necessary to account for the additional skin friction arising from the secondary flow caused by blade-to-blade pressure differences. But secondary flow losses might be conveniently described by an appropriate adjustment of the diffusion loss factor.

A good diffusion description is especially important for inducers with two-phase flow, since the sudden disappearance of vapor that can occur probably results in a dumping of at least part of the accompanying change in relative velocity head (references 32 and 33). This sudden diffusion head loss, (see equation I. 13), from station j to j + 1 in the inducer may be given by

$$H_{L,d} = \zeta \left(\frac{W_j^2 - W_{j+1}^2}{2g_o} \right) \tag{IV-9}$$

where $W_{j+1} < W_j$. In our model we expressed ζ as a function of the ratio W_{j+1}/W_j (equation I. 15), making it possible for us to describe only a discontinuous change of W. If the factor ζ is to include separation losses that occur over some finite distance, we would need to modify this function (equation I. 15) in one or more of the following ways: (a) limit the number stations j; (b) increase the strength of ζ; (c) make ζ a constant that is independent of W; or (d) make ζ dependent on the diffusion factor D. A measure of the overall blade loading, (see definition on page 153 of reference 33), the distribution of D would first need to be estimated from a preliminary solution or one-dimensional analysis of the machine.

As a result of our inducer solutions with loss, it appears that some combination of (a), (b) and (c) would give better answers and could be easily

included in the analysis. It is interesting to note the types of these inertial losses that can occur and the attendant values of ζ. For this purpose, a more general expression of equation (I.15) would be

$$\zeta = \zeta_c + \frac{1 - \dfrac{W_{j+1}}{W_j}}{1 - \zeta' \dfrac{W_{j+1}}{W_j}} \qquad \text{(IV. 10)}$$

where in our analysis we chose $\zeta_c = 0$ and $\zeta' = -1$, (see equation I.15), and where

$$\zeta \equiv \frac{H_{L,d}}{(W_j^2 - W_{j+1})/(2g_o)} = \text{(incompressibly)} \frac{\left[(p_j - p_{j+1})/\rho\right] + \left[(W_j^2 - W_{j+1}^2)/(2g_o)\right]}{(W_j^2 - W_{j+1}^2)/(2g_o)}$$

Now, applying the momentum equation incompressibly and one-dimensionally with $\zeta_c = 0$, one obtains $\zeta' = -1$ for symmetrical sudden diffusion (no turning) - the Borda-Carnot loss, which would appear to be a minimum sudden diffusion loss. On the other hand the largest loss would be for $\zeta' = \zeta = 1$, which probably occurs for a flow that suddenly diffuses while making a sharp 90° turn. (Such a turn usually causes an additional head loss of some fraction of $W_j^2/2g_o$ due to separation and secondary flow.) Figure IV.2 shows the results for a variation of ζ' between these extremes. Using e.g., $\zeta' = 1/2$ (instead of the weaker $\zeta' = -1$ that we used in our analysis) might suffice for any discontinuous velocity change such as that due to inlet incidence or to bubble collapse, (reference 34 and 35). ζ_c could be made to depend on the rate of velocity decrease with distance. This would account for diffusion in a continuous velocity field and could eliminate the need for the other term in equation (IV.10).

To account for tip leakage loss the complete loss equation (I.13) might need an additive term $t_l W^2/2$, where t_l would be a function of clearance, of blade-to-blade pressure difference and of position (as with D_h) such that this loss is greatest in the tip region or any other region as required. This could also account for secondary flow losses that would not be covered by equation (IV.10) as just discussed.

These and other modifications to the portions of the analytical programs where losses are calculated are needed, particularly to improve our description of the cavitation head breakdown process.

Several investigators have done work that gives insight into this head breakdown problem. The concept of a cavity on part of the suction side of the blade that causes a sudden diffusion loss downstream was introduced by Stripling and Acosta (reference 34 and 35). Our model suggests the

130

Configuration (a)

Diffusion
Loss
Factor ζ

($\zeta_c = 0$)

ζ' = +1

.9

Configuration (b)

ζ' = -1

1/2

0

Ratio of Downstream
to Upstream Relative
Velocities

$\dfrac{W_{j+1}}{W_j}$

W_j

p_j

W_{j+1}

j + 1

$(p_j - p_{j+1}) = 0$

W_j

p_j

j

j+1

p_{j+1}

W_{j+1}

$(p_j - p_{j+1}) = \dfrac{\rho W_{j+1}}{g_o} (W_{j+1} - W_j)$

Configuration (a)

Diffusion in Sharp 90° Turn

Configuration (b)

Symmetrical Sudden Diffusion

(Borda-Carnot Loss)
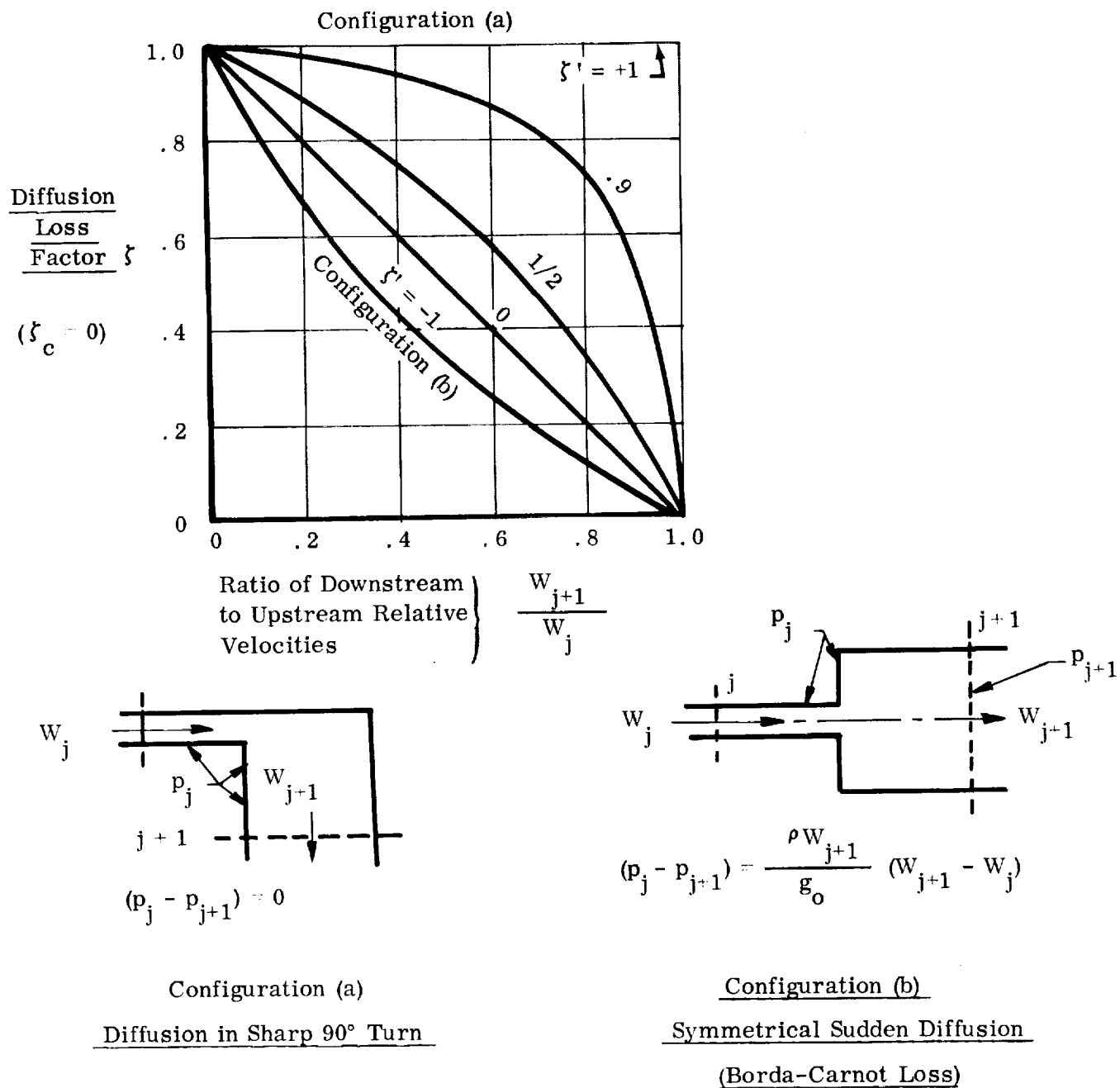
FIGURE IV. 2. SUDDEN DIFFUSION LOSS FACTOR, ζ. For discontinuous relative
velocity changes. Also applicable to continuous changes where appropriate spacing
of stations j in a finite difference calculation scheme is employed.
(See Equations IV. 9 and IV. 10).

131

presence of such a cavity by yielding a low density in that region (see figures III. 21 and 22). The shock theory of Jakobsen (reference 36) combined the cavity analysis with thermal concepts and could be used to advantage in improving the loss descriptions in our three-dimensional programs. Two-phase sonic velocities (reference 37) can be very low, and the attendant mass-flow limiting process should occur, (reference 38 and reference 8, p. 4-55). Our model does produce choking if a solution at too low a NPSH is attempted, and this is discussed in the following section.

B. PERFORMANCE AND SCALE EFFECTS WITH TWO-PHASE FLOW

1. Low-NPSH Tests of Inducers by the Analytical Program

We made a series of solutions with the approximate analysis program, which includes unmodified loss relations (equations I. 13, 14, 15) to determine the net positive suction head requirements of the two sample inducers, (figures II. 12 and II. 18). All these analytical runs were made at the same values of flow coefficient $\emptyset_1$, stated in table III. 1 for the respective inducers. However two runs, A-6 and A-15, had negative values of cavitation number k at inlet and therefore had two-phase flow upstream of the blading. The liquid flow coefficient $\emptyset_{1,f}$ was therefore lower than $\emptyset_1$ for these two cases only (see footnotes to table III. 1), both of which used $\Theta = 10$. For the other data, we conducted three series of runs at $\Theta = 10$, 40, and 1000 respectively on each inducer. In each series we started at high NPSH, where the dimensionless form Ψ_s is given by

$$\Psi_s \equiv \frac{g_o \, (\text{NPSH})}{U_{t,1}{}^2} = \Psi_{sp} + \frac{\emptyset_1{}^2}{2} \quad , \quad (\, \Psi_{sp} \geq 0) \tag{IV. 11}$$

and we lowered Ψ_{sp} until no solution could be obtained (choked flow), or until $\Psi_{sp} = 0$, (table III. 1). Table III. 1 lists only those two-phase solutions that were obtained for the lowest possible Ψ_{sp}.

Figures IV. 3 and IV. 4 show the kind of pressure-rise-deterioration curves that we obtained, starting with the value of Ψ_{sp} required to prevent cavitation entirely and ending with the value for which no solution was obtainable — except in the case of $\Theta = 10$, where solutions for $\Psi_{sp} = 0$ did exist. For comparison, actual cold water $(\Theta \approx 1,000,000)$ test results of a NASA 12° constant-lead inducer are also shown in figure IV. 4, (reference 31, p. 47). Even though this reference inducer is somewhat different from our 12° machine, the results indicate that our analytical model reasonably predicts the choked-flow or zero-performance condition. However, our curves have sharp breaks and therefore do not yield the

132

Run No.	Vaporization Parameter Θ	Reynolds No. R_m	Flow Coefficient $\emptyset_{1,f}$	Key
A-7	10	2.5×10^7	0.083	○
A-4, A-8	40	5.0×10^7	0.083	□
A-5, A-9	1000	2.5×10^7	0.083	△
A-6	10	2.5×10^7	0.080	◇

TABLE III. 1 Gives Additional Data for Points Identified by Run Numbers

Cavitation Coefficient, $\Psi_{sp} = \left(\bar{p}_1 - p_{sat}\right)\Big/\left(\frac{\rho_f}{g_o} U_{t,1}^2\right)$

Cavitation Number, $k \equiv \left(\bar{p}_1 - p_{sat}\right)\Big/\left[\left(\rho_f U_{t,1}^2/2g_o\right)\left(1 + \emptyset_{1,f}^2\right)\right]$

Suction Specific Speed, $S \equiv N\sqrt{Q_f}\Big/\left(g_o \, NPSH\right)^{3/4}$
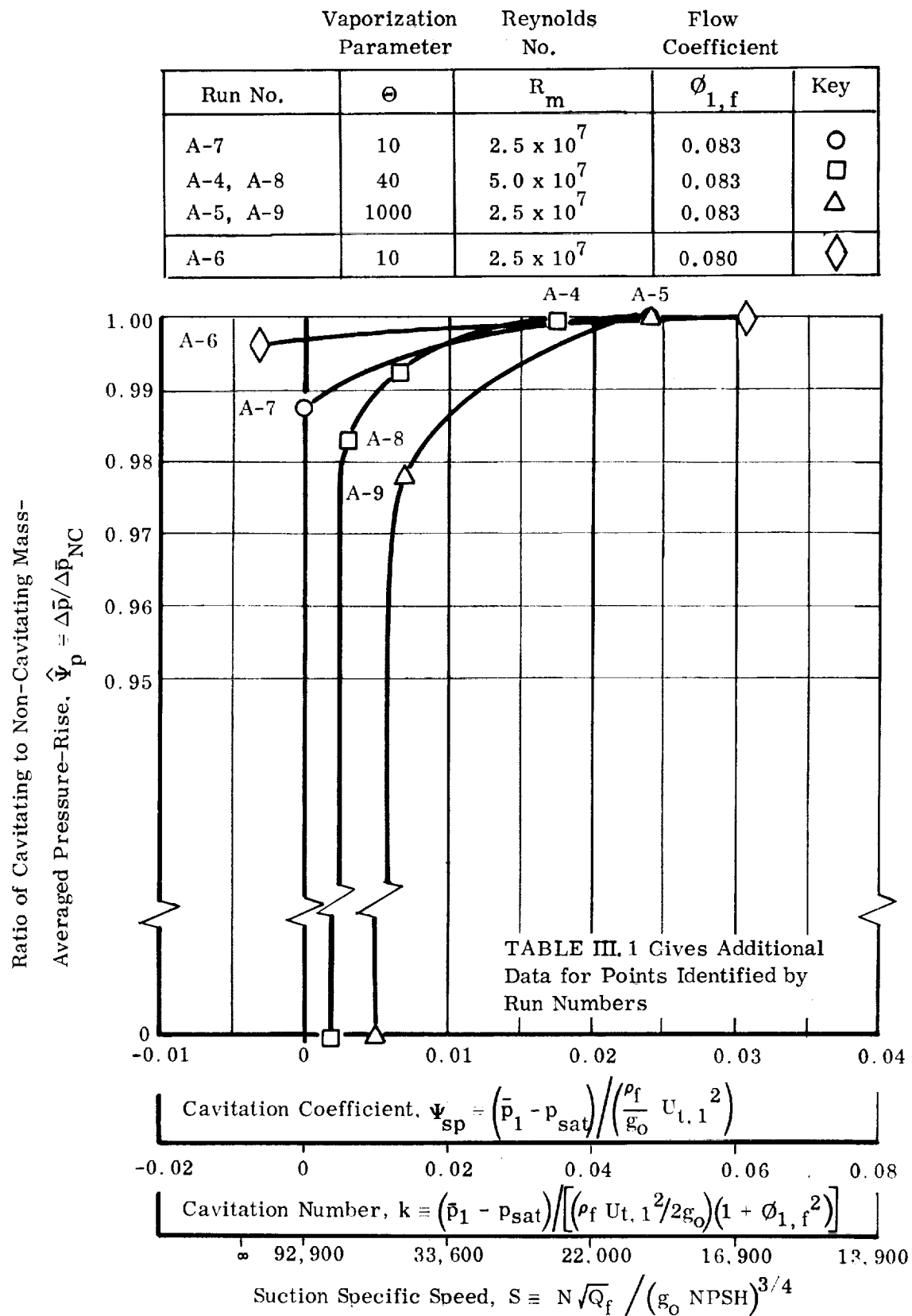
FIGURE IV. 3.   EFFECTS OF CAVITATION AND VAPORIZATION PARAMETERS ON COMPUTED MASS-AVERAGED PRESSURE RISE OF 6. 2° INDUCER. Minimum possible values of cavitation coefficient for incompressible operation are shown for $\Delta\bar{p}/\Delta\bar{p}_{NC}$ 1.

133

Run No.	Vaporization Parameter Θ	Reynolds No. R_m	Flow Coefficient $\emptyset_{1,f}$	KEY
A-14, A-16	10	2.5×10^7	0.1763	○
A-17	40	5.0×10^7	0.1763	□
A-13, A-18	1000	2.5×10^7	0.1763	△
A-15	10	2.5×10^7	0.1540	◇
NASA Tests (Ref. 31)	1,000,000	4.0×10^6	0.14	- - -

Ratio of Cavitating to Non-Cavitating Mass-Averaged Pressure Rise $\hat{\Psi}_p = \dfrac{\overline{\Delta p}}{\overline{\Delta p}_{NC}}$

TABLE III.1 gives additional data for points identified by run numbers.

Cavitation Coefficient, $\Psi_{sp} \equiv \left(\overline{p}_i - p_{sat}\right)\Big/\left(\rho_f/g_o \, U_{t,1}^2\right)$

Cavitation Coefficient, $k = \left(\overline{p}_1 - p_{sat}\right)\Big/\left[\left(\dfrac{\rho_f U_{t,1}}{2\,g_o}\right)\left(1 + \emptyset_{1,f}^2\right)\right]$

Suction Specific Speeds, $S \equiv N\sqrt{Q_f}\Big/ (g_o \, NPSH)^{3/4}$
(S given for $\emptyset \simeq 0.173$, but error is small for other $\emptyset$)
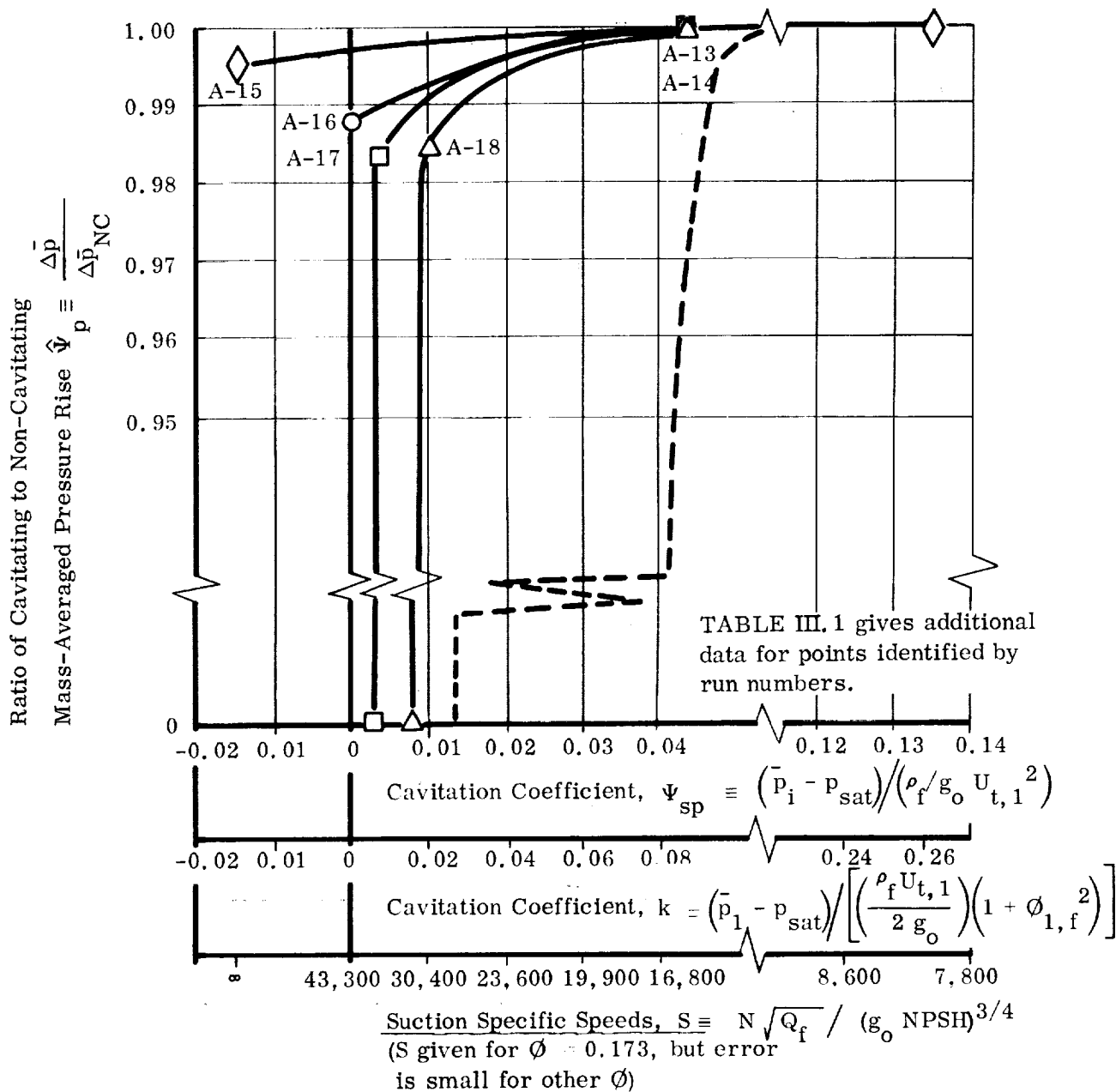
FIGURE IV.4. EFFECTS OF CAVITATION AND VAPORIZATION PARAMETERS ON COMPUTED MASS-AVERAGED PRESSURE RISE OF 12° INDUCER.
Minimum possible values of cavitation coefficient for incompressible operation are shown for $\Delta\overline{p}/\Delta\overline{p}_{NC} = 1$

134

the gradual decay of pressure rise with decreasing Ψ_{sp} evidenced by actual tests. This means that modifications to the loss factors and the annulus positioning as inlet, as discussed in the foregoing section, are probably necessary to extend the two-phase regions farther into the inducers and to describe more accurately the losses due to bubble collapse, i. e. the sudden disappearance of these regions, as illustrated in figures III. 23 and III. 24.

Such adjustments could also serve as a substitute for any lack of barotropicity. Specifically, in the discussion of Section I. A. 1 we spoke of the rise of vapor pressure of the liquid due to losses. If such a rise occurs before all vapor is condensed by the rising inducer pressure, the domain and effects of the remaining vapor could be significantly increased. A stronger friction loss factor than that of equation (I. 14) might artificially reproduce this by retarding the rise of inducer pressure by the slight amount of the simulated vapor pressure change.

Table IV. 1 shows dimensional examples to which these analytical performance results apply. According to our equilibrium theory, then, liquid hydrogen can be pumped at 224 ft. per sec. inlet blade tip speed in typical inducers at zero cavitation number. Doubling the tip speed makes $\Theta = 40$; and, as equation (IV. 8) shows, this causes more vapor at a given pressure drop coefficient in the blading, preventing a solution at $k = 0$.

2. Theory of Fluid and Scale Effects

The complete inducer analysis that we employ to find the NPSH limits actually contains the explicit relationship, however complicated, between the independent dimensionless parameters, R_m, Ψ_{sp} and Θ that determine the performance Ψ, (expressed by the functional equation III. 32). However, we should try to discern in these and other results a simpler, underlying theory for these fluid and scale effects; especially the influence of Ψ_{sp} and Θ. We might then be able to determine the important inducer design factors.

Specifically we are interested in how to predict the NPSH requirements for various fluids and sizes of a given geometry for a fixed flow coefficient $\emptyset_{1,f}$. Therefore, we require the minimum value of the NPSH parameter Ψ_s for which stable inducer performance is possible or for which the head coefficient Ψ is some reasonably high percentage of the noncavitating value Ψ_{NC}, (i. e. the value of no Ψ_s and Θ influence). If Reynolds number effects are small compared to those of fluid vaporization, the functional equation (III. 32) reduces for these purposes to

$$\left(\frac{\Psi}{\Psi_{NC}}\right)_{REQ'D} = \text{Constant} = \left(\frac{\Psi}{\Psi_{NC}}\right)_{REQ'D} \left(\Psi_{s,\,min},\,\Theta\right) \qquad (IV. 12)$$

135

TABLE IV.1

DIMENSIONAL EXAMPLES OF SAMPLE INDUCERS

For inducers having same geometry as in Figure II.12 of II.18

Dimensionless Parameters of Solution		Consistent Set of Dimensional Conditions to Which Solution Applies			
Vaporization Parameter	Machine Reynolds Number	Liquid and Temp.	Inlet Tip Dia. *	Rotative Speed*	Blade Tip Speed at Inlet
Θ	R_m		$D_{t,1}$ (Inches)	N (rpm)	$U_{t,1}$ (ft/sec.)
10	2.5×10^7	Hydrogen @ 36°R	5.37	9,550	224
40	5.0×10^7	Hydrogen @ 36°R	5.37	19,100	447
1000	2.5×10^7	Water @ 267°F	6.00	9,550	250

*NOTE: The only parameter that is directly connected with the inlet diameter $D_{t,1}$ or the speed N is the machine Reynolds number. For the usual range of sizes, R_m appears to have a small effect; so, the important limitation for equilibrium two-phase flow is not $D_{t,1}$ or N, but their product, the tip speed

$$U_{t,1} = \Omega r_{t,1} = \pi D_{t,1} N$$

which is connected with the cavitation and vaporization parameters; (see Table III.1).

136

or

$$\Psi_{s,\,min} = \Psi_{s,\,min}(\Theta) \tag{IV.13}$$

Because $\emptyset_{1,f}$ is fixed in this problem, we could substitute either k_{min} or S_{max} for $\Psi_{s,\,min}$, where dimensionless relations between them (see equations III.34, 35, 37, 38 and IV.11) are

$$k = \frac{2\,\Psi_{sp}}{1 + \emptyset_{1,f}^2} \tag{IV.14}$$

and

$$S \equiv \frac{N\sqrt{Q_f}}{(g_o NPSH)^{3/4}} = \frac{\sqrt{\emptyset_{1,f}\,\dfrac{A_1}{\pi\,r_{t,1}2}}}{2\sqrt{\pi}\,(\Psi_s)^{3/4}} \tag{IV.15}$$

When applied to axial inducer inlets where $A_1 = \pi r_{t,1}^2 (1 - \xi_1^2)$, this general form for the suction specific speed becomes

$$S = \frac{\sqrt{\emptyset_{1,f}\,(1 - \xi_1^2)}}{2\sqrt{\pi}\,(\Psi_s)^{3/4}} \tag{IV.16}$$

Thus we are looking for the following function, (equivalent to equation IV.13):

$$S_{max} = S_{max}(\Theta)_{\emptyset_{1,f}} \tag{IV.17}$$

or, dimensionally:

$$NPSH_{min} = NPSH_{min}(B)_{Q_f} \tag{IV.18}$$

Investigators have found empirical correlations that tend to support the validity of the equilibrium equation (IV.18). Stahl and Stepanoff (reference 13 and 14) first proposed a remarkably simple theory for that relationship, also presenting their results. The basis of this theory is that the breakdown of head rise under cavitating conditions is caused by a performance average vapor-to-liquid volume ratio $(V/L)_p$. Salemann's observations (reference 17) lend more support to this idea; and so does the work of Spraker, who also defines the thermodynamic constant $(B = \rho_f T^*)$ so that the relative vaporization characteristics of various fluids can be easily identified. For

137
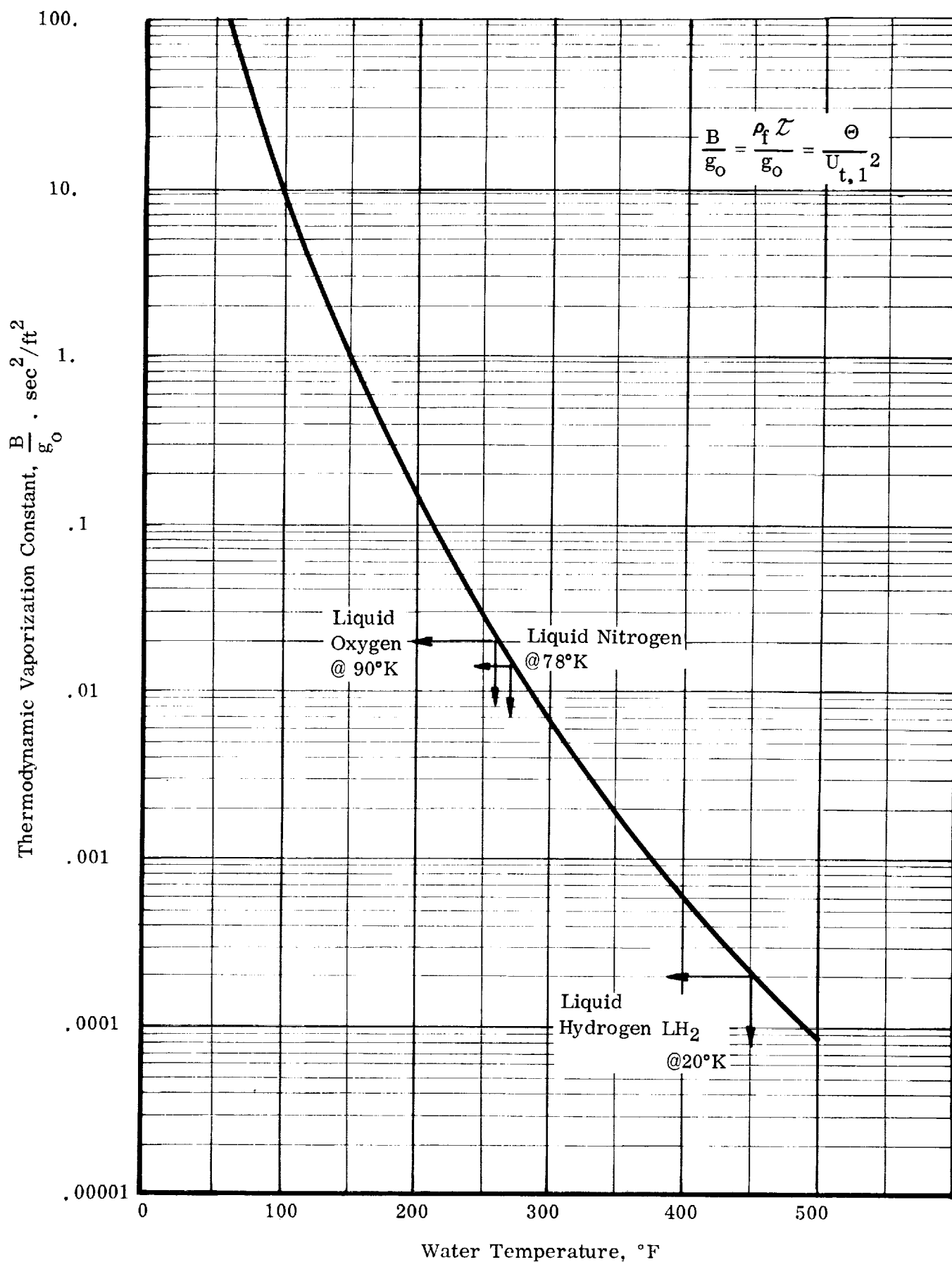
FIGURE IV. 5.   FLUID THERMODYNAMIC VAPORIZATION CONSTANT FOR WATER.
THE EFFECT OF TEMPERATURE IS SHOWN. Water corresponds to some other
fluids in the values of this constant at the temperatures shown.

example, figure IV. 5 shows the variation with temperature of the equilibrium thermodynamic vaporization constant $\frac{B}{g_0} \equiv \frac{\rho_f T^*}{g_0}$ for water. Values for some other liquids are shown, indicating the temperatures at which water has similar vaporization properties. The parameter $(V/L)_p$, which connects B and $NPSH_{min}$ varies with geometry and flow coefficient. Our model uses T^* in the detailed flow calculations, but $(V/L)_p$ is an average that must be found empirically. We can attempt this with the performance results of our analytical solutions as with test data.

Figure IV. 6 illustrates the usual empirical method of finding the constant $(V/L)_p$, which is assumed to exist when sufficient choking occurs to cause the inducer pressure-rise $\Delta \bar{p}$ to deteriorate appreciably from its corresponding non-cavitating value $\Delta \bar{p}_{NC}$. We make the evaluation when $\hat{\Psi}_p \equiv \frac{\Delta \bar{p}}{\Delta \bar{p}_{NC}}$ reaches the minimum critical value that still insures reliable, stable operation of the machine. This need not be interpreted as requiring uniform $\hat{\Psi}_p$ in all cases — even with the same geometry and flow coefficient; although equation (IV. 12) and figure IV. 6 conveniently show it that way. TSH is the difference between the values of $NPSH_{min}$ for fluids having respectively infinite and finite values of B.

The physical significance of B can be seen from its effect on V/L through equations I. 7, 8 and IV. 4. Infinite B leads to infinite vapor volume (for any depression of static pressure below vapor pressure) and the essentially direct effect that V/L has on head breakdown. Accordingly, zero B means that vaporization produces no effect on performance.

The theory that connects $NPSH_{min}$ and B can now be stated emplicitly by referring to equation (IV. 4) which defines V/L:

$$(NPSH_{min, \ B \to \infty} - NPSH_{min, B}) = \frac{\left(\frac{V}{L}\right)_p}{B} \tag{IV. 19}$$

where $B \to \infty$ is approximated, e. g. , by cold water, (figure IV. 5). This is the explicit relation suggested by equation (IV. 18), and it can be similarly written as

$$TSH = \frac{\left(\frac{V}{L}\right)_p}{B} \tag{IV. 20}$$
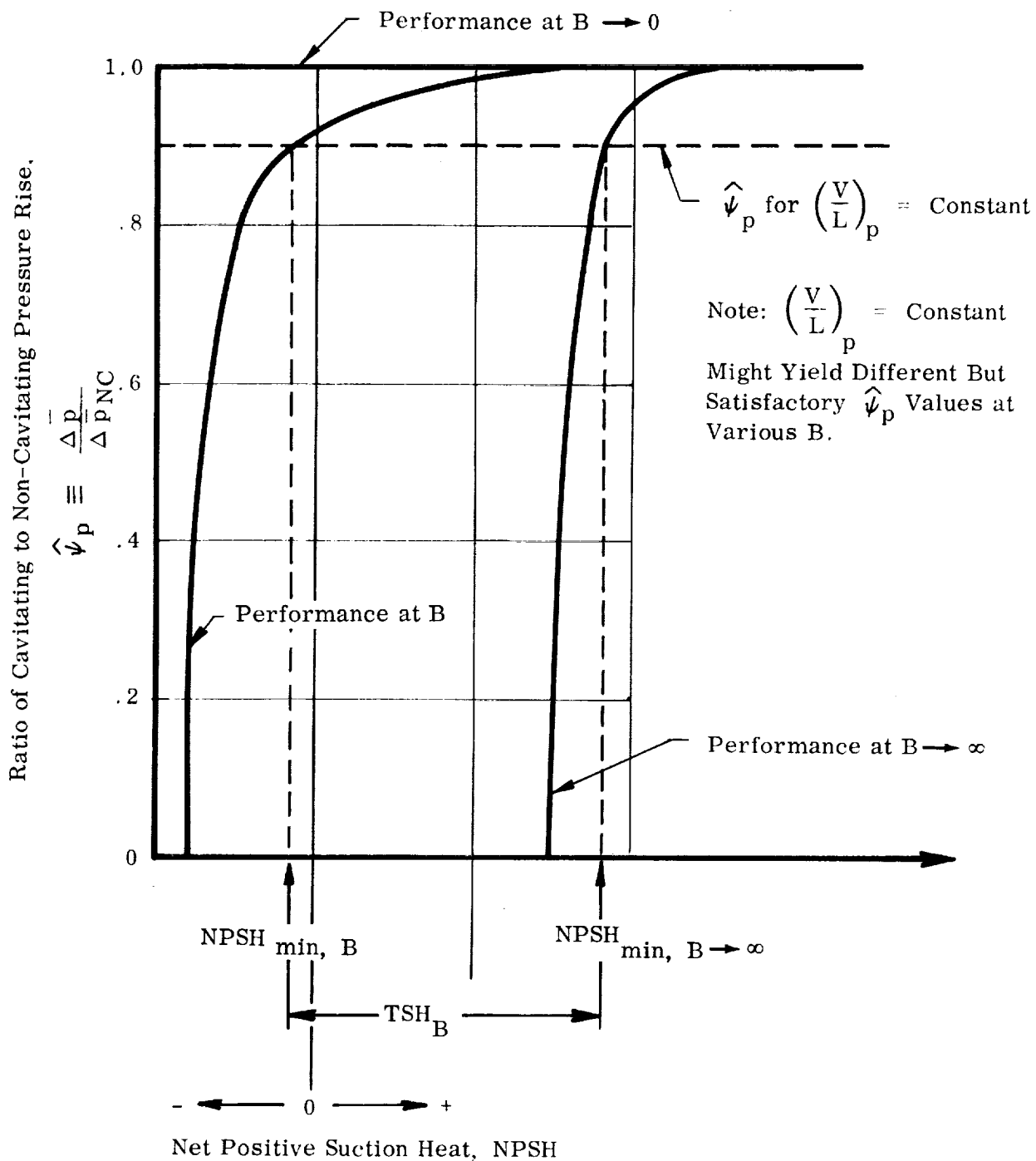
FIGURE IV.6. NET POSITIVE SUCTION HEAD REQUIREMENTS FOR
INDUCERS. The influence of the thermodynamic vaporization
constant B is shown.

or dimensionlessly as

$$(\Psi_{s,\,min,\,\Theta\to\infty} - \Psi_{s,\,min,\,\Theta}) = \frac{\left(\frac{V}{L}\right)_p}{\Theta} \tag{IV.21}$$

In terms of S this becomes, (noting equation IV.17, and using equation IV.16).

$$S_{max,\,\Theta} = \frac{S_{max,\,\Theta\to\infty}}{\left\{1 - \frac{\left(2\,S_{max,\,\Theta\to\infty}\right)^{4/3}\left(\frac{V}{L}\right)_p}{\left[\frac{\varnothing_{1,f}}{\pi}\left(1 - \xi_1^2\right)\right]^{2/3}\,\Theta}\right\}^{3/4}} \tag{IV.22}$$

3. Analysis of Results

Our analytical tests of two inducers for $NPSH_{min}$ can be empirically examined using of these equivalent relations, say equation (IV.22). We have three data points at constant $\varnothing_{1,f}$ (table III.1) for each inducer, viz. runs A-7, 8, 9 and A-16, 17, 18 respectively; but only the latter two points of each set yielded flows sufficiently close to choking for us to be able to say that S_{max} existed, (see figures IV.3 and IV.4). Taking the corresponding values of S_{max} and Θ of these two points, we solved the two resulting equations (IV.22) for $\left(\frac{V}{L}\right)_p$ and $S_{max,\,\Theta\to\infty}$ for each geometry. Furthermore, the type of fluid that yields infinite suction specific speed is now related to the latter (cold water) S_{max}:

$$\Theta_{S_{max\to\infty}} = \left(\frac{V}{L}\right)_p \frac{\left(2\,S_{max,\,\Theta\to\infty}\right)^{4/3}}{\left[\frac{\varnothing_{1,f}}{\pi}\left(1 - \xi_1^2\right)\right]^{2/3}} \tag{IV.23}$$

If this value of $\left(\frac{V}{L}\right)_p$ does produce similar head-rise performance for all Θ, we may plot S_{max} versus Θ using equation (IV.22). Figure IV.7 shows the results.

Whether similar analytical, critical performance points for other values of Θ would lie on the appropriate curves of figure IV.7 remains to be proven. Even though runs A-7 and A-16 had less-than-critical cavitating head-rise deterioration, (see figures III.21 to 24 and IV.3, 4), they are shown there for reference only. Observe that $S_{max,\,\Theta\to\infty}$ (cold water S_{max}) is considerably greater than that for which two-phase activity begins (as shown in figures IV.3, 4), since inducers and pumps are always cavitating when performing at S_{max} conditions. Also $\Theta = 1000$ gives nearly

141

the same S_{max} as at $\Theta \to \infty$. Finally, the 12° inducer has the greater $(V/L)_p$ capability, which could be attributed to the larger amount of the inlet fluid relative incidence i not compensated by blade thickness. Note that computations were made for faired blades, (figures II. 12, 18), which in both inducers would have taken 0.64° of the incidence had full thickness existed at inlet; i.e., all incidence in excess of this blockage amount then causes leading edge blade loading and the attendant flow adjustments to the internal two-phase activity.

A well-known experimental fact, the evident $(V/L)_p$ capability of this blade fairing is illustrated by the two-phase no-loss run E-9 of the exact analysis method (table II. 1). Here, the presently unadjusted upstream stagnation stream surfaces are set at the relative flow angle (i = 0), and the light load taken by them — as they now act like faired blades — nearly eliminates two-phase activity within the blading itself, (figures II. 28 and 29). This "additional blading" enabled us to obtain that solution with a lower NPSH ($\Psi_{sp} = 0$ at $\Theta = 40$) than was possible by the approximate method, which produced loading only on the actual blading.

To the extent that the preceding correlations and the experimental data of references 13, 14, 17, 18 support the $(V/L)_p$ theory as the connection between S and Θ, we can propose a concluding theory about two-phase activity within inducers. The observation that two-phase flow exists at a much higher value of NPSH than the critical one suggests that two fairly distinct flow regimes exist over the NPSH range:

a) For the range

$$\text{NPSH}_{\substack{\text{incompressible} \\ \text{flow}}} > \text{NPSH} \ge \text{NPSH}_{\text{min, } \Theta \to \infty}$$

enough vapor forms to unload the inducer blades at inlet by an amount compatible with the NPSH. This prevents the far greater volume of vapor that would have choked the passage had the blade suction-side pressure-drop not been reduced by the unloading (see figures III. 21 and 22). The extent of and density distribution of the vaporous region vary with NPSH; but performance is affected only slightly, because the losses associated with these redistributions of load near the leading edge are small. Thus there are no Θ effects over this NPSH range, (figure IV. 7).

b) In the range

$$\text{NPSH}_{\text{min, } \Theta \to \infty} \ge \text{NPSH} \ge \text{NPSH}_{\text{min, } \Theta}$$

the passage is in the process of choking due to the formation of vapor which is in excess of that required to satisfactorily unload the blades. In contrast with regime (a), the flow in the leading portion of the inducer

142

is essentially one-dimensional. The additional V/L formation with diminishing NPSH is more nearly uniform across the passage and is the only V/L contributing to $(V/L)_p$. Thus the extent of this NPSH range depends on Θ (equation IV.21); and when $(V/L)_p$ is reached, the passage is sufficiently choked to produce the critical performance at $NPSH_{min}$.

Every geometry and flow-coefficient combination has the capability of handling a specific amount of this excess vapor (V/L). The results in figure IV.7 suggest that $(V/L)_p$ may be more or less directly dependent on the amount of available incidence in excess of that required for blade blockage. Thus if $i = 3°$ or $4°$ total, a typical inducer might be capable of $(V/L)_p = 0.5$. The resulting plot of equation (IV.22) using $S_{max, \Theta \to \infty} = 2$, (= 2 x 17,180 = 34,360 in "rpm-gpm-ft" units), is shown in figure IV.7. A similar curve for typical centrifugal pumps is also shown using $S_{max, \Theta \to \infty} = 1/2$ (or 8,590). Higher incidence probably leads to more vapor due to excessive loading; therefore, no further gain of $(V/L)_p$ results. Observe that if Θ is large, the magnitude of $(V/L)_p$ is of no consequence, since negligible NPSH reduction is possible in the regime (b), (equation IV.21). In this case (typical for cold water) regime (a) exists over the entire NPSH range, and regime (b) exists virtually at the point $NPSH_{min}$ only.

This theory may work empirically in the thermodynamic non-equilibrium case, provided the resulting time delay or other effects are uniform. There is no assurance that even this is true in all cases. For example, the work by Sandercock et al (reference 39) shows some improvement in performance with a Θ increase. However Θ was very high (cold water), so that in view of the foregoing discussion it should have no influence. Also, their results could be partly a Reynolds number effect. Ruggeri and Gelder have shown that considerable local departures from equilibrium are possible, (references 16, 40, 41); and Holl and Treaster have reported work in this area, (reference 42). The sudden diffusion due to incidence, other turbulent conditions, and a fairly one-dimensional two-phase motion might reduce these departures to some uniformly minimum value for inducers. If a correlation with the constant $(V/L)_p$ theory is then still possible, corresponding empirical corrections to the analytical flow model might also be possible, (section IV.A.2).

C. OPTIMIZATION OF GEOMETRY

The foregoing analysis of performance results indicates that certain important features of inducer design should be optimized with the help of the analytical programs that are available (Appendixes C and D). As observed from the data accumulated in this work, we now discuss these design features:

143

Curve No.	$\left(\dfrac{V}{L}\right)_p$	Description
1	.167	Correlation with 6.2° Inducer Runs A-8, A-9
2	.271	Correlation with 12° Inducer Runs A-17, A-18
3	.500	Estimated Performance: Typ. Inducers, $\left(\varnothing_{1,f} = .1 \dfrac{\pi r_{t,1}^2}{A_1}\right)$
4	.500	Estimated Performance: Typ. Centrifugal Pumps. $\left(\varnothing_{1,f} = .1 \dfrac{\pi r_{t,1}^2}{A_1}\right)$

Suction Specific Speed, $S = \dfrac{N\sqrt{Q_f}}{(NPSH)^{3/4}}$

$\left.\begin{array}{l} N\colon \text{ rpm} \\ Q_f\colon \text{ gpm} \\ NPSH\colon \text{ ft.''} \end{array}\right\}$

Vaporization Parameter. $\textcircled{1} = \dfrac{B}{g_o}\; U_{1,t}^2 = \dfrac{\rho_f\, T^*}{g_o}\; U_{1,t}^2$
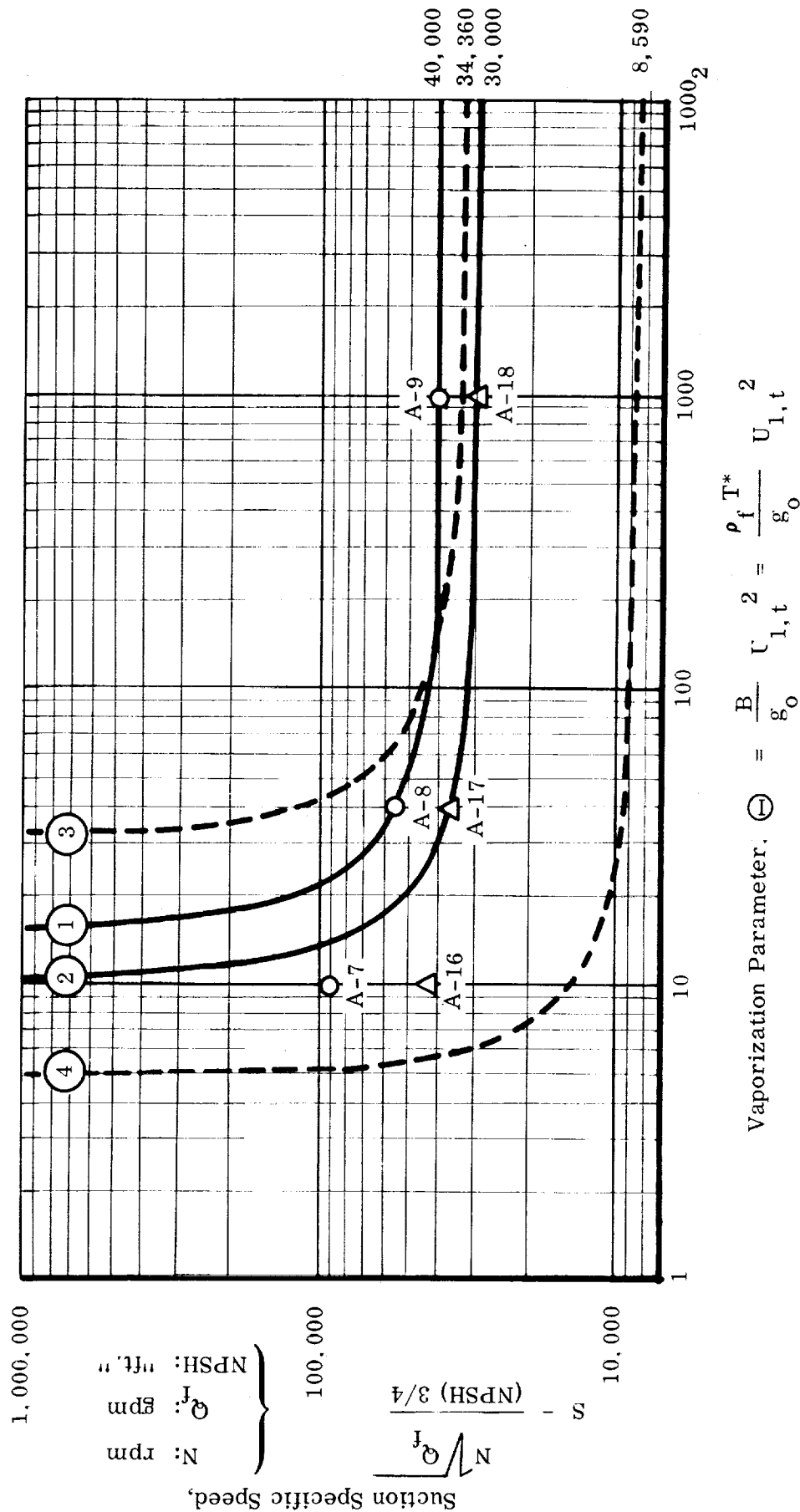
FIGURE IV.7 THEORETICAL FLUID VAPORIZATION EFFECTS ON SUCTION SPECIFIC
SPEED CAPABILITY, SHOWING THE EFFECT OF DIFFERENT GEOMETRIES AND
VALUES OF THE PERFORMANCE VAPOR-TO-LIQUID RATIO $\left(\dfrac{V}{L}\right)_p$. Note: Table III.1
gives additional data for points identified by run numbers.

144

a)   Head coefficient Ψ

If the loading is maintained light (equation IV. 24) the head coefficient in a reasonable length will not be great. However, attention to maximum possible deceleration criteria and diffusion factors are necessary to prevent loss of control of the flow, (reference 33). In the interest of restricting vapor cavities to narrow regions, relative velocity diffusion should probably be minimized while keeping losses to a minimum.

b)   Inlet tip blade angle, $\beta_{b,t,1}$

Feature (c) should lead to low blade angles throughout the inducer which are shown to be necessary in other optimizations (references 7, 34 and 35). Even with light loads, low β's are necessary. This is probably because the incidence at high blade angles for reasonable leading edge loadings is not sufficient to avoid the choking problem; i.e., $1/\beta_{flow}$ is probably closely related $(V/L)_p$ for low angles. However, two problems arise if β is too low; viz., higher losses due to the low hydraulic diameter of the resulting passage cross section, and a higher Θ with the consequent NPSH difficulties. This latter problem arises for a given fluid, mass flow rate and rotative speed, because a lower blade angle requires a higher inlet diameter and tip speed.

c)   Incidence   i

This difference between the blade and relative flow angle should be greater than that required to compensate for blade blockage. The amount of incidence should be sufficient to avoid choking the passage by vapor formation at too high a value of NPSH. Too high an incidence is undesirable because of the back flow and instability that develops especially at high NPSH, and because of vapor formation arising from the attendant loading.

d)   Solidity σ, or length m.

A large solidity or inducer length is necessary to contain the two-phase fluid in the front or leading portion of the machine. Liquid is required at exit in order to obtain the pressure rise. Also, the blade loading must be very light to prevent excessive vapor generation by reduced pressure on the suction sides of the blades. The moment of momentum relation shows both these points when expressed in the following form:

$$p_p - p_s = \frac{w}{n_b \, r \, \Omega \, b} \frac{dH_i}{dm} \qquad\qquad \text{(IV. 24)}$$

where the ideal head $H_i = UV_\theta/g_o$ and b is the blade height of the passage in which mass flow rate w exists.

The computer programs for analyzing the three-dimensional flow field are probably necessary to optimize these features successfully where two-phase flow with losses is involved. The primary object of a design so evaluated is to avoid the choking phenomenon as uniformly as possible in all sections of the inducer. The exact three-dimensional method has the capability of analyzing thermodynamic non-equilibrium cases with the appropriate changes in the loss and density expressions. If acceptable, the approximate method would be more easily adapted to this problem simply by empirical corrections to the equilibrium loss factors.

CONCLUSIONS

We have obtained solutions to the set of simultaneous differential equations and boundary conditions required for a general continuum description of single and two-phase three-dimensional flow with losses in turbo-pump inducers. Because of this generality, both the exact and approximate methods of solution that we developed are also applicable to other turbomachines. Although we used a thermodynamic equilibrium model with empirical loss factors to account for the two-phase and loss effects, this feature of the analysis is purposely subject to change without destroying the basic system of equations or mathematical iterations.

The exact three-dimensional method of solution successfully employed the total residual relaxation concept for the simultaneous finite difference solution of four non-linear differential equations and the attendant boundary conditions and additional fluid equations. We obtained results for nine runs without losses, and the concluding remarks at the end of Section II contain observations of the numerical and fluid dynamic phenomena in each run. Together, these empirically demonstrate the validity of the method. The first five runs were special cases for which known answers were available. These runs, which described both liquid and two-phase axial flow through paddle-wheel channels demonstrate that the relaxation procedure converges with good results. They also show that a large number of finite difference field points gives more accurate answers.

Of the four runs on the sample 6.2° and 12° variable-lead inducers, all were for incompressible flow except one on the 12° machine. This one revealed that the inclusion of these two-phase effects required a negligible increase in computing time. One incompressible run on each inducer gave reasonable overall performance results even with the coarse, highly non-orthogonal grid that we used for these low-angle channels. The more detailed internal distributions differed from those obtained by simple radial equilibrium techniques, but were qualitatively reasonable. The distributions resulting for the one special run with pressures forced to satisfy the streamline momentum equation for no loss were more familiar. This showed that reasonably accurate results are possible with a grid that is too coarse for the relaxation procedure to produce low enough residuals to guarantee them. The initial positions of the upstream and downstream stagnation stream surfaces were not changed as the progress of the solutions indicated that some load existed on these extensions of the blades. However, as one compares the differences in these runs, the inaccuracies of the coarse grid (e.g. 5 x 5 x 22) that we used (for reasonable computer running time) appear to have had more effect on the answers. We have presented detailed recommendations at the end of Section II that contemplate satisfactorily accurate three-dimensional answers for lossless flow in typical inducers with a 10 x 10 x 50 grid, about twelve hours on good computing equipment, and appropriate hand adjustment of the blade extensions. Losses are easily included and may require a finer grid and more time.

The approximate method of solution was more rapid, but it employed assumptions that amount to combining two quasi-two-dimensional solutions to get answers in three dimensions. However, it is a step forward because it does combine these solutions

with two-phase flow and loss effects. The method of solution by balancing initially-assumed streamline positions makes it possible to get satisfactory answers for a very small number of these streamlines. Results of over eighteen runs demonstrate the capability of this method as a rapid way of judging or grading an inducer; e.g., by the results of several runs at various inlet conditions. This would determine if and at what condition a particular inducer should be analyzed further by the more detailed and lengthy exact method. About half of these approximate runs contained two-phase flow with losses. The others were incompressible runs with and without losses. This data clearly describes blade leading edge unloading that occurs for cavitating conditions (low NPSH). In fact, several resulting inducer pressure-rise-versus-NPSH curves at different values of vaporization parameter show that our model for these real fluid effects qualitatively produces the familiar head breakdown curve. Stronger loss factors appear to be necessary to reproduce the shape of this curve more exactly; although "choked" or minimum NPSH conditions for complete head breakdown correlate reasonably with test results. The basic restrictions of our approximate method may be partly responsible for this lack of complete correlation.

These results include the fluid and scale effects of the cavitation and thermodynamic vaporization parameters that are part of the analysis model. However, further study shows that this data has some correlation with the well-known, simplified, vapor-to-liquid volume ratio theory for minimum allowable inducer NPSH. The fact that two-phase motion exists with negligible inducer performance effects over a wide range of higher values of NPSH indicates that two cavitating regimes exist over the NPSH range, viz., "unloading" and "choking". The simplified theory probably predicts these fluid and scale effects as well as it does by being of importance in only the choking regime, which causes complete head breakdown regardless of non-cavitating pressure rise.

This theory and data indicate that inducer design optimization with these analysis methods can be done by examining different designs for the effects of (a) head coefficient, (b) inlet blade angle, (c) inlet incidence angle, and (d) blade solidity. Empirical modifications to the programs appear to be necessary to improve the existing thermodynamic equilibrium model for two-phase flow and loss effects. This may be sufficient to describe the non-equilibrium phenomena if they are not separately distinguishable in the experimental test results that would be used for the purpose. Fortran IV listings of both the exact and approximate analyses are included in this report, and the programs are ready for further use.

APPENDIX A

TRANSFORMATION FROM CYLINDRICAL
TO GENERAL, OBLIQUE COORDINATES

The desirability of a natural coordinate system for which the boundaries of the flow channel become coordinate surfaces was mentioned in Sections II. A. 1 and II. B. 3. Such a transformation is described in this appendix and the wall boundary condition (equation I. 16)) is stated in terms of these natural coordinates. We start by designating the hub and shroud as surfaces of constant α , the blade surfaces as surfaces of constant β , and the inlet and exit throughflow surfaces of the channel as surfaces of constant γ (see figure A. 1). Knowing the cylindrical-coordinate description of the physical boundaries of the flow channel, a transformation is induced between the cylindrical coordinates (r, θ, z) and the family of γ-surfaces (hub to shroud), β-surfaces (blade-to-blade) and γ-surfaces (inlet-to-outlet) as follows

$$r = r\,(\alpha, \beta, \gamma)$$

$$\theta = \theta\,(\alpha, \beta, \gamma)$$

$$z = z\,(\alpha, \beta, \gamma) \tag{A. 1}$$

This transformation has a Jacobian matrix denoted by

$$J\left(\frac{r, \theta, z}{\alpha, \beta, \gamma}\right) = \begin{bmatrix} \dfrac{\partial r}{\partial \alpha} & \dfrac{\partial \theta}{\partial \alpha} & \dfrac{\partial z}{\partial \alpha} \\[2mm] \dfrac{\partial r}{\partial \beta} & \dfrac{\partial \theta}{\partial \beta} & \dfrac{\partial z}{\partial \beta} \\[2mm] \dfrac{\partial r}{\partial \gamma} & \dfrac{\partial \theta}{\partial \gamma} & \dfrac{\partial z}{\partial \gamma} \end{bmatrix} \tag{A. 2}$$

We now apply the "chain rule" (reference 43) and rewrite all the partial derivatives which appear in equations (II. 1) through (II. 4) in terms of the natural coordinates so that

$$\frac{\partial}{\partial r} = \frac{\partial \alpha}{\partial r}\frac{\partial}{\partial \alpha} + \frac{\partial \beta}{\partial r}\frac{\partial}{\partial \beta} + \frac{\partial \gamma}{\partial r}\frac{\partial}{\partial \gamma}$$

$$\frac{\partial}{\partial \theta} = \frac{\partial \alpha}{\partial \theta}\frac{\partial}{\partial \alpha} + \frac{\partial \beta}{\partial \theta}\frac{\partial}{\partial \beta} + \frac{\partial \gamma}{\partial \theta}\frac{\partial}{\partial \gamma} \tag{A. 3}$$

$$\frac{\partial}{\partial z} = \frac{\partial \alpha}{\partial z}\frac{\partial}{\partial \alpha} + \frac{\partial \beta}{\partial z}\frac{\partial}{\partial \beta} + \frac{\partial \gamma}{\partial z}\frac{\partial}{\partial \gamma}$$

149

Constant β

Constant α

Shroud

Blade

Shroud

Hub

Blade

a) Crossectional View

Shroud

Hub

b) Meridional View

Constant γ

Constant γ

Blade

Constant β

Blade

c) Developed View

FIGURE A.1. NATURAL COORDINATE SURFACES FOR GENERAL CHANNEL GEOMETRY.

Using the notation of equation (A. 2), we see that the nine coefficients in equations (A. 3) are the elements of the Jacobian matrix

$$
J\left(\frac{\alpha,\beta,\gamma}{r,\theta,z}\right) =
\begin{bmatrix}
\dfrac{\partial\alpha}{\partial r} & \dfrac{\partial\beta}{\partial r} & \dfrac{\partial\gamma}{\partial r} \\[2mm]
\dfrac{\partial\alpha}{\partial\theta} & \dfrac{\partial\beta}{\partial\theta} & \dfrac{\partial\gamma}{\partial\theta} \\[2mm]
\dfrac{\partial\alpha}{\partial z} & \dfrac{\partial\beta}{\partial z} & \dfrac{\partial\gamma}{\partial z}
\end{bmatrix}
\tag{A. 4}
$$

which is the matrix inverse of $J\left(\dfrac{r,\theta,z}{\alpha,\beta,\gamma}\right)$ (reference 44). Therefore, the nine coefficients needed for the evaluation of $\dfrac{\partial}{\partial r}$, $\dfrac{\partial}{\partial\theta}$ and $\dfrac{\partial}{\partial\gamma}$ are calculable from

$$
\left.
\begin{aligned}
\frac{\partial\alpha}{\partial r} &= \left(\frac{\partial\theta}{\partial\beta}\frac{\partial z}{\partial\gamma} - \frac{\partial\theta}{\partial\gamma}\frac{\partial z}{\partial\beta}\right)\frac{1}{D} \\[2mm]
\frac{\partial\beta}{\partial r} &= \left(\frac{\partial\theta}{\partial\gamma}\frac{\partial z}{\partial\alpha} - \frac{\partial\theta}{\partial\alpha}\frac{\partial z}{\partial\gamma}\right)\frac{1}{D} \\[2mm]
\frac{\partial\gamma}{\partial r} &= \left(\frac{\partial\theta}{\partial\alpha}\frac{\partial z}{\partial\beta} - \frac{\partial\theta}{\partial\beta}\frac{\partial z}{\partial\alpha}\right)\frac{1}{D} \\[2mm]
\frac{\partial\alpha}{\partial\theta} &= \left(\frac{\partial z}{\partial\beta}\frac{\partial r}{\partial\gamma} - \frac{\partial z}{\partial\gamma}\frac{\partial r}{\partial\beta}\right)\frac{1}{D} \\[2mm]
\frac{\partial\beta}{\partial\theta} &= \left(\frac{\partial z}{\partial\gamma}\frac{\partial r}{\partial\alpha} - \frac{\partial z}{\partial\alpha}\frac{\partial r}{\partial\gamma}\right)\frac{1}{D} \\[2mm]
\frac{\partial\gamma}{\partial\theta} &= \left(\frac{\partial z}{\partial\alpha}\frac{\partial r}{\partial\beta} - \frac{\partial z}{\partial\beta}\frac{\partial r}{\partial\alpha}\right)\frac{1}{D} \\[2mm]
\frac{\partial\alpha}{\partial z} &= \left(\frac{\partial r}{\partial\beta}\frac{\partial\theta}{\partial\gamma} - \frac{\partial r}{\partial\gamma}\frac{\partial\theta}{\partial\beta}\right)\frac{1}{D} \\[2mm]
\frac{\partial\beta}{\partial z} &= \left(\frac{\partial r}{\partial\gamma}\frac{\partial\theta}{\partial\alpha} - \frac{\partial r}{\partial\alpha}\frac{\partial\theta}{\partial\gamma}\right)\frac{1}{D} \\[2mm]
\frac{\partial\gamma}{\partial z} &= \left(\frac{\partial r}{\partial\alpha}\frac{\partial\theta}{\partial\beta} - \frac{\partial r}{\partial\beta}\frac{\partial\theta}{\partial\alpha}\right)\frac{1}{D}
\end{aligned}
\right\}
\tag{A. 5}
$$

where the determinant of $J\left(\dfrac{r,\theta,z}{\alpha,\beta,\gamma}\right)$ is given by

$$
D = \frac{\partial r}{\partial\alpha}\left(\frac{\partial\theta}{\partial\beta}\frac{\partial z}{\partial\gamma} - \frac{\partial\theta}{\partial\gamma}\frac{\partial z}{\partial\beta}\right) + \frac{\partial r}{\partial\beta}\left(\frac{\partial\theta}{\partial\gamma}\frac{\partial z}{\partial\alpha} - \frac{\partial\theta}{\partial\alpha}\frac{\partial z}{\partial\gamma}\right) + \frac{\partial r}{\partial\gamma}\left(\frac{\partial\theta}{\partial\alpha}\frac{\partial z}{\partial\beta} - \frac{\partial\theta}{\partial\beta}\frac{\partial z}{\partial\alpha}\right)
\tag{A. 6}
$$

The main analysis program, described in Appendix C, uses formulae (A. 3) for calculating all the partial derivatives of the variables appearing in the residuals as given by equations (II. 5) through (II. 8). The necessary transformation coefficients are calculated by a subroutine from the (r, θ, z)-coordinates of the grid points using formulae (A. 5) and (A. 6).

For a typical inducer channel the degree of obliqueness of the (α,β,γ)-system is largely due to the blade angle. For example, at the blade leading edge of the 6. 2°

151

inducer channel, with which run E-6 was made, a typical "star" of grid points is highly oblique because of the shallow blade angle. Figure A.2 shows such a star near the blade leading edge at the root-mean-square radius of $r = 0.7454$ where the blade angle is $8.4°$ (see equation (II.40)). In the interior of the channel, where Δz is 0.23524 instead of 0.10857, the distance $\Delta \gamma$ is even greater relative to the distances $\Delta \alpha = \Delta r$ and $\Delta \beta = r\Delta\theta$.

This situation may be alleviated by taking the γ-surfaces to be quasi-orthogonal to the blade surfaces rather than perpendicular to the z-axis. One drawback this has is that many more γ-stations are required. Also, if the grid points do not lie on planes of constant z, the determination of blade loadings and of throughflow boundary conditions is rather difficult. A simpler remedy is to form a denser grid of points although this increases computer time per relaxation cycle. We again point to the quality of our results in Section II.B and recommend that for any particular channel geometry a reasonable grid be selected based on qualitative diagrams similar to figure A.2.

The treatment of the wall boundary condition

$$\tilde{W} \cdot \tilde{n} = 0 \tag{I.16}$$

is as follows:

At a point on a blade we can let the normal vector, $\tilde{n}$, be $\nabla\beta$ because the blades are surfaces of constant β. Thus

$$\tilde{W} \cdot \tilde{n} = \tilde{W} \cdot \nabla\beta = 0$$

or

$$u \frac{\partial\beta}{\partial r} + \frac{v}{r} \frac{\partial\beta}{\partial\theta} + w \frac{\partial\beta}{\partial z} = 0 \tag{A.7}$$

Similarly, since the hub and shroud are surfaces of constant α, a normal vector at such a point is $\nabla\alpha$ and we have

$$u \frac{\partial\alpha}{\partial r} + \frac{v}{r} \frac{\partial\alpha}{\partial\theta} + w \frac{\partial\alpha}{\partial z} = 0$$

Since the hub and shroud are surfaces of revolution, i.e. $\frac{\partial\alpha}{\partial\theta} = 0$, on a hub or shroud point the condition is

$$u \frac{\partial\alpha}{\partial r} + w \frac{\partial\alpha}{\partial z} = 0 \tag{A.8}$$

At an "edge" point, i.e. where a blade meets the hub or shroud, equations (A.7) and (A.8) must be satisfied simultaneously.
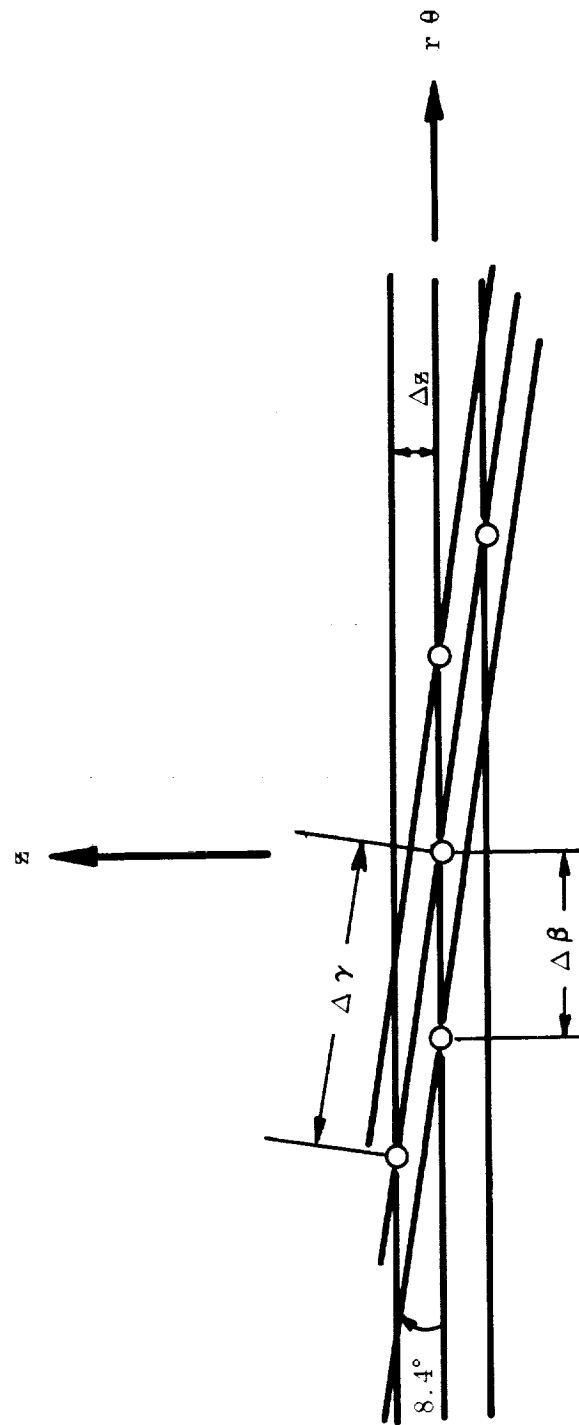
FIGURE A.2. TYPICAL STAR OF GRID POINTS NEAR INLET OF 6.2°
INDUCER CHANNEL SHOWING HIGHLY OBLIQUE INTERSECTIONS
OF β – AND γ – SURFACES.

In the computer program in its present form (see Appendix C) equations (A.7) and (A.8) are respectively solved for w and u, i.e.

$$w = - \left(u \; \frac{\partial \beta}{\partial r} + \frac{v}{r} \; \frac{\partial \beta}{\partial \theta} \right) \Big/ \frac{\partial \beta}{\partial z} \qquad \text{(A.9)}$$

$$u = - w \; \frac{\partial \alpha}{\partial z} \Big/ \frac{\partial \alpha}{\partial r} \qquad \text{(A.10)}$$

Thus, on a blade surface w is explicitly dependent on u and v. On the hub or shroud u is directly determined by w. This is because, for the blade angles we have been considering, the dominant coefficients are $\partial \beta / \partial z$ and $\partial \alpha / \partial r$. In fact, equations (A.9) and (A.10) may be used successfully for blade angles and hub and shroud slopes of up to 60° to 70°. This method is used merely for convenience of programming — every grid point has four residuals associated with it. To make the program completely general with respect to channel geometry, equations (A.7) and (A.8) can be treated as "boundary condition residuals", in which case there would be five residuals at boundary points instead of the usual four (see Section II.C.2).

Finally, the (α, β, γ) -surfaces need not be uniformly spaced as concerns the validity of the transformation formulae. Thus, with a proper choice of these surfaces the grid can be made denser in the boundary regions relative to the interior of the flow channel, thereby achieving greater accuracy close to the boundaries where the discretization discrepancy is the greatest (see Section II.A.5).

154

APPENDIX B

COMPLEMENTARY STREAM FUNCTIONS

In this appendix are discussed the development and applications of a pair of complementary stream functions to the solution of the three-dimensional fluid flow problem, as outlined in Section I. The advantages and disadvantages are weighed against each other and it is concluded that, although the approach is aesthetically appealing, much more development is required before it can be applied as a practical solution method.

Observe that a vector can always be represented as lying along the intersection of two nonparallel planes (which are not necessarily orthogonal to each other). Specifically, we can represent the relative velocity vector, $\widetilde{W}$, at a point as lying along the intersection of two planes, each of which is tangent to one of a pair of surfaces at that point. Designating two such families of intersecting surfaces as

$$\left.\begin{array}{l} \mu\ (r,\ \theta,\ z) = \text{constant} \\ \\ \sigma\ (r,\ \theta,\ z) = \text{constant} \end{array}\right\} \tag{B.1}$$

yields (see figure B.1)

$$\widetilde{W} = \lambda\ \nabla\mu \times \nabla\sigma \tag{B.2}$$

Here λ is some proportionality function whose nature can be determined by satisfying the continuity equation as follows:

$$\nabla \cdot \widetilde{W} = \nabla\lambda \cdot (\nabla\mu \times \nabla\sigma) + \lambda\nabla \cdot (\nabla\mu \times \nabla\sigma)$$

$$= \nabla\lambda \cdot (\nabla\mu \times \nabla\sigma)$$

$$= \nabla\lambda \cdot \widetilde{W}/\lambda = 0$$

i.e. λ is constant along streamlines. Therefore λ is a function of μ and λ only and, hence, no generality is lost by taking λ as unity, or

$$\widetilde{W} = \nabla\mu \times \nabla\sigma \tag{B.3}$$

No rigorous treatment of the conditions under which such families of surfaces exist is given here. Maeder and Wood (reference 11) simply assume their existence whereas Yih (reference 10) derives them as solutions to the differential equations which describe streamlines. Additional justification for taking λ as unity is given by Yih as well as by Benton (reference 45).

155

$$\overrightarrow{W} = \lambda \, \nabla \mu \; \times \; \nabla \sigma$$

σ = Constant

$\nabla \mu$

μ = Constant

$\nabla \sigma$
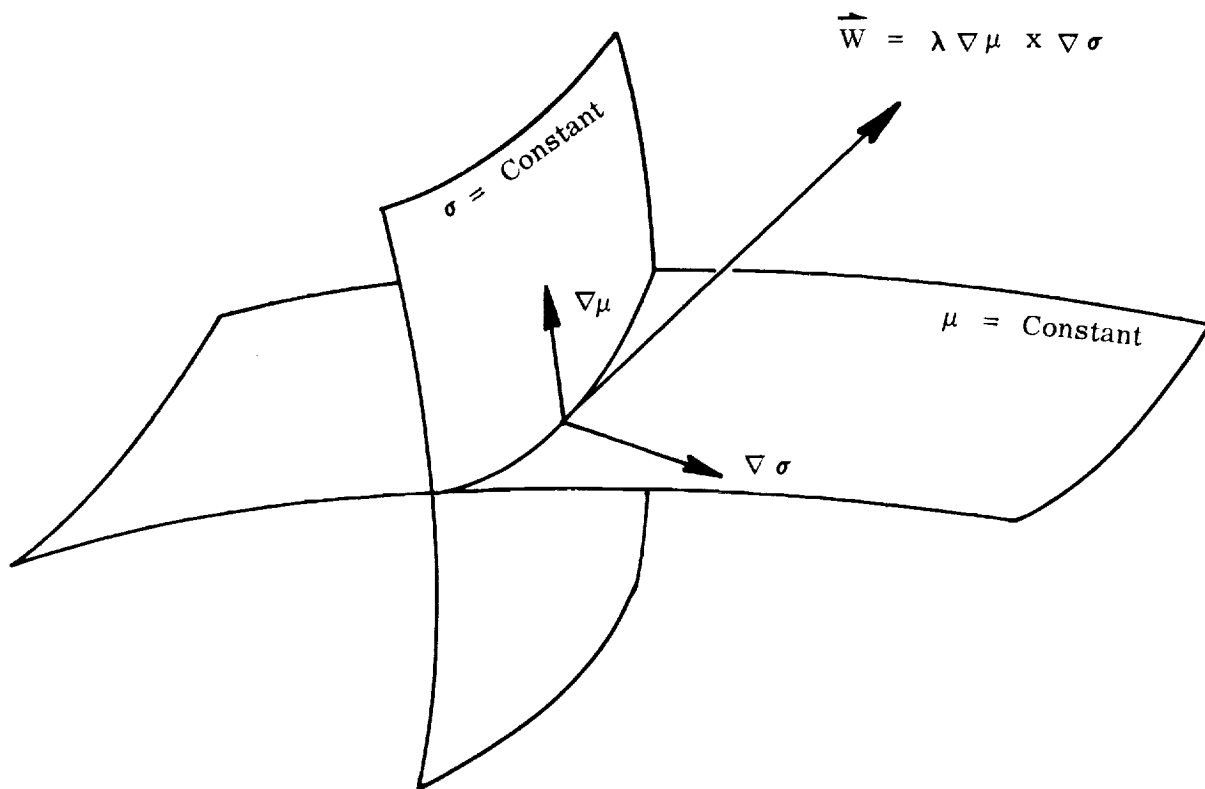
FIGURE B.1.   PORTION OF A STREAMLINE SHOWN AS THE CURVE OF
INTERSECTION OF A PAIR OF STREAM SURFACES.

For the case of a compressible (or two-phase) fluid, the above development is repeated with the flux vector, $\rho\vec{W}$, to obtain

$$\vec{W} = \frac{1}{\rho} \; \nabla\mu \times \nabla\sigma \tag{B.4}$$

One immediate advantage of this transformation is that the continuity equation is satisfied identically because of

$$\nabla\cdot(\rho\,\vec{W}) = \nabla\cdot(\nabla\mu \times \nabla\sigma) = 0$$

which is a vector identity. Also, the three velocity components are now expressed in terms of two functions. Thus the problem is reduced to solving the resulting three momentum partial differential equations for p, μ and σ.

Another advantage is the ease with which the wall boundary conditions are met. If a portion of a wall boundary is considered as a surface of constant σ, for example, then a normal vector to this surface is given by $\nabla\sigma$. Thus

$$\vec{W} \cdot \vec{n} = \frac{1}{\rho} \; \nabla\mu \times \nabla\sigma = 0 \tag{B.5}$$

which is again a vector identity. Placing μ or σ surfaces on the boundaries, therefore automatically satisfies the wall boundary condition. This is consistent with the geometric interpretation of the μ and σ surfaces as stream surfaces. With this in mind, we tried two systems of arranging these surfaces in the flow channel.

In the first system, the hub and shroud are σ -surfaces and the blades are μ -surfaces (figure B.2a). It is shown in reference 10 that the total mass-flux across an area bounded by two pairs of surfaces such as $\sigma = \sigma_1$, $\sigma = \sigma_2$, $\mu = \mu_1$, and $\mu = \mu_2$ is given by

$$w = (\mu_2 - \mu_1) \; (\sigma_2 - \sigma_1) \tag{B.6}$$

Thus, making the hub be a surface $\sigma = 0$, the shroud $\sigma = w_T$ and the blades $\mu = 0$ and $\mu = 1.0$, satisfied mass-conservation in the large. This "natural" way of arranging the stream surfaces does, however, prevent a streamline from crossing from a blade onto the shroud, say; i.e. the "edges" of the channel are forced to be streamlines themselves. How much of a drawback this is is not clear because the streamlines a finite distance away from the boundaries can still produce the counterrotation observed in typical inducer flows. On the one hand it is easy to show that a streamline which touches an edge must at least be tangent to it at the point of contact. On the other hand, in two-dimensional potential flow near a corner, fluid particles on the boundary do go around the corner if the corner angle is obtuse*. We also foresaw possible numerical

---

* This example was brought to our attention by Doug Anderson of the Lewis Research Center, NASA, Cleveland.

157

difficulties due to the "bunching" of stream surfaces near the boundaries resulting from the relative rotation of the fluid in the passage.

For these reasons we decided to try another system of steam surfaces (figure B. 2b). In this system the entire channel boundary is made a σ-surface of value σ = q, with other σ-surfaces nested inside. The μ-surfaces radiate from the surface σ = 0 (this degenerate surface is actually a curve) so that a typical cross section resembles a spider web. With this system the question of streamlines moving across the edges of the channel is immaterial. One very serious drawback is the singularity which exists about the curve σ = 0. We were unable to surmount the numerical problems associated with this singularity in any practical way. A lesser disadvantage is the discontinuity due to the coinciding of the surfaces μ = 0 and μ = 1.0, similar to the discontinuity which is present in an ordinary polar coordinate system where the rays θ = 0 and θ = 2π coincide. By use of a special algorithm which permitted the μ-surfaces in the vicinity of this apparent discontinuity to be two-valued, we were able to compute μ-derivates in the usual fashion.

The form of the governing equations is independent of which system of stream surfaces is used. When the transformation (B. 4) is applied to the vector momentum equation (I. 4) the result is

$$g_0 \nabla p + \nabla \mu \times \frac{d}{dt} \nabla \sigma - \nabla \sigma \times \frac{d}{dt} \nabla \mu - \frac{1}{\rho} (\nabla \mu \times \nabla \sigma) \frac{d\rho}{dt}$$

$$+ 2\vec{\Omega} \times (\nabla \mu \times \nabla \sigma) + \rho \vec{\Omega} \times (\vec{\Omega} \times \vec{r}) + \rho \vec{F} \qquad \text{(B. 7)}$$

The three scalar components of this equation can also be obtained from equations (II. 1), (II. 2) and II. 3) by substituting into them

$$u = \frac{1}{r\rho} \left(\frac{\partial \mu}{\partial \theta} \frac{\partial \sigma}{\partial z} - \frac{\partial \sigma}{\partial \theta} \frac{\partial \mu}{\partial z} \right)$$

$$v = \frac{1}{\rho} \left(\frac{\partial \mu}{\partial z} \frac{\partial \sigma}{\partial r} - \frac{\partial \sigma}{\partial z} \frac{\partial \mu}{\partial r} \right) \qquad \text{(B. 8)}$$

$$w = \frac{1}{r\rho} \left(\frac{\partial \mu}{\partial r} \frac{\partial \sigma}{\partial \theta} - \frac{\partial \sigma}{\partial r} \frac{\partial \mu}{\partial \theta} \right)$$

which are merely the components of equation (B. 4).

The resulting scalar equations contain pure as well as mixed second order partial derivatives of μ and σ. The typical star of grid points for the corresponding finite-difference equations would contain 19 points instead of the seven points we are now using (figure II. 2). The drawbacks of this are apparent.

158
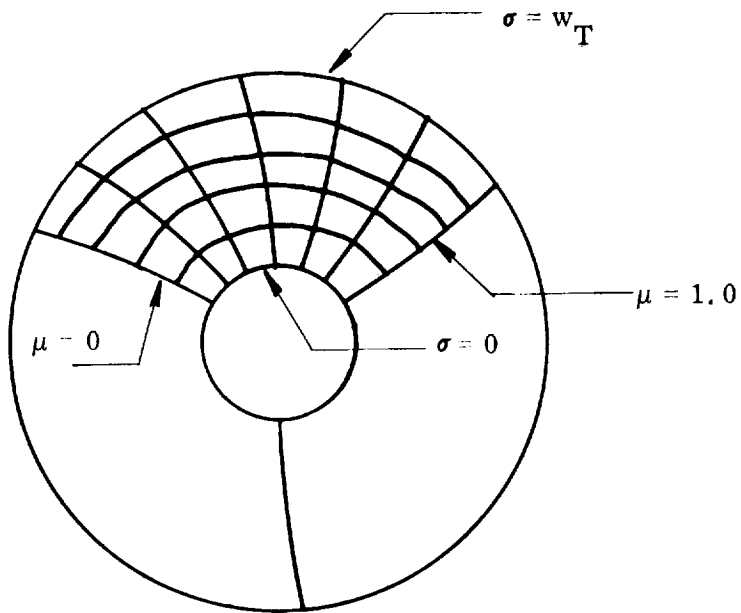
a) "Quasi-Orthogonal" System
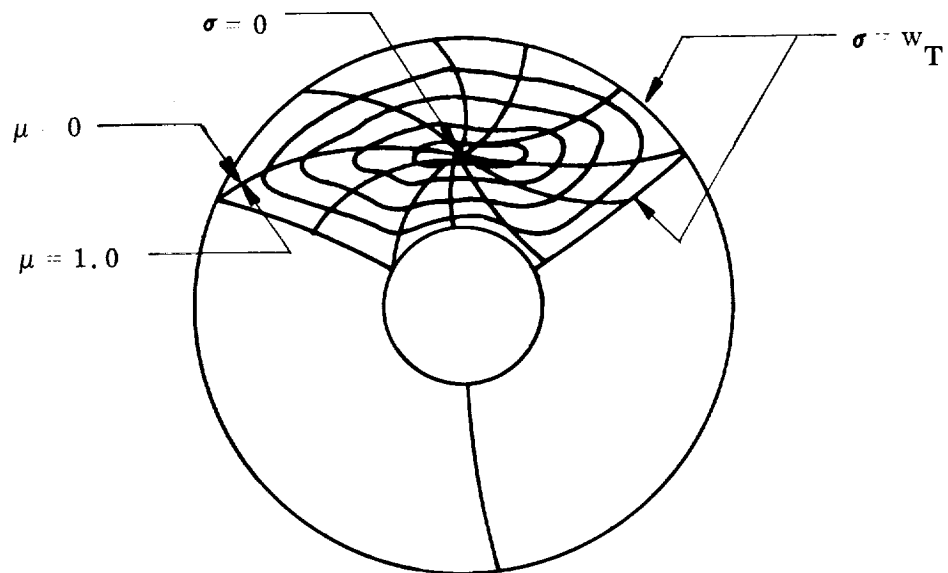
b) "Spider Web" System

FIGURE B. 2. TWO ARRANGEMENTS OF μ- and σ-SURFACES

We felt that the above-mentioned difficulties made the use of these complementary stream functions an impractical approach at the present, compared to the direct numerical solution of the untransformed equations as presented in this report. We recommend, however, that the use of these (μ, σ) -surfaces be investigated further, because, with the use of differential geometry, they may lead to a rigorous analysis of the throughflow boundary conditions needed for the general three-dimensional problem in turbomachinery.

APPENDIX C

INSTRUCTIONS FOR USE OF
EXACT SOLUTION COMPUTER PROGRAMS

The main analysis program for the exact solution method (see Section II. A. 3) and the accompanying data reduction program (see Section II. A. 6) are described in this Appendix. Both programs are written in Fortran IV. Their inputs and outputs are described, followed by their respective Fortran listings. In the case of the main program a block diagram is included.

a) Main Analysis Program

The main program and its five subroutines have a common storage requirement of 39,638 locations. The running time per relaxation cycle can be estimated as in the following example:

> For a 5 x 5 x 22 grid there are 1585 independent discrete variables (see equation (II.14)). For M=3, a maximum of six values of R* will have to be calculated for each of these variables (see Section II. A. 3) making a maximum of 9510 star residuals to be computed during one relaxation cycle. A UNIVAC 1107 can calculate approximately 40 star residuals per second, this having been established experimentally. Thus it would take at most 238 seconds, or four minutes for each relaxation cycle.

The input to the program consists of the cylindrical (r, θ, z) -coordinates of the selected grid points, certain numbers which control the nature of the relaxation processs, information describing the fluid, and initial values for the field of velocity components and pressures. A definition of these input quantities follows. For the exact format in which these inputs are to be given, please see the corresponding Fortran listing.

IMAX, JMAX, KMAX:	The number of radial (hub-to-shroud), circumferential (blade-to-blade) and throughflow (upstream-to-downstream) grid stations, respectively. I = 1 on the hub and I = IMAX on the shroud; J = 1 on the pressure (driving) blade surface and J = JMAX on the suction (driven) blade surface; K = 1 on the upstream throughflow boundary and K = KMAX on the downstream one.
KLE, KTE:	The K-index of the axial stations corresponding, respectively, to the blade leading and trailing edges.
R(I, J, K):	The radial coordinates, r, or the grid points.
T(I, J, K):	The circumferential coordinates, θ (in radians), of the grid points.

Z(I, J, K):	The axial coordinates, z, of the grid points.
TITLE:	Any type of run identifying information which may consist of up to 80 characters (including blank spaces). None of this information is processed by the computer.
KOUNT:	The number of the first cycle of the current run (for "book-keeping" reasons only).
NUM:	The number of relaxation cycles to be executed by the current run. If NUM = 0, no relaxation is performed: All residuals and the overall RMS value are computed and the regular output is presented.
M:	The number of adjustment magnitudes to be tried with each variable (see Section II. A. 3). Recommended: M = 3.
NSEQ(1), NSEQ(2), NSEQ(3), NSEQ(4):	The sequential order in which the four variables are to be adjusted at each grid point where the four variables are identified by the computer as follows: u is 1, v is 2, w is 3 and p is 4. Thus, for the recommended sequence (see the discussion following Run E-6 in Section II. B. 3), NSEQ(1) = 4, NSEQ(2) = 3, NSEQ(3) = 2, NSEQ(4) = 1, resulting in an adjustment of sequence of (p, w, v, u).
DMAX(1), DMAX(2), DMAX(3), DMAX(4):	The four starting trial adjustment magnitudes δu, δv, δw, δp, respectively (see Section II. A. 3). Recommended: DMAX(1) = DMAX(2) = DMAX(3) = DMAX(4) = 0.1.
A:	The successive adjustment ratio, (see Section II. A. 3). Recommended: $\alpha = 0.1$
CRIT:	The accuracy criterion, such as the quantity $\Omega^2 r_{t,1}$ of equation (II. 19).
E:	The convergence parameter, ϵ, of equation (II. 19).
REV, DLIQ, PSAT, TT, VISC:	The values of rotative speed, Ω, liquid density, ρ_f/g_0, saturation pressure, p_{sat}, vaporization constant, T^*, and kinematic viscosity, ν, respectively.
U(I, J, K):	The values of radial velocity, u, at each grid point.
V(I, J, K):	The values of relative circumferential velocity, v, at each grid point.
W(I, J, K):	The values of axial velocity, w, at each grid point.
P(I, J, K):	The values of static pressure, p, at each grid point.

This completes the list of input quantities.

The output of the program consists of punched and printed output. After executing NUM relaxation cycles the entire list of quantities, starting with TITLE, is punched onto cards in exactly the same format and order as for the corresponding inputs. The values of NUM, DMAX(1), DMAX(2), DMAX(3), DMAX(4), U(I, J, K), V(I, J, K), W(I, J, K) and P(I, J, K) are the latest values. Thus the punched output of one run may be used to continue the same run at a later time without having to rerun the relaxation cycles of the first run.

The first line of the printed output consists of the entire contents of TITLE, thereby providing any desired way of identifying the computer run. The size of grid is identified next, followed by the values of M, α, Ω, ρ_f/g_o, p_{sat}, T^* and ν. Then the sequence in which the variables are adjusted, is stated. The next portion of the printed output concerns the cycle-by-cycle progress of the relaxation scheme. It is printed in columns with the following headings:

RELAX CYCLE:	The sequential number of each relaxation cycle, the first cycle of the current run having the number KOUNT as given in the input.
NO. OF TRIES:	The total number of trial adjustments that were made during each cycle. Note that this number cannot exceed 2 x M x D, where D is given by equation (II.14).
TOTAL RMS RESIDUAL:	The root-mean-square value of all residuals in the entire grid of points.
MAX. RMS RESIDUAL:	The largest root-mean-square value of the four point residuals as given by equations (II. 5) through (II. 8).
MIN. RMS RESIDUAL:	The smallest root-mean-square value of the four point residuals as given by equations (II. 5) through (II. 8).
MAGNITUDE OF BIGGEST ACCEPTED ADJUSTMENT FOR U, V, W, P:	The magnitudes of the largest adjustments δu, δv, δw and δp which were accepted during each cycle.

The last portion of the output presents the latest values of the variables at all grid points. This information is printed in columns with the following headings:

I, J, K	The three indexes of each grid point. Recall that I = 1 on the hub and I = IMAX on the shroud; J = 1 on the pressure (driving) blade surface and J=JMAX on the suction (driven) blade surface; K = 1 on the upstream throughflow boundary and K = KMAX on the downstream throughflow boundary.

U:	The radial velocity component, u.
V:	The relative circumferential velocity component, v.
W:	The axial velocity component, w.
P:	The static pressure, p.
D:	The point density, ρ/g_0.
RES:	The sum of the squares of the four point residuals, as given by equations (II. 5) through (II. 8).

The program will continue until either the largest root-mean-square of the four point residuals is less than CRIT times E (see equation II. 19) or until NUM relaxation cycles have been executed. Accordingly, the message "CONVERGED" or "MAXIMUM NUMBER OF CYCLES EXECUTED" will be printed on the output sheet. In either case, the computer will stop with an input tape end-of-file condition.

b) Data Reduction Program

The Data Reduction Program and its two subroutines have a common storage requirement of 23,757 locations. A UNIVAC 1107 requires between 25 and 30 seconds to reduce the data of a 5 x 5 x 22 grid.

The input to the Data Reduction Program is identical to the input to the Main Analysis Program. Thus, the input describing the grid point coordinates can be combined with the punched output of any given run of the Main Analysis Program to form a complete input set for the Data Reduction Program.

The first line of the output consists of the entire contents of TITLE, thereby giving the reduced data exactly the same identification as the corresponding main analysis run. The second line identifies the number of the relaxation cycle whose results are being reduced. Next, a station-by-station listing is given of hub-to-tip distributions of quantities which are area-averaged over annular regions on each axial station. The column headings are:

AXIAL STATION:	The z-value of each station. The stations corresponding to the blade leading edge (K = KLE) and trailing edge (K = KTE) are so designated.
RADIAL STATION:	The mean r-value of each annular region.
RADIAL VELOCITY:	The area-averaged value of V_r.

164

TANGENTIAL
VELOCITY: The area-averaged value of V_θ.

AXIAL
VELOCITY: The area-averaged value of V_z.

STATIC
PRESSURE: The area-averaged value of p.

DENSITY: The area-averaged value of ρ/g_0.

This is followed by a station-by-station listing of the hub-to-tip distributions of blade-to-blade pressure loadings, calculated simply as

$$\Delta p = p_p - p_s$$

The first column lists the values of z and the remaining columns (read from left to right) list the hub-to-tip values of Δp for each annulus.

The last portion of the output gives the following mass-averaged, overall performance parameters:

Inlet and exit pressure head: $\overline{p/\rho}$ as calculated from equation (II. 26).

Inlet and exit absolute velocity head: $\overline{1/2\ V^2}$, as calculated from equation (II. 28).

Total head rise: $\Delta \overline{H}$, as calculated from equation (II. 30).

Shaft power per channel: P_s, as calculated from equation (II. 31).

Overall efficiency: $\overline{\eta}$, as calculated from equation (II. 32).

Mass flow rate per channel: w_T, as calculated from equation (II. 27).

This program will also terminate with an input tape end-of-file condition.

FIGURE C. 1
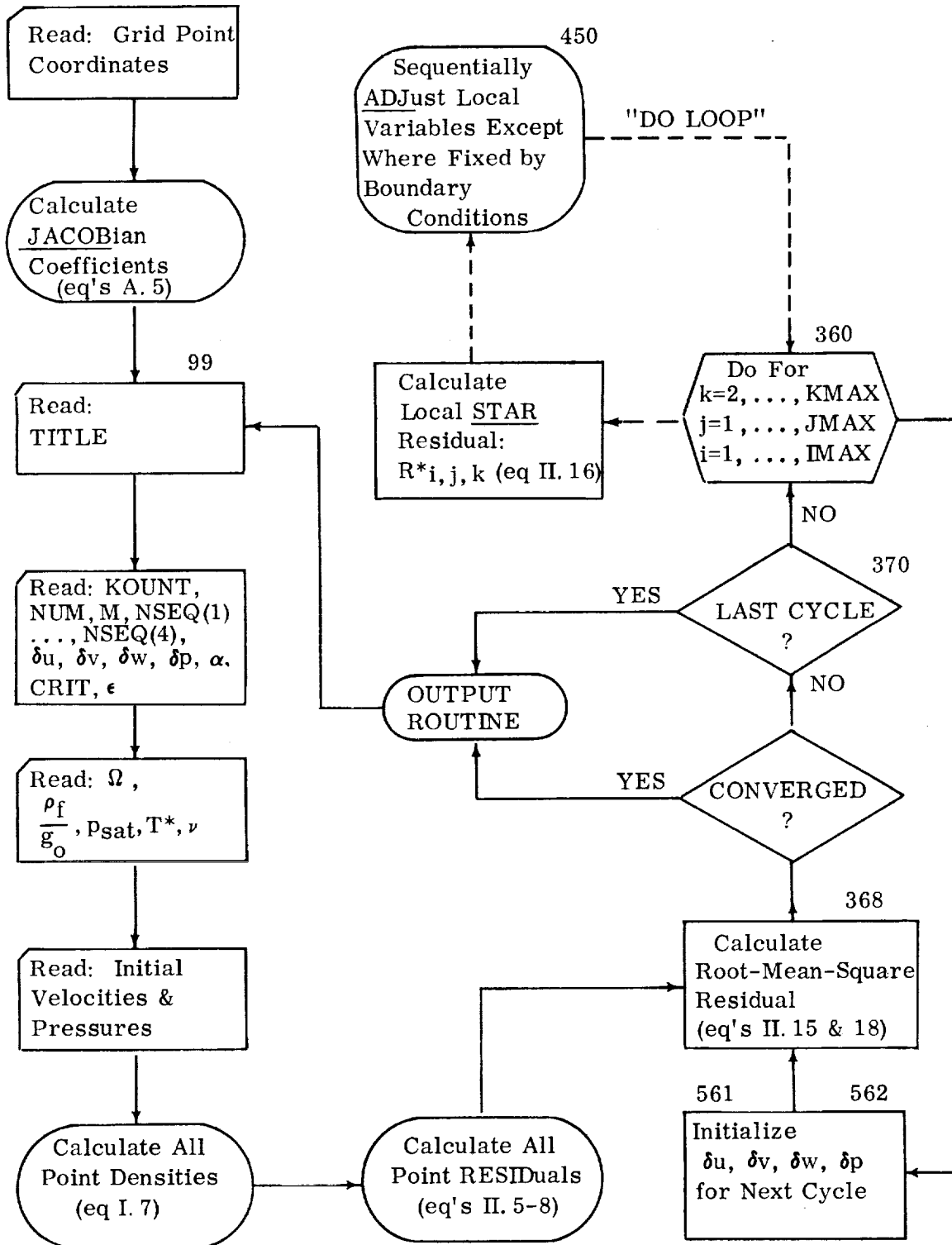
a) **BLOCK DIAGRAM FOR MAIN ANALYSIS PROGRAM**

(Numbers above boxes refer to key Fortran statement numbers in the main program)

166

FIGURE C.1 (Continued)

99

┌─────────────────────────────┐
│ Satisfy Wall Boundary   │
│ Conditions: │
│ eq A.9 on blades   │
│ eq A.10 on hub, shroud   │
│ eq's A.9 & 10 at "edges"   │
└─────────────────────────────┘

Subroutine RESID →

351

┌─────────────────────────────┐
│ Calculate All   │
│ Derivatives: │
│ $\frac{\partial}{\partial\alpha}$, $\frac{\partial}{\partial\beta}$, $\frac{\partial}{\partial\gamma}$ │
└─────────────────────────────┘

367

┌─────────────────────────────┐
│ Convert All Derivatives to │
│ Cylindrical Coordinates: │
│ $\frac{\partial}{\partial r}$, $\frac{\partial}{\partial\theta}$, $\frac{\partial}{\partial\gamma}$ │
│ (eq's A.3)   │
└─────────────────────────────┘

385

┌─────────────────────────────┐
│ Calculate Loss   │
│ Terms: │
│ F_r, F_θ, F_z │
│ (Only if $\nu \neq 0$)   │
└─────────────────────────────┘

391

┌─────────────────────────────┐
│ Calculate Point   │
│ Residuals: │
│ R1, R2, R3, R4   │
│ (eq's II.5-8)   │
└─────────────────────────────┘

┌─────────────────────────────┐
│ RES (I, J, K) =   │   (RETURN)
│ $R1^2 + R2^2 +$ │ →
│ $R3^2 + R4^2$ │
└─────────────────────────────┘
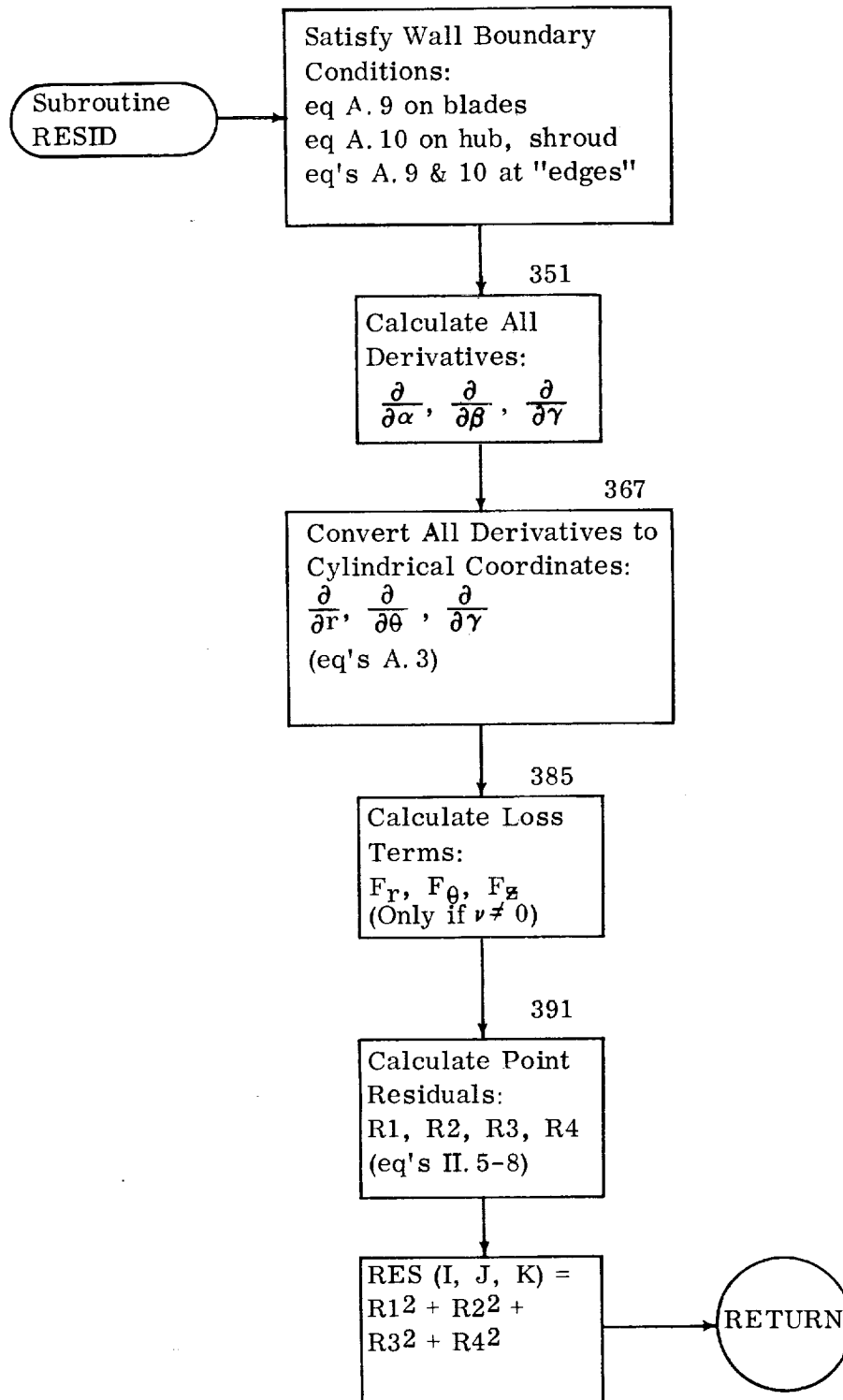
b) **BLOCK DIAGRAM FOR SUBROUTINE "RESID"**

(Numbers above boxes refer to key Fortran statement numbers in the subroutine)

167

FIGURE C.1 (Concluded)

Subroutine ADJ → Temporarily Store Values of the Seven Affected Residuals

$RHLD = R^*_{i,j,k}$

$DX = \delta x$

$HX = x_{i,j,k}$

NOTE: The symbol "x" stands for u, v, w or p.

Do M times   "DO LOOP"

420
$x_{i,j,k} = HX + DX$

445
Restore Local Variables and Affected Residuals to Original Values

421
Recalculate Local Star Residual: $R^*_{i,j,k}$ (eq II. 16)

432
DX = -DX

433
DX = -αDX

RETURN   YES ← Is $R^*_{i,j,k} < RHLD$?   NO →   430 Is DX > 0 ?   YES   NO
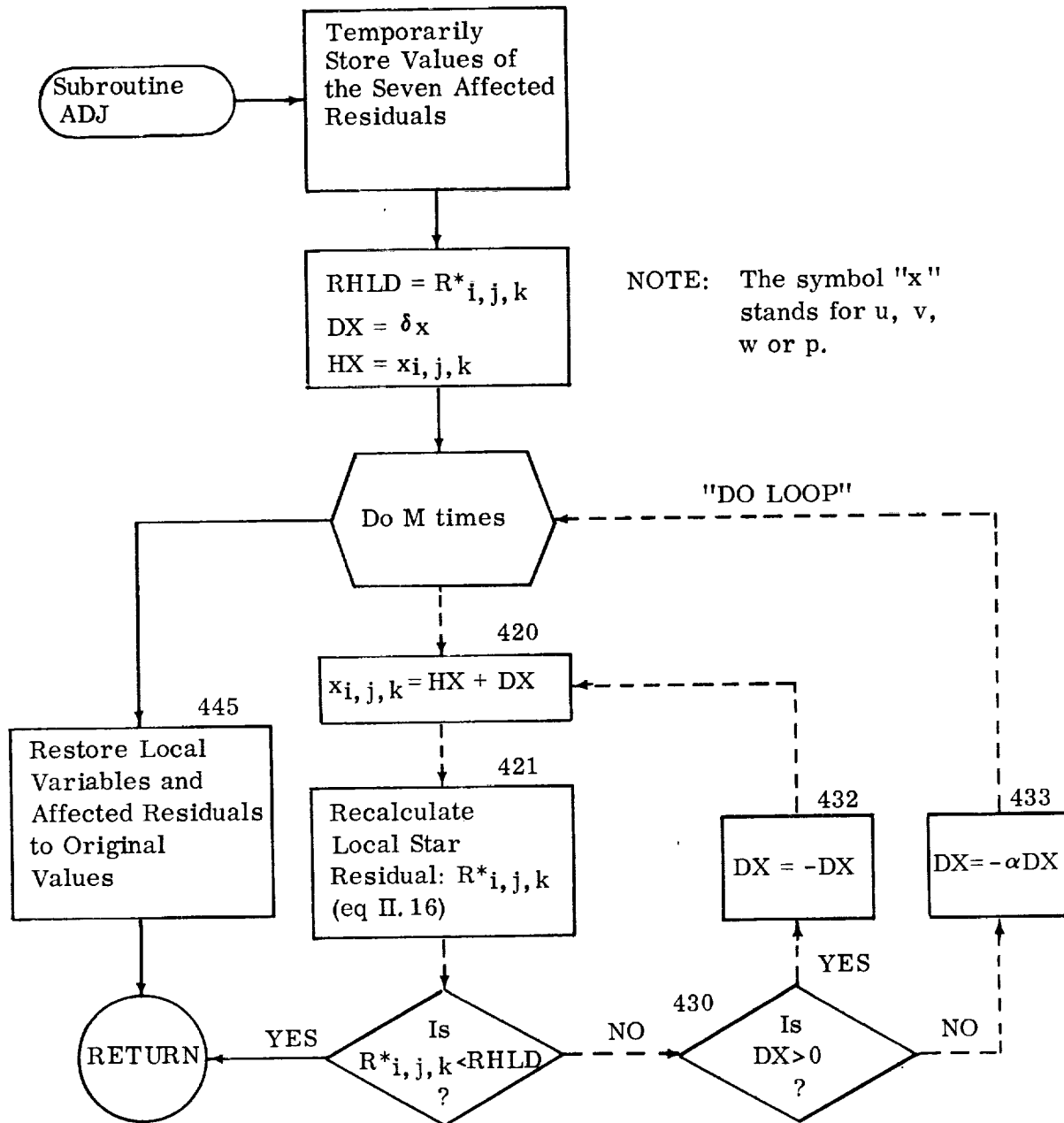
c) BLOCK DIAGRAM FOR SUBROUTINE "ADJ"

(Numbers above boxes refer to key Fortran statements in the subroutine)

TABLE C.1
FORTRAN IV LISTING OF EXACT ANALYSIS COMPUTER PROGRAM

```
C           THREE-DIMENSIONAL FLOW ANALYSIS FOR ROTATING CHANNEL
C           OF ARBITRARY BOUNDARY SHAPE
C           USING METHOD OF STAR RESIDUALS IN TERMS OF
C           RELATIVE VELOCITY COMPONENTS AND PRESSURE
C
C           TRW ACCESSORIES DIVISION, CLEVELAND          6AUG65
C
      DIMENSION TITLE(16)
      COMMON U(10,10,22),V(10,10,22),W(10,10,22),P(10,10,22),
     1 D(10,10,22),R(10,10,22),T(10,10,22),Z(10,10,22),FR,FT,FZ,DMAX(4),
     2 DELX(4),NSEQ(4),      RES(10,10,22),AR(10,10,22),AT(10,10,22),
     3 AZ(10,10,22),BR(10,10,22),BT(10,10,22),BZ(10,10,22),CR(10,10,22),
     4 CT(10,10,22),CZ(10,10,22),XH,RSTAR,TT,PSAT,DLIQ,REV,A,M,NVAR,NTR,
     5 IRSTAR,DX,I,J,K,II,JJ,KK,IMAX,JMAX,KMAX,VISC,NBD,KLE,KTE
      READ 1001, IMAX,JMAX,KMAX,KLE,KTE
      READ 1008,    (((R(I,J,K),I=1,IMAX),J=1,JMAX),K=1,KMAX)
      READ 1008,    (((T(I,J,K),I=1,IMAX),J=1,JMAX),K=1,KMAX)
      READ 1008,    (((Z(I,J,K),I=1,IMAX),J=1,JMAX),K=1,KMAX)
      CALL JACOB
   99 READ 1000,    TITLE
      PRINT 1004, TITLE
      READ 1001, KOUNT,NUM,M,(NSEQ(L),L=1,4)
      READ 1002, (DMAX(L),L=1,4),A,CRIT,E
      READ 1002,      REV,DLIQ,PSAT,TT,VISC
      READ 1002,    (((U(I,J,K),I=1,IMAX),J=1,JMAX),K=1,KMAX)
      READ 1002,    (((V(I,J,K),I=1,IMAX),J=1,JMAX),K=1,KMAX)
      READ 1002,    (((W(I,J,K),I=1,IMAX),J=1,JMAX),K=1,KMAX)
      READ 1002,    (((P(I,J,K),I=1,IMAX),J=1,JMAX),K=1,KMAX)
      NMAX=KOUNT+NUM
      PRINT 1007, IMAX,JMAX,KMAX,M,A,REV,DLIQ,PSAT,TT,VISC
      PRINT 1006, (NSEQ(L),L=1,4)
      NTR=0
      ANR = 4*IMAX*JMAX*KMAX
      DO 150 L=1,4
  150 DELX(L)=DMAX(L)
CALCULATE POINT DENSITIES
      DO 501 K=1,KMAX
      DO 501 J=1,JMAX
      DO 501 I=1,IMAX
      IF(TT)502,503,502
  502 CALL STATE
      GO TO 501
  503 D   (I,J,K)=DLIQ
  501 CONTINUE
CALCULATE ALL POINT RESIDUALS
      NBD=1
      DO 350 K=1,KMAX
      DO 350 J=1,JMAX
      DO 350 I=1,IMAX
      IF(D   (I,J,K))500,500,500
500      CALL RESID
  350 CONTINUE
      PRINT 1012
CALCULATE TOTAL ROOT-MEAN-SQUARE RESIDUAL
  467 RT=0.0
      RESMAX = 0.0
      RESMIN = RES(1,1,1)
      DO 368 K=1,KMAX
      DO 368 J=1,JMAX
      DO 368 I=1,IMAX
```

169

```
         IF(RES(I,J,K)-RESMAX)403,403,402
     402 RESMAX=RES(I,J,K)
         GO TO 368
     403 IF(RES(I,J,K)-RESMIN)404,368,368
     404 RESMIN = RES(I,J,K)
     368 RT=RT+RES(I,J,K)
         RMS = SQRT(RT/ANR)
         RESMAX=SQRT(RESMAX/4.)
         RESMIN=SQRT(RESMIN/4.)
         PRINT 1013, KOUNT,NTR,RMS,RESMAX,RESMIN,(DMAX(L),L=1,4)
         DO 151 L=1,4
     151 DMAX(L)=0.0
         IF(RESMAX-CRIT*E)369,369,370
     370 KOUNT=KOUNT+1
         NTR=0
         IF(KOUNT-NMAX)360,360,371
C-START SUCCESSIVE VARIATIONS CYCLE
     360 DO 460 KK=2,KMAX
         DO 460 JJ=1,JMAX
         DO 460 II=1,IMAX
         IRSTAR=1
         CALL STAR
         DO 460 L=1,4
         NVAR=NSEQ(L)
         GO TO (111,222,333,450),NVAR
     111 IF(KK-2)460,460,611
     611 IF((II-1)*(IMAX-II))460,460,450
     222 IF(KK-2)460,460,481
     481 IF(KK-KMAX)450,482,460
     482 IF((JJ-1)*(JMAX-JJ))460,460,450
     333 IF(KK-2)460,485,486
     485 IF((JJ-1)*(JMAX-JJ))460,460,471
     471 IF((II-1)*(IMAX-II))460,472,450
     472 IF(AZ(II,JJ,KK))460,450,460
     486 IF(KK-KMAX)487,460,460
     487 IF((JJ-1)*(JMAX-JJ))460,460,450
     450 CALL ADJ
     460 CONTINUE
         DO 153 L=1,4
         IF (DMAX(L)) 561,562,561
     561 DELX(L)=DMAX(L)
         GO TO 153
     562 DELX(L)=DELX(L)*A
     153 CONTINUE
         GO TO 467
C        ***      OUTPUT     ROUTINE      ***
      98 PUNCH 1000, TITLE
         KOUNT=KOUNT-1
         PUNCH 1001, KOUNT,NUM,M,(NSEQ(L),L=1,4)
         PUNCH 1002, (DELX(L),L=1,4),A,CRIT,E
         PUNCH 1002, REV,DLIQ,PSAT,TT,VISC
         PUNCH 1002,    (((U(I,J,K),I=1,IMAX),J=1,JMAX),K=1,KMAX)
         PUNCH 1002,    (((V(I,J,K),I=1,IMAX),J=1,JMAX),K=1,KMAX)
         PUNCH 1002,    (((W(I,J,K),I=1,IMAX),J=1,JMAX),K=1,KMAX)
         PUNCH 1002,    (((P(I,J,K),I=1,IMAX),J=1,JMAX),K=1,KMAX)
         PRINT 1004, TITLE
         DO 97 K=1,KMAX
         PRINT 1005
      97 PRINT 1003,   ( (I,J,K,U(I,J,K),V(I,J,K),W(I,J,K),P(I,J,K),D(I,J,K)
        1  ,RES(I,J,K),I=1,IMAX),J=1,JMAX)
```

```
          GO TO 99
      369 PRINT 1014
          GO TO 98
      371 PRINT 1015
          GO TO 98
C     ***        INPUT-OUTPUT    FORMATS      ***
     1000 FORMAT(16A5)
     1001 FORMAT(26I3)
     1002 FORMAT(8F10.7)
     1003 FORMAT(3I3,1P6E18.6)
     1004 FORMAT(16A5///)
     1005 FORMAT(//2X,1HI,2X,1HJ,2X,1HK, 9X,1HU,17X,1HV,17X,1HW,17X,1HP,17X,
         11HD,   15X,3HRES/ )
     1006 FORMAT(2X23HADJUSTMENT SEQUENCE IS ,4I1,38H WHERE U IS 1, V IS 2,
         1W IS 3, P IS 4.///)
     1007 FORMAT(I3,1HX,I2,1HX,I2,5H GRID,6X,2HM=,I2,6X,2HA=,1PE10.4//
         1 5H REV=,1PE10.4,5X,5HDLIQ=,1PE10.4,5X,5HPSAT=,1PE10.4,5X,3HTT=,
         2 1PE10.4,5X,5HVISC=,1PE10.4/)
     1008 FORMAT(1P6E13.7)
     1012 FORMAT(6H RELAX,3X,5HNO OF,5X,9HTOTAL RMS,7X,7HMAX RMS,7X,
         1 7HMIN RMS,16X,44HMAGNITUDE OF BIGGEST ACCEPTED ADJUSTMENT FOR/
         2 6H CYCLE,3X,5HTRIES,3(6X,8HRESIDUAL),17X,1HU,13X,1HV,13X,1HW,
         3 13X,1HP/)
     1013 FORMAT(I6,I8,1P3E14.4,8X,1P4E14.4)
     1014 FORMAT(/20X,9HCONVERGED/)
     1015 FORMAT(/20X,33HMAXIMUM NUMBER OF CYCLES EXECUTED/)
          END
```

```
      SUBROUTINE JACOB
CALCULATION OF JACOBIAN COEFFICIENTS FOR GENERAL-TO-CYLINDRICAL
COORDINATE TRANSFORMATION
      COMMON U(10,10,22),V(10,10,22),W(10,10,22),P(10,10,22),
   1 D(10,10,22),R(10,10,22),T(10,10,22),Z(10,10,22),FR,FT,FZ,DMAX(4),
   2 DELX(4),NSEQ(4),      RES(10,10,22),AR(10,10,22),AT(10,10,22),
   3 AZ(10,10,22),BR(10,10,22),BT(10,10,22),BZ(10,10,22),CR(10,10,22),
   4 CT(10,10,22),CZ(10,10,22),XH,RSTAR,TT,PSAT,DLIQ,REV,A,M,NVAR,NTR,
   5 IRSTAR,DX,I,J,K,II,JJ,KK,IMAX,JMAX,KMAX,VISC,NBD,KLE,KTE
      DO 18 K=1,KMAX
      DO 18 J=1,JMAX
      DO 18 I=1,IMAX
      IF (I-1)3,3,4
   3 RA =    R(I+1,J,K)-R(I,J,K)
     TA =    T(I+1,J,K)-T(I,J,K)
     ZA =    Z(I+1,J,K)-Z(I,J,K)
      GO TO 7
   4 IF (I-IMAX)5,6,6
   5 RA = (R(I+1,J,K)-R(I-1,J,K))/2.
     TA = (T(I+1,J,K)-T(I-1,J,K))/2.
     ZA = (Z(I+1,J,K)-Z(I-1,J,K))/2.
      GO TO 7
   6 RA =    R(I,J,K)-R(I-1,J,K)
     TA =    T(I,J,K)-T(I-1,J,K)
     ZA =    Z(I,J,K)-Z(I-1,J,K)
   7 IF (J-1)8,8,9
   8 RB =    R(I,J+1,K)-R(I,J,K)
     TB =    T(I,J+1,K)-T(I,J,K)
     ZB =    Z(I,J+1,K)-Z(I,J,K)
      GO TO 12
   9 IF (J-JMAX)10,11,11
  10 RB = (R(I,J+1,K)-R(I,J-1,K))/2.
     TB = (T(I,J+1,K)-T(I,J-1,K))/2.
     ZB = (Z(I,J+1,K)-Z(I,J-1,K))/2.
      GO TO 12
  11 RB = R(I,J,K)-R(I,J-1,K)
     TB = T(I,J,K)-T(I,J-1,K)
     ZB = Z(I,J,K)-Z(I,J-1,K)
  12 IF (K-1)13,13,14
  13 RC = R(I,J,K+1)-R(I,J,K)
     TC = T(I,J,K+1)-T(I,J,K)
     ZC = Z(I,J,K+1)-Z(I,J,K)
      GO TO 17
  14 IF (K-KMAX)15,16,16
  15 RC = (R(I,J,K+1)-R(I,J,K-1))/2.
     TC = (T(I,J,K+1)-T(I,J,K-1))/2.
     ZC = (Z(I,J,K+1)-Z(I,J,K-1))/2.
      GO TO 17
  16 RC = R(I,J,K)-R(I,J,K-1)
     TC = T(I,J,K)-T(I,J,K-1)
     ZC = Z(I,J,K)-Z(I,J,K-1)
  17 D = RA*(TB*ZC-TC*ZB)+RB*(TC*ZA-TA*ZC)+RC*(TA*ZB-TB*ZA)
     AR(I,J,K)=(TB*ZC-TC*ZB)/D
     BR(I,J,K)=(TC*ZA-TA*ZC)/D
     CR(I,J,K)=(TA*ZB-TB*ZA)/D
     AT(I,J,K)=(ZB*RC-ZC*RB)/D
     BT(I,J,K)=(ZC*RA-ZA*RC)/D
     CT(I,J,K)=(ZA*RB-ZB*RA)/D
     AZ(I,J,K)=(RB*TC-RC*TB)/D
     BZ(I,J,K)=(RC*TA-RA*TC)/D
```

```
18 CZ(I,J,K)=(RA*TB-RB*TA)/D
   RETURN
   END
```

```
      SUBROUTINE ADJ
C-REDUCTION OF TOTAL RESIDUAL BY SUCCESSIVE VARIATIONS OF U, V, W, P
      COMMON U(10,10,22),V(10,10,22),W(10,10,22),P(10,10,22),
     1 D(10,10,22),R(10,10,22),T(10,10,22),Z(10,10,22),FR,FT,FZ,DMAX(4),
     2 DELX(4),NSEQ(4),      RES(10,10,22),AR(10,10,22),AT(10,10,22),
     3 AZ(10,10,22),BR(10,10,22),BT(10,10,22),BZ(10,10,22),CR(10,10,22),
     4 CT(10,10,22),CZ(10,10,22),XH,RSTAR,TT,PSAT,DLIG,REV,A,M,NVAR,NTR,
     5 IRSTAR,DX,I,J,K,II,JJ,KK,IMAX,JMAX,KMAX,VISC,NBD,KLE,KTE
CURRENT VALUES OF ALL AFFECTED QUANTITIES TEMPORARILY STORED
      H1=RES(II,JJ,KK)
      H2=RES(II-1,JJ,KK)
      H3=RES(II+1,JJ,KK)
      H4=RES(II,JJ-1,KK)
      H5=RES(II,JJ+1,KK)
      H6=RES(II,JJ,KK-1)
      H7=RES(II,JJ,KK+1)
      RHLD=RSTAR
      DX=DELX(NVAR)
      HU=U(II,JJ,KK)
      HV=V(II,JJ,KK)
      HW=W(II,JJ,KK)
      HP=P(II,JJ,KK)
      HD=D(II,JJ,KK)
C-SUCCESSIVELY APPLY TRIAL VARIATIONS TO U, V, W, P
    5 DO 480 MA=1,M
  420 GO TO (422,423,424,425),NVAR
  422 U(II,JJ,KK)=HU+DX
      GO TO 421
  423 V(II,JJ,KK)=HV+DX
      GO TO 421
  424 W(II,JJ,KK)=HW+DX
      GO TO 421
  425 P(II,JJ,KK)=HP+DX
      IF(TT)461,421,461
  461 I=II
      J=JJ
      K=KK
      CALL STATE
  421 NTR=NTR+1
      IRSTAR=2
      CALL STAR
      IF(RHLD-RSTAR)430,430,431
  431 IF(ABS(DX)-DMAX(NVAR))457,457,920
  920 DMAX(NVAR)=ABS(DX)
      GO TO 457
  430 IF(DX)433,457,432
  432 DX=-DX
      GO TO 420
  433 DX=-A*DX
  480 CONTINUE
C-RESTORE ALL AFFECTED QUANTITIES TO ORIGINAL VALUES
      U(II,JJ,KK)=HU
      V(II,JJ,KK)=HV
      W(II,JJ,KK)=HW
      P(II,JJ,KK)=HP
      D(II,JJ,KK)=HD
  445 RSTAR=RHLD
      RES(II,JJ,KK)=H1
      IF(II-1)446,446,447
  447 RES(II-1,JJ,KK)=H2
```

```
446 IF(II-IMAX)449,448,448
449 RES(II+1,JJ,KK)=H3
448 IF(JJ-1)450,450,451
451 RES(II,JJ-1,KK)=H4
450 IF(JJ-JMAX)453,452,452
453 RES(II,JJ+1,KK)=H5
452 IF(KK-1)454,454,455
455 RES(II,JJ,KK-1)=H6
454 IF(KK-KMAX)456,457,457
456 RES(II,JJ,KK+1)=H7
457 RETURN
    END
```

```
      SUBROUTINE DLOSS
CALCULATION OF LOSS TERMS IN MOMENTUM EQUATIONS
      COMMON U(10,10,22),V(10,10,22),W(10,10,22),P(10,10,22),
     1 D(10,10,22),R(10,10,22),T(10,10,22),Z(10,10,22),FR,FT,FZ,DMAX(4),
     2 DELX(4),NSEQ(4),     RES(10,10,22),AR(10,10,22),AT(10,10,22),
     3 AZ(10,10,22),BR(10,10,22),BT(10,10,22),BZ(10,10,22),CR(10,10,22),
     4 CT(10,10,22),CZ(10,10,22),XH,RSTAR,TT,PSAT,DLIQ,REV,A,M,NVAR,NTR,
     5 IRSTAR,DX,I,J,K,II,JJ,KK,IMAX,JMAX,KMAX,VISC,NBD,KLE,KTE
      FR=0.0
      FT=0.0
      FZ=0.0
      RETURN
      END
```

```
      SUBROUTINE RESID
CALCULATION OF POINT RESIDUAL
      COMMON U(10,10,22),V(10,10,22),W(10,10,22),P(10,10,22),
     1 D(10,10,22),R(10,10,22),T(10,10,22),Z(10,10,22),FR,FT,FZ,DMAX(4),
     2 DELX(4),NSEQ(4),     RES(10,10,22),AR(10,10,22),AT(10,10,22),
     3 AZ(10,10,22),BR(10,10,22),BT(10,10,22),BZ(10,10,22),CR(10,10,22),
     4 CT(10,10,22),CZ(10,10,22),XH,RSTAR,TT,PSAT,DLIQ,REV,A,M,NVAR,NTR,
     5 IRSTAR,DX,I,J,K,II,JJ,KK,IMAX,JMAX,KMAX,VISC,NBD,KLE,KTE
      IF(NBD)400,351,99
CHECK WALL BOUNDARY CONDITIONS
   99 IF(K-2)351,100,103
C     ***     K=2     ***
  100 IF((I-1)*(IMAX-I))400,121,124
  121 IF((J-1)*(JMAX-J))400,102,122
  122 IF(AZ(I,J,K))123,351,123
  123 W(I,J,K)=-U(I,J,K)*AR(I,J,K)/AZ(I,J,K)
      GO TO 351
  124 IF((J-1)*(JMAX-J))400,111,351
  102 DDD=(BT(I,J,K)/R(I,J,K))/(AR(I,J,K)*BZ(I,J,K)-BR(I,J,K)*AZ(I,J,K))
      W(I,J,K) = -V(I,J,K)*AR(I,J,K)*DDD
      GO TO 351
  103 IF(K-KMAX)108,104,400
C     ***     K=KMAX     ***
  104 IF((I-1)*(IMAX-I))400,105,106
  105 U(I,J,K) = -W(I,J,K)*AZ(I,J,K)/AR(I,J,K)
  106 IF((J-1)*(JMAX-J))400,107,351
  107 V(I,J,K) = -R(I,J,K)*(U(I,J,K)*BR(I,J,K)+W(I,J,K)*BZ(I,J,K))/
     1      BT(I,J,K)
      GO TO 351
C     ***     K IS NEITHER 2 NOR KMAX     ***
  108 IF((I-1)*(IMAX-I))400,109,110
  109 IF((J-1)*(JMAX-J))400,112,114
  110 IF((J-1)*(JMAX-J))400,111,351
  111 W(I,J,K) = -(U(I,J,K)*BR(I,J,K)+V(I,J,K)*BT(I,J,K)/R(I,J,K))/
     1            BZ(I,J,K)
      GO TO 351
  112 DDD=(BT(I,J,K)/R(I,J,K))/(AR(I,J,K)*BZ(I,J,K)-BR(I,J,K)*AZ(I,J,K))
      W(I,J,K) = -V(I,J,K)*AR(I,J,K)*DDD
      U(I,J,K) = V(I,J,K)*AZ(I,J,K)*DDD
      GO TO 351
  114 U(I,J,K) = -W(I,J,K)*AZ(I,J,K)/AR(I,J,K)
CALCULATE ALL DERIVATIVES
  351 IF(I-1)400,354,353
  354 UA=(U(I+1,J,K)-U(I,J,K))
      VA=(V(I+1,J,K)-V(I,J,K))
      WA=(W(I+1,J,K)-W(I,J,K))
      PA=(P(I+1,J,K)-P(I,J,K))
      IF(TT)511,357,511
  511 DA=(D(I+1,J,K)-D(I,J,K))
      GO TO 357
  353 IF(I-IMAX)355,356,400
  355 UA=(U(I,J,K)-U(I-1,J,K))
      VA=(V(I,J,K)-V(I-1,J,K))
      WA=(W(I,J,K)-W(I-1,J,K))
      PA=(P(I,J,K)-P(I-1,J,K))
      IF(TT)521,357,521
  521 DA=(D(I,J,K)-D(I-1,J,K))
      GO TO 357
  355 UA=(U(I+1,J,K)-U(I-1,J,K))/ 2.
      VA=(V(I+1,J,K)-V(I-1,J,K))/ 2.
```

```
      WA=(W(I+1,J,K)-W(I-1,J,K))/ 2.
      PA=(P(I+1,J,K)-P(I-1,J,K))/ 2.
      IF(TT)531,357,531
  531 DA=(D(I+1,J,K)-D(I-1,J,K))/ 2.
  357 IF(J-1)400,359,358
  359 UB=(U(I,J+1,K)-U(I,J,K))
      VB=(V(I,J+1,K)-V(I,J,K))
      WB=(W(I,J+1,K)-W(I,J,K))
      PB=(P(I,J+1,K)-P(I,J,K))
      IF(TT)541,362,541
  541 DB=(D(I,J+1,K)-D(I,J,K))
      GO TO 362
  358 IF(J-JMAX)360,361,400
  361 UB=(U(I,J,K)-U(I,J-1,K))
      VB=(V(I,J,K)-V(I,J-1,K))
      WB=(W(I,J,K)-W(I,J-1,K))
      PB=(P(I,J,K)-P(I,J-1,K))
      IF(TT)551,362,551
  551 DB=(D(I,J,K)-D(I,J-1,K))
      GO TO 362
  360 UB=(U(I,J+1,K)-U(I,J-1,K))/ 2.
      VB=(V(I,J+1,K)-V(I,J-1,K))/ 2.
      WB=(W(I,J+1,K)-W(I,J-1,K))/ 2.
      PB=(P(I,J+1,K)-P(I,J-1,K))/ 2.
      IF(TT)561,362,561
  561 DB=(D(I,J+1,K)-D(I,J-1,K))/ 2.
  362 IF(K-1)400,364,363
  364 UC=(U(I,J,K+1)-U(I,J,K))
      VC=(V(I,J,K+1)-V(I,J,K))
      WC=(W(I,J,K+1)-W(I,J,K))
      PC=(P(I,J,K+1)-P(I,J,K))
      IF(TT)571,367,571
  571 DC=(D(I,J,K+1)-D(I,J,K))
      GO TO 367
  363 IF(K-KMAX)365,366,400
  366 UC=(U(I,J,K)-U(I,J,K-1))
      VC=(V(I,J,K)-V(I,J,K-1))
      WC=(W(I,J,K)-W(I,J,K-1))
      PC=(P(I,J,K)-P(I,J,K-1))
      IF(TT)581,367,581
  581 DC=(D(I,J,K)-D(I,J,K-1))
      GO TO 367
  365 UC=(U(I,J,K+1)-U(I,J,K-1))/ 2.
      VC=(V(I,J,K+1)-V(I,J,K-1))/ 2.
      WC=(W(I,J,K+1)-W(I,J,K-1))/ 2.
      PC=(P(I,J,K+1)-P(I,J,K-1))/ 2.
      IF(TT)591,367,591
  591 DC=(D(I,J,K+1)-D(I,J,K-1))/ 2.
CONVERT ALL DERIVATIVES FROM GENERAL TO CYLINDRICAL COORDINATES
  367 UR=AR(I,J,K)*UA+BR(I,J,K)*UB+CR(I,J,K)*UC
      UT=AT(I,J,K)*UA+BT(I,J,K)*UB+CT(I,J,K)*UC
      UZ=AZ(I,J,K)*UA+BZ(I,J,K)*UB+CZ(I,J,K)*UC
      VR=AR(I,J,K)*VA+BR(I,J,K)*VB+CR(I,J,K)*VC
      VT=AT(I,J,K)*VA+BT(I,J,K)*VB+CT(I,J,K)*VC
      VZ=AZ(I,J,K)*VA+BZ(I,J,K)*VB+CZ(I,J,K)*VC
      WR=AR(I,J,K)*WA+BR(I,J,K)*WB+CR(I,J,K)*WC
      WT=AT(I,J,K)*WA+BT(I,J,K)*WB+CT(I,J,K)*WC
      WZ=AZ(I,J,K)*WA+BZ(I,J,K)*WB+CZ(I,J,K)*WC
      PR=AR(I,J,K)*PA+BR(I,J,K)*PB+CR(I,J,K)*PC
      PT=AT(I,J,K)*PA+BT(I,J,K)*PB+CT(I,J,K)*PC
```

```
          PZ=AZ(I,J,K)*PA+BZ(I,J,K)*PB+CZ(I,J,K)*PC
          IF(TT)370,375,370
      370 DR=AR(I,J,K)*DA+BR(I,J,K)*DB+CR(I,J,K)*DC
          DT=AT(I,J,K)*DA+BT(I,J,K)*DB+CT(I,J,K)*DC
          DZ=AZ(I,J,K)*DA+BZ(I,J,K)*DB+CZ(I,J,K)*DC
          GO TO 380
      375 DR=0.0
          DT=0.0
          DZ=0.0
      380 UU=U(I,J,K)
          VV=V(I,J,K)
          WW=W(I,J,K)
          DD=D(I,J,K)
          RR=R(I,J,K)
CALCULATE LOSS TERMS
          IF(VISC)385,390,385
      385 CALL DLOSS
          GO TO 391
      390 FR=0.0
          FT=0.0
          FZ=0.0
CALCULATE POINT RESIDUAL
      391 R1=PR/DD  +UU*UR+VV*UT/RR+WW*UZ-((VV+RR*REV)**2.)/RR+FR
          R2=PT/(DD*RR)+UU*VR+VV*VT/RR+WW*VZ+UU*VV/RR+2.*UU*REV+FT
          R3=PZ/DD+UU*WR+VV*WT/RR+WW*WZ+FZ
          R4=UU/RR+UR+VT/RR+WZ+(UU*DR  +VV*DT  /RR+WW*DZ  )/DD
          RES(I,J,K)=R1*R1+R2*R2+R3*R3+(R4*REV*R(5,1,KLE))**2.
      400 RETURN
          END
```

```
      SUBROUTINE STAR
CALCULATION OF LOCAL STAR RESIDUAL
      COMMON U(10,10,22),V(10,10,22),W(10,10,22),P(10,10,22),
     1 D(10,10,22),R(10,10,22),T(10,10,22),Z(10,10,22),FR,FT,FZ,DMAX(4),
     2 DELX(4),NSEQ(4),      RES(10,10,22),AR(10,10,22),AT(10,10,22),
     3 AZ(10,10,22),BR(10,10,22),BT(10,10,22),BZ(10,10,22),CR(10,10,22),
     4 CT(10,10,22),CZ(10,10,22),XH,RSTAR,TT,PSAT,DLIQ,REV,A,M,NVAR,NTR,
     5 IRSTAR,DX,I,J,K,II,JJ,KK,IMAX,JMAX,KMAX,VISC,NBD,KLE,KTE
      RSTAR=0.0
      IGO=0
      I=II
      J=JJ
      K=KK
      NBD=1
  389 GO TO(375,378),IRSTAR
  378 CALL RESID
  375 RSTAR=RSTAR+RES(I,J,K)
      NBD=0
  400 IGO=IGO+1
      GO TO (391,392,393,394,395,396,402),IGO
  391 I=II-1
      IF(I-1)400,389,389
  392 I=II+1
      IF(I-IMAX)389,389,400
  393 I=II
      J=JJ-1
      IF(J-1)400,389,389
  394 J=JJ+1
      IF(J-JMAX)389,389,400
  395 J=JJ
      K=KK-1
      IF(K-1)400,389,389
  396 K=KK+1
      IF(K-KMAX)389,389,400
  402 RETURN
      END
```

```
      SUBROUTINE STATE
CALCULATION OF POINT DENSITY
      COMMON U(10,10,22),V(10,10,22),W(10,10,22),P(10,10,22),
     1 D(10,10,22),R(10,10,22),T(10,10,22),Z(10,10,22),FR,FT,FZ,DMAX(4),
     2 DELX(4),NSEQ(4),     RES(10,10,22),AR(10,10,22),AT(10,10,22),
     3 AZ(10,10,22),BR(10,10,22),BT(10,10,22),BZ(10,10,22),CR(10,10,22),
     4 CT(10,10,22),CZ(10,10,22),XH,RSTAR,TT,PSAT,DLIQ,REV,A,M,NVAR,NTR,
     5 IRSTAR,DX,I,J,K,II,JJ,KK,IMAX,JMAX,KMAX,VISC,NBD,KLE,KTE
      PSP=PSAT-P(I,J,K)
      IF(PSP)101,101,102
  101 D(I,J,K) = DLIQ
      GO TO 103
  102 D(I,J,K) = DLIQ/(1.+TT*PSP)
  103 RETURN
      END
```

```
C         DATA REDUCTION PROGRAM FOR RESULTS OF EXACT
C         THREE-DIMENSIONAL INDUCER ANALYSIS PROGRAM
C
C            TRW ACCESSORIES DIVISION, CLEVELAND            6AUG65
C
      DIMENSION TITLE(16)
      COMMON U(10,10,22),V(10,10,22),W(10,10,22),P(10,10,22),D(10,10,22)
     1 ,R(10,10,22),T(10,10,22),Z(10,10,22),A(10,10,22),Q(10,10,22),
     2 UB(10,22),VB(10,22),WB(10,22),PB(10,22),DB(10,22),RB(10,22),
     3 DELP(10,22),X(10,10),Y(10,10),REV,DLIQ,PSAT,TT,IGO,I,J,K,IMAX,
     4 JMAX,KMAX,IM1,JM1,B,SUB,TOT,QTOT
      READ 1001,IMAX,JMAX,KMAX,KLE,KTE
      READ 1003,(((R(I,J,K),I=1,IMAX),J=1,JMAX),K=1,KMAX)
      READ 1003,(((T(I,J,K),I=1,IMAX),J=1,JMAX),K=1,KMAX)
      READ 1003,(((Z(I,J,K),I=1,IMAX),J=1,JMAX),K=1,KMAX)
  999 READ 1000,TITLE
      PRINT 1000,TITLE
      READ 1001,KOUNT
      PRINT 1012,KOUNT
      READ 1002,BLANK
      READ 1002,REV,DLIQ,PSAT,TT
      READ 1002,(((U(I,J,K),I=1,IMAX),J=1,JMAX),K=1,KMAX)
      READ 1002,(((V(I,J,K),I=1,IMAX),J=1,JMAX),K=1,KMAX)
      READ 1002,(((W(I,J,K),I=1,IMAX),J=1,JMAX),K=1,KMAX)
      READ 1002,(((P(I,J,K),I=1,IMAX),J=1,JMAX),K=1,KMAX)
CONVERT FROM ABSOLUTE TO RELATIVE VELOCITIES AND
CALCULATE POINT DENSITIES
      DO 1 K=1,KMAX
      DO 1 J=1,JMAX
      DO 1 I=1,IMAX
      V(I,J,K)=R(I,J,K)*REV+V(I,J,K)
      IF(TT)2,3,2
    2 PSP=PSAT-P(I,J,K)
      IF(PSP)3,3,21
   21 D(I,J,K)=DLIQ/(1.+TT*PSP)
      GO TO 1
    3 D(I,J,K)=DLIQ
    1 CONTINUE
CALCULATE INCREMENTAL THROUGHFLOW AREAS AND MASS FLOW RATES
      IM1=IMAX-1
      JM1=JMAX-1
      DO 4 K=1,KMAX
      DO 4 I=1,IM1
      RB(I,K)=(R(I,1,K)+R(I+1,1,K))/2.
      DO 4 J=1,JM1
      A(I,J,K)=RB(I,K)*(R(I+1,1,K)-R(I,1,K))*(T(I+1,J+1,K)+T(I,J+1,K)
     1         -T(I+1,J,K)-T(I,J,K))/2.
    4 Q(I,J,K)=A(I,J,K)*(W(I,J,K)+W(I,J+1,K)+W(I+1,J,K)+W(I+1,J+1,K))*
     1         (D(I,J,K)+D(I,J+1,K)+D(I+1,J,K)+D(I+1,J+1,K))/16.
CALCULATE AREA-AVERAGED QUANTITIES
      DO 6 IGO=1,5
      DO 6 K=1,KMAX
      DO 5 J=1,JMAX
      DO 5 I=1,IMAX
      GO TO (51,52,53,54,55),IGO
   51 X(I,J)=U(I,J,K)
      GO TO 5
   52 X(I,J)=V(I,J,K)
      GO TO 5
   53 X(I,J)=W(I,J,K)
```

182

```
         GO TO 5
      54 X(I,J)=P(I,J,K)
         GO TO 5
      55 X(I,J)=D(I,J,K)
       5 Y(I,J)=A(I,J,K)
         DO 6 I=1,IM1
         CALL SUM
         GO TO (61,62,63,64,65),IGO
      61 UB(I,K)=SUB/TOT
         GO TO 6
      62 VB(I,K)=SUB/TOT
         GO TO 6
      63 WB(I,K)=SUB/TOT
         GO TO 6
      64 PB(I,K)=SUB/TOT
         GO TO 6
      65 DB(I,K)=SUB/TOT
       6 CONTINUE
   CALCULATE MASS FLOW RATE PER CHANNEL
         QTOT=0.0
         DO 7 I=1,IM1
         DO 7 J=1,JM1
       7 QTOT=QTOT+Q(I,J,1)
   CALCULATE MASS-AVERAGED QUANTITIES
         K=KLE
      80 DO 8 IGO=1,3
         CALL MAV
         GO TO (81,82,83),IGO
      81 PD=B
         GO TO 8
      82 V2=B
         GO TO 8
      83 UV=B
       8 CONTINUE
         IF(K-1)10,9,10
       9 PDIN=PD
         V2IN=V2/2.
         UVIN=UV
         K=KTE
         GO TO 80
      10 PDEX=PD
         V2EX=V2/2.
         UVEX=UV
         DH=PDEX+V2EX-PDIN-V2IN
         PSH=(UVEX-UVIN)*QTOT
         EFF=DH*QTOT/PSH
   CALCULATE BLADE-TO-BLADE PRESSURE LOADING
         DO 12 K=1,KMAX
         DO 12 I=1,IMAX
      12 DELP(I,K)=P(I,1,K)-P(I,JMAX,K)
   C     ***      OUTPUT     ROUTINE      ***
         PRINT 1004
         DO 11 K=1,KMAX
         IF(K-KLE)111,112,113
     112 PRINT 1005
         GO TO 111
     113 IF(K-KTE)111,114,111
     114 PRINT 1006
     111 PRINT 1007, Z(1,1,K),RB(1,K),UB(1,K),VB(1,K),WB(1,K),PB(1,K),
        1             DB(1,K)
```

183

```
   11 PRINT 1008,(RB(I,K),UB(I,K),VB(I,K),WB(I,K),PB(I,K),DB(I,K),
      1             I=2,IM1)
      PRINT 1010
      DO 131 K=1,KMAX
      IF(K-KLE)131,132,133
  132 PRINT 1005
      GO TO 131
  133 IF(K-KTE)131,134,131
  134 PRINT 1006
  131 PRINT 1011,Z(1,1,K),(DELP(I,K),I=1,IMAX)
      PRINT 1009, PDIN,PDEX,V2IN,V2EX,DH,PSH,EFF,QTOT
      GO TO 999
C     ***      INPUT-OUTPUT    FORMATS      ***
 1000 FORMAT(16A5)
 1001 FORMAT(26I3)
 1002 FORMAT(8F10.7)
 1003 FORMAT(1P6E13.7)
 1004 FORMAT(//10X52HHUB-TO-TIP DISTRIBUTOINS OF AREA-AVERAGED QUANTITIF
     1S///    10X5HAXIAL,2(9X6HRADIAL),5X10HTANGENTIAL,10X5HAXIAL,
     1    9X6HSTATIC/2(8X7HSTATION),3(7X8HVELOCITY),7X8HPRESSURE,
     2    8X7HDENSITY//)
 1005 FORMAT(1X18HBLADE LEADING EDGE)
 1006 FORMAT(1X19HBLADE TRAILING EDGE)
 1007 FORMAT(/7F15.5)
 1008 FORMAT(15X6F15.5)
 1009 FORMAT(///20X24HMASS-AVERAGED QUANTITIES//2(10X5HINLET,11X4HEXIT),
     1 10X5HTOTAL,8X7HCHANNEL,8X7HOVERALL,8X7HCHANNEL/2(7X8HPRESSURE),
     2 2(7X8HVELOCITY),11X4HHEAD,10X5HSHAFT,5X10HEFFICIENCY,
     3 6X9HMASS-FLOW/4(11X4HHEAD),11X4HRISE,10X5HPOWER,26X4HRATE//8F15.5
 1010 FORMAT(//2X9HZ-STATION,9X58HHUB-TO-TIP DISTRIBUTION OF BLADE-TO-BL
     1ADE PRESSURE LOADING//)
 1011 FORMAT(  F11.4,9X1P10E10.4)
 1012 FORMAT(/23HREDUCED OUTPUT OF CYCLE,I3)
      END
```

184

```
      SUBROUTINE SUM
CALCULATE WEIGHTED SUM
      COMMON U(10,10,22),V(10,10,22),W(10,10,22),P(10,10,22),D(10,10,22)
     1 ,R(10,10,22),T(10,10,22),Z(10,10,22),A(10,10,22),Q(10,10,22),
     2 UB(10,22),VB(10,22),WB(10,22),PB(10,22),DB(10,22),RB(10,22),
     3 DELP(10,22),X(10,10),Y(10,10),REV,DLIQ,PSAT,TT,IGO,I,J,K,IMAX,
     4 JMAX,KMAX,IM1,JM1,B,SUB,TOT,QTOT
      SUB=0.0
      TOT=0.0
      DO 1 J=1,JM1
      SUB=SUB+Y(I,J)*(X(I,J)+X(I,J+1)+X(I+1,J)+X(I+1,J+1))/4.
    1 TOT=TOT+Y(I,J)
      RETURN
      END
```

```
      SUBROUTINE MAV
CALCULATE MASS-AVERAGES
      COMMON U(10,10,22),V(10,10,22),W(10,10,22),P(10,10,22),D(10,10,22)
     1 ,R(10,10,22),T(10,10,22),Z(10,10,22),A(10,10,22),Q(10,10,22),
     2 UB(10,22),VB(10,22),WB(10,22),PB(10,22),DB(10,22),RB(10,22),
     3 DELP(10,22),X(10,10),Y(10,10),REV,DLIQ,PSAT,TT,IGO,I,J,K,IMAX,
     4 JMAX,KMAX,IM1,JM1,B,SUB,TOT,QTOT
      DO 10 J=1,JMAX
      DO 10 I=1,IMAX
      GO TO (1,2,3),IGO
    1 X(I,J)=P(I,J,K)/D(I,J,K)
      GO TO 10
    2 X(I,J)=U(I,J,K)**2+V(I,J,K)**2+W(I,J,K)**2
      GO TO 10
    3 X(I,J)=R(I,J,K)*REV*V(I,J,K)
   10 Y(I,J)=Q(I,J,K)
      B=0.0
      DO 20 I=1,IM1
      CALL SUM
   20 B=B+SUB
      B=B/QTOT
      RETURN
      END
```

APPENDIX D

INSTRUCTIONS FOR USE OF APPROXIMATE
SOLUTION COMPUTER PROGRAM

This appendix describes the approximate analysis program including its two subroutines. The latter one of these finds blade coordinates for any full blades having radial elements, constant thickness with or without radial taper and leading edge faring, and a quadratically-varying lead. Any other shape would require a new blade coordinate subroutine. The inputs and outputs are described, and block diagrams are included with a complete Fortran IV listing.

1. Computer Running Information

   The main program and its two subroutines have a common storage requirement of 13,513 locations. The maximum field capability is 11 streamlines including hub and shroud, and 21 stations including blade leading and trailing edges; i.e. an 11 x 21 field. The minimum is a 2 x 2 field.

   Computer running time depends on the size of the field and the accuracy required. The following estimates roughly summarize our experience on computer times:

   a) Time α No. stations

   b) Time α (No. streamlines)^4

   c) Time α $\sqrt[3]{\dfrac{1}{\text{allowable unbalance}}}$

   d) Time at stations where two-phase flow exists is double that for incompressible flow.

   For example, an 8 x 16 field with incompressible flow and an allowable unbalance of .001 took about 400 seconds on a UNIVAC 1107, while a .01 unbalance took 185 seconds. A similar 4 x 6 field at .001 balance took 24 seconds.

2. Input Data

   The inputs to the program consist of (a) the title and program control numbers; (b) the geometrical data for locating quasi-normal stations and the streamlines at the blade leading edge; (c) the blade contour data; (d) the speed, fluid properties and accuracy required; (e) the distributions of fluid pressure, velocity and density at inlet; and (f) the various sets of

fluid data ν, p_{sat} and T^* for which solutions with the foregoing inputs are desired. Note that for splitter blades a separate problem should be solved up to the splitter point, and the output should be used with a change in the number of blades n_b to solve a new problem downstream of that point.

Following is a definition of each program input in the order required by the computer; (the format is given in the Fortran listing):

TITLE: Any identifying information consuming up to 80 spaces.

NQI, NQJ: The number of streamlines (i or I) and one more than the number of stations (j or J) respectively. The extra station J = NQJ is required for blade angle data at station J = NQJ-1. I = 1 on the hub, and I = NQI on the shroud; J = 1 on the blade leading edge and J = NQJ-1 on the blade trailing edge. The "field" stated in table III. 1 quotes NQI x (NQJ-1), = q_i x q_j

MNC: The maximum allowable number of hub-to-shroud iteration cycles at any one station. This limits the running time if the maximum allowable streamline unbalance error EN (see below) is too small. In such a case the computing continues and the resulting maximum unbalance is printed out. We used MNC = 25 in our 4 x 16 runs, (see results in table III. 1), and 1000 for 8 x 16. The actual number of cycles NC is dependent on EN and was usually 1/4 to 1/2 of MNC except in two-phase cases.

NDATA: The output data control number, specified as 0, 1, or 2. The use of NDATA is described in the output description further on. This number makes it possible to omit all field data between the inlet and outlet, thus saving considerable computing time when several runs with small fields (say 4 x 16) are required simply to establish overall performance at various combinations of R_m, NPSH, and T^*. With a 4 x 16 field, up to half the running time is consumed in the format and printing activity of the computer.

NDB: A control number that is normally equal to zero. If NDB = 1, a cycle-by-cycle account of the reduction of the total unbalance $\left(\dfrac{\rho_f}{g_o} \sum\limits_i U_i, j \right)$ is printed out together with the attendant streamline adjustment magnitudes $\delta n'$ for stations
$2 \leq J \leq$ NQJ-1. Following are the geometrical inputs:

Z(I, 1):   The inlet axial positions z_i of streamlines at J = 1 from hub to tip. $1 \leq I \leq$ NQI.

R(I, 1):   The radial positions r_i at J = 1. $1 \leq I \leq$ NQI.

188

Z(1, J):   The axial positions of the stations j along the hub; i. e., the locations of the hub-ends of the quasi-normals.

$$I = 1 \text{ and } 2 \leq J \leq NQJ.$$

R(1, J):   The radial positions of the stations along the hub. $I = 1$ and $2 \leq J \leq NQJ$.

Z(NQI, J) and R(NQI, J):   The axial and radial positions respectively along the shroud.

$$I = NQI \text{ and } 2 \leq J \leq NQJ.$$

At this point, the following data is required by the blade subroutine:

AA, BB, CC: The lead constants a, b, and c respectively, which described the radial-element pressure side of the blade according to the formula

$$\frac{d\theta}{dz} = a + bz + cz^2 \tag{D.1}$$

DSEX: The exit boundary layer displacement thickness δ_{ex}^*, which is assumed to exist on each side of the blade. The program distributes δ^* linearly by station from zero at inlet, adding it to the blade thickness.

T1T: The blade thickness t at the radial location R1T — usually at the inlet tip.

DTR: The radial blade taper constant where the blade thickness throughout the machine (except in the fared region) is a function of radius only and is given by

$$t = (T1T) + \frac{dt}{dr} \left[(R1T) - r \right] \tag{D.2}$$

We used no taper in our tuns.

ANB: The number of blades n_b

TF(1,2,3):   The blade suction-side fairing constants at stations 1, 2, and 3. The blade thickness t at these stations is given by the product of TF and the t of equation (A.2). $0 \leq TF \leq 1$, and all material is removed from the suction side only. We used TF(1) = 0 and TF(2 and 3) = 1. Continuing now with the remaining inputs to the main program, we have the fluid data:

EN: The maximum allowable streamline unbalance $\frac{\rho_f}{g_o} U_{max}$.

As noted earlier, this value is exceeded if a balance cannot be achieved in MNC cycles at any station J.

RHOF: The liquid density ρ_f

OMEGA: The rotative speed Ω, radians per unit time.

GO: Constant in Newton's second law, g_o

RHO (I, 1):   The fluid density ρ_i' in the middle of each annulus i or I at the blade leading edge where J = 1. $1 \leq I \leq NQI-1$, since the number of annuli is one less than the number of streamlines.

P(I, 1):   The fluid static pressure p_i' in each annulus. J = 1 and $1 \leq I \leq NQI-1$.

VM1(I):   The velocity component in each annulus normal to the blade leading edge at that point in the meridional plane. $1 \leq I \leq NQI-1$.

DELTAE(I):   The exit deviation angle $\delta_{ex,i}'$ of the relative flow from the direction of the blade in each annulus. This deviation is distributed from zero at inlet according to the sixth power of the number of stations ($\approx m^6$), thus approximating an unloading condition near the outlet. We used $\delta_{ex} = 0$ for all our runs.

VTB(I, 1):   The tangential absolute velocity component $V_{\theta,i'}$ at the inlet of each annulus. J = 1 and $1 \leq I \leq NQI-1$.

V: The fluid kinematic viscosity

PSAT: The liquid saturation of vapor pressure p_{sat}

T: The fluid thermodynamic constant T^*

As many combinations of these three final inputs V, PSAT and T may be added to the other data as the number of solutions desired for unchanged values of all other inputs. For example, NPSH depends on the difference between P(I, 1) and PSAT, whereby a reduction of PSAT with constant values of say zero for P(I,1) increases the NPSH.

3. Output Data

All output data is printed in groups. Each is here defined together with the value of the input control number NDATA for which that group can be obtained — in the order of their appearance and under the following headings:

a) Input data except for V, PSAT, T.

   NDATA = 0, 1, or 2. No headings.

The following data groups are printed at station J = 1:

b) Streamline and blade data at station J.

   NDATA = 2: Printed in columns headed as follows for streamlines
               I = 1, 2, 3 ..., NQI:

   I: The streamline identifying number i.

   J: The station identifying number j.

   R: The streamline radial position r_i.

   Z: The streamline axial position z_i.

   N: The streamline position n'_i corresponding to r and z;
               viz., the approximate meridional arc distance along
               the blade leading edge from the hub.

   TS: The circumferential position $\theta_{s,i}$ of the suction surface
               of the channel at location n' — outside the boundary layer
               displacement thickness.

   TP: The same for the pressure surface

c) Average fluid data at station J.

   NDATA = 0, 1, or 2. Columns for annuli I = 1, 2, 3, ..., NQI-1:

   I: The annulus identifying number i.

   J: The station identifying number j.

   RAV: The annulus mean radial position r_i'.

   ZAV: The annulus mean axial position z_i'.

P: The static pressure p_i'.

W: The relative velocity W_i'.

VM: The component of velocity $V_{m, i}'$ in the meridional streamline direction, except at the leading edge (J = 1) where this quantity is the input value VM1 normal to the blade leading edge.

VR: The radial velocity component $V_{r, i}'$.

VZ: The axial velocity component $V_{z, i}$.

D: The density ρ_i'.

d) The first or next set of the final inputs V, PSAT, T (ν, p_{sat}, T*) now appears for NDATA = 0, 1, or 2 under the following heading:

> KIN VISCOSITY, VAPOR PRESS,
> VAPORZN CONST. — THESE INPUTS USED
> FOR THE FOLLOWING DATA.

The following output sequence is repeated for $2 \leq J \leq NQJ-1$; i.e., through the blade trailing edge station.

e) Only if NDB = 1, the special cycle iteration data discussed under input appears for NDATA = 0, 1 or 2.

f) Same as output (b) with the following additions: (NDATA = 2)

U: The resulting streamline unbalance $\dfrac{\rho_f}{g_o} U_i$.

NC: The total number of cycles executed at this station.

g) Blade-to-blade fluid data between stations J and J −1. (i.e., at station j')

NDATA = 1 or 2. Columns for annuli I = 1, 2, 3, ..., NQI-1 with two rows of data for each annulus. The first row gives I, J, RAV, and ZAV as in input (c), and the following:

DWDT: The constant slope $\dfrac{dW}{d\theta}$ of the blade-to-blade relative velocity distribution.

P: The mid-passage static pressure $\overline{p}_i'$.

PP: The channel pressure-side static pressure $p_{p, i}'$.

W: The mid-passage (mean) relative velocity $\overline{W}_i{}'$.

WP: The pressure-side relative velocity $W_{p,i}{}'$.

D: The average density $\overline{\rho}_i{}'$.

DP: The pressure-side density $\rho_{p,i}{}'$

              The second row repeats NC and U from output (f).
              Also it gives the corresponding channel suction-
              side data PS, WS, and DS.

h) Same as output (c). NDATA = 2, except at trailing edge (J = NQJ-1) where this information is printed for NDATA = 0, 1, or 2.

The following additional data is printed for NDATA = 0, 1, or 2 after reaching the trailing edge:

i) Blade element data at exit.

Columns for annuli I = 1, 2, 3, ..., NQI-1.

LOSS COEFF: $\overline{\omega}_i{}'$ calculated by equation (III. 22).

EFFICIENCY: $\eta_i{}'$ calculated by equation (III. 23).

DEVIAT, ANGLE: $\delta_{ex,i}{}'$ given by input DELTAE (I).

j) Overall performance data.

Listed in the following order, each having an appropriate heading:

$\Delta\overline{H}$ calculated by equation (III. 25)

$\overline{p}_1$ calculated by equation (III. 26)

$\overline{p}_2$ calculated by equation (III. 26)

$\overline{V_1{}^2/2g_o}$ calculated by equation (III. 27)

$\overline{V_2{}^2/2g_o}$ calculated by equation (III. 27)

w_T calculated by equation (III. 24)

T^* calculated by equation (III. 28)

P_s calculated by equation (III. 29)

$\bar{\eta}$ calculated by equation (III. 30)

Ω , p_{sat} and T^* given by input, as is the value of after the next two items.

UNBAL ALLOW: $\left(\dfrac{\rho_f}{g_o}\ U_{max}\right)$ desired. This is the value of EN used at input. The program stores it unchanged under the name CRN.

MAX UNBAL ERR: $\left(\dfrac{\rho_f}{g_o}\ U_{max}\right)$ obtained. This is the resulting value of EN, which is the same as CRN if NC < MNC throughout the calculations.

For each additional set of ν, p_{sat} and T^*, a further set of outputs is printed, beginning with (e) and continuing through (j). For any set that gives no complete solution due to choking at low NPSH, the message "NPSH too low for two-phase solution if NC less than MNC" is printed at the point where this occurs, and the computer passes on to the next set. It is safe to say that for typical MNC, even NC = MNC means no solution is possible at larger numbers of streamline balancing iteration cycles NC. The computer will stop with an input tape end-of-file condition.

FIGURE D. 1

Read: TITLE, coordinates of streamlines at leading edge and of hub and shroud stations

795

Calculate leading edge BLADE Coord's. (eq's A. 1 and A. 2)

Read: Speed, fluid properties, and inlet distributions of press's., velocities, and densities

99

Read: ν, p_{sat}, and T^*

$j = 1$

15

$j = j + 1$

160

Estimate positions n' of streamlines along quasi-normal at j, and find associated coord's r_i and z_i for all i.

Last Station ?

YES

NO

713

Calculate blade surface data for all i': $(p_p, p_s, W_p, W_s, \rho_p, \rho_s)_{i'}$ (eq's III. 13, 14, 15, 17)

34

max. no. cycles exceeded ?

YES

NO

11

Is $U_i \leq U_{max}$ for all i ?

YES

NO

935

Calculate exit blade element data $(\overline{\omega}, \eta)_{i'}$ for all i' (eq's III 22, 23) and overall performance data $\Delta \overline{H}$, $\overline{p}_1$, $\overline{p}_2$, $\overline{\eta}$, etc. (eq's III. 25 to 30)

202

Calculate unbalances U_i of all streamlines i, (eq III. 10)

Calculate ANNULus average fluid data: $(p, W, V_m, V_r, V_\theta, V_z, \rho)_{i'}$ for all i', (eq's III. 8, III. 9)

176

Adjust streamline loc'ns. n' for each i from hub to shroud successively (eq III. 12)

18

Calculate BLADE coord's. $\theta_{s,i}$ and $\theta_{p,i}$ and flow angles $\beta_{i',j}$ for all i (eq's A. 1, A. 2 et al)

a) BLOCK DIAGRAM FOR MAIN PROGRAM

(Numbers above boxes refer to key Fortran statements in the main program)

195

FIGURE D.1 (Continued)

Subroutine ANNUL

Assume liquid flow, i.e.
$\rho_{i',j} = \rho_f$

48

Calculate Annulus Outlet Velocity Diagram
$(W,\ V_m,\ V_\theta)_{i',j}$
(eq's. III.8, et al)

Are Losses Calculated ?

YES

NO

1

Set dL = 0

6, 7

Calculate Losses dL (eq. I.13)

5

Calculate Annulus Outlet Pressure, $p_{i',j}$ (eq III.9)

16 et al

Calculate Blade-to-Blade W and Distributions (eq's III.14 et al)

21, 24

Is Two-Phase Flow In Passage ?

YES

NO

38

Calculate Blade-to-Blade Average Density
$\bar{\rho}_{i',j'}$ (eq III.19)

50

Assume New Two-Phase $\rho_{i',j}$

NO   41

Continuity
$\bar{\rho}_{i',j} \overset{?}{=} \left(\dfrac{\rho_{i,j} + \rho_{i,j-1}}{2} \right)$
Test

YES

40

RETURN

b) <u>BLOCK DIAGRAM FOR SUBROUTINE "ANNUL"</u>

(Numbers above boxes refer to key Fortran statements in the subroutine)

196

FIGURE D. 1 (Concluded)

Read: Blade lead constants a, b, c; Blade and boundary layer thickness data and number of blades

(1st time only)

24
Calculate passage hydraulic diameters $D_{h,j}$ for all j

Subroutine BLADE

6, 5, 8, 10 or 11
Calculate angle θ_p of pressure side of channel (eq. A.1)

30
Calculate blade thickness t (eq. A.2) including boundary layer thickness δ^*

Calculate angle θ_s of suction side of channel

RETURN
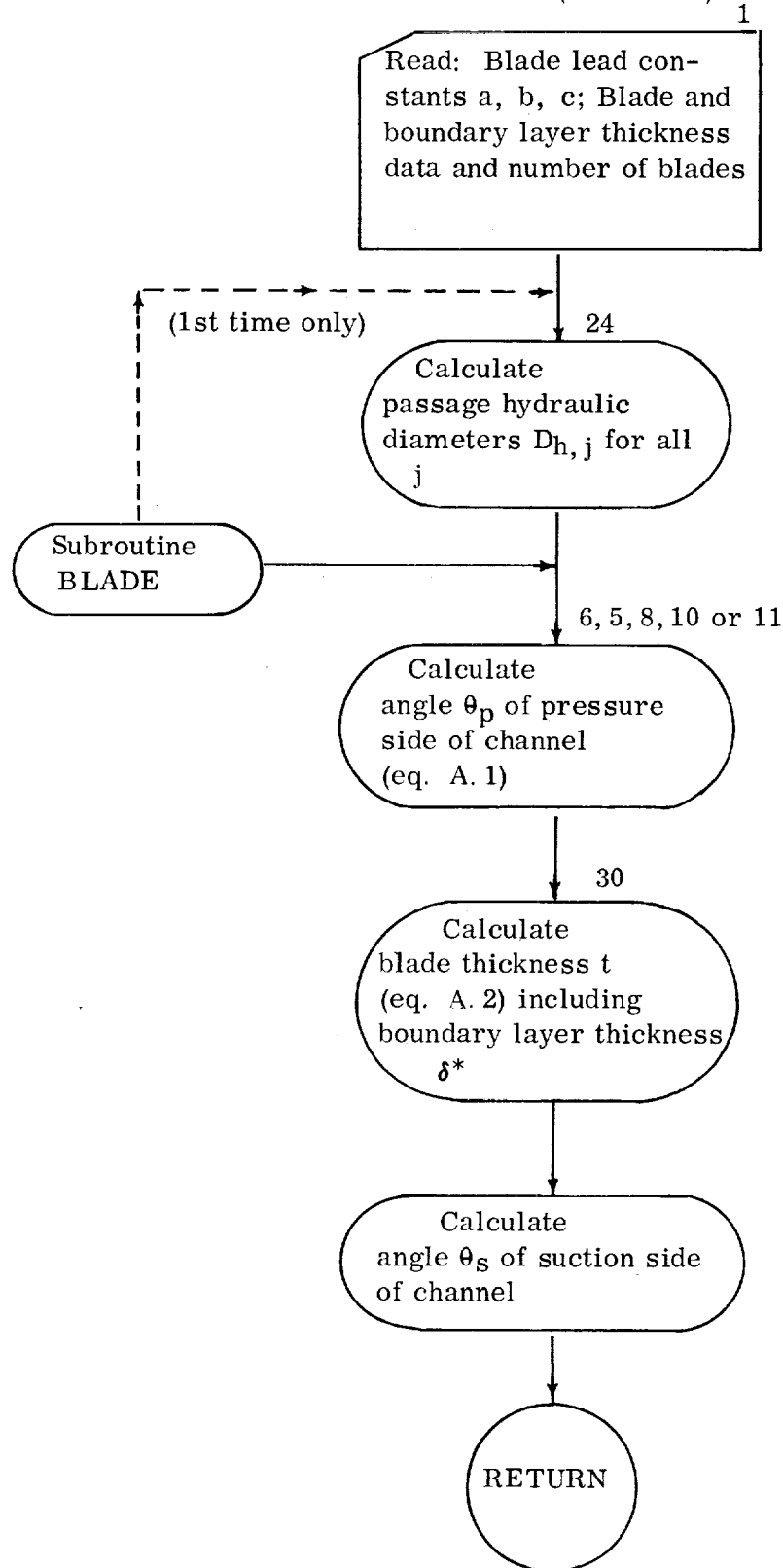
c) BLOCK DIAGRAM FOR SUBROUTINE "BLADE"

(Numbers above boxes refer to key Fortran statement numbers in the subroutine)

197

TABLE D.1
FORTRAN IV LISTING OF APPROXIMATE ANALYSIS PROGRAM

```
C     APPROXIMATE 3-DIML INDUCER ANALYSIS FOR NASA      AUGUST 20, 1965
C
C     TRW ACCESSORIES DIVISION, CLEVELAND, OHIO
C
      DIMENSION Z(11,22),R(11,22),AN(11,22),TP(11,22),TS(11,22),RHO(10,
     121),RB(10,22),ZB(10,22),TPA(10),TSA(10),TA(10),SBFA(10),SBF(10),
     2CBF(10),DT2(10),FLC(10),RVT(10),DEM(10),P(10,21),VTB(10,21),WB(10,
     321),DELDB(11,22),AK(10,21),U(11,21),ACOSGJ(22),SJ(22),W(10),DELTAE
     4(10),B(10),VM1(1Y),VM2(10),V1(10),AM1(10),VR1(10),VZ1(10),VR(10),
     5VZ(10),ALOSS(10),DHP(22),ANN(10),CONV(10)
      COMMON AN,RR,ZZ,R,Z,TPP,TSS,PB1,PB2,WB1,WB2,RHOB1,RHOB2,RHOF,PSAT,
     1GO,ANB,PIE,AK2,T,DHP,J,NQI,NQJ,V,FC,FR,FSA,SBF2,CBF2,TBP,TBS,TDB,
     2RB2,RVT1,ISTART,AW,VBT2,OMEGA,AC2,VBM2,CNV
 1000 FORMAT(80H
     1                                )
 1001 FORMAT(16I5)
 1002 FORMAT(8F10.4)
 1003 FORMAT(//2X,38HSTREAMLINE AND BLADE DATA AT STATION J/4X,1HI,
     1    4X,1HJ,7X,1HR,14X,1HZ,14X,1HN,14X,2HTS,13X,2HTP/(2I5,1P5E15.7))
 1004 FORMAT(//2X,38HSTREAMLINE AND BLADE DATA AT STATION J/4X,1HI,
     1    4X,1HJ,7X,1HR,14X,1HZ,14X,1HN,14X,2HTS,13X,2HTP,13X,1HU,10X,
     22HNC/(2I5,1P6E15.7,1I8))
 1005 FORMAT(//2X,31HAVERAGE FLUID DATA AT STATION J/4X,1HI,4X,1HJ,
     1    6X,3HRAV,9X,3HZAV,            9X,1HP,11X,1HW,11X,2HVM,10X,
     2    2HVR,10X,2HVT,10X,2HVZ,10X,1HD/(2I5,1P9E12.4))
 1008 FORMAT(//2X,52HBLADE-TO-BLADE FLUID DATA BETWEEN STATIONS J AND J-
     11/4X,1HI,4X,1HJ,6X,3HRAV,9X,3HZAV,8X,4HDWDT,9X,1HP,11X,2HPP,10X,
     21HW,11X,2HWP,10X,1HD,11X,2HDP/28X,2HNC,11X,1HU,22X,2HPS,22X,2HWS,
     322X,2HDS)
 1009 FORMAT(2I5,1P9F12.4)
 1010 FORMAT(26X,1I5,3X,1P1E12.4,12X,1P1E12.4,12X,1P1E12.4,12X,1P1E12.4)
 1011 FORMAT(Y/2X,26HBLADE ELEMENT DATA AT EXIT/4X,1HI,5X,10HLOSS COEFF,
     15X,10HE.FICIENCY,3X,12HDEVIAT ANGLE/(1I5,1P3F15.7))
 1012 FORMAT(///2X,24HOVERALL PERFORMANCE DATA//3X,12HTOT HEAD CHG,4X,
     111HPRESSURE IN,3X,12HPRESSURE OUT,3X,12HVELY HEAD IN,2X,13HVELY HE
     2AD OUT,1X,14HMASS FLOW RATE,9X,6HTORQUE,4X,11HSHAFT POWER/
     31P8E15.7)
 1013 FORMAT(//3X,12HOVERALL EFFY,3X,12HANGULAR VELY,4X,11HLIQ DENSITY,
     14X,11HVAPOR PRESS,2X,13HVAPORZN CONST,4X,11HUNBAL ALLOW,2X,13HMAX
     2UNBAL ERR,3X,12HNO OF BLADES/1P8E15.7)
 1015 FORMAT(1P8E15.7)
 1016 FORMAT(//////2X,13HKIN VISCOSITY,4X,11HVAPOR PRESS,2X,
     113HVAPORZN CONST,6X,41H-THESE INPUTS USED FOR THE FOLLOWING DATA)
 1020 FORMAT(//4X,1HJ,3X,5HCYCLE,4X,12HSTLN ADJ MAG,4X,11HTOTAL UNBAL)
 1021 FORMAT(1I5,1I7,3X,1P2E15.7)
 1022 FORMAT(//2X,71HNPSH TOO LOW FOR TWO-PHASE SOLUTION WITH THIS FLUID
     1 IF NC LESS THAN MNC)
      PIE=3.1415927
      ISTART=1
      READ                1000
      PRINT               1000
      READ 1001,NQI,NQJ,MNC,NDATA,NDB
      PRINT 1001,NQI,NQJ,MNC,NDATA,NDB
      READ                1002,(Z(I,1),I=1,NQI)
      PRINT 1015,(Z(I,1),I=1,NQI)
      READ                1002,(R(I,1),I=1,NQI)
      PRINT 1015,(R(I,1),I=1,NQI)
      READ                1002,(Z(1,I),I=2,NQJ)
      PRINT 1015,(Z(1,I),I=2,NQJ)
      READ 1002,(R(1,I),I=2,NQJ)
```

```
      PRINT 1015,(R(1,I),I=2,NQJ)
      READ                1002,(Z(NQI,I),I=2,NQJ)
      PRINT 1015,(Z(NQI,I),I=2,NQJ)
      READ                1002,(R(NQI,I),I=2,NQJ)
      PRINT 1015,(R(NQI,I),I=2,NQJ)
C
C     SET UP FIELD OF HUB, SHROUD AND LEADING EDGE COORDINATES
C
      AN(1,1)=0.0
      I=1
      DO 795 J=1,NQJ
      RR=R(1,J)
      ZZ=Z(1,J)
      CALL BLADE
      TP(I,J)=TPP
  795 TS(I,J)=TSS
      J=1
    1 I=I+1
      AN(I,1)=AN(I-1,1)+SQRT(((Z(I,1)-Z(I-1,1))**2.)+((R(I,1)-R(I-1,1))*
     1*2.))
      RR=R(I,1)
      ZZ=Z(I,1)
      CALL BLADE
      TP(I,1)=TPP
      TS(I,1)=TSS
      IF(NQI-I)7,7,1
    7 J=J+1
      AN(NQI,J)=SQRT(((R(NQI,J)-R(1,J))**2.)+((Z(NQI,J)-Z(1,J))**2.))
      ACOSGJ(J)=(R(NQI,J)-R(1,J))/AN(NQI,J)
      SJ(J)=(Z(NQI,J)-Z(1,J))/AN(NQI,J)
    5 IF(J-NQJ)7,6,6
    6 NQII=NQI-1
      ANQQ=NQII
      READ 1002,EN,RHOF,OMEGA,GO
      PRINT 1015,EN,RHOF,OMEGA,GO
      READ                1002,(RHO(I,1),I=1,NQII)
      PRINT 1015,(RHO(I,1),I=1,NQII)
      READ                1002,(P(I,1),I=1,NQII)
      PRINT 1015,(P(I,1),I=1,NQII)
      READ 1002,(VM1(I),I=1,NQII)
      PRINT 1015,(VM1(I),I=1,NQII)
      READ                1002,(DELTAE(I),I=1,NQII)
      PRINT 1015,(DELTAE(I),I=1,NQII)
      READ                1002,(VTB(I,1),I=1,NQII)
      PRINT 1015,(VTB(I,1),I=1,NQII)
      DO 2 I=1,NQII
      RB(I,1)=(R(I,1)+R(I+1,1))/2.
      B(I)=AN(I+1,1)-AN(I,1)
      DELDB(I,1)=0.
         ZB(I,1)=(Z(I,1)+Z(I+1,1))/2.
      VR1(I)=VM1(I)*(Z(I,1)-Z(I+1,1))/B(I)
      VZ1(I)=VM1(I)*(R(I+1,1)-R(I,1))/B(I)
      W(I)=VM1(I)*2.*PIE*RB(I,1)*B(I)*RHO(I,1)
      V1(I)=VTB(I,1)*VTB(I,1)+VM1(I)*VM1(I)
      AM1(I)=RB(I,1)*VTB(I,1)
    2 WB(I,1)=SQRT(((OMEGA*RB(I,1)-VTB(I,1))**2.)+VM1(I)*VM1(I))
      J=1
      IF(NDATA-1)45,45,44
   44 PRINT 1003,(I,J,R(I,J),Z(I,J),AN(I,J),TS(I,J),TP(I,J),I=1,NQI)
   45 PRINT 1005,(I,J,RB(I,J),ZB(I,J),P(I,1),WB(I,1),VM1(I),
```

```
    1 VR1(I),VTB(I,1),VZ1(I),RHO(I,1),I=1,NQII)
      NQJE=NQJ-1
      AQJ=NQJE-1
      CRN=RHOF*OMEGA*OMEGA*R(NQI,1)*EN/GO
   99 ISS=2
      READ 1002,V,PSAT,T
      PRINT 1016
      PRINT 1015,V,PSAT,T
      J=1
      DO 43 I=1,NQII
   43 CONV(I)=1.
      CNV=1.
      UMAX=0.0
      NCDM=0
      DNMAX=R(NQI,1)*.005/ANQQ
      ADJQ=0.
C
C     ESTIMATE STREAMLINE POSITIONS AT EACH STATION FROM INLET TO OUTLET
C
  117 DO 42 I=1,NQII
      IF(CONV(I))41,41,42
   41 PRINT 1022
      GO TO 99
   42 CONTINUE
      I=0
      N=0
   15 J=J+1
      DO 8 I=1,NQII
      AN(I,J)=(AN(I,J-1)/AN(NQI,J-1))*AN(NQI,J)
      AJJ=J-1
    8 DELDB(I,J)=DELTAE(I)*((AJJ/AQJ)**6.)
    9 IF(N)13,13,14
   13 N=1
      GO TO 15
   14 N=0
   16 I=1
   17 I=I+1
  160 R(I,J)=R(1,J)+AN(I,J)*ACOSGJ(J)
      Z(I,J)=Z(1,J)+AN(I,J)*SJ(J)
   12 RR=R(I,J)
      ZZ=Z(I,J)
      IF(N-2)18,18,19
   19 I=I-1
      GO TO 105
   18 CALL BLADE
      TP(I,J)=TPP
      TS(I,J)=TSS
      IF(I-NQI)27,20,20
   27 IF(N-1)17,28,17
   28 I=I+1
      GO TO 12
   20 IF(N-1)21,118,22
   21 N=2
      J=J-1
      GO TO 16
   22 JJ=J+1
      DO 26 I=1,NQII
      DO 23 K=J,JJ
      RB(I,K)=(R(I,K)+R(I+1,K))/2.
   23 ZB(I,K)=(Z(I,K)+Z(I+1,K))/2.
```

```
      DDM=SQRT((RB(I,J)-RB(I,J-1))**2.+(ZB(I,J)-ZB(I,J-1))**2.)
      DEM(I)=SQRT((RB(I,J+1)-RB(I,J-1))**2.+(ZB(I,J+1)-ZB(I,J-1))**2.)
      DT2(I)=(TS(I,J)+TS(I+1,J)-TP(I,J)-TP(I+1,J))/2.
      TB1=(TS(I,J-1)+TP(I,J-1)+TS(I+1,J-1)+TP(I+1,J-1))/4.
      TB2=(TS(I,J)+TP(I,J)+TS(I+1,J)+TP(I+1,J))/4.
      TB3=(TS(I,J+1)+TP(I,J+1)+TS(I+1,J+1)+TP(I+1,J+1))/4.
      DT2(I)=DT2(I)*SIN(ASIN(ABS((ZB(I,J+1)-ZB(I,J-1))/DEM(I)))+ACOS(
     1ABS(ACOSGJ(J))))
      RVT(I)=RB(I,J-1)*VTB(I,J-1)
      BB2=ATAN(DEM(I)/((TB1-TB3)*RB(I,J)))
      BF2=BB2-DELDB(I,J)
      SBF(I)=SIN(BF2)
      CBF(I)=COS(BF2)
      BBB=ATAN(DDM/((TB1-TB2)*((RB(I,J)+RB(I,J-1))/2.)))
      BBF=BBB-(DELDB(I,J)+DELDB(I,J-1))/2.
      SBFA(I)=SIN(BBF)/DDM
      TPA(I)=(TP(I,J-1)+TP(I+1,J-1)+TP(I,J)+TP(I+1,J))/4.
      TSA(I)=(TS(I,J-1)+TS(I+1,J-1)+TS(I,J)+TS(I+1,J))/4.
      TA(I)=(TPA(I)+TSA(I))/2.
      IF(V)24,24,25
C     CALCULATE FRICTION LOSS EFFICIENT
   24 FLC(I)=0.
      GO TO 26
   25 FLC(I)=(.00714+.6104/((WB(I,J-1)*DHP(J)/V)**.35))/
     1 (2.*DHP(J)*SBFA(I))
   26 CONTINUE
      I=0
  104 I=I+1
  105 RB(I,J)=(R(I,J)+R(I+1,J))/2.
      FR=(OMEGA*OMEGA/2.)*(RB(I,J)*RB(I,J)-RB(I,J-1)*RB(I,J-1))
      AC2=RB(I,J)*DT2(I)*SQRT((R(I+1,J)-R(I,J))**
     1 2.+(Z(I+1,J)-Z(I,J))**2.)
      FC=FLC(I)
      FSA=SBFA(I)
      SBF2=SBF(I)
      CBF2=CBF(I)
      TBP=TPA(I)
      TBS=TSA(I)
      TDB=TA(I)
      RVT1=RVT(I)
      RB2=RB(I,J)
      RHOB1=RHO(I,J-1)
      PB1=P(I,J-1)
      WB1=WB(I,J-1)
      AW=W(I)
      CALL ANNUL
      RHO(I,J)=RHOB2
      P(I,J)=PB2
      WB(I,J)=WB2
      VTB(I,J)=VBT2
      VM2(I)=VBM2
      AK(I,J)=AK2
      CONV(I)=CNV
      IF(N-3)100,101,102
  100 IF(I-NQI+2)104,104,103
  101 N=4
      I=I+1
      GO TO 105
  102 N=3
      GO TO 107
```

```
  103 NC=0
      DELLN=DNMAX
      N=3
      U(1,J)=0.0
      U(NQI,J)=0.0
      IF(NQI-2)118,118,202
  178 I=1
      NADJ=0
C
C     CHECK ACCURACY OF STREAMLINE BALANCE FROM HUB TO SHROUD
C          IF SATISFACTORY, PROCEED TO STATION OUTPUT CALCULATIONS
C          IF UNSATISFACTORY, PERFORM STREAMLINE ADJUSTMENTS
C
  113 I=I+1
      IF(U(I,J)-CRN)111,111,34
  111 IF(I-NQII)113,29,29
   34 IF(MNC-NC)804,804,112
  804 DO 50 I=2,NQII
      IF(U(I,J)-UMAX)50,50,40
   40 UMAX=U(I,J)
      EN=EN*UMAX/CRN
   50 CONTINUE
   29 N=1
      I=2
      GO TO 12
C
C     PERFORM STREAMLINE ADJUSTMENT SEQUENCE
C
  112 NC=NC+1
      I=1
  172 I=I+1
      VMH1=VM2(I-1)
      VMH2=VM2(I)
      CNVH1=CONV(I-1)
      CNVH2=CONV(I)
      AKH1=AK(I-1,J)
      RHOBH1=RHO(I-1,J)
      PBH1=P(I-1,J)
      WBH1=WB(I-1,J)
      VTBH1=VTB(I-1,J)
      UH1=U(I-1,J)
      UH2=U(I,J)
      UH3=U(I+1,J)
      AKH2=AK(I,J)
      RHOBH2=RHO(I,J)
      PBH2=P(I,J)
      WBH2=WB(I,J)
      VTBH2=VTB(I,J)
      ANH=AN(I,J)
      RHLD=R(I,J)
      ZHLD=Z(I,J)
      USTAR=U(I-1,J)*U(I-1,J)+U(I,J)*U(I,J)+U(I+1,J)*U(I+1,J)
  176 AN(I,J)=ANH+DELLN
      GO TO 160
  750 USTARD= U(I-1,J)*U(I-1,J)+U(I,J)*U(I,J)+U(I+1,J)*U(I+1,J)
      IF(DELLN)613,808,610
  808    STOP 808
  610 IF(ADJQ)612,612,611
  611    ADJQ=0.
      IF(USTARD-USTAR) 170,615,615
```

```
612    USTARP=USTARD
       DELLN=-DELLN
       GO TO 176
613    USTARM=USTARD
       DELLN=ABS(DELLN)
       UND2=(USTARP+USTARM-2.*USTAR)/(DELLN*DELLN)
6135   IF(UND2)  615,615, 614
614    USND=(USTARP-USTARM)/(2.*DELLN)
       AN(I,J) = ANH-USND/UND2
169    ADJQ=1.
       GO TO 160
615    IF(USTARP-USTAR) 618,616,616
616    IF(USTARM-USTAR) 620,617,617
617    AN(I,J)=ANH
       IF(NCDM)30,30,31
  30   DELLN=DELLN/10.
       NCDM=1
       GO TO 176
  31   DELLN=DELLN*10.
       GO TO 179
618    IF(USTARM-USTARP) 620,619,619
619    AN(I,J)= ANH+DELLN
       GO TO 169
620    AN(I,J)=ANH-DELLN
       GO TO 169
170    NADJ=1
180    NCDM=0
152    IF(I-NQII)172,173,173
 32    IF(NADJ)174,174,178
174    IF(DELLN-DNMAX/1000.)178,178,35
173    IF(NDB-1)32,33,175
 33    PRINT 1020
       NDB=2
175    TOTAL=0.0
       DO 177 K8=2,NQII
177    TOTAL=TOTAL+U(K8,J)
       PRINT 1021,J,NC,DELLN,TOTAL
       GO TO 32
 35    DELLN=DELLN/10.
       GO TO 178
179    AK(I-1,J)=AKH1
       VM2(I-1)=VMH1
       VM2(I)=VMH2
       CONV(I-1)=CNVH1
       CONV(I)=CNVH2
       RHO(I-1,J)=RHOBH1
       P(I-1,J)=PBH1
       WB(I-1,J)=WBH1
       VTB(I-1,J)=VTBH1
       U(I-1,J)=UH1
       U(I,J)=UH2
       U(I+1,J)=UH3
       AK(I,J)=AKH2
       RHO(I,J)=RHOBH2
       P(I,J)=PBH2
       WB(I,J)=WBH2
       VTB(I,J)=VTBH2
       AN(I,J)=ANH
       R(I,J)=RHLD
       Z(I,J)=ZHLD
```

203

```
      GO TO 180
  202 DO 181 I=2,NQII
C
C     CHECK STREAMLINE UNBALANCE
C
  181 U(I,J)=ABS(((P(I,J)-P(I-1,J))/(.5*(AN(I+1,J)-AN(I-1,J))))-(ACOSGJ(
     1J)*(RHO(I-1,J)+RHO(I,J))*(VTB(I-1,J)*VTB(I-1,J)+VTB(I,J)*VTB(I,J))
     2/(4.*GO*R(I,J))))
      GO TO 178
  107 U(I,J)=ABS(((P(I,J)-P(I-1,J))/(.5*(AN(I+1,J)-AN(I-1,J))))-(ACOSGJ(
     1J)*(RHO(I-1,J)+RHO(I,J))*(VTB(I-1,J)*VTB(I-1,J)+VTB(I,J)*VTB(I,J))
     2/(4.*GO*R(I,J))))
      IF(I-2)150,150,183
  150 IF(NQI-3)750,750,182
  182 U(3,J)=ABS((P(3,J)-P(2,J))/(.5*(AN(4,J)-AN(2,J)))-                  A
     1COSGJ(J)*(RHO(2,J)+RHO(3,J))*(VTB(2,J)*VTB(2,J)+                    V
     2TB(3,J)*VTB(3,J))/(4.*GO*R(3,J)))
      GO TO 750
  183 IF(I-NQII)185,186,186
  185 U(I+1,J)=ABS((P(I+1,J)-P(I,J))/(.5*                                 (
     1AN(I+2,J)-AN(I,J)))-ACOSGJ(J)*                                      (
     2RHO(I,J)+RHO(I+1,J))*(VTB(I,J)*VTB(I,J)+                            V
     3TB(I+1,J)*VTB(I+1,J))/(4.*GO*R(I+1,J)))
  186 U(I-1,J)=ABS(((P(I-1,J)-P(I-2,J))/(.5*(AN(I,J)-AN(I-2,J))))-ACOSGJ
     1(J)*(RHO(I-2,J)+RHO(I-1,J))*(VTB(I-2,J)*VTB(I-2,J)+VTB(I-1,J)*      V
     2TB(I-1,J))/(4.*GO*R(I-1,J)))
      GO TO 750
C
C     END OF STREAMLINE BALANCING PROCEDURE
C
C     CALCULATE STATION OUTPUT AND FINAL BLADE TO BLADE DATA
C
  118 IF(NDATA-1)119,903,120
  119 IF(J-NQJE)117,901,901
  120 PRINT 1004,(I,J,R(I,J),Z(I,J),AN(I,J),TS(I,J),TP(I,J),U(I,J),NC,
     1I=1,NQI)
  903 I=0
  929 I=I+1
      AK2=AK(I,J)
      RHOB2=RHO(I,J)
      PB2=P(I,J)
      WB2=WB(I,J)
      RHOB1=RHO(I,J-1)
      PB1=P(I,J-1)
      WB1=WB(I,J-1)
      TBP=TPA(I)
      TBS=TSA(I)
      TDB=TA(I)
      PDB=.5*(PB1+PB2)
      RHOB12=.5*(RHOB1+RHOB2)
      WDB=.5*(WB1+WB2)
      ZB(I,J)=(Z(I,J)+Z(I+1,J))/2.
      RAV=(RB(I,J)+RB(I,J-1))/2.
      ZAV=(ZB(I,J)+ZB(I,J-1))/2.
      IF(T)794,794,793
  794 WS=WDB+AK2*(TBS-TDB)
      WP=WDB-AK2*(TDB-TBP)
      RHOTDB=RHOF
      GO TO 792
  793 AK3=AK2*WDB-AK2*AK2*TDB
```

204

```
      IF(AK2)700,700,775
700   WS=WDB
      WP=WDB
      PS=PDB
      PP=PDB
      IF(AK2)728,725,725
728   RHOS=RHOB12
      RHOP=RHOB12
      RHOTDB=RHOB12
      GO TO 788
725   IF(PDB-PSAT)726,727,727
726   RHOS=RHOF/(1.+T*(PSAT-PDB))
      RHOP=RHOS
      RHOTDB=RHOS
      GO TO 788
727   RHOS=RHOF
      RHOP=RHOF
      RHOTDB=RHOF
      GO TO 788
775   TBWO=TDB-WDB/AK2
      WS=WDB+AK2*(TBS-TDB)
      IF(TBP-TBWO)730,731,731
730   WP=0.0
      TBPP=TBWO
      GO TO 115
731   TBPP=TBP
      WP=WDB-AK2*(TDB-TBPP)
115   IF(PDB-PSAT)744,745,746
744   RHOTDB=RHOF/(1.+T*(PSAT-PDB))
      WSAT2=WDB*WDB-(GO*RHOF/T)*((1./(RHOTDB*RHOTDB))-(1./(RHOF*RHOF)))
      IF(WSAT2-WP*WP)760,760,761
760   J8=1
      A7=TBS
      A13=RHOTDB
765   A8=SQRT(1./((2.*T/(GO*RHOF))*(AK3*(A7-TDB)+AK2*AK2*.5*(A7*A7-TDB*T
     1DB))+1./(A13*A13)))
      A5=PSAT+(1./T)*(1.-RHOF/A8)
      IF(J8-2)766,767,713
766   J8=2
      A7=TBP
      RHOS=A8
      PS=A5
      GO TO 765
767   RHOP=A8
      PP=A5
      GO TO 788
761   WTBSAT=SQRT(WSAT2)
      GO TO 779
745   RHOTDB=RHOF
      RHOP=RHOF
      J8=3
      A7=TBS
      A13=RHOF
      GO TO 765
713   RHOS=A8
      PP=PDB+(RHOF/(2.*GO))*(WDB*WDB-WP*WP)
      PS=PSAT+(1./T)*(1.-RHOF/RHOS)
      GO TO 788
746   RHOTDB=RHOF
      WTBSAT=SQRT((2.*GO/RHOF)*(PDB-PSAT)+WDB*WDB)
```

```
      IF(WTBSAT-WS)779,792,792
  779 TBSAT=TDB+(WTBSAT-WDB)/AK2
      RHOP=RHOF
      RHOS=SQRT(1./((2.*T/(GO*RHOF))*(AK3*(TBS-TBSAT)+AK2*AK2*.5*(TBS* T
     1BS-TBSAT*TBSAT))+(1./(RHOF*RHOF))))
      PS=PSAT+(1./T)*(1.-RHOF/RHOS)
      PP=PSAT+(RHOF/(2.*GO))*(WTBSAT*WTBSAT-WP*WP)
      GO TO 788
  792 RHOP=RHOF
      RHOS=RHOF
      PP=PDB+(RHOF/(2.*GO))*(WDB*WDB-WP*WP)
      PS=PDB+(RHOF/(2.*GO))*(WDB*WDB-WS*WS)
  788 IF(ISS-2)925,925,926
  925 PRINT                      1008
      ISS=3
  926 PRINT 1009,I,J,RAV,ZAV,AK2,PDB,PP,WDB,WP,RHOB12,RHOP
      PRINT 1010,NC,U(I,J),PS,WS,RHOS
      IF(I-NGII)929,928,928
  928 IF(NDATA-1)900,900,901
  900 IF(J-NQJE)117,901,901
  901 DO 902 I=1,NQII
      DELZ=ZB(I,J+1)-ZB(I,J-1)
      VR(I)=VM2(I)*(RB(I,J+1)-RB(I,J-1))/DEM(I)
  902 VZ(I)=VM2(I)*DELZ/DEM(I)
      PRINT 1005,(I,J,RB(I,J),ZB(I,J),P(I,J),WB(I,J),VM2(I),VR(I),VTB(I,
     1J),VZ(I),RHO(I,J),I=1,NQII)
      IF(J-NQJE)936,935,935
  936 ISS=2
      GO TO 117
C
C
C     END OF REPETITIVE CALCULATIONS AT EACH STATION FROM INLET TO EXIT
C
C     OBTAIN MASS-AVERAGED OUTLET FLUID DATA AND PERFORMANCE
C
  935 WT=0.0
      DO 938 I=1,NQII
  938 WT=WT+W(I)
      PB2=0.0
      DO 939 I=1,NQII
  939 PB2=PB2+P(I,NQJE)*W(I)
      PB2=PB2/WT
      PB1=0.0
      DO 940 I=1,NQII
  940 PB1=PB1+P(I,1)*W(I)
      PB1=PB1/WT
      VH1=0.0
      DO 941 I=1,NQII
  941 VH1=VH1+V1(I)*W(I)
      VH1=VH1/(2.*WT*GO)
      VH2=0.0
      DO 942 I=1,NQII
  942 VH2=VH2+(VTB(I,NQJE)*VTB(I,NQJE)+VM2(I)*VM2(I))*W(I)
      VH2=VH2/(2.*WT*GO)
      DAM=0.0
      DO 943 I=1,NQII
  943 DAM=DAM+W(I)*(RB(I,J)*VTB(I,NQJE)-AM1(I))/GO
      DELH=0.0
      PS=OMEGA*DAM
      ANN=0.0
      DO 944 I=1,NQII
```

206

```
      PH1=P(I,1)/RHOF
      PH2=P(I,NQJE)/RHOF
      CH1=V1(I)/(2.*GO)
      CH2=(VTB(I,NQJE)*VTB(I,NQJE)+VM2(I)*VM2(I))/(2.*GO)
      TLHI=CH2-CH1+PH2-PH1
      DELH=DELH+W(I)*TLHI/WT
      DAMI=RB(I,J)*VTB(I,NQJE)-AM1(I)
      ALOSS(I)=(OMEGA*DAMI-TLHI*GO)/((WB(I,1)*WB(I,1))/2.)
944   ANN(I)=TLHI*GO/(OMEGA*DAMI)
      ANNOV=WT*DELH/PS
      PRINT 1011,(I,ALOSS(I),ANN(I),DELTAE(I),I=1,NQII)
      PRINT 1012,DELH,PB1,PB2,VH1,VH2,WT,DAM,PS
      PRINT 1013,ANNOV,OMEGA,RHOF,PSAT,T,CRN,EN,ANB
      GO TO 99
      END
```

```
      SUBROUTINE ANNUL

C
C     SUBROUTINE FOR ANNULUS VELOCITY DIAGRAMS AND OTHER FLUID DATA
C         FOR GIVEN STREAMLINE POSITIONS
C
      DIMENSION Z(11,22),R(11,22),AN(11,22),DHP(22)
      COMMON AN,RR,ZZ,R,Z,TPP,TSS,PB1,PB2,WB1,WB2,RHOB1,RHOB2,RHOF,PSAT,
     1GO,ANB,PIE,AK2,T,DHP,J,NQI,NQJ,V,FC,FR,FSA,SBF2,CBF2,TBP,TBS,TDB,
     2RB2,RVT1,ISTART,AW,VBT2,OMEGA,AC2,VBM2,CNV
      L=0
      RHOB2=RHOF
      AP=0.1
      ATT=RHOF
      ADP=0.1
   48 VBM2=AW/(RHOB2*AC2*ANB)
      WB2=VBM2/SBF2
      VBT2=OMEGA*RB2-WB2*CBF2
      WDB=(WB1+WB2)/2.
      AK2=FSA*(RB2*VBT2-RVT1)
      RHOB12=(RHOB1+RHOB2)/2.
      IF(V)1,1,4
    1 AL12=0.0
      GO TO 5
C
C     BEGIN LOSS CALCULATION
C
    4 IF(WB1-WB2)6,6,7
    7 AK=(1.-WB2/WB1)/(2.*(1.+WB2/WB1))
      AL12=FC*WDB*WDB+AK*(WB1*WB1-WB2*WB2)
      GO TO 5
    6 AL12=FC*WDB*WDB
C
C     COMPLETE LOSS CALCULATION
C
    5 PB2=PB1+(RHOB12/GO)*(FR-AL12-.5*(WB2*WB2-WB1*WB1))
      IF(T)40,40,55
   55 PDB=(PB2+PB1)/2.
      AK3=AK2*WDB-AK2*AK2*TDB
      IF(AK2)8,9,10
    8 IF(RHOF-RHOB2)61,61,12
   12 IF(AP-0.001)9,9,15
    9 L=100
      IF(PDB-PSAT)16,17,17
C
C     ENTER TWO-PHASE FLOW ITERATION LOOP
C
   16 RHODB=RHOF/(1.+T*(PSAT-PDB))
      GO TO 41
   17 RHODB=RHOF
      GO TO 41
   10 TBW=TDB-WDB/AK2
      WS=WDB+AK2*(TBS-TDB)
      IF(TBP-TBW)19,20,20
   19 WP=0.0
      TBPP=TBW
      GO TO 21
   20 TBPP=TBP
      WP=WDB-AK2*(TDB-TBPP)
   21 IF(PDB-PSAT)22,23,24
   22 RHOTDB=RHOF/(1.+T*(PSAT-PDB))
```

```
      WSAT2=WDB*WDB-(GO*RHOF/T)*(1./(RHOTDB*RHOTDB)-1./(RHOF*RHOF))
      IF(WSAT2-WP*WP)25,25,26
 26   WTBSAT=SQRT(WSAT2)
 29   TBSAT=TDB+(WTBSAT-WDB)/AK2
      GO TO 27
 24   WTBSAT=SQRT((2.*GO/RHOF)*(PDB-PSAT)+WDB*WDB)
      IF(WTBSAT-WS)29,28,28
 28   RHODB=RHOF
      GO TO 41
 23   NN=1
      X1=TDB
      X2=TBS
      A1=(2.*T/(GO*RHOF))*(-AK3*TDB-.5*AK2*AK2*TDB*TDB)+1./(RHOF*RHOF)
      GO TO 31
 27   NN=2
      X1=TBSAT
      X2=TBS
      A1=(2.*T/(GO*RHOF))*(-AK3*TBSAT-.5*AK2*AK2*TBSAT*TBSAT)+1./(RHOF*R
     1HOF)
      GO TO 31
 25   NN=3
      X1=TBPP
      X2=TBS
      A1=(2.*T/(GO*RHOF))*(-AK3*TDB-.5*AK2*AK2*TDB*TDB)+1./(RHOTDB*RHOTD
     1B)
      DD=SQRT(1./((2.*T/(GO*RHOF))*(AK3*(TBPP-TDB)+.5*AK2*AK2*(TBPP*TBPP
     1-TDB*TDB))+1./(RHOTDB*RHOTDB)))
 31   B1=2.*T*AK3/(GO*RHOF)
      C1=2.*T*AK2*AK2/(GO*RHOF*2.)
      CAPX1=A1+B1*X1+C1*X1*X1
      CAPX2=A1+B1*X2+C1*X2*X2
      CONST1=(1./SQRT(C1))*ALOG(SQRT(CAPX1)+X1*SQRT(C1)+B1/(2.*SQRT(C1))
     1)
      CONST2=(1./SQRT(C1))*ALOG(SQRT(CAPX2)+X2*SQRT(C1)+B1/(2.*SQRT(C1))
     1)
      GO TO (32,33,34),NN
 32   AA=RHOF*(TDB-TBPP)+CONST2-CONST1
      GO TO 30
 33   AA=RHOF*(TBSAT-TBPP)+CONST2-CONST1
      GO TO 30
 34   AA=CONST2-CONST1
 35   IF(TBP-TBW)36,37,37
 36   RHOP=DD
      GO TO 38
 30   IF(TBP-TBW)39,37,37
 39   RHOP=RHOF
      GO TO 38
 37   RHOP=0.0
 38   RHODB=RHOP*(TBPP-TBP)/(TBS-TBP)+AA/(TBS-TBP)
 41   IF(ABS((RHODB-RHOB12)/RHOB12)-0.001)61,61,42
 42   IF(L-100)43,44,44
 44   CNV=0.
      GO TO 40
 43   IF(RHODB-RHOB12)45,51,46
 46   IF(L)61,61,15
 45   IF(L)701,701,702
 701  TT=RHOB2
      TTP=ATT
      BTT=RHODB
      ATT=RHOB12
```

209

```
    ADP=AP
    GO TO 50
702 IF(AP-0.001)701,701,711
711 IF(AP-ADP)701,707,707
707 IF(RHOB12-RHODB-ATT+BTT)701,62,62
 50 L=L+1
    RHOB2=TT*(1.-AP)
    GO TO 48
 62 TT=2.*TTP-RHOB1
 15 AP=AP/10.
    GO TO 50
 61 CNV=1.
 40 RETURN
    END
```

```
      SUBROUTINE BLADE
C
C     SUBROUTINE FOR BLADE SURFACE COORDINATES TP AND TS FROM GIVEN R,Z
C
      DIMENSION Z(11,22),R(11,22),AN(11,22),DHP(22),TF(22)
      COMMON AN,RR,ZZ,R,Z,TPP,TSS,PB1,PB2,WB1,WB2,RHOB1,RHOB2,RHOF,PSAT,
     1GO,ANB,PIE,AK2,T,DHP,J,NQI,NQJ,V,FC,FR,FSA,SBF2,CBF2,T3P,TBS,TDB,
     2RB2,RVT1,ISTART,AW,VBT2,OMEGA,AC2,VBM2,CNV
 1006 FORMAT(8F10.4)
 1007 FORMAT(1P8E15.7)
      GO TO (1,6,5,10,8,11),ISTART
    1 READ 1006,             AA,BB,CC,DSEX,T1T,R1T,DTR,ANB,TF(1),TF(2),
     1TF(3)
      PRINT 1007,AA,BB,CC,DSEX,T1T,R1T,DTR,ANB,TF(1),TF(2),
     1TF(3)
      IF(NQJ-4)75,76,76
   76 DO 23 K=4,NQJ
   23 TF(K)=1.
   75 TPNB=2.*PIE/ANB
      DO 24 K=1,NQJ
      TTH=TF(K)*(T1T+DTR*(R1T-R(1,K)))
      TTT=TF(K)*(T1T+DTR*(R1T-R(NQI,K)))
      DZDT=AA+BB*Z(NQI,K)+CC*Z(NQI,K)*Z(NQI,K)
      ADHP=TPNB*DZDT
      ADH=ADHP-TTT
      BDH=ADHP-TTH
      CDH=AN(NQI,K)
   24 DHP(K)=1./(1./(2.*CDH)+1./(ADH+BDH))
      DO 27 K=2,NQJ
   27 DHP(K)=(DHP(K-1)+DHP(K))/2.
      IF(CC)3,4,3
    4 IF(BB)25,26,25
   25 ISTART=2
      GO TO 6
   25 ISTART=3
      GO TO 5
    3 Q=4.*AA*CC-BB*BB
      IF(Q)7,28,9
   28 ISTART=5
      GO TO 8
    7 SQ=SQRT(-Q)
      RSQ=1./SQ
      BMSQ=BB-SQ
      BPSQ=BB+SQ
      FBSQ=BMSQ/BPSQ
      ISTART=4
      GO TO 10
    9 SQ=SQRT(Q)
      SQ2=2./SQ
      TQ=SQ2*ATAN(BB/SQ)
      ISTART=6
      GO TO 11
    6 TPP=-ZZ/AA
      RSBB=RR*SIN(ATAN(AA/RR))
      GO TO 30
    5 TPP=(-1./BB)*ALOG((AA+BB*ZZ)/AA)
      RSBB=RR*SIN(ATAN((AA+BB*ZZ)/RR))
      GO TO 30
   10 TPP=-RSQ*ALOG(((2.*CC*ZZ+BMSQ)/(2.*CC*ZZ+BPSQ))/FBSQ)
   31 RSBB=RR*SIN(ATAN((AA+BB*ZZ+CC*ZZ*ZZ)/RR))
```

211

```
      GO TO 30
  8 TPP=(1./(BB+CC*ZZ))-1./BB
      GO TO 31
 11 TPP=-SQ2*(ATAN((2.*CC*ZZ+BB)/SQ))+TQ
      GO TO 31
 30 TT=T1T+DTR*(R1T-RR)
      TTF=TT*TF(J)
      AJ=J-1
      QQJ=NQJ-1
      TDS=2.*DSEX*(AJ/QQJ)
      TSS=TPP+TPNB-(TTF+TDS)/RSBB
      RETURN
      END
```

REFERENCES

(1) Stanitz, John D.; and Prian, Vasily D.: A Rapid Approximate Method for Determining Velocity Distribution on Impeller Blades of Centrifugal Compressors. NACA TN 2421, 1951.

(2) Hamrick, Joseph T; Ginsburg, Ambrose; and Osborn, Walter M.: Method of Analysis for Compressible Flow Through Mixed-Flow Centrifugal Impellers of Arbitrary Design. NACA Report 1082, 1952.

(3) Eichenberger, H. P.: A Contribution to the Aerodynamic Design of Mixed-Flow Compressors. ASME Paper No. 57-A-61, July 1957.

(4) Stockman, Norbert O.; and Kramer, John L.: Method for Design of Pump Impellers Using a High-Speed Digital Computer. NASA TN D-1562, 1963.

(5) Katsanis, Theodore: Use of Arbitrary Quasi-Orthogonals for Calculating Flow Distribution in the Meridional Plane of a Turbomachine. NASA TN D-2546, 1964.

(6) Montgomery, John C.: Analytical Performance Characteristics and Outlet Flow Conditions of Constant and Variable Lead Helical Inducers for Cryogenic Pumps. NASA TN D-583, 1961.

(7) Ross, C. C.; and Banerian, G.: Some Aspects of High Suction Specific Speed Pump Inducers. ASME Paper No. 55-A-124, August 1955.

(8) Bosch, H. B.; Cooper, P.; and Stoermer, W. F.: Advanced Inducer Study. ER-5288 (NASA Document No. N63-21124), TRW, Inc., Cleveland, May 1963.

(9) Wu, Chung-Hua: A General Theory of Three-Dimensional Flow in Subsonic and Supersonic Turbomachines of Axial-, and Mixed-Flow Types. NACA TN 2604, 1952.

(10) Yih, Chia-Shun: "Stream Functions in Three-Dimensional Flows". La Houille Blanche, No. 3, 1957, pp. 445-450. Also available as State University of Iowa Reprints in Engineering No. 158.

(11) Maeder, P. F.; and Wood, A. D.: Stream Functions and Transonic Similarity in Three-Dimensional Flow. Technical Report WT-14(OSR-TN-54-339), Division of Engineering, Brown University, October 1954.

(12) Ellis, Gaylord O.; and Stanitz, John D.: Comparison of Two- and Three-Dimensional Potential-Flow Solutions in a Rotating Impeller Passage. NACA TN 2806, 1952

(13) Stahl, H. A.; and Stepanoff, A. J.: Thermodynamic Aspects of Cavitation in Centrifugal Pumps. ASME Paper No. 55-A-136, November 1955.

(14) Stepanoff, A. J.: Cavitation Properties of Liquids. ASME Paper No. 63-AHGT-22, March 1963.

(15) Vavra, M. H.: Aero-Thermodynamics and Flow in Turbomachines. John Wiley & Sons, Inc., 1960.

(16) Ruggeri, Robert S.; and Gelder, Thomas F.: Effects of Air Content and Water Purity on Liquid Tension at Incipient Cavitation in Venturi Flow. NASA TN D-1459, 1963.

(17) Salemann, Victor: Cavitation and NPSH Requirements of Various Liquids. ASME Paper No. 58-A-82, December 1958.

(18) Spraker, W. A.: The Effects of Fluid Properties on Cavitation in Centrifugal Pumps. ASME Paper No. 64-WA/FE-14, December 1964.

(19) Roder, Hans M.; and Goodwin, Robert D.: Provisional Thermodynamic Functions for Para-Hydrogen. NBS TN-130, 1961

(20) Keenan, Joseph H.: Thermodynamics. John Wiley & Sons, Inc., 1956, p. 329.

(21) Marks, L. S.: Mechanical Engineers' Handbook. Fifth Edition, McGraw-Hill Book Co., Inc., 1951, p. 250.

(22) Stanitz, John D.: Two Dimensional Compressible Flow in Turbomachines with Conic Flow Surfaces. NACA Report 935, 1949.

(23) Kramer, James J.; Stockman, Norbert O.; and Bean, Ralph J.: Nonviscous Flow Through a Pump Impeller on a Blade-to-Blade Surface of Revolution. NASA TN D-1108, 1962.

(24) Kramer, James J.; Stockman Norbert O.; and Bean, Ralph J.: Incompressible Nonviscous Blade-to-Blade Flow Through a Pump Rotor with Splitter Vanes. NASA TN D-1186, 1962.

(25) Martin, M. H.: "On the Uniqueness of Harmonic Functions Under Boundary Conditions". Journal of Mathematics and Physics, Volume 17, No. 1, March 1963, pp. 1-13.

(26) Levin, Simon A.: Uniqueness and Nonlinearity. Technical Note BN-354 (NASA Document No. N64-25777, DDC No. AD-602033), University of Maryland, May 1964.

(27) Crandall, Stephen H.: *Engineering Analysis.* McGraw-Hill Book Co., Inc., 1956.

(28) Whittaker, E.; and Robinson, G.: The Calculus of Observations. Fourth Edition, Blackie & Son Limited, 1956.

(29) Marquardt, Donald W.: "An Algorithm for Least-Square Estimation of Non-linear Parameters". SIAM Journal, Volume 11, No. 2, June 1963, pp. 431-441.

(30) Goldfeld, Stephen M.; Quandt, Richard E.; and Trotter, Hale F.: Maximiation by Quadratic Hill-Climbing. Research Memorandum No. 72, Princeton University Econometric Research Program, January 1965.

(31) Soltis, Richard F.; Anderson, Douglas A.; and Sandercock, Donald M.: Investigation of the Performance of a 78° Flat-Plate Helical Inducer. NASA TN D-1170, 1962.

(32) Adams, Harold E.: Pumping Boiling Fluids When the Available Static Head is Zero or Less. ASME Paper No. 63-WA-220, November 1963.

(33) Johnsen, Irving A.; and Bullock, Robert O., editors: Aerodynamic Design of Axial-Flow Compressors. Volume I. NACA RM E56B03, 1956.

(34) Stripling, L. B.; and Acosta, A. J.: Cavitation in Turbopumps - Part I. ASME Paper No. 61-WA-112, December 1961.

(35) Stripling, L. B.: Cavitation in Turbopumps - Part 2. ASME Paper No. 61-WA-98, December 1961.

(36) Jakobsen, J. K.: On the Mechanism of Head Breakdown in Cavitating Inducers. ASME Paper No. 63-AHGT-29, March 1963.

(37) Gouse, S. W. Jr.; and Brown, George A.: A Survey of the Velocity of Sound in Two-Phase Mixtures. ASME Paper No. 64-WA/FE-35, December 1964.

(38) Smith, R. W.: Some Idealized Solutions for Choking, Two-Phase Flow of Hydrogen, Nitrogen and Oxygen. Adv. in Cryogenic Engineering, Volume 8, New York, Plenim Press, 1963, pp. 563-573.

(39) Sandercock, Donald M.; Soltis, Richard F.; and Anderson, Douglas A.: Cavitation and Noncavitation Performance of an 80.6° Flat-Plate Helical Inducer at Three Rotational Speeds. NASA TN D-1439, 1962.

(40) Ruggeri, Robert S.; and Gelder, Thomas F.: Cavitation and Effective Liquid Tension of Nitrogen in A Tunnel Venturi. NASA TN D-2088, 1964.

(41)   Gelder, Thomas F.; and Ruggeri, Robert S.: Incipient Cavitation of Freon-114 in a Tunnel Venturi. NASA TN D-2662, 1965.

(42)   Holl, William J.; and Treaster, A. L.: Cavitation Hysteresis. ASME Paper No. 65-FE-9, June 1965.

(43)   Apostol, Tom M.: Calculus. Volume II. Blaisdell Publishing Co., 1962.

(44)   Spiegel, Murray R.: Vector Analysis. Schaum Publishing Co., 1959.

(45)   Benton, Thomas C.: "An Example of the Need for Two Stream Functions in Three-Dimensional Flows". Quarterly Applied Mathematics, Volume 21, No. 3, October 1963, pp. 235-237.

DISTRIBUTION LIST

Copies	Recipient	Designee
	NASA Headquarters, Washington, D.C. 20546	
1	Contracting Officer, BCA	( )
1	Patent Office, AGP	( )
	NASA Lewis Research Center	
	21000 Brookpark Road, Cleveland, Ohio 44135	
1	Office of Technical Information	(X)
1	Contracting Officer	(X)
1	Patent Office	(X)
	NASA Marshall Space Flight Center	
	Huntsville, Alabama 35812	
1	Office of Technical Information, M-MS-IPC	( )
1	Purchasing Office, PR-CH	( )
1	Patent Office, M-PAT	( )
1	Keith Chandler, R-P&VE-PA	( )
	NASA Western Operations Office	
	150 Pico Boulevard, Santa Monica, California 90406	
1	Office of Technical Information	( )
1	Contracts Management Division	( )
1	General Counsel for Patent Matters	( )
4	Chief, Liquid Propulsion Technology, RPL	(X)
	Office of Advanced Research and Technology	
	NASA Headquarters	
	Washington, D.C. 20546	
26	NASA Scientific and Technical Information Facility	(X)
	P.O. Box 33	
	College Park, Maryland 20740	
1	Mr. Vincent L. Johnson	(X)
	Director, Launch Vehicles and Propulsion, SV	
	Office of Space Science and Applications	
	NASA Headquarters, Washington, D.C. 20546	
1	Mr. Edward L. Gray	(X)
	Director, Advanced Manned Missions, MT	
	Office of Manned Space Flight	
	NASA Headquarters, Washington, D.C. 20546	

Copies	Receipient	Designee
1	Mr. Clarence A. Syvertson Mission Analysis Division NASA Ames Research Center Moffett Field, California 24035	(X)
10	(Technical Monitor) Mr. Werner Britsch Lewis Research Center Cleveland, Ohio 44135	(X)
1	Mr. Loren Gross Marshall Space Flight Center Huntsville, Alabama 35812	

NASA FIELD CENTERS

Copies	Recipient	Designee
2	Ames Research Center Moffett Field, California 94035	Harold Hornby Mission Analysis Div.
2	Goddard Space Flight Center Greenbelt, Maryland 20771	Merland L. Moseson Code 620
2	Jet Propulsion Laboratory California Institute of Technology 4800 Oak Grove Drive Pasadena, California 91103	Henry Burlage, Jr. Propulsion Div., 38
2	Langley Research Center Langley Station Hampton, Virginia 23365	Dr. Floyd L. Thompson Director
2	Lewis Research Center 21000 Brookpark Road Cleveland, Ohio 44135	Dr. Abe Silverstein Director
2	Marshall Space Flight Center Huntsville, Alabama 35812	Hans G. Paul Code R-P&VED
2	Manned Spacecraft Center Houston, Texas 77001	Dr. Robert R. Gilruth Director
2	Western Operations Office 150 Pico Boulevard Santa Monica, California 90406	Robert W. Kamm Director
2	John F. Kennedy Space Center, NASA Cocoa Beach, Florida 32931	Dr. Kurt H. Debus

GOVERNMENT INSTALLATIONS

Copies	Recipient	Designee
1	Aeronautical Systems Division Air Force Systems Command Wright-Patterson Air Force Base	D. L. Schmidt Code ASRCNC-2
1	Air Force Missile Development Center Holloman Air Force Base, New Mexico	Maj. R. E. Bracken Code MDGRT
1	Air Force Missile Test Center Patrick Air Force Base, Florida	L. J. Ullian
1	Air Force Systems Division Air Force Unit Post Office Los Angeles 45, California	Col. Clark Technical Data Center
1	Arnold Engineering Development Center Arnold Air Force Station Tullahoma, Tennessee	Dr. H. K. Doetsch
1	Bureau of Naval Weapons Department of the Navy Washington, D. C.	J. Kay RTMS-41
1	Defense Documentation Center Headquarters Camerson Station, Building 5 5010 Duke Street Alexandria, Virginia 22314 ATTN: TISIA	
1	Headquarters, U. S. Air Force Washington 25, D. C.	Col. C. K. Stambaugh AFRST
1	Picatinny Arsenal Dover, New Jersey 07801	I. Forsten, Chief Liquid Propulsion Laboratory, SMUPA-DL
1	Air Force Rocket Propulsion Laboratory Research and Technology Division Air Force Systems Command Edwards, California 93523	RPRR/Mr. H. Main

GOVERNMENT INSTALLATIONS

Copies	Recipient	Designee
1	U. S. Atomic Energy Commission Technical Information Services Box 62 Oak Ridge, Tennessee	A. P. Huber Oak Ridge Gaseous Diffusion Plant (ORGDP) P O. Box P
1	U. S. Army Missile Command Redstone Arsenal Alabama 35809	Dr. Walter Wharton
1	U. S. Naval Ordnance Test Station China Lake California 93557	Code 4562 Chief, Missile Propulsion Div.

CPIA

1	Chemical Propulsion Information Agency Applied Physics Laboratory 8621 Georgia Avenue Silver Spring, Maryland 20910	Neil Safeer

INDUSTRY CONTRACTORS

Copies	Recipient	Designee
1	Aerojet-General Corporation P. O. Box 296 Azusa, California 91703	L. F. Kohrs
1	Aerojet-General Corporation P. O. Box 1947 Technical Library, Bldg. 2015, Dept. 2410 Sacramento, California 95809	R. Stiff
1	Aeronautronic Philco Corporation Ford Road Newport Beach, California 92663	D. A. Carrison
1	Aerospace Corporation 2400 East El Segundo Blvd. P. O. Box 95085 Los Angeles, California 90045	John G. Wilder MS-2293 Propulsion Dept.
1	Arthur D. Little, Inc. 20 Acorn Park Cambridge, Massachusetts 02140	E. Karl Bastress
1	Astropower Laboratory Douglas Aircraft Company 2121 Paularino Newport Beach, California 92663	Dr. George Moc Director, Research
1	Bell Aerosystems Company P. O. Box 1 Buffalo, New York 14240	W. M. Smith
1	Northrop Space Laboratories 3401 West Broadway Hawthorne, California	Dr. William Howard
1	Stanford Research Institute 333 Ravenswood Avenue Menlo Park, California 94025	Lionel Dickinson
1	TRW Systems TRW Incorporated One Space Park Redondo Beach, California 90278	G. W. Elverum

INDUSTRY CONTRACTORS

Copies	Recipient	Designee
1	Research Laboratories United Aircraft Corporation 400 Main Street East Hartford, Connecticut 06108	Erle Martin
1	Bendix Systems Division Bendix Corporation 3300 Plymouth Road Ann Arbor, Michigan	John M. Brueger
1	Boeing Company P. O. Box 3707 Seattle, Washington 98124	J. D. Alexander
1	Missile Division Chrysler Corporation P. O. Box 2628 Detroit, Michigan 48231	John Gates
1	Wright Aeronautical Division Curtiss-Wright Corporation Wood-Ridge, New Jersey 07075	G. Kelley
1	Missile and Space Systems Division Douglas Aircraft Company, Inc. 3000 Ocean Park Boulevard Santa Monica, California 90406	R. W. Hallet Chief Engineer Advanced Space Tech.
1	Aircraft Missiles Division Fairchild Hiller Corporation Hagerstown, Maryland 10	J. S. Kerr
1	General Dynamics/Astronautics Library & Information Services (128-00) P. O. Box 1128 San Diego, California 92112	Frank Dore
1	Re-Entry Systems Department General Electric Company 3198 Chestnut Street Philadlphia, Pennsylvania 19101	F. E. Schultz

INDUSTRY CONTRACTORS

Copies	Recipient	Designee
1	Advanced Engine & Technology Dept. General Electric Company Cincinnati, Ohio 45215	D. Suichu
1	Grumman Aircraft Engineering Corp. Bethpage, Long Island New York	Joseph Gavin
1	Lockheed California Company 2555 North Hollywood Way Burbank, California 91503	G. D. Brewer
1	Lockheed Missiles and Space Co. Attn: Technical Information Center P. O. Box 504 Sunnyvale, California 94088	Y. C. Lee
1	Lockheed Propulsion Company P. O. Box 111 Redlands, California 92374	H. L. Thackwell
1	The Marquardt Corporation 16555 Staticoy Street Van Nuys, California 91409	Warren P. Boardman, Jr.
1	Baltimore Division Martin Marietta Corporation Baltimore, Maryland 21203	John Calathes (3214)
1	Denver Division Martin Marietta Corporation P. O. Box 179 Denver, Colorado 80201	J. D. Goodlette (A-241)
1	McDonnell Aircraft Corporation P. O. Box 516 Municipal Airport St. Louis, Missouri 63166	R. A Herzmark
1	Space & Information Systems Division North American Aviation, Inc. 12214 Lakewood Boulevard Downey, California 90241	H. Storms

INDUSTRY CONTRACTORS

Copies	Recipient	Designee
1	Rocketdyne (Library 586-306) North American Aviation, Inc. 6633 Canoga Avenue Canoga Park, California 91304	E. B. Monteath
1	United Technology Center 587 Methilda Avenue P. O. Box 358 Sunnyvale, California 94088	B. Abelman
1	Aerospace Operations Walter Kidde and Company, Inc. 567 Main Street Belleville, New Jersey 07109	R. J. Hanville Director of Research Engineering
1	Florida Research and Development Pratt and Whitney Aircraft United Aircraft Corporation P. O. Box 2691 West Palm Beach, Florida 33402	R. J. Coar
1	Rocket Research Corporation 520 South Portland Street Seattle, Washington 98108	Foy McCullough, Jr.
1	Pennsylvania State University P. O. Box 30 State College, Pa. 16801	Dr. Wislicenus
1	Iowa State University Department of Mechnical Engineering Ames, Iowa	Dr. Serovy
1	Worthington Corporation 401 Worthington Avenue Harrison, New Jersey 07029	Mr. Walter Jekat